SOFT ROBOTICS BY INTEGRATING STRUCTURE, MATERIALS, FLUIDS, CONTROL DESIGN, AND SIGNAL PROCESSING USING THE TENSEGRITY PARADIGM

A Dissertation

by

MUHAO CHEN

Submitted to the Office of Graduate and Professional Studies of
Texas A&M University
in partial fulfillment of the requirements for the degree of

DOCTOR OF PHILOSOPHY

Chair of Committee,	Robert E. Skelton
Co-Chair of Committee,	Manoranjan Majji
Committee Members,	Freddie Witherden
	Pilwon Hur
Head of Department,	Srinivas Rao Vadali

May 2021

Major Subject: Aerospace Engineering

ABSTRACT

We should give the soul of soft robotics by enlarging the concepts of structure design, material science, fluid mechanics, control theory, and signal processing to embrace the more noble task of system design. By system design, we refer to design the components that make up the system, given only the requirements of the overall system. The fundamental challenge is to create theories of system modeling. The existing design approaches deal with what is sufficient rather than necessary, locked into the classical thinking of component technology. That is, design the structure first, followed by material studies and fluid analysis, and add control and signal processing later. The critical question that we should ask is that whether dramatic performance improvements are possible by combining different disciplines as a communal pool of resources such that engineers in different disciplines have more freedom and can talk to each other in design space to solve a joint optimization problem.

This research studies the approaches to the system design of soft robotics by integrating structure, materials, fluids, control design, and signal processing using the tensegrity paradigm. Biological systems perhaps provide the greatest evidence that tensegrity is the most efficient structure. Thus, the tensegrity paradigm is chosen for this study.

In this research, we first developed the tensegrity structure minimal mass design methods by nonlinear optimizations. This approach allows one to design any solid or hollow bar tensegrity structures with any given external forces (w/o gravity) subject to the structure equilibrium conditions and the maximum stress constraints of structure members (strings yield, bars yield or buckle).

Secondly, the tensegrity system dynamics in fluids are derived and studied in two aspects: 1). Tensegrity structures interface fluid directly. Both Class-1 and Class-k tensegrity dynamics with fluid forces incorporated are formulated. 2). Tensegrity structures interface fluid by a skin (membrane) on the structure. The fluid forces are transferred to the structure by the skin on the tensegrity structure. The algorithms enable our ability to perform Fluid-Structure Interaction (FSI) studies of any fluid-based (underwater or in the air) tensegrity structures.

Thirdly, general tensegrity dynamics equations based on the Finite Element Method (FEM) and the Lagrangian method with nodal coordinate vectors as the generalized coordinates are presented. This approach allows one to perform nonlinear dynamics, linearized dynamics, and modal analysis of any tensegrity structures with elastic or plastic deformations subject to any boundary constraints.

Then, to achieve shape control of tensegrity robots, a nonlinear model-based control law is derived. The control variables (force densities in the strings) appear linearly in the nonlinear control. To study the control performance, we demonstrated a shape controllable tensegrity airfoil, whose topology is based on shape accuracy. This shape control method is suitable for the control of any general tensegrity robots.

Finally, a systematic design approach to integrating the sensor/actuator selection (SAS) and covariance control design for tensegrity robots are also studied. The SAS method and the feedback control law problem are converted into an equivalent convex problem, given by a set of LMIs (linear matrix inequalities). The principles can be used to guide sensor and actuator selections, analyze the system performance, and work as an interface to integrate structure, control, and signal processing designs. The theories developed in this research include but are not limited to tensegrity structures.

ACKNOWLEDGMENTS

This section is limited to four pages, so I have some space to share and record what has been kept in my mind in these years. I want first to thank my advisor, Prof. Robert E. Skelton, for his great help, guidance, and support in my study and research. His experience, perspective, and passion for life and research will be continuing influencing my life and career in years to come. Prof. Skelton has more than ten years of work experience in the industry and about fifty years of experience in teaching and research. I will keep benefiting for life long from his wealth in knowledge, vision in the future, diligence in work, rigors in research, optimistic attitude about life, strong will, creative minds, and critical thinking. Here, I want to list some of the most important things I have learned from him on studying, doing research, and work.

How to study?

1. The only purpose of school is learning how to learn. 90% of what you might learn of a given subject will be outdated in five years after you leave, so you have to learn how to learn new things to catch up with a career in engineering.

2. There is no enough time for the professor to say anything that you need to learn, so the professor is capsulizing isolated information. The students have to integrate them, spend three hours outside class for every 1 hour inside the class to integrate the material to master it with the lectures given.

3. Many students spend 10% of time on the book and 90% of time on homework, which is wrong. Students should spend the most time understanding the concepts and theory. The homework is trivial. It is what you put in the hours, not how many hours you put in.

4. Most students read a book, from concept, example, and follow the author's solution. You are deceiving yourself, thinking that you could do that because it is easier to follow someone's logic than generate logic yourself. The way you read a book is you read the concept, the statement of the example, and solve it by yourself. Now, you got stuck, and put some mantle energy in it and then see what the author did. You are prepared to see the truth.

5. Read the lecture before you hear the lecture. Come to class with questions because if you have questions, you are teaching your head. The class either answers the question, or you ask it. So do not leave the room without your question being answered.

6. Work for understanding, not for grades. Photographic memory is not learning anything. You are supposed to know something. A short-term memory will go in two weeks. This is a disaster.

7. Mature in the study, nobody tells you what kind of books to read, what examples to do, you have to learn what to do, spend your time wisely. Do not be spoon-fed. Students will develop a dependence on someone else to ask the questions, and they are just answering those questions. It is not good because knowing what questions to ask is the most important thing in research.

8. From machine language to machine learning, the world is changing rapidly. However, you should know the fundamentals, and these are the building blocks for the entire engineering world.

How to do research?

1. Find the right time to go to the library, because for a given topic, you may come up with some original ideas which can be the best in the world. If you check other people's work too early, your thoughts will be limited.

2. Prove the theory by yourself, put something in your head, teaching by yourself.

3. Present what you know, be responsible for everything you put on your slides. Well prepare the slides, label pictures, see them in different aspects and times, know exactly what you put in the slides. Welcome to all kinds of questions on your topic or presentations; they are helping you.

4. Be honest. There is nothing wrong to say I don't know, and I didn't do that. Everybody has a boundary in knowledge. Confidence in what you know, dare to say what you are not sure, and you don't know.

5. Think about your problem while you are eating, sleeping, and working. One day, the light bulb will light up. After your bulb lights up, it will never go out.

6. Be excited about your topic and spend as much time as you can to work it out. This is building your career, not your advisor's.

7. You will benefit more from strict professors, he is helping you.

8. State problem step by step, do not jump, think it deeply, solve it, and then move to another.

8. State the problem precisely by using mathematical language. Theory in math is a poem.

10. It is more important to ask the right question.

How to work?

1. Work extremely hard.

2. Be thankful to your advisor. He is the man who is feeding you right now.

3. Tell your manager what you know and what you should say, not what the manager wants to hear. Because he is the man to make decisions where the money should be spent, he might not be an expert in your area, so you are responsible for what you know. It is your fault that if money is wasted or not spend wisely.

4. Answer a question short before you give a detailed description or explanation. It is more difficult but more important to say or describe something in a short sentence than a longer one.

5. When you write something, all your fame is on that. You should be crystal clear. When you go to the museum and see the beautiful arts, you can see the fingerprints left by that artist. You can feel the time and labor work in it. When you write something, read it several times, you can always find a better way to describe it.

I want to thank Prof. Manoranjan Majji. I have learned a lot from him as well in various aspects: research, communication skills, project management, time management, and collaboration. Prof. Majji is very knowledgeable. I learned and benefit from his perspective and experience in engineering. He can quickly capture the major issues of the problem and is also good at tearing complex and hard engineering problems into smaller mathematical ones that are both practical and easy to handle. He also taught me many communication skills with technical and non-technical professionals. His diligence in work and positive attitude towards life encourages me a lot as well.

I want to thank Prof. Freddie Witherden and Prof. Pilwon Hur for serving on my doctoral committee. I want to thank Prof. Witherden for having a few research discussions with him. His insight in research is sharp, in-depth, and helpful. Prof. Hur has a very good reputation in the Department of Mechanical Engineering, I luckily attended his short lecture on control three years

ago, and I still remember that his passion and devote to robotics encouraged the audience a lot.

I want to thank our great research group and LASR Lab. Dr. Raman Goyal, his sharp mind and precise in math, influenced and helped me a lot. Haresh Karnan, I learned a lot from his practical skills in research, and his cheerful mood in life infects all the people around him. Yuling Shen, I want to thank him for his much help in both life and research. Prof. Shuo Ma, I enjoy doing sports with him and appreciate the many helpful discussions in pushing research ideas. Christopher Plantz, I enjoy discussing research and share life stories with him. Dr. Xiaowen Su, her patience in dealing with the complex electromagnetic equations, impressed me greatly, and I learned a lot about this field from her. Prof. Edwin Peraza Hernandez, his professionalism at work and research is like a lighthouse. Dr. Jun Chen, her rigorous math, influenced me a lot, and she taught me to identify the major part of fluids. Dr. Utku Boz, I had a deeper understanding of D-Bar structures from his equations. Dr. Maziar Izadi, his codes are professional. Dr. Shuhui Jiang, her diligence treats all year 365 days like one normal day. Xiaolong Bai, I miss the cozy coffee research time. Vishala, she is always happy and cares about others. Jiacheng Liu, his enthusiasm for coding and algorithms motivate people around him, and I learned a lot of programming skills from him. David Capps, his hands-on skill in making models, i.e., tensegrity domes, is elegant. Tyler Bryant, we had many helpful discussions on space systems. Ran Wang, a cool guy and friend indeed. Xuan Yang, a knowledgeable storyteller, I learned a lot about airplanes, rockets, and space from him.

I want to thank my parents, Cong Chen, Wenbo Chen, Ruichen Chen, and Kangying Zhou. These years, being 7751.23 mi. away from them, I was not able to do much for them, but I can feel the strongest support, greatest encouragement, and selfless love from every single call with them.

I want to thank the great faculties and nice staff in the Department of Aerospace Engineering, Texas A&M University, for their wonderful lectures and kindness in helping students.

Special thanks to Judy Skelton. For so many times, we students held Prof. Skelton in research meetings on off-work hours, weekends, and holidays in the office, at home, or in the garage. But she is always so nice and patient. I also want to thank her for her greetings, warm care, delicious Thanksgiving and Christmas dinners, and kindness in helping me get in touch with Prof. Skelton.

CONTRIBUTORS AND FUNDING SOURCES

Contributors

This work was supported by a dissertation committee consisting of Professor Robert E. Skelton, Professor Manoranjan Majji of the Department of Aerospace Engineering, Professor Freddie Witherden of the Department of Ocean Engineering, and Professor Pilwon Hur of the Department of Mechanical Engineering.

Part of this research was conducted as part of a collaborative effort. A previous postdoc Dr. Jun Chen contributed to the discussion of the tensegrity dynamics in fluids, and visiting student Dr. Shuo Ma contributed to the discussion of the finite element method. Their work and the guidance from my advisor Dr. Skleton have led my research in the right direction. The tool used in the airfoil research, namely XFOIL, is an open-source tool developed by third parties. Usage of the tool has been duly cited in the dissertation.

All other work conducted for the dissertation was completed by the student independently.

Funding Sources

Graduate study was supported by a graduate research assistantship and AERO Grad Excellence fellowship from the Department of Aerospace Engineering, Texas A&M University. The research project was funded by Texas A&M University Chancellor's Research Initiative, No. 02-292113-10000, NASA Innovative Advanced Concepts (NIAC) phase I and phase II projects, Maestro ID M1603020, and Texas A&M Triad for Transformation (T3) initiative.

TABLE OF CONTENTS

Page

LIST OF FIGURES

FIGURE Page

LIST OF TABLES

TABLE Page

1. INTRODUCTION AND MOTIVATION

1.1 Motivation

Interdisciplinary Engineering: A typical structural control or robotics design problem normally contains the design of these components: structure, materials, manufacturing, construction, sensing, computing algorithm, signal processing, and control design. Engineering universities teach these isolated disciplines. Currently, the theory and education for these isolated disciplines are quite mature. However, their interactions, which describe the behavior of the interaction of all the isolated disciplines, are still quite immature.

However, it is straightforward to ask these questions: Why we need to integrate different disciplines, is there any benefit? How to integrate different disciplines? Should we start at the state of the art of each discipline? Or should we simply add control after the structure is designed? Or should we spend more money and effort on the negotiation of engineers with different backgrounds? While this is the tradition, and indeed there are many useful applications in retrofitting, this isolation is not the way to obtain the best performance. Synergy is a popular idea, but when is the whole less than the sum of the parts. The answer is usually. Because we over-design components for lack of coordination in their design or waste money on components that are not necessary or make a component much more precise than required.

A misconception is that "The best system is made from the best components". That is certainly not true. Often, we gain more in integrating two disciplines than making exceptional improvements in one discipline. For example, in the airplane wing, aerodynamics engineers first designed the best shape based on their knowledge in fluid dynamics, then the control engineer came and break the beautiful shape for control objectives. This is certainly not the right way. A systematic approach would be to modify shape not by pushing against a reference equilibrium but by modifying the equilibrium. Of course, this would require much less control effort.

It is important to identify the performance-limiting technologies in a system, such as manufacturing

precision, signal processing and control algorithms, computational precision, better models for physics, location of sensors and actuators, etc. However, a system theory is not available that even allows us to answers these questions. Now, the fact is that there are no instructions on how to put the isolated and sophisticated component technologies together. We believe that the next great challenge in engineering is integrating the different disciplines to embrace the much more general problem of system design. By *system design* we refer to given the requirements of the overall system, find the design components that make up the system. This thesis takes some steps toward system design: *the integration of structure, fluids, materials, control, and signal processing*.

The Tensegrity Paradigm: Now, the question becomes what kind of structure would be a suitable paradigm for the integration of various engineering disciplines? For decades, people are also trying to integrate structure and control design by bending and torturing classical continua with control forces to make the systems do something that they did not want to do. This is neither structure effective nor control efficient. Instead of forcing continua and adding actuators to the old paradigm such as beams, plates, and shells, the integration of the structure and control disciplines should begin by looking for a new paradigm, looking for ways to integrate choices of structure design, material, and control architecture. Biological systems perhaps provide the greatest evidence that tensegrity is the most efficient structure. Many of the macro and microbiological structures are consistent with tensegrity models. For example, in the living cells, micro-filaments and micro-tubules are working as tensile and compressive members to control the substrate traction [1], shown in Figure 1.1. The structure of DNA bundles is consistent with a tensegrity prism structure [2], shown in Figure 1.2. In human bones, muscles, elbows, spines, they are all tensegrity structures [8, 9], shown in Figure 1.3. Even in the spider fiber, there are also tensile and compressive members in its molecular structures [10].

Tensegrity is a coined word: tension and integrity, by Buckminister Fuller [11] for the art form created by Ioganson (1921) and Snelson (1948) [12]. The tensegrity system is a stable network of compressive members (bars/struts) and tensile members (strings/cables). By definition, it is clear that the most fundamental property of the tensegrity system is that all the one-dimensional

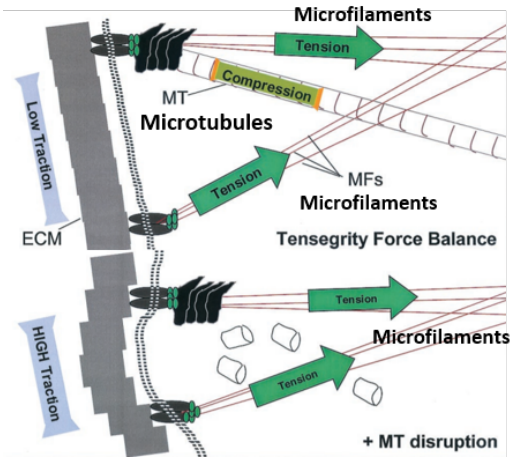

Figure 1.1: Mechanical behavior in living cells consistent with the tensegrity model. Reprinted from [1].

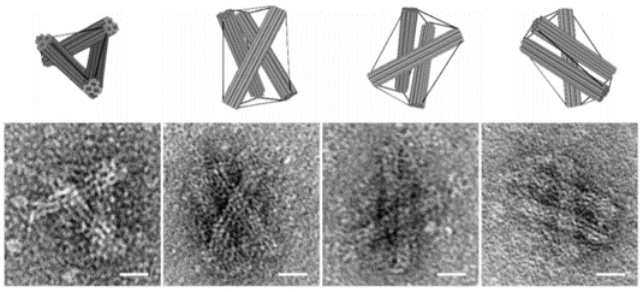

Figure 1.2: Electron micro-graphs and cylinder models of DNA tensegrity prisms. Reprinted from [2].

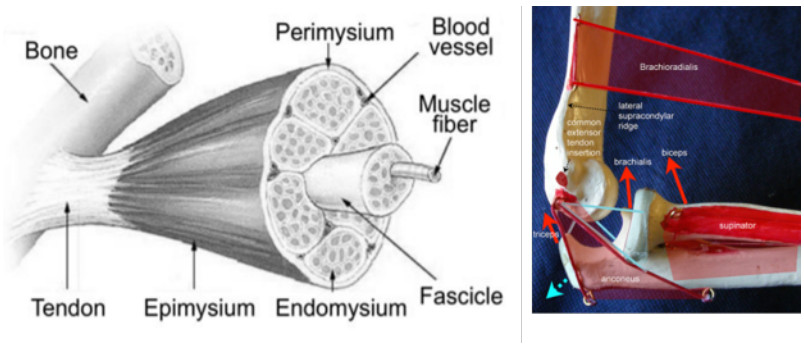

Figure 1.3: Bone, muscle, and intramuscular connective tissue. Reprinted from [3] (left). Hhuman right elbow. Reprinted from [4] (right).

structural members are axially loaded [13]. That is to say, the overall structure can be designed along the load path to make the best of each structure member since bars are best in taking compression, and strings are best in taking tension. In fact, a few research on form-finding [14, 15, 16] and topology optimization [17, 18, 19] have shown the ways to find the optimal load path and to locate structure members with given design objectives.

After decades of study, tensegrity structure has demonstrated its many advantages: 1. Mass efficiency: the material is only needed in the essential load path, not the orthogonal one [20, 21, 17]. Tensegrity networks can be arranged to achieve strength with little mass. Minimum mass structure solutions for five fundamental loading conditions in engineering mechanics (compression [22], tension [23], cantilever [13], torsion [24], and simply supported [25]), as shown in Figure 1.4. 2. Tension stabilizing: One can change shape/stiffness without changing stiffness/shape [26, 27, 28]. 3. Accurate model: there is no material bending, the deformation of each structure member is only one dimensional, so the uncertainty is only in one direction. Thus, we can get better stability margins with dedicated materials [29]. Moreover, more accurate structure models can give more precise control [30]. 4. Less control energy: the flexible structure has an infinite number of equilibrium states. By sliding along the equilibrium, less control energy is required to morph and maintain the structure shape [31, 32]. 5. Redundant control inputs (both strings and bars can be actuators) provide robustness. 6. Energy absorber/harvester: the soft structure and strings can be used to absorb impact energy [33, 34, 35, 36]. 7. Promote the integration of structure and control design [7, 37, 38]. Thus, tensegrity structures provide a promising paradigm for integrating these disciplines.

1.2 Contributions of This Dissertation

This dissertation contains innovative work on soft robotics by integrating structure, materials, fluids, materials, and control design using the tensegrity paradigm. The major contributions are listed below:

1. Provided a general approach for the minimal mass design of any solid or hollow bar tensegrity structures with any given external forces (w/o gravity) subject to the structure equilibrium

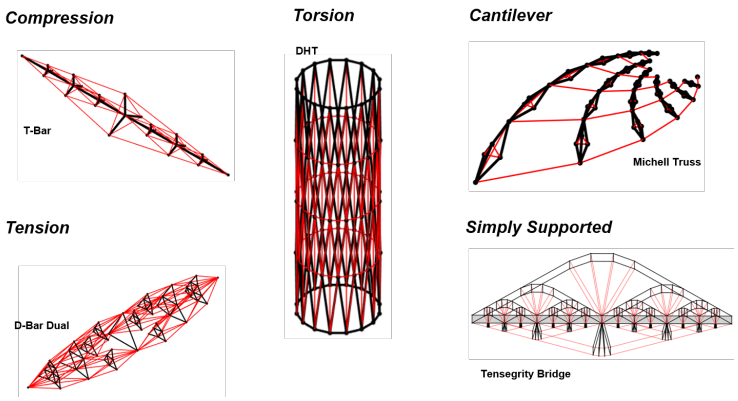

Figure 1.4: Tensegrity solutions to the five fundamental problems in engineering mechanics.

conditions and the maximum stress constraints of structure members (strings yield, bars yield, or buckle) in a compact matrix form. The methodology yields several nonlinear programming problems. The principles developed in this research demonstrate a fundamental insight into both materials and structures.

2. Presented the study of tensegrity system dynamics in fluids, 1). tensegrity structures interface fluid directly. 2). tensegrity structures interface fluid by a skin (membrane) on the tensegrity structure. For the first one, we developed Class-1 and Class-k tensegrity dynamics with fluid force incorporated. For the second one, we demonstrated how the fluid forces can be transferred to the structure by the skin on the tensegrity structure. This work enables the ability to do fluid-structure interaction studies of any tensegrity structures. The principles developed here can also be used for analyzing various kinds of tensegrity structures operating in the air or underwater.

3. Developed a finite element analysis approach to nonlinear and linearized tensegrity dynamics based on the Lagrangian method with nodal coordinate vectors as the generalized coordinates. The developed approach is capable of conducting comprehensive dynamics studies for any tensegrity structures, including rigid body dynamics, FEM dynamics (bars and strings can have elastic or plastic deformations), dealing with various kinds of boundary conditions, and accurate modal analysis. This study provides a deep insight into structures, materials,

performances, as well as an interface towards integrating control theories.

4. Nonlinear model-based shape control algorithm for Class-1 and Class-k structures with massless/massive strings. This work paves a road towards integrating structure and control design. The principles developed here can also be used for 3D morphing airfoil design and control of various kinds of tensegrity structures.

5. Presented a systematic design approach to integrating the economic sensor/actuator selection and covariance control design for tensegrity robots. The principles developed in this chapter can be used to analyze the performance of various types of structures as well as an interface to integrate structure, control, and signal processing designs. These methods include but are not limited to tensegrity structures.

1.3 Outline of this Dissertation

Chapter 1 introduces the main themes of this dissertation and the critical issues of interdisciplinary engineering for structural control and the tensegrity paradigm.

Chapter 2 presents an integration of structures and materials for the static design of tensegrity structures. We provide a general approach to the minimal mass design of tensegrity structures with solid and hollow bar cross-sections subject to any given external forces and gravity. The load stability of structural members is assured by checking the modes of failure of all the structure members, and global stability is guaranteed by solving a linear matrix inequality with the derived stiffness matrix. The methodology yields several nonlinear programming problems. The influence of cross-section of bars and joints on structure mass is also discussed. The algorithms are verified by D-Bar examples. A deployable tensegrity tower in the presence of lunar gravity to support space mining is also designed and studied.

Chapter 3 presents an integration of structures and fluids for the analysis of the dynamics of tensegrity structures. This chapter has two major parts based on how the fluid and tensegrity structures are interfaced with each other: 1). tensegrity structures interface fluid directly. 2). tensegrity structures interface fluid by a skin (membrane) on the tensegrity structure. For the first

part, this chapter provides compact vector and matrix forms of the nonlinear dynamics of class-1 and class-k tensegrity systems with fluid forces incorporated. For the second part, this chapter studies tensegrity airfoil/hydrofoil interfaces fluid by the skin on the structure. The fluid forces on the foil surface are obtained by the panel method. Then, we develop a method for discretizing continuous airfoil curves based on shape accuracy. This method is compared with conventional methods (i.e., evenly spacing and cosine spacing methods). A tensegrity topology for shape controllable airfoil is proposed. The surface fluid forces are integrated into the surface supporting nodes of the structure, which can be used as the external force to simulate the tensegrity system dynamics. Finally, the airfoil and hydrofoil examples are studied and compared to demonstrate the approach.

Chapter 4 presents a finite element analysis approach to nonlinear and linearized tensegrity dynamics based on the Lagrangian method with nodal coordinate vectors as the generalized coordinates. In this chapter, nonlinear tensegrity dynamics with and without constraints are first derived. The equilibrium equations in three standard forms (in terms of nodal coordinate, force density, and force vectors) and the compatibility equation are also given. Then, we present the linearized dynamics and modal analysis equations with and without constraints. The developed approach is capable of conducting the following comprehensive dynamics studies for any tensegrity structures accurately: 1. Performing rigid body dynamics with acceptable errors, which is achieved by setting relatively high stiffness for bars in the simulation. 2. Simulating FEM dynamics accurately, where bars and strings can have elastic or plastic deformations. 3. Dealing with various kinds of boundary conditions, for example, fixing or applying static/dynamic loads at any nodes in any direction (i.e., gravitational force, some specified forces, or arbitrary seismic vibrations). 4. Conducting accurate modal analysis, including natural frequency and corresponding modes. Three examples, a double pendulum, a cantilever truss with external force, and a double prism tensegrity tower, are carefully selected and studied. The results are compared with rigid body dynamics and FEM software ANSYS.

Chapter 5 presents a general approach of design, dynamics, and control for tensegrity morphing

airfoils. Based on reduced order Class-k tensegrity dynamics, a nonlinear shape control law for any tensegrity systems is derived. A morphing tensegrity airfoil example is given to demonstrate successful shape control. The approach can be used for the shape control of any tensegrity structures.

Chapter 6 presents a systematic design approach to integrate the economic sensor/actuator selection and covariance control design for tensegrity robots. The objective is to minimize the output covariance of the tensegrity robots subject to the specified sensor/actuator budget and control covariance upper bounds by solving the precision of sensor/actuator and output feedback control law problems simultaneously. To achieve this goal, we first derived the linearized tensegrity dynamics with any constraints by taking the total derivative of the nonlinear tensegrity dynamics and keeping the linear terms. Followed by an uncertainty study of joints in the tensegrity structures with no control. Then, together with a linear dynamic output-feedback controller, we give the closed-loop system formulation. The economic sensor/actuator selection method and the feedback control law problem are converted into an equivalent convex problem, given by a set of LMIs (linear matrix inequalities). To verify the proposed algorithms, the error of the nonlinear and linearized dynamics are first compared and checked. A 2D tensegrity morphing airfoil is then implemented to examine the integrated algorithm.

Chapter 7 summarizes the major conclusions of the work.

2. INTEGRATING STRUCTURE DESIGN AND MATERIALS: STATIC DESIGN OF TENSEGRITY STRUCTURES*

This chapter provides a general approach to the minimal mass design of any solid or hollow bar tensegrity structures with any given external forces subject to the structure equilibrium conditions and the maximum stress constraints of structure members (strings yield, bars yield, or buckle) in a compact matrix form. The methodology yields several nonlinear programming problems. Local stability is assured by checking the modes of failure of all the structure members, and global stability is guaranteed by solving a linear matrix inequality with the derived stiffness matrix. To further reduce mass, the choice of the cross-section of bars is also discussed. For practical problems, joint mass is considered as a penalty to the total structure mass. The principles developed in this chapter demonstrate a fundamental insight into both materials and structures.

2.1 Introduction

There are five fundamental problems in engineering mechanics: compression, tension, torsion, cantilever, and simply supported. Each subject has been well studied in continuum mechanics for hundreds of years. However, does continuum guarantee a minimal mass structure? The answer is not always. In fact, the minimal mass solution to all these five fundamental questions is tensegrity structures. For example, Skelton and de Oliveira [39] proved T-Bar and D-Bar systems cost much less mass than a single continuum bar in taking compression. Inspired by spider fiber, Skelton and Nagase demonstrated an efficient tensile tensegrity structure with required stiffness constraints [40]. Nagase and Skelton presented the design of double helix tensegrity (DHT) Structures, which requires less mass to take torsional loads than continuum cylinders [24]. Ma et al. showed that a discrete tensegrity truss is more mass efficient in taking cantilever load [18]. Gerardo et al. demonstrated a mass efficient tensegrity bridge for taking simply supported loads [25].

To design a tensegrity structure, there are two critical issues: 1. specify the connection patterns

*Part of this chapter is reprinted with permission from "A general approach to minimal mass tensegrity" by Muhao Chen and Robert E. Skelton, 2020. Composite Structures, Volume 248, 112454, Copyright [2020] by Elsevier Ltd.

of bars and strings. 2. determine the thickness of all the structure members. The first one is called a form-finding problem, which has been widely studied. For example, Tibert and Pellegrino classified and discussed the properties of kinematical and static form-finding approaches for tensegrity structures [41]. Milenko et al. presented a general form-finding method for symmetric tensegrity structures with shape constraints [42]. Zhang et al. derived an efficient form-finding method based on the structural stiffness matrix, and the total potential energy [43]. Koohestani proposed a computationally efficient algorithm for the analytical form-finding of tensegrity structures [14]. Lee et al. implemented a genetic algorithm by using the force density method to get tensegrity structure topology [17]. The second one is called a minimal mass problem. Few studies have been conducted. For example, Skelton and de Oliveira introduced a minimal mass method by introducing a self-similar fractal considering yielding and buckling of structures [39]. Nagase and Skelton presented major aspects of minimal mass tensegrity problems, but the linear programming algorithms they presented are for bar and string yielding calculations [44]. Carpentieri et al. gave a minimal mass design of tensile reinforcements of masonry structures with arbitrary shapes [45]. Fraternali et al. showed a topology optimization and minimal mass design strategy for masonry domes and vaults [46].

However, none of them present a minimal mass design approach to solid and hollow bar tensegrity structures without prescribing the mode of failure of bars as well as considering the structure gravity, stiffness, and structure member cross-sections. This chapter presents a systematic minimal mass tensegrity framework in a compact matrix form. The principles developed in this chapter can be used to compute the minimal mass and stiffness of solid and hollow bar tensegrity structures considering yielding and buckling constraints of each structural member with or without gravity.

This chapter is structured as follows: Section 2.2 gives the definition of tensegrity structures and assumptions for static structure designs. Section 2.3 defines the notations of nodal coordinate, connectivity, structure member, and external force matrices. Section 2.4 formulates the tensegrity equilibrium equation in terms of force densities in the strings and bars. The force density is used

as the variable to link structure equilibria, structure mass, and structure stiffness. Section 2.5 derives the minimal mass tensegrity design formulation for both solid and hollow bar tensegrity structures in terms of structure force density. Section 2.6 presents the minimal mass tensegrity design algorithms for both solid and hollow bar tensegrity structures w/o gravity. A 2D D-Bar example is examined to verify the developed algorithms. Section 2.7 derives the general form of structure stiffness for both solid bar and hollow bar tensegrity. Section 2.8 presents an algorithm to design minimal mass tensegrity structure subject to gravity and global buckling. Section 2.9 shows a way of mass saving by changing the shape of bar cross-sections of both solid and hollow bar tensegrity. Section 2.10 discusses the joint mass penalty for practical considerations. Section 2.11 demonstrates a 3D T_5D_1 deployable lunar tower to support lunar mining. The details of topology design, deployment, the study of design parameters, drag analysis, and material studies are given. And Section 2.12 presents the conclusions.

2.2 Tensegrity Structure Definition and Assumptions

For engineering study and application purposes, we must start with definitions and assumptions of the word *tensegrity* and then show the mathematical formulations. The tensegrity has both compressive and tensile parts, and we label the compressive ones as *bars* and tensile ones as *strings*. Strings and bars may be connected to each other at their nodes, and the connection pattern is denoted as *connectivity*. We also distinguish the connections of strings and the connections of bars and call them *string connectivity* and *bar connectivity*. The forces that do not come from strings within the structure are defined as *external forces*. Then, the definition of *tensegrity* is as follows [5].

Definition 2.2.1. *The tensegrity or tensegrity structure or tensegrity system is a stable network of bars and strings, where bars only take compression and strings only take tension.*

From the definition, it is clear that there is no bending in the materials. This is a great advantage in proving us actuate system models because models who have materials bending are not as accurate as those who do not have [39]. In a tensegrity structure, if all the bars are hollow pipes,

we call the structure *hollow bar tensegrity*; if all the bars are solid rods, we call the structure *solid bar tensegrity*. Based on the pattern of how bars and strings are connected, the tensegrity structures can be classified: 1). *Class-0 structure*, the structure is a pure string to string network; 2). *Class-1 structure*, bars in the tensegrity network are only connected to strings; 3). *Class-k structure*, bars in the tensegrity network are connected to other bars, and the maximum number of bars connected to one node in the structure is k ($k \geq 2 \in \mathbb{N}$). To establish the mathematical descriptions of static laws and minimal mass design approaches for any tensegrity structures, our assumptions are listed as follows.

Assumption 2.2.1. *The structural members (bars and strings) in the tensegrity system have these properties:*

1. The structural members are axially loaded. There is no material bending.

2. All the structural members have torqueless connections, e.g., via negligible small and frictionless ball-joints.

3. The structure configuration is not changing for the minimal mass design. In other words, the minimal mass design approach is for the loaded case of the tensegrity structures.

4. Each structural member is homogeneous along its length, so the mass of each structural member is distributed uniformly along its length.

5. A string can never push along its length. If $||\boldsymbol{s}_{i0}|| > ||\boldsymbol{s}_i||$, tension in the string should be substituted to zero, where the rest length and actual length of the ith string are denoted by $||\boldsymbol{s}_{i0}||$ and $||\boldsymbol{s}_i||$, and $\|\boldsymbol{v}\|$ is the Euclidean norm of vector $\boldsymbol{v}$.

2.3 Tensegrity Notations

2.3.1 Nodal Coordinates

The position of each node in the tensegrity structure can be expressed in any frame, we choose to label them with Cartesian coordinates in an inertially fixed frame. Assume the tensegrity structure has n_n number of nodes, the X-, Y-, and Z-coordinates of the *i*th node $\boldsymbol{n}_i$ ($i = 1, 2, \cdots, n_n$)

can be labeled as x_i, y_i, and z_i. One can write $\boldsymbol{n}_i \in \mathbb{R}^3$ in a vector form:

$$\boldsymbol{n}_i = \begin{bmatrix} x_i & y_i & z_i \end{bmatrix}^T. \tag{2.1}$$

By stacking all the nodes together, we can obtain the nodal matrix $N \in \mathbb{R}^{3\times n_n}$:

$$N = \begin{bmatrix} \boldsymbol{n}_1 & \boldsymbol{n}_2 & \cdots & \boldsymbol{n}_{n_n} \end{bmatrix}. \tag{2.2}$$

2.3.2 Connectivity Matrix

Connectivity matrices denote the topology of the structure or, in other words, how the structural members (bars and strings) are connected at each node. Conventionally, the connectivity matrices contain two types: string connectivity and bar connectivity, labeled as $C_s \in \mathbb{R}^{\alpha\times n_n}$ and $C_b \in \mathbb{R}^{\beta\times n_n}$, where α and β are the numbers of strings and bars in the structure. There are two ways to write the connectivity matrices. The details of the two methods are as follows.

Method 1: Write the connectivity matrices directly. The *i*th row of C_b, denoted as $C_{bi} = [C_b]_{(i,:)} \in \mathbb{R}^{1\times\beta}$, represents the *i*th bar, starting form node *j* ($j = 1, 2, \cdots, \beta$) to node *k* ($k = 1, 2, \cdots, \beta$). The *m*th ($m = 1, 2, \cdots, \beta$) entry of C_{bi} satisfies:

$$[C_b]_{im} = \begin{cases} -1, \ m = j \\ \ \ 1, \ m = k \\ \ \ 0, \ m = else \end{cases}. \tag{2.3}$$

For β number of bars, the overall structure connectivity matrix $C_{bi} = [C_b]_{(i,:)} \in \mathbb{R}^{1\times\beta}$ can be written as:

$$C_b = \begin{bmatrix} C_{b1}^T & C_{b2}^T & \cdots & C_{b\beta}^T \end{bmatrix}^T. \tag{2.4}$$

The *i*th row of C_s, denoted as $C_{si} = [C_s]_{(i,:)} \in \mathbb{R}^{1\times\alpha}$, represents the *i*th string, starting form

node j ($j = 1, 2, \cdots, \alpha$) to node k ($k = 1, 2, \cdots, \alpha$). The mth ($m = 1, 2, \cdots, \alpha$) entry of C_{si} satisfies:

$$[C_s]_{im} = \begin{cases} -1, \ m = j \\ 1, \ m = k \\ 0, \ m = else \end{cases} . \tag{2.5}$$

For α number of strings, the overall structure connectivity matrix $C_s \in \mathbb{R}^{n \times \alpha}$ can be written as:

$$C_s = \begin{bmatrix} C_{s1}^T & C_{s2}^T & \cdots & C_{s\alpha}^T \end{bmatrix}^T . \tag{2.6}$$

Method 2: Write the node indices to generate the connectivity matrices. One can write $C_{b_{in}} \in \mathbb{R}^{\beta \times 2}$ and $C_{s_{in}} \in \mathbb{R}^{\alpha \times 2}$ whose two elements in each row denotes the start and end node indices of one bar or string. Then, a function *tenseg_ind2C.m* can be written to convert $C_{b_{in}}$ and $C_{s_{in}}$ to C_b and C_s [47]. The two methods are equivalent for modeling structures. However, one can get the insight of the bar/string vectors by method 1. Method 2 is easier to understand the connectivity relationships and is a better way to go for complex tensegrity structures.

2.3.3 Bars, Strings, and External Force Matrices

The string and bar vectors are contained in the string matrix $S = \begin{bmatrix} \boldsymbol{s}_1 & \boldsymbol{s}_2 & \cdots & \boldsymbol{s}_\alpha \end{bmatrix} \in \mathbb{R}^{3 \times \alpha}$ and in the bar matrix $B = \begin{bmatrix} \boldsymbol{b}_1 & \boldsymbol{b}_2 & \cdots & \boldsymbol{b}_\beta \end{bmatrix} \in \mathbb{R}^{3 \times \beta}$ respectively, which satisfy:

$$S = NC_s^T, \ B = NC_b^T. \tag{2.7}$$

The external force (in X-, Y-, and Z-directions) on each node $\boldsymbol{w}_i \in \mathbb{R}^3$ $(i = 1, \cdots, n_n)$ can be written into a vector form:

$$\boldsymbol{w}_i = \begin{bmatrix} \boldsymbol{w}_{ix} & \boldsymbol{w}_{iy} & \boldsymbol{w}_{iz} \end{bmatrix}^T. \tag{2.8}$$

By stacking $\boldsymbol{w}_i$ for $i = 1, 2, \cdots, n_n$ together, we can obtain the external force matrix $W \in \mathbb{R}^{3\times n_n}$:

$$W = \begin{bmatrix} \boldsymbol{w}_1 & \boldsymbol{w}_2 & \cdots & \boldsymbol{w}_{n_n} \end{bmatrix}. \tag{2.9}$$

We describe the force information in the structure members by force density (force per unit length) vectors of the stings and bars, denoted as $\gamma \in \mathbb{R}^\alpha$ and $\lambda \in \mathbb{R}^\beta$.

2.4 Equilibria of Tensegrity Structures

Theorem 2.4.1. *All tensegrity structures equilibria satisfy:*

$$NK = W,\ K = C_s^{\mathsf{T}} \hat{\gamma} C_s - C_b^{\mathsf{T}} \hat{\lambda} C_b, \tag{2.10}$$

has the equivalent form:

$$Ax = W_{vec},\ x = \begin{bmatrix} \gamma \\ \lambda \end{bmatrix}, \tag{2.11}$$

where the ith row of the matrix A and W_{vec} are:

$$A(i,:) = S\widehat{(C_s e_i)} - B\widehat{(C_b e_i)},\ W_{vec}(i,:) = W e_i, \tag{2.12}$$

and $e_i = \begin{bmatrix} 0 & 0 & \cdots & 1 & \cdots & 0 & 0 \end{bmatrix}^T$ is a column operator with 1 in the ith element and zeros elsewhere, $\hat{\bullet}$ is an operator that convert a vector into a diagonal matrix.

Proof. For a given tensegrity structure and external force at an equilibrium state we have [39]:

$$NK = W,\ K = C_s^{\mathsf{T}}\hat{\gamma}C_s - C_b^{\mathsf{T}}\hat{\lambda}C_b. \tag{2.13}$$

Substitute Eq. (2.7) into Eq. (2.13), we get:

$$S\hat{\gamma}C_s - B\hat{\lambda}C_b = W. \tag{2.14}$$

Take the ith $(i = 1,\ 2,\ \cdots,\ n_n)$ column of Eq. (2.14):

$$S\hat{\gamma}C_s e_i - B\hat{\lambda}C_b e_i = We_i, \tag{2.15}$$

Using the identity $\hat{x}y = \hat{y}x$ for x and y being column vectors, we have:

$$S\widehat{(C_s e_i)}\gamma - B\widehat{(C_b e_i)}\lambda = We_i. \tag{2.16}$$

Eq. (4.3.3) can be written in the following matrix form:

$$\underbrace{\begin{bmatrix} \widehat{} & \widehat{} \\ S(C_s e_1) & -B(C_b e_1) \\ \widehat{} & \widehat{} \\ S(C_s e_2) & -B(C_b e_2) \\ \vdots & \vdots \\ \widehat{} & \widehat{} \\ S(C_s e_n) & -B(C_b e_n) \end{bmatrix}}_{A \in \mathbb{R}^{n_n \times (\alpha+\beta)}} \begin{bmatrix} \gamma \\ \lambda \end{bmatrix} = \underbrace{\begin{bmatrix} We_1 \\ We_2 \\ \vdots \\ We_n \end{bmatrix}}_{W_{vec} \in \mathbb{R}^{n_n}}, \tag{2.17}$$

which can be simply written as:

$$Ax = W_{vec},\ x = \begin{bmatrix} \gamma \\ \lambda \end{bmatrix}. \tag{2.18}$$

□

One may observe from Eq. (2.18) is that matrix A is determined by the topology of the tensegrity structure, and W_{vec} is given by the loading requirements of the structure. Since normally tensegrity structures have self-stress modes, the matrix A is not full column rank, and from linear algebra, we know, $(I - AA^{+})W_{vec} = 0$ is satisfied, all the solutions of x are given by [48]:

$$x = A^{+}W_{vec} + (I - A^{+}A)z, \tag{2.19}$$

where $A^{+} \in \mathbb{R}^{(\alpha+\beta)\times n_n}$ is the Moore-Penrose inverse of matrix A, $z \in \mathbb{R}^{(\alpha+\beta)}$ is an arbitrary vector. Thus, once the topology and loading requirements are given, one can compute the internal

forces of each structure member. From Eq. (2.19) we know that the solution may not be unique with the free variable z. The physical meaning is that we can tune the prestress of the tensegrity structure by the free variable to change the structure stiffness without changing the shape. In addition, since the force density vector x provides the insight loading information of the structure members, which can be used as stress bound of each structure member to guide us to achieve a minimal mass design with stability guaranteed. The design approaches will be discussed in the following sections.

2.5 Structure Mass Formulation

Let us consider two general tensegrity structure cases: bars are solid rods or hollow pipes (both kinds of bars have a circular cross-section). To simplify the name, we call them solid bar tensegrity and hollow bar tensegrity.

2.5.1 Mass Formulation for Solid Bar Tensegrity

Theorem 2.5.1. *The minimal mass of a solid bar tensegrity system is achieved when all structure members fail at the same time:*

$$M^S = \frac{\rho_s}{\sigma_s}\sum_{i=1}^{\alpha}\gamma_i||\boldsymbol{s}_i||^2 + \sum_{j=1}^{\beta} max\{\frac{\rho_b}{\sigma_b}\lambda_j||\boldsymbol{b}_j||^2, 2\rho_b\lambda_j^{\frac{1}{2}}(\frac{||\boldsymbol{b}_j||^5}{\pi E_b})^{\frac{1}{2}}\}, \tag{2.20}$$

has the equivalent form:

$$M^S = \frac{\rho_s}{\sigma_s}(vec(\lfloor S^T S\rfloor))^T\gamma + \frac{\rho_b}{\sigma_b}(vec(\lfloor B^T B\rfloor(I-Q)))^T\lambda + \frac{2\rho_b}{\sqrt{\pi E_b}}(vec(\lfloor B^T B\rfloor^{\frac{5}{4}}Q))^T\lambda^{\frac{1}{2}}, \tag{2.21}$$

where ρ_s, ρ_b, σ_s, σ_b are the density and yield strength of strings and bars, γ_i, λ_j, $||\boldsymbol{s}_i||$, and $||\boldsymbol{b}_j||$ ($i = 1, 2, \cdots, \alpha$, α is number of strings; $j = 1, 2, \cdots, \beta$, β is number of bars) are the force densities (force over member length) and length of each string and each bar, and E_b is Young's modulus of bars. $Q \in \mathbb{R}^{\beta\times\beta}$ is a square matrix with 0s or 1s in its diagonal and 0s elsewhere, where the diagonal indices of the 1s denotes the buckling bars, and the diagonal indices of the 1s

of $(I-Q) \in \mathbb{R}^{\beta \times \beta}$ *labels the yielding bars.* $\lfloor \bullet \rfloor$ *is an operator taking only the diagonal elements of a matrix and set the off-diagnal elements into 0s,* $vec(\bullet)$ *is an operator taking the diagonal elements of the matrix in the parentheses to form a vector.*

Proof. The structure minimal mass M^S can be achieved when every string yields and every bar yields or buckles at the same time. We do not know the mode of failure for each bar in advance, but the bar mass is equivalent to take the maximum value of these two. Then, total mass can be written as:

$$M^S = \frac{\rho_s}{\sigma_s} \sum_{i=1}^{\alpha} \gamma_i ||\boldsymbol{s}_i||^2 + \sum_{j=1}^{\beta} max\{\frac{\rho_b}{\sigma_b} \lambda_j ||\boldsymbol{b}_j||^2, 2\rho_b \lambda_j^{\frac{1}{2}} (\frac{||\boldsymbol{b}_j||^5}{\pi E_b})^{\frac{1}{2}}\}. \tag{2.22}$$

To simplify the notations, we introduce a label matrix $Q \in \mathbb{R}^{\beta \times \beta}$ to identify and record the mode of failure for each bar:

$$Q_{jj} = \begin{cases} 0 & \lambda_j \geq \dfrac{4\sigma_b^2 ||\boldsymbol{b}_j||}{\pi E_b}, \text{ bar yields} \\ 1 & \lambda_j < \dfrac{4\sigma_b^2 ||\boldsymbol{b}_j||}{\pi E_b}, \text{ bar buckles} \end{cases}, \tag{2.23}$$

the off diagonal elements of Q are zeros.

The diagonal elements of matrix Q with ones denote buckling as the mode of failure of those bars, and the diagonal elements of the matrix $(I-Q)$ with ones represent yielding is the mode of failure of those bars. The bars are now separated into two parts, and the minimal mass formula can be well defined in a matrix form:

$$M^S = \frac{\rho_s}{\sigma_s} (vec(\lfloor S^T S \rfloor))^T \gamma + \frac{\rho_b}{\sigma_b} (vec(\lfloor B^T B \rfloor (I-Q)))^T \lambda + \frac{2\rho_b}{\sqrt{\pi E_b}} (vec(\lfloor B^T B \rfloor^{\frac{5}{4}} Q))^T \lambda^{\frac{1}{2}}. \tag{2.24}$$

□

2.5.2 Mass Formulation for Hollow Bar Tensegrity

Theorem 2.5.2. *The minimal mass of a hollow bar tensegrity system is achieved when all structure members fail at the same time:*

$$M^H = \frac{\rho_s}{\sigma_s}\sum_{i=1}^{\alpha}\gamma_i||\boldsymbol{s}_i||^2 + \sum_{j=1}^{\beta} max\{\frac{\rho_b}{\sigma_b}\lambda_j||\boldsymbol{b}_j||^2, \frac{\rho_b||\boldsymbol{b}_j||}{\sqrt{\pi E_b}}(\sqrt{\pi^3 E_b r_{j_{in}}^4 + 4\lambda_j||\boldsymbol{b}_j||^3} - \pi r_{j_{in}}^2\sqrt{\pi E_b})\}, \tag{2.25}$$

has the equivalent form:

$$\begin{aligned} M^H = &\frac{\rho_s}{\sigma_s}(vec(\lfloor S^T S\rfloor))^T\gamma + \frac{\rho_b}{\sigma_b}(vec(\lfloor B^T B\rfloor(I-Q)))^T\lambda \\ &+ \frac{\rho_b(vec(\lfloor B^T B\rfloor^{\frac{1}{2}}Q))^T}{\sqrt{\pi E_b}}(\sqrt{\pi^3 E_b r_{in}^4 + 4(\lfloor B^T B\rfloor^{\frac{3}{2}}Q)\lambda} - \pi r_{in}^2\sqrt{\pi E_b}), \end{aligned} \tag{2.26}$$

where ρ_s, ρ_b, σ_s, σ_b are the density and yield strength of strings and bars, γ_i, λ_j, $||s_i||$, and $||b_j||$ ($i = 1, 2, \cdots, \alpha$; $j = 1, 2, \cdots, \beta$) are the force densities and length of each string and each bar, and E_b is Young's modulus of bars. $Q \in \mathbb{R}^{\beta\times\beta}$ is the label matrix to identify the mode of failure of each bar. $r_{in} = \begin{bmatrix} r_{1_{in}} & \cdots & r_{j_{in}} & \cdots & r_{\beta_{in}} \end{bmatrix}^T$ is a vector of the inner radius of all the bars.

Proof. Assume yielding is the mode of failure for strings, yielding and buckling are mode of failures for bars, the structure minimal mass M^H can be achieved when all strings yield and each bars yields or buckles (take the maximum mass of these two) at the same time:

$$M^H = \frac{\rho_s}{\sigma_s}\sum_{i=1}^{\alpha}\gamma_i||\boldsymbol{s}_i||^2 + \sum_{j=1}^{\beta} \max\{\frac{\rho_b}{\sigma_b}\lambda_j||\boldsymbol{b}_j||^2, \frac{\rho_b||\boldsymbol{b}_j||}{\sqrt{\pi E_b}}(\sqrt{\pi^3 E_b r_{j_{in}}^4 + 4\lambda_j||b_j||^3} - \pi r_{j_{in}}^2\sqrt{\pi E_b})\}. \tag{2.27}$$

Similarly, we define a label matrix $Q \in \mathbb{R}^{\beta\times\beta}$ to identify whether each bar is yielding or buckling:

$$Q_{jj} = \begin{cases} 0 & \lambda_j \geq \dfrac{4\sigma_b^2||\boldsymbol{b}_j||}{\pi E_b} - \dfrac{2\sigma_b\pi r_{j_{in}}^2}{||\boldsymbol{b}_j||}, \text{ bar yields} \\ 1 & 0 < \lambda_j < \dfrac{4\sigma_b^2||\boldsymbol{b}_j||}{\pi E_b} - \dfrac{2\sigma_b\pi r_{j_{in}}^2}{||\boldsymbol{b}_j||}, \text{ bar buckles} \end{cases}, \tag{2.28}$$

the off diagonal elements of Q are zeros.

Similarly, the minimal mass formula for hollow bar tensegrity is given below in a matrix form:

$$M^H = \frac{\rho_s}{\sigma_s}(vec(\lfloor S^T S \rfloor))^T \gamma + \frac{\rho_b}{\sigma_b}(vec(\lfloor B^T B \rfloor (I - Q)))^T \lambda + \frac{\rho_b (vec(\lfloor B^T B \rfloor^{\frac{1}{2}} Q))^T}{\sqrt{\pi E_b}} (\sqrt{\pi^3 E_b r_{in}^4 + 4(\lfloor B^T B \rfloor^{\frac{3}{2}} Q)\lambda} - \pi r_{in}^2 \sqrt{\pi E_b}). \tag{2.29}$$

□

2.6 Minimal Mass Tensegrity Design w/o Gravity

In this section, we present algorithms in designing the structure member thickness to achieve structure minimal mass subject to the load requirements and given topology. The idea is that the static equilibrium equation can be written in terms of force density x of the structure members. Minimal mass design is to calculate the critical mass that every structure member fails at the same time. Then, the mass is a function of force density x (bar mass subject to buckling is nonlinear in its force density). Structure gravity can be viewed as an external force on the structure, but it is also coupled with structure mass. Thus, the minimal mass tensegrity design problem yields to find the optimal force density x for given loads and topology of the structure, which can be formulated as a nonlinear optimization problem.

Theorem 2.6.1. *The minimal mass of a tensegrity system at an equilibrium in the given configuration with external forces is given by a non-linear programming problem:*

$$\begin{cases} \underset{x}{\textit{minimize}} & M \\ \textit{subject to} & Ax = W_{vec},\ x \geq \epsilon\ (\epsilon \geq 0) \end{cases}, \tag{2.30}$$

where M is M^S or M^H depends on using solid or hollow bars for the structure, ϵ is the prestress lower bound assigned to the strings, and $\epsilon \geq 0$ is a constant vector that guarantees that all strings are in tension and all bars are in compression.

Since gravity is unlike a given set of specific external forces that apply to the structure, it is

determined by the mass of the structure itself. In other words, the statics mass optimization process is coupled with the gravity force. We separate total force W into two parts $W = W_e + W_g$, where W_g is the gravity force, W_e is other applied external force, and $\boldsymbol{g}$ is the gravitational acceleration, i.e., $\boldsymbol{g} = \begin{bmatrix} 0 & 0 & -9.8 \end{bmatrix}^T$ is the gravity vector on the Earth.

2.6.1 Minimal Mass Tensegrity Design without Gravity Algorithm

Corollary 2.6.1. *The minimal mass of a tensegrity system at an equilibrium in the given configuration with external forces without considering gravity is given by a non-linear programming problem:*

$$\begin{cases} \underset{x}{\textit{minimize}} & M \\ \textit{subject to} & Ax = W_{e\ vec},\ x \geq \epsilon\ (\epsilon \geq 0) \end{cases}, \tag{2.31}$$

where ϵ is the prestress lower bound assigned to the strings, and $\epsilon \geq 0$ is a constant vector that guarantees that all strings are in tension and all bars in compression.

Notice that to solve Eq. (2.31), one need to specify the label matrix Q. However, one cannot exactly specify Q for any structure in advance, since it is determined by structure topology and external force. To obtain a global solution, the nonlinear optimization problem can be solved in an iterative manner, shown in Algorithm 1.

Algorithm 1: Minimal Mass No Gravity

1) Given tensegrity structure topology N, C_b, C_s and external force W, compute A and $W_{e\ vec}$ from Eq. (2.17).

2) Assumes all bar buckles, $Q = I^{\beta\times\beta}$.

3) Compute force densities x:

while $\underline{Q_{i+1} \neq Q_i}$ **do**

$$\begin{cases} \underset{x}{\text{minimize}}\ M \\ \text{subject to } Ax = W_{e\ vec},\ x \geq \epsilon\ (\epsilon \geq 0). \end{cases}$$

Take λ out of x, check Eq. (2.23) or (2.28), update Q.

$i \leftarrow i + 1$.

end while

2.6.2 Minimal Mass Tensegrity Design with Gravity

The gravity force can be modeled by lumped forces equally distributed on the member nodes [44].

2.6.2.1 Gravity Formulation for Solid Bar Tensegrity

The gravity force of bars and strings can be expressed as:

$$\begin{aligned} W_g^S = &\frac{1}{2}\boldsymbol{g}\frac{\rho_s}{\sigma_s}(vec(\lfloor S^T S\rfloor))^T\hat{\gamma}|C_s| + \frac{1}{2}\boldsymbol{g}\frac{\rho_b}{\sigma_b}(vec(\lfloor B^T B\rfloor(I-Q)))^T\hat{\lambda}|C_b| \\ &+ \frac{1}{2}\boldsymbol{g}\frac{2\rho_b}{\sqrt{\pi E_b}}(vec(\lfloor B^T B\rfloor^{\frac{5}{4}}Q))^T\hat{\lambda}^{\frac{1}{2}}|C_b|, \end{aligned} \tag{2.32}$$

where $|\bullet|$ is an operator getting the absolute value of each element for a given matrix. Take the ith column of the above equation, we get:

$$\begin{aligned} W_{gi}^{S} =& \frac{1}{2}\boldsymbol{g}\frac{\rho_s}{\sigma_s}(vec(\lfloor S^T S \rfloor))^T \hat{\gamma}|C_s|e_i + \frac{1}{2}\boldsymbol{g}\frac{\rho_b}{\sigma_b}(vec(\lfloor B^T B \rfloor (I-Q)))^T \hat{\lambda}|C_b|e_i \\ &+ \frac{1}{2}\boldsymbol{g}\frac{2\rho_b}{\sqrt{\pi E_b}}(vec(\lfloor B^T B \rfloor^{\frac{5}{4}} Q))^T \hat{\lambda}^{\frac{1}{2}}|C_b|e_i \end{aligned} \tag{2.33}$$

$$\begin{aligned} =& \frac{1}{2}\boldsymbol{g}\frac{\rho_s}{\sigma_s}(vec(\lfloor S^T S \rfloor))^T \widehat{|C_s e_i|}\gamma + \frac{1}{2}\boldsymbol{g}\frac{\rho_b}{\sigma_b}(vec(\lfloor B^T B \rfloor (I-Q)))^T \widehat{|C_b e_i|}\lambda \\ &+ \frac{1}{2}\boldsymbol{g}\frac{2\rho_b}{\sqrt{\pi E_b}}(vec(\lfloor B^T B \rfloor^{\frac{5}{4}} Q))^T \widehat{|C_b e_i|}\lambda^{\frac{1}{2}}. \end{aligned} \tag{2.34}$$

Arrange all the columns, we get:

$$W_{g\ vec}^{S} = \begin{bmatrix} W_{g1}^{S\,T} & \cdots & W_{gi}^{S\,T} & \cdots & W_{gn}^{S\,T} \end{bmatrix}^T. \tag{2.35}$$

2.6.2.2 Gravity Formulation for Hollow Bar Tensegrity

For hollow bar tensegrity, the gravity force of bars and strings can be expressed as:

$$\begin{aligned} W_{g}^{H} =& \frac{1}{2}\boldsymbol{g}\frac{\rho_s}{\sigma_s}(vec(\lfloor S^T S \rfloor))^T \hat{\gamma}|C_s| + \frac{1}{2}\boldsymbol{g}\frac{\rho_b}{\sigma_b}(vec(\lfloor B^T B \rfloor (I-Q)))^T \hat{\lambda}|C_b| \\ &+ \frac{1}{2}\boldsymbol{g}\frac{\rho_b (vec(\lfloor B^T B \rfloor^{\frac{1}{2}} Q))^T}{\sqrt{\pi E_b}}(\sqrt{\pi^3 E_b \hat{r}_{in}^4 + 4(\lfloor B^T B \rfloor^{\frac{3}{2}} Q)\hat{\lambda}} - \pi \hat{r}_{in}^2 \sqrt{\pi E_b})|C_b|. \end{aligned} \tag{2.36}$$

Take the ith column of the above equation, we get:

$$\begin{aligned} W_{gi}^H =& \frac{1}{2}\boldsymbol{g}\frac{\rho_s}{\sigma_s}(vec(\lfloor S^T S \rfloor))^T \hat{\gamma}|C_s|e_i + \frac{1}{2}\boldsymbol{g}\frac{\rho_b}{\sigma_b}(vec(\lfloor B^T B \rfloor (I-Q)))^T \hat{\lambda}|C_b|e_i \\ &+ \frac{1}{2}\boldsymbol{g}\frac{\rho_b (vec(\lfloor B^T B \rfloor^{\frac{1}{2}} Q))^T}{\sqrt{\pi E_b}}(\sqrt{\pi^3 E_b \hat{r}_{in}^4 + 4(\lfloor B^T B \rfloor^{\frac{3}{2}} Q)\hat{\lambda}} - \pi \hat{r}_{in}^2 \sqrt{\pi E_b})|C_b|e_i \qquad (2.37) \end{aligned}$$

$$\begin{aligned} =& \frac{1}{2}\boldsymbol{g}\frac{\rho_s}{\sigma_s}(vec(\lfloor S^T S \rfloor))^T \widehat{|C_s e_i|\gamma} + \frac{1}{2}\boldsymbol{g}\frac{\rho_b}{\sigma_b}(vec(\lfloor B^T B \rfloor (I-Q)))^T \widehat{|C_b e_i|\lambda} \\ &+ \frac{1}{2}\boldsymbol{g}\frac{\rho_b (vec(\lfloor B^T B \rfloor^{\frac{1}{2}} Q))^T}{\sqrt{\pi E_b}} \widehat{|C_b e_i|}(\sqrt{\pi^3 E_b r_{in}^4 + 4(\lfloor B^T B \rfloor^{\frac{3}{2}} Q)\lambda} - \pi r_{in}^2 \sqrt{\pi E_b}). \qquad (2.38) \end{aligned}$$

Arrange all the columns, we get:

$$W_{g\ vec}^H = \begin{bmatrix} W_{g1}^{HT} & \cdots & W_{gi}^{HT} & \cdots & W_{gn}^{HT} \end{bmatrix}^T. \qquad (2.39)$$

2.6.2.3 Minimal Mass Tensegrity Design with Gravity Algorithm

Corollary 2.6.2. *The minimal mass of a tensegrity system at an equilibrium in the given configuration with external forces in the presence of gravity is given by a non-linear programming problem:*

$$\begin{cases} \underset{x}{\textit{minimize}} & M \\ \textit{subject to} & Ax = W_{e\ vec} + W_{g\ vec},\ x \geq \epsilon\ (\epsilon \geq 0) \end{cases}, \qquad (2.40)$$

where M, $W_{g\ vec}$ are M^S, $W_{g\ vec}^S$ or M^H, $W_{g\ vec}^H$ which depend on using solid or hollow bars for the structure, ϵ is the prestress lower bound assigned to the strings, and $\epsilon \geq 0$ is a constant vector that guarantees that all strings are in tension and all bars in compression.

Similarly to Algorithm 4 for solid bar, to solve Eq. (2.40), one need to specify the label matrix Q. To obtain a global solution for hollow bar tensegrity considering gravity, the nonlinear

optimization problem can be solved in an iterative manner, see Algorithm 2.

Algorithm 2: Minimal Mass with Gravity

1) Given tensegrity structure topology N, C_b, C_s and external force W, compute A and $W_{e\ vec}$ from Eq. (2.17).

2) Assumes all bar buckles, $Q = I^{\beta\times\beta}$ and $W_{g\ vec} = 0$.

3) Compute force densities x:

while $\underline{Q_{i+1} \neq Q_i}$ **do**

$$\begin{cases} \underset{x}{\text{minimize}}\ M \\ \text{subject to } Ax = W_{e\ vec} + W_{g\ vec},\ x \geq \epsilon\ (\epsilon \geq 0). \end{cases}$$

Take λ out of x, check Eq. (2.23) or (2.28), update Q.

Update $W_{g\ vec}$ from Eq. (2.35) or (2.39).

$i \leftarrow i + 1$.

end while

2.6.3 Example: D-Bar Structure w/o Gravity

D-Bar structure has been studied in many composite structure studies. For example, Boz et al. [49] showed the D-Bar structure could be used as both actuators and sensors. Skelton and de Oliveira presented that the microstructure of a spider fiber is like a D-Bar structure, and they implemented a D-Bar structure to build a wave-powered station-keeping buoy (WPSB) System. Goyal et al. [50] studied mass efficient landers based on D-Bar structures. Zhao and Hernandez [36] analyzed tunable energy dissipation by D-Bar structures. Thus, we choose a 2D D-Bar structure as an example, shown in Figure 2.1 is chosen to verify the minimal mass algorithms. Four kinds of combinations of solid and hollow bars with and without gravity are studied. Using the same material (aluminum) for all the bars and strings, material information is given in Table 2.1. For convenience in subsequent comparison, the inner radii for all the hollow bars are set to be 0.02 m.

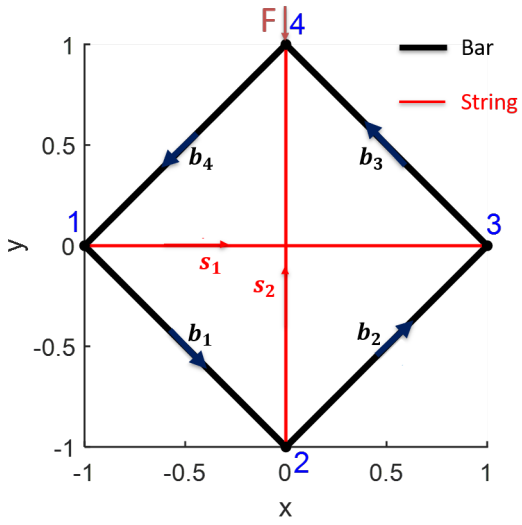

Figure 2.1: 2D tensegrity D-Bar structure, downward vertical force F (marked in maroon) is applied at node 4 (marked in blue), node 2 is fixed to the ground. Reprinted with permission from [5]. Reprinted with permission from [5].

Table 2.1: Material Property for the D-Bar Structure (Aluminum).

Properties	Value	Units
Yield Stress	$\sigma = 1.1 \times 10^8$	Pa
Young's Modulus	$E = 6 \times 10^{10}$	Pa
Mass Density	$\rho = 2.7 \times 10^3$	kg/m^3

2.6.3.1 D-Bar without Gravity

Firstly, a vertical downward external load $F = 1.0 \times 10^4$ N is applied at the top, and the bottom node is fixed in both x and y directions to the ground. The results show that all bars buckle under this load, shown in Figure 2.2. The load is then increased to $F = 1.0 \times 10^6$ N, where all bars yield, shown in Figure 2.4. These results agree with the analytical solutions.

Figure 2.2 gives the failure information of bars of the D-Bar structures with solid bars and hollow bars, respectively. The results are listed in Table 2. It is shown that for solid bar structure, buckling is the mode of failure for all the bars. The bar mass distributes evenly, and only string 1 has mass. For hollow bars, the mass distribution is the same. The only difference is that the hollow

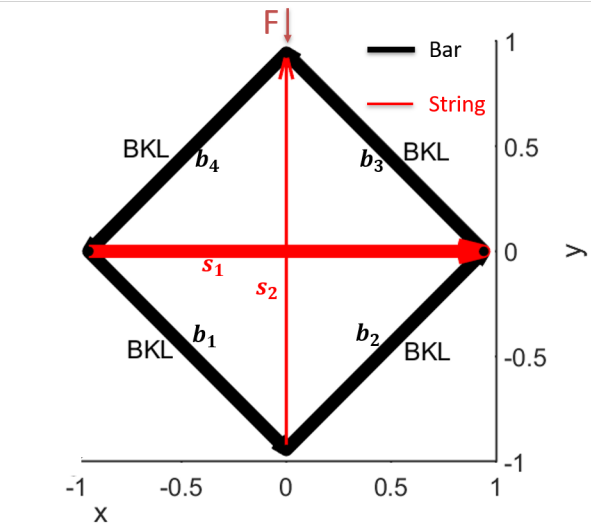

Figure 2.2: Tensegrity D-Bar structure, $F = 1.0 \times 10^4$ N, all bar buckle. Reprinted with permission from [5].

bar structure has less mass than the solid bar one.

Table 2.3 indicates that all bars yield when the external load is $F = 1 \times 10^6$ N. This supplemental case also proves that the hollow bar design does not save mass when yielding in the mode of failure of bars.

2.6.3.2 D-Bar with Gravity

Table 2.4 gives similar information as Table 2.2: hollow bar tensegrity cost less mass than a solid bar one. And Table 2.4 together with Table 2.2 indicates that for both solid bar and hollow bar design, minimal structure mass with gravity is slightly larger than without gravity which agrees well with the physics.

Table 2.2: Member information of D-Bar structure, $F = 1.0 \times 10^4$ N, without gravity. BKL and YLD represent buckling and yielding. Reprinted with permission from [5].

Solid/Hollow		**No Gravity**		
Load[N]		1.0×10^4		
Solid Bars	Failure	$\lambda[N/m]$	Mass$[kg]$	r$[m]$
b_1	BKL	5000	2.092	0.0132
b_2	BKL	5000	2.092	0.0132
b_3	BKL	5000	2.092	0.0132
b_4	BKL	5000	2.092	0.0132
Strings	Failure	$\gamma[N/m]$	Mass$[kg]$	R $[m]$
s_1	YLD	5000	0.491	0.005
s_2	YLD	0	0	0
Mass Sum			8.858	
Hollow Bars	Failure	$\lambda[N/m]$	Mass$[kg]$	$r_{out}[m]$
b_1	BKL	5000	2.080	0.021
b_2	BKL	5000	2.080	0.021
b_3	BKL	5000	2.080	0.021
b_4	BKL	5000	2.080	0.021
Strings	Failure	$\gamma[N/m]$	Mass$[kg]$	r$[m]$
s_1	YLD	5000	0.491	0.011
s_2	YLD	0	0	0
Mass Sum			8.810	

Table 2.3: Structure mass of D-Bar structure, $F = 1.0 \times 10^6$ N, without gravity. Reprinted with permission from [5].

Solid/Hollow	Value	Units
External Load	$F = 1.0 \times 10^6$	N
Minimal Mass (Solid)	$M = 147.273$	kg/m^3
Minimal Mass (Hollow)	$M = 147.273$	kg/m^3

Figure 2.3: Structure mass of D-Bar structure, $F = 1.0 \times 10^6$ N, without gravity. Reprinted with permission from [5].

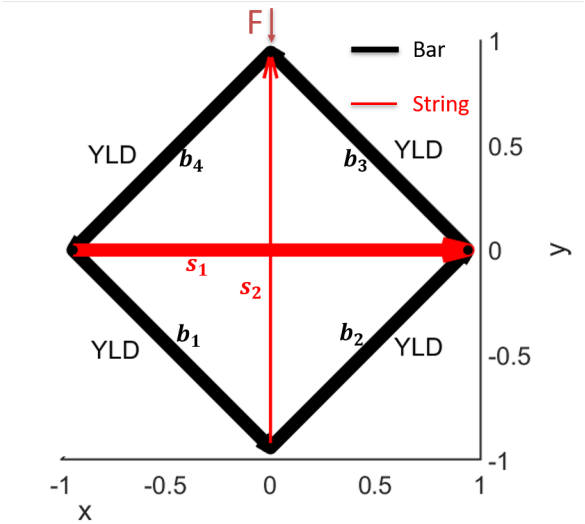

Figure 2.4: Tensegrity D-Bar structure, $F = 1.0 \times 10^6$ N, all bar yield. Reprinted with permission from [5].

Table 2.4: Member information of D-Bar structure, $F = 1.0 \times 10^4$ N, with 1-g gravity. BKL and YLD represent buckling and yielding. Reprinted with permission from [5].

Solid/Hollow		**With Gravity**		
Load[N]		1.0×10^4		
Solid Bars	Failure	$\lambda[N/m]$	Mass$[kg]$	r$[m]$
b_1	BKL	5033.220	2.099	0.0132
b_2	BKL	5033.220	2.099	0.0132
b_3	BKL	5033.220	2.099	0.0132
b_4	BKL	5033.220	2.099	0.0132
Strings	Failure	$\gamma[N/m]$	Mass$[kg]$	r$[m]$
s_1	YLD	5021.740	0.493	0.005
s_2	YLD	0	0	0
Mass Sum			8.878	
Hollow Bars	Failure	$\lambda[N/m]$	Mass$[kg]$	$r_{out}[m]$
b_1	BKL	5033.044	2.087	0.021
b_2	BKL	5033.044	2.087	0.021
b_3	BKL	5010.202	2.082	0.021
b_4	BKL	5010.202	2.082	0.021
Strings	Failure	$\gamma[N/m]$	Mass$[kg]$	r$[m]$
s_1	YLD	5021.623	0.493	0.011
s_2	YLD	0	0	0
Mass Sum			8.830	

2.7 Tensegrity Structure Stiffness Matrix

2.7.1 Stiffness Matrix for Solid Bar Tensegrity

Theorem 2.7.1. *The stiffness matrix K_n for any solid bar tensegrity structure subject to yielding and buckling constraints is given by:*

$$K_n vec(dN) = vec(dW), \tag{2.41}$$

where

$$K_n = (C_s^T \otimes I_3)\textbf{\textit{b.d.(}}K_{s1}\textbf{\textit{,}}\cdots\textbf{\textit{,}}K_{s\alpha})(C_s \otimes I_3) - (C_b^T \otimes I_3)\textbf{\textit{b.d.(}}K_{b1}\textbf{\textit{,}}\cdots\textbf{\textit{,}}K_{b\beta})(C_b \otimes I_3), \tag{2.42}$$

and

$$\begin{aligned} K_{si} =& \gamma_i(I_3 + \frac{E_{si}}{\sigma_s}\frac{\boldsymbol{s}_i\boldsymbol{s}_i^T}{||\boldsymbol{s}_i||^2}), \\ K_{bj} =& \lambda_j(I_3 - (1-Q_{jj})\frac{E_{bj}}{\sigma_b}\frac{\boldsymbol{b}_j\boldsymbol{b}_j^T}{||\boldsymbol{b}_j||^2}) - 2Q_{jj}\sqrt{\frac{E_{bj}}{\pi}}\frac{\boldsymbol{b}_j\boldsymbol{b}_j^T}{||\boldsymbol{b}_j||^{\frac{3}{2}}}\lambda_j^{\frac{1}{2}}. \end{aligned}$$

Proof. Consider a small variation around the equilibrium, $N + dN = \begin{bmatrix}\cdots & (\boldsymbol{n}_k + d\boldsymbol{n}_k) & \cdots\end{bmatrix}$, $W+dW = \begin{bmatrix}\cdots & (\boldsymbol{w}_k + d\boldsymbol{w}_k) & \cdots\end{bmatrix}$, $\gamma+d\gamma = \begin{bmatrix}\cdots & (\gamma_i + d\gamma_i) & \cdots\end{bmatrix}^T$, $\lambda+d\lambda = \begin{bmatrix}\cdots & (\lambda_j + d\lambda_j) & \cdots\end{bmatrix}^T$, the statics equation can be written as:

$$(N + dN)C_s^T\widehat{(\gamma + d\gamma)}C_s - (N + dN)C_b^T\widehat{(\lambda + d\lambda)}C_b = W + dW. \tag{2.43}$$

Notice $\gamma = \begin{bmatrix}\cdots & \gamma_i & \cdots\end{bmatrix}^T$ and $\lambda = \begin{bmatrix}\cdots & \lambda_j & \cdots\end{bmatrix}^T$, we have $d\gamma = \begin{bmatrix}\cdots & d\gamma_i & \cdots\end{bmatrix}^T$ and

$d\lambda = \begin{bmatrix} \cdots & d\lambda_i & \cdots \end{bmatrix}^T$, then we get:

$$(N + dN)C_s^T(\hat{\gamma} + d\hat{\gamma})C_s - (N + dN)C_b^T(\hat{\lambda} + d\hat{\lambda})C_b = W + dW. \tag{2.44}$$

Then, we have:

$$\begin{aligned} &NC_s^T\hat{\gamma}C_s + dNC_s^T\hat{\gamma}C_s + NC_s^Td\hat{\gamma}C_s + dNC_s^Td\hat{\gamma}C_s - \\ &NC_b^T\hat{\lambda}C_b - dNC_b^T\hat{\lambda}C_b - NC_b^Td\hat{\lambda}C_b - dNC_b^Td\hat{\lambda}C_b = W + dW. \end{aligned} \tag{2.45}$$

Using the fact $N(C_s^{\mathsf{T}}\hat{\gamma}C_s - C_b^{\mathsf{T}}\hat{\lambda}C_b) = W$ and neglect the higher order terms:

$$(dNC_s^T\hat{\gamma} + NC_s^Td\hat{\gamma})C_s - (dNC_b^T\hat{\lambda} + NC_b^Td\hat{\lambda})C_b = dW. \tag{2.46}$$

Since $S + dS = \begin{bmatrix} \cdots & (\boldsymbol{s}_i + d\boldsymbol{s}_i) & \cdots \end{bmatrix}$, $B + dB = \begin{bmatrix} \cdots & (\boldsymbol{b}_j + d\boldsymbol{b}_j) & \cdots \end{bmatrix}$, we have $dS = dNC_s^T$, $dB = dNC_b^T$,

$$(dS\hat{\gamma} + Sd\hat{\gamma})C_s - (dB\hat{\lambda} + Bd\hat{\lambda})C_b = dW. \tag{2.47}$$

Let us take a close look at each string and each bar:

$$[\cdots \underbrace{(d\boldsymbol{s}_i\gamma_i + \boldsymbol{s}_i d\gamma_i)}_{K_{si}d\boldsymbol{s}_i} \cdots]C_s - [\cdots \underbrace{(d\boldsymbol{b}_j\lambda_j + \boldsymbol{b}_j d\lambda_j)}_{K_{bj}d\boldsymbol{b}_j} \cdots]C_b = dW. \tag{2.48}$$

Eq. (2.48) can be written as:

$$\begin{bmatrix} K_{s1}d\boldsymbol{s}_1 & \cdots & K_{s\alpha}d\boldsymbol{s}_\alpha \end{bmatrix} C_s - \begin{bmatrix} K_{b1}d\boldsymbol{b}_1 & \cdots & K_{b\beta}d\boldsymbol{b}_\beta \end{bmatrix} C_b = dW \tag{2.49}$$

Vectorize the equation on both sides, we have:

$$vec(\begin{bmatrix} K_{s1}d\boldsymbol{s}_1 & \cdots & K_{s\alpha}d\boldsymbol{s}_\alpha \end{bmatrix} C_s) - vec(\begin{bmatrix} K_{b1}d\boldsymbol{b}_1 & \cdots & K_{b\beta}d\boldsymbol{b}_\beta \end{bmatrix} C_b) = vec(dW). \tag{2.50}$$

Use the properties of the vec operator $vec(AXB) = (B^T \otimes A)vec(X)$:

$$\begin{aligned} &(C_s^T \otimes I_3)vec(\begin{bmatrix} K_{s1}d\boldsymbol{s}_1 & \cdots & K_{s\alpha}d\boldsymbol{s}_\alpha \end{bmatrix}) - (C_b^T \otimes I_3) \\ &vec(\begin{bmatrix} K_{b1}d\boldsymbol{b}_1 & \cdots & K_{b\beta}d\boldsymbol{b}_\beta \end{bmatrix}) = vec(dW). \end{aligned} \tag{2.51}$$

This can be written as:

$$\begin{aligned} &(C_s^T \otimes I_3) \begin{bmatrix} K_{s1} & & \\ & \ddots & \\ & & K_{s\alpha} \end{bmatrix} vec(\begin{bmatrix} d\boldsymbol{s}_1 & \cdots & d\boldsymbol{s}_\alpha \end{bmatrix}) - \\ &(C_b^T \otimes I_3) \begin{bmatrix} K_{b1} & & \\ & \cdots & \\ & & K_{b\beta} \end{bmatrix} vec(\begin{bmatrix} d\boldsymbol{b}_1 & \cdots & d\boldsymbol{b}_\beta \end{bmatrix}) = vec(dW). \end{aligned} \tag{2.52}$$

As $dS = \begin{bmatrix} d\boldsymbol{s}_1 & \cdots & d\boldsymbol{s}_\alpha \end{bmatrix}$ and $dB = \begin{bmatrix} d\boldsymbol{b}_1 & \cdots & d\boldsymbol{b}_\beta \end{bmatrix}$,

$$\begin{aligned} &(C_s^T \otimes I_3)\textbf{b.d.}(K_{s1},\cdots,K_{s\alpha})vec(dS) \ - (C_b^T \otimes I_3) \\ &\textbf{b.d.}(K_{b1},\cdots,K_{b\beta})vec(dB) \ = vec(dW), \end{aligned} \tag{2.53}$$

where **b.d.**$(\bullet)$ is an operator that generates block diagonal matrices in the parentheses.

Use $dS = dNC_s^T$ and $dB = dNC_b^T$, we get:

$$\begin{aligned} &(C_s^T \otimes I_3)\textbf{b.d.}(K_{s1},\cdots,K_{s\alpha})vec\{dNC_s^T\} - (C_b^T \otimes I_3) \\ &\textbf{b.d.}(K_{b1},\cdots,K_{b\beta})vec\{dNC_b^T\} = vec(dW). \end{aligned} \tag{2.54}$$

Use the properties of the vec operator $vec(AXB) = (B^T \otimes A)vec(X)$:

$$
\begin{aligned}
&(C_s^T \otimes I_3)\textbf{b.d.}(K_{s1},\cdots,K_{s\alpha})(C_s \otimes I_3)vec(dN) - \\
&(C_b^T \otimes I_3)\textbf{b.d.}(K_{b1},\cdots,K_{b\beta})(C_b \otimes I_3)vec(dN) = vec(dW).
\end{aligned} \tag{2.55}
$$

Then, we get:

$$
\begin{aligned}
&\{\underbrace{(C_s^T \otimes I_3)\textbf{b.d.}(K_{s1},\cdots,K_{s\alpha})(C_s \otimes I_3) - (C_b^T \otimes I_3)\textbf{b.d.}(K_{b1},\cdots,K_{b\beta})(C_b \otimes I_3)}_{K_n}\} \\
&vec(dN) = vec(dW),
\end{aligned} \tag{2.56}
$$

where K_n is the stiffness matrix.

Let us take a look at K_{si} and K_{bj}:

$$
\begin{aligned}
K_{si} &= \frac{d\boldsymbol{s}_i\gamma_i + \boldsymbol{s}_i d\gamma_i}{d\boldsymbol{s}_i} = \gamma_i I_3 + \boldsymbol{s}_i \frac{d\gamma_i}{d\boldsymbol{s}_i}, \\
K_{bj} &= \frac{d\boldsymbol{b}_j\lambda_j + \boldsymbol{b}_j d\lambda_j}{d\boldsymbol{b}_j} = \lambda_j I_3 + \boldsymbol{b}_j \frac{d\lambda_j}{d\boldsymbol{b}_j}.
\end{aligned} \tag{2.57}
$$

We assume the materials are Hookean, the force densities (string in tension, bar in compression) can be expressed as:

$$
\gamma_i = k_{si}(1 - \frac{||\boldsymbol{s}_{i0}||}{||\boldsymbol{s}_i||}),\ \lambda_j = -k_{bj}(1 - \frac{||\boldsymbol{b}_{j0}||}{||\boldsymbol{b}_j||}), \tag{2.58}
$$

where $||\boldsymbol{s}_{i0}||$ and $||\boldsymbol{b}_{j0}||$ are the rest length of the ith string and jth bar. Take the derivative of Eq. (2.58), we get:

$$
\frac{d\gamma_i}{d\boldsymbol{s}_i} = k_{si}||\boldsymbol{s}_{i0}||\frac{\boldsymbol{s}_i^T}{||\boldsymbol{s}_i||^3},\ \frac{d\lambda_j}{d\boldsymbol{b}_j} = -k_{bj}||\boldsymbol{b}_{j0}||\frac{\boldsymbol{b}_j^T}{||\boldsymbol{b}_j||^3}, \tag{2.59}
$$

where k_{si} and k_{bj} are spring constants. They satisfy:

$$k_{si} = \frac{E_{si}A_{si}}{||\boldsymbol{s}_{i0}||},\ k_{bj} = \frac{E_{bj}A_{bj}}{||\boldsymbol{b}_{j0}||}, \tag{2.60}$$

where A_{si} and A_{bj} are cross section areas, E_{si} and E_{bj} are Young's modules of the strings and bars.

Substitute Eq. (2.59) and Eq. (2.60) to Eq. (2.57), we get:

$$K_{si} = \gamma_i I_3 + \boldsymbol{s}_i(k_{si}||\boldsymbol{s}_{i0}||\frac{\boldsymbol{s}_i^T}{||\boldsymbol{s}_i||^3}) = \gamma_i I_3 + \frac{E_{si}A_{si}}{||\boldsymbol{s}_i||^3}\boldsymbol{s}_i\boldsymbol{s}_i^T, \tag{2.61}$$

$$K_{bj} = \lambda_j I_3 + \boldsymbol{b}_j(-k_{bj}||\boldsymbol{b}_{j0}||\frac{\boldsymbol{b}_j^T}{||\boldsymbol{b}_j||^3}) = \lambda_j I_3 - \frac{E_{bj}A_{bj}}{||\boldsymbol{b}_j||^3}\boldsymbol{b}_j\boldsymbol{b}_j^T. \tag{2.62}$$

For solid bar tensegrity, use the information of label matrix Q, the mass of a string and mass of a bar are:

$$\begin{aligned} m_{si} &= \frac{\rho_s}{\sigma_s}||\boldsymbol{s}_i||^2\gamma_i, \\ m_{bj} &= (1-Q_{jj})\frac{\rho_b}{\sigma_b}||\boldsymbol{b}_j||^2\lambda_j + Q_{jj}\frac{2\rho_b}{\sqrt{\pi E_{bj}}}||\boldsymbol{b}_j||^{\frac{5}{2}}\lambda_j^{\frac{1}{2}}. \end{aligned} \tag{2.63}$$

Then, the cross section area of a bar and string are given by:

$$\begin{aligned} A_{si} &= \frac{m_{si}}{\rho_s||\boldsymbol{s}_i||} = \frac{||\boldsymbol{s}_i||\gamma_i}{\sigma_s}, \\ A_{bj} &= \frac{m_{bj}}{\rho_b||\boldsymbol{b}_j||} = (1-Q_{jj})\frac{||\boldsymbol{b}_i||\lambda_j}{\sigma_b} + Q_{jj}\frac{2||\boldsymbol{b}_j||^{\frac{3}{2}}\lambda_j^{\frac{1}{2}}}{\sqrt{\pi E_{bj}}}. \end{aligned} \tag{2.64}$$

Substitute Eq. (2.64) into Eq. (2.61):

$$\begin{aligned} K_{si} &= \gamma_i(I_3 + \frac{E_{si}}{\sigma_s}\frac{\boldsymbol{s}_i\boldsymbol{s}_i^T}{||\boldsymbol{s}_i||^2}), \\ K_{bj} &= \lambda_j(I_3 - (1-Q_{jj})\frac{E_{bj}}{\sigma_b}\frac{\boldsymbol{b}_j\boldsymbol{b}_j^T}{||\boldsymbol{b}_j||^2}) - 2Q_{jj}\sqrt{\frac{E_{bj}}{\pi}}\frac{\boldsymbol{b}_j\boldsymbol{b}_j^T}{||\boldsymbol{b}_j||^{\frac{3}{2}}}\lambda_j^{\frac{1}{2}}. \end{aligned} \tag{2.65}$$

Summarize Eq. (2.56) and Eq. (2.65) we get stiffness matrix K_n for tensegrity structure subject

to yielding and buckling constraints is given by:

$$K_n vec(dN) = vec(dW), \tag{2.66}$$

where

$$K_n = (C_s^T \otimes I_3)\textbf{b.d.}(K_{s1},\cdots,K_{s\alpha})(C_s \otimes I_3) - (C_b^T \otimes I_3)\textbf{b.d.}(K_{b1}, \cdots, K_{b\beta})(C_b \otimes I_3), \tag{2.67}$$

and

$$K_{si} = \gamma_i(I_3 + \frac{E_{si}}{\sigma_s}\frac{\boldsymbol{s}_i\boldsymbol{s}_i^T}{||\boldsymbol{s}_i||^2}), \tag{2.68}$$

$$K_{bj} = \lambda_j(I_3 - (1 - Q_{jj})\frac{E_{bj}}{\sigma_b}\frac{\boldsymbol{b}_j\boldsymbol{b}_j^T}{||\boldsymbol{b}_j||^2}) - 2Q_{jj}\sqrt{\frac{E_{bj}}{\pi}}\frac{\boldsymbol{b}_j\boldsymbol{b}_j^T}{||\boldsymbol{b}_j||^{\frac{3}{2}}}\lambda_j^{\frac{1}{2}}. \tag{2.69}$$

□

2.7.2 Stiffness Matrix for Hollow Bar Tensegrity

Theorem 2.7.2. *The stiffness matrix K_n for any hollow bar tensegrity structure subject to yielding and buckling constraints is given by:*

$$K_n vec(dN) = vec(dW), \tag{2.70}$$

where

$$K_n = (C_s^T \otimes I_3)\textbf{\textit{b.d.}}(K_{s1},\cdots,K_{s\alpha})(C_s \otimes I_3) - (C_b^T \otimes I_3)\textbf{\textit{b.d.}}(K_{b1}, \cdots, K_{b\beta})(C_b \otimes I_3),$$

and

$$K_{si} = \gamma_i(I_3 + \frac{E_{si}}{\sigma_s}\frac{\boldsymbol{s}_i\boldsymbol{s}_i^T}{||\boldsymbol{s}_i||^2}),$$
$$K_{bj} = \lambda_j(I_3 - (1-Q_{jj})\frac{E_{bj}}{\sigma_b}\frac{\boldsymbol{b}_j\boldsymbol{b}_j^T}{||\boldsymbol{b}_j||^2}) - Q_{jj}\frac{E_{bj}}{\sqrt{\pi E_{bj}}}(\sqrt{\pi^3 E_{bj} r_{j_{in}}^4 + 4\lambda_j||\boldsymbol{b}_j||^3} - \pi r_{j_{in}}^2\sqrt{\pi E_{bj}})\frac{\boldsymbol{b}_j\boldsymbol{b}_j^T}{||\boldsymbol{b}_j||^3}.$$

Proof. For hollow bar tensegrity, use the information of label matrix Q, the mass of a string and a bar are:

$$\begin{aligned} m_{si} =& \frac{\rho_s}{\sigma_s}||\boldsymbol{s}_i||^2\gamma_i, \\ m_{bj} =& (1-Q_{jj})\frac{\rho_b}{\sigma_b}||\boldsymbol{b}_j||^2\lambda_j + Q_{jj}\frac{\rho_b||\boldsymbol{b}_j||}{\sqrt{\pi E_b}}(\sqrt{\pi^3 E_{bj} r_{j_{in}}^4 + 4\lambda_j||\boldsymbol{b}_j||^3} - \pi r_{j_{in}}^2\sqrt{\pi E_b}). \end{aligned} \tag{2.71}$$

Then, the cross-section area of a bar and string are given by:

$$\begin{aligned} A_{si} =& \frac{m_{si}}{\rho_s||\boldsymbol{s}_i||} = \frac{||\boldsymbol{s}_i||\gamma_i}{\sigma_s}, \\ A_{bj} =& \frac{m_{bj}}{\rho_b||\boldsymbol{b}_j||} = (1-Q_{jj})\frac{||\boldsymbol{b}_i||\lambda_j}{\sigma_b} + Q_{jj}\frac{1}{\sqrt{\pi E_{bj}}}(\sqrt{\pi^3 E_b r_{j_{in}}^4 + 4\lambda_j||\boldsymbol{b}_j||^3} - \pi r_{j_{in}}^2\sqrt{\pi E_b}). \end{aligned} \tag{2.72}$$

Substitute Eq. (2.72) into Eq. (2.61):

$$K_{si} = \gamma_i(I_3 + \frac{E_{si}}{\sigma_s}\frac{\boldsymbol{s}_i\boldsymbol{s}_i^T}{||\boldsymbol{s}_i||^2}), \tag{2.73}$$

$$\begin{aligned} K_{bj} =& \lambda_j(I_3 - (1-Q_{jj})\frac{E_{bj}}{\sigma_b}\frac{\boldsymbol{b}_j\boldsymbol{b}_j^T}{||\boldsymbol{b}_j||^2}) - Q_{jj}\frac{E_{bj}}{\sqrt{\pi E_{bj}}} \\ & (\sqrt{\pi^3 E_{bj} r_{j_{in}}^4 + 4\lambda_j||\boldsymbol{b}_j||^3} - \pi r_{j_{in}}^2\sqrt{\pi E_{bj}})\frac{\boldsymbol{b}_j\boldsymbol{b}_j^T}{||\boldsymbol{b}_j||^3}. \end{aligned} \tag{2.74}$$

Summarize Eq. (2.56) and Eq. (2.73) we get stiffness matrix K_n for tensegrity structure subject to yielding and buckling constraints is given by:

$$K_n vec(dN) = vec(dW), \tag{2.75}$$

where

$$K_n = (C_s^T \otimes I_3)\textbf{b.d.}(K_{s1},\cdots,K_{s\alpha})(C_s \otimes I_3) - (C_b^T \otimes I_3)\textbf{b.d.}(K_{b1}, \cdots, K_{b\beta})(C_b \otimes I_3), \quad (2.76)$$

and

$$K_{si} = \gamma_i(I_3 + \frac{E_{si}}{\sigma_s}\frac{\boldsymbol{s}_i\boldsymbol{s}_i^T}{||\boldsymbol{s}_i||^2}), \quad (2.77)$$

$$\begin{aligned} K_{bj} =& \lambda_j(I_3 - (1-Q_{jj})\frac{E_{bj}}{\sigma_b}\frac{\boldsymbol{b}_j\boldsymbol{b}_j^T}{||\boldsymbol{b}_j||^2}) - Q_{jj}\frac{E_{bj}}{\sqrt{\pi E_{bj}}} \\ & (\sqrt{\pi^3 E_{bj} r_{j_{in}}^4 + 4\lambda_j||\boldsymbol{b}_j||^3} - \pi r_{j_{in}}^2\sqrt{\pi E_{bj}})\frac{\boldsymbol{b}_j\boldsymbol{b}_j^T}{||\boldsymbol{b}_j||^3}. \end{aligned} \quad (2.78)$$

□

2.8 Minimal Mass Tensegrity Structure Design with Gravity and no Global Buckling

Theorem 2.8.1. *The minimal mass of tensegrity system at an equilibrium is globally stable in the given configuration with external forces is given by a non-linear programming problem: The minimal mass problems can be formulated as:*

$$\begin{cases} \underset{x}{\textit{minimize}} & M \\ \textit{subject to} & Ax = W_{e\ vec} + W_{g\ vec},\ x \geq \epsilon_0, \textit{and}\ eig(K_n) > \mu I \end{cases}, \quad (2.79)$$

where ϵ_0 is the prestress lower bound assigned to the strings, and $\epsilon_0 \geq 0$ guarantees that all strings are in tension and all bars are in compression, $eig(K_n)$ returns the eigenvalues of the matrix K_n, and the system is globally stable at the equilibrium for $\mu \geq 0$.

Notice that to solve Eq. (2.79), one needs to specify the label matrix Q. However, one cannot exactly tell Q for any structure in advance because it is determined by structure topology and external force. To obtain a global solution, the nonlinear optimization problem can be solved in an iterative manner as described in Algorithm 4.

Algorithm 3: Minimal Mass Tensegrity subject to Stability and Gravity

1) Given tensegrity structure topology N, C_b, C_s and external force W, compute A and $W_{e\ vec}$ from Eq. (2.17).
2) Let $Q = I^{\beta\times\beta}$, $W_{g\ vec} = 0$, $\epsilon_0 = 0$, $\delta\epsilon = 0.01$, $\mu = 0$.
3) Compute force densities x:
while $\underline{\min\{eig(K_n)\} < \mu}$ **do**
  while $\underline{Q_{i+1} \neq Q_i}$ **do**

$$\begin{cases} \underset{x}{\text{minimize}}\ M \\ \text{subject to } Ax = W_{e\ vec} + W_{g\ vec},\ x \geq \epsilon_0. \end{cases}$$

  Compute λ from x, check Eq. (2.23), update Q.
  Update $W_{g\ vec}$ from Eq. (2.35).
  $i \leftarrow i + 1$.
  end while
  Compute stiffness matrix K_n from Eq. (2.42).
  $\epsilon_0 \leftarrow \epsilon_0 + \delta\epsilon$.
end while

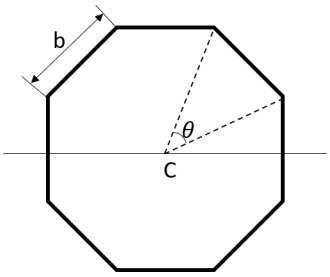

Figure 2.5: Solid regular polygon bar cross-section with p sides. Reprinted with permission from [5].

2.9 Variable Bar Cross-sections

Let a solid or hollow bar has length l_0, density ρ_b, cross-section area A, moment of inertia $I(A)$, which is a function of bar cross-section shape), Young's modulus E_b, and yield strength σ_b, and the bar is under compressive load $f(l_0)$. If a bar yields, the bar mass is:

$$m_Y(l_0) = \rho_b A l_0,\ f(l_0) = \sigma_b A,\ \rightarrow m_Y(l_0) = \frac{\rho_b}{\sigma_b} f(l_0) l_0. \tag{2.80}$$

If a bar buckles, the bar mass is:

$$m_B(l_0) = \rho_b A l_0,\ f(l_0) = \frac{\pi^2 E_b}{l_0^2} I(A). \tag{2.81}$$

From the above equation, we know that the mass of a bar subject to yielding is independent of the bar cross-section shape. In other words, given compressive load $f(l_0)$, bar length l_0, and bar material, bar mass cannot be reduced by changing the solid bar cross-section shape if the bar yields. However, if a bar buckles, bar mass is related to the bar cross-section shape, which is discussed as follows.

2.9.1 Variable Bar Cross-sections for Solid Bar Tensegrity

Theorem 2.9.1. *For solid bar tensegrity, one can save mass by using regular polygon bars with p sides,*

$$\begin{aligned} M^S =& \frac{\rho_s}{\sigma_s}(vec(\lfloor S^T S \rfloor))^T \gamma + \frac{\rho_b}{\sigma_b}(vec(\lfloor B^T B \rfloor (I - Q)))^T \lambda \\ &+ \zeta_{sp} \frac{2\rho_b}{\sqrt{\pi E_b}}(vec(\lfloor B^T B \rfloor^{\frac{5}{4}} Q))^T \lambda^{\frac{1}{2}}, \end{aligned} \tag{2.82}$$

where the mass reduction coefficient $\zeta_{sp} = \frac{1}{\pi}\sqrt{\frac{3p\pi}{3cot\frac{\pi}{p} + tan\frac{\pi}{p}}}$, for different cross section shape, triangle $\zeta_3 = 0.9094$, square $\zeta_4 = 0.9772$, pentagon $\zeta_5 = 0.9916$, hexagon $\zeta_6 = 0.9962$.

Proof. Let a solid bar with regular polygon with p sides, as shown in Figure 2.5, C is centroid (at the center of the polygon), p is number of sides ($p \geq 3$), b is length of the side, $\theta = \frac{2\pi}{p}$ is central angle for one side, moment of inertia of the regular polygon I_{ppoly} with p sides is given as [51]:

$$I_{ppoly} = \frac{A_{ppoly}^2}{12p}(3cot\frac{\pi}{p} + tan\frac{\pi}{p}),\ A_{ppoly} = \frac{pb^2}{4} cot\frac{\pi}{p}, \tag{2.83}$$

where A_{ppoly} is the area of the polygon cross-section.

For a constant cross-section area A_{ppoly}, Take the first derivative of Eq. (2.83) with respect to

p, we get:

$$\begin{aligned}\frac{\partial I_{ppoly}}{\partial p} =& \frac{2A_{ppoly}}{12p}(3cot\frac{\pi}{p} + tan\frac{\pi}{p})(\frac{b^2}{4}cot\frac{\pi}{p} + \frac{\pi b^2}{4p}csc^2\frac{\pi}{p}) \\ & - \frac{A^2_{ppoly}}{12p^2}(3cot\frac{\pi}{p} + tan\frac{\pi}{p}) - \frac{\pi A^2_{ppoly}}{12p^3}(-3csc^2\frac{\pi}{p} + sec^2\frac{\pi}{p}) < 0. \end{aligned} \tag{2.84}$$

From Eq. (2.84), we know as p increases, the moment of inertia I_{ppoly} decreases. Mass of a solid bar subject to buckling with a polygon cross-section is given by:

$$m_{ppoly} = \frac{\rho_b l_0^2}{\pi}\sqrt{\frac{12pf(l_0)}{(3cot\frac{\pi}{p} + tan\frac{\pi}{p})E_b}}. \tag{2.85}$$

Moment of inertia of the circle is:

$$I_{cir} = \frac{\pi r^4}{4},\ A_{cir} = \pi r^2. \tag{2.86}$$

Mass of a solid bar subject to buckling with a circular cross-section is given by:

$$m_{cir} = 2\rho_b l_0^2\sqrt{\frac{f(l_0)}{\pi E_b}}. \tag{2.87}$$

Then to take the same compressive load $f(l_0)$, we can compare the mass of a polygon and a circular cross-section bar:

$$\zeta_{sp} = \frac{m_{ppoly}}{m_{cir}} = \frac{1}{\pi}\sqrt{\frac{3p\pi}{3cot\frac{\pi}{p} + tan\frac{\pi}{p}}},\ p = 3, 4, 5, \cdots. \tag{2.88}$$

From Figure 2.6, we know that to take the same compressive load, the mass of a polygon cross-section bar is smaller than a circular one. As the polygon sides increase, the bar mass increases. A triangle cross-section gives the minimal mass, which is 90.94% of a circular one. In other words, a triangular cross-section bar can save 9.06% mass compared to a circular one.

Here, we introduce a mass reduction coefficient ζ_{sp}, which satisfies $m_{ppoly} = \zeta_{sp} m_{cir},\ (p =$

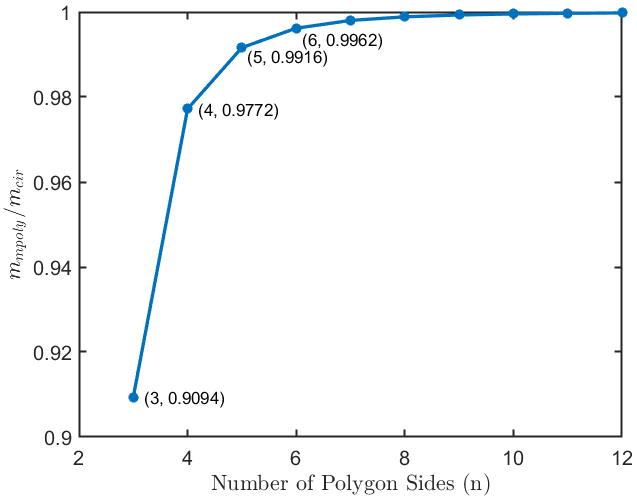

Figure 2.6: Mass ratio of a solid bar with polygon and circular cross section v.s. polygon sides (p). Reprinted with permission from [5].

$3,\ 4,\ 5, \cdots$). For different cross section shape, for example, triangle $\zeta_3 = 0.9094$, square $\zeta_4 = 0.9772$, pentagon $\zeta_5 = 0.9916$, hexagon $\zeta_6 = 0.9962$.

Eq. (2.24) are for circular solid bars. When buckling is the mode of failure of one bar, we can replace it with a regular polygon bar to save mass. Then, Eq. (2.24) can be written as:

$$\begin{aligned} M^S =& \frac{\rho_s}{\sigma_s}(vec(\lfloor S^T S \rfloor))^T \gamma + \frac{\rho_b}{\sigma_b}(vec(\lfloor B^T B \rfloor (I - Q)))^T \lambda \\ &+ \zeta_{sp} \frac{2\rho_b}{\sqrt{\pi E_b}}(vec(\lfloor B^T B \rfloor^{\frac{5}{4}} Q))^T \lambda^{\frac{1}{2}}. \end{aligned} \tag{2.89}$$

□

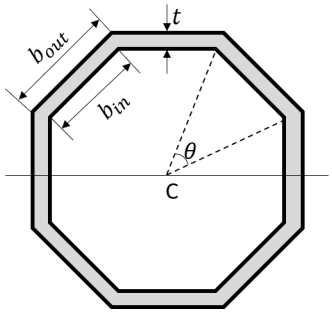

Figure 2.7: Hollow regular polygon bar cross-section with p sides. Reprinted with permission from [5].

2.9.2 Variable Bar Cross-sections for Hollow Bar Tensegrity

Theorem 2.9.2. *For hollow bar tensegrity, one can save mass by using regular polygon bars with p sides,*

$$\begin{aligned} M^H =& \frac{\rho_s}{\sigma_s}(vec(\lfloor S^T S \rfloor))^T \gamma + \frac{\rho_b}{\sigma_b}(vec(\lfloor B^T B \rfloor (I - Q)))^T \lambda \\ &+ \zeta_{hp} \frac{\rho_b (vec(\lfloor B^T B \rfloor^{\frac{1}{2}} Q))^T}{\sqrt{\pi E_b}} (\sqrt{\pi^3 E_b r_{in}^4 + 4(\lfloor B^T B \rfloor^{\frac{3}{2}} Q)\lambda} - \pi r_{in}^2 \sqrt{\pi E_b}), \end{aligned} \tag{2.90}$$

where the mass reduction coefficient $\zeta_{hp} = (\sqrt{\frac{12 f(l_0) l_0^2 p}{\pi^4 E_b r_{in}^4 (3cot\frac{\pi}{p} + tan\frac{\pi}{p})} + 1} - 1)/(\sqrt{1 + \frac{4 f(l_0) l_0^2}{\pi^3 E_b r_{in}^4}} - 1)$*,* $f(l_0)$*,* l_0*, and* E_b *are the force, length, and Young's modulus of the buckling bar,* r_{in} *is the radius of the hollow pipe, for different cross section shape, triangle* $\zeta_3 = 0.8270$*, square* $\zeta_4 = 0.9549$*, pentagon* $\zeta_5 = 0.9833$*, hexagon* $\zeta_6 = 0.9924$*.*

Proof. Let a hollow bar with regular polygon with p sides, as shown in Figure 2.7, C is centroid (at center of polygon), p is number of sides ($p \geq 3$), b_{out} and b_{in} are length of the outer and inner sides, A_{out} and A_{in} are area of the outer and inner polygon, $\theta = \frac{2\pi}{p}$ is central angle for one side,

moment of inertia of the regular polygon I_{ppoly} with p sides is given as [51]:

$$I_{ppoly} = \frac{(A_{out}^2 - A_{in}^2)}{12p}(3cot\frac{\pi}{p} + tan\frac{\pi}{p}), \tag{2.91}$$

$$A_{out} = \frac{pb_{out}^2}{4}cot\frac{\pi}{p},\ A_{in} = \frac{pb_{in}^2}{4}cot\frac{\pi}{p}. \tag{2.92}$$

Mass of a hollow bar can be written as:

$$m = \rho_b l_0(A_{out} - A_{in}) = \rho_b l_0 \frac{p}{4}cot\frac{\pi}{p}b_{in}^2((\frac{b_{out}}{b_{in}})^2 - 1). \tag{2.93}$$

Moment of inertia for a hollow bar can be written as:

$$I_{ppoly} = \frac{1}{12p}(\frac{p^2}{16}b_{out}^4 cot^2\frac{\pi}{p} - \frac{p^2}{16}b_{in}^4 cot^2\frac{\pi}{p})(3cot\frac{\pi}{p} + tan\frac{\pi}{p}) \tag{2.94}$$

$$= \frac{p}{192}cot^2\frac{\pi}{p}b_{in}^4((\frac{b_{out}}{b_{in}})^4 - 1)(3cot\frac{\pi}{p} + tan\frac{\pi}{p}) \tag{2.95}$$

$$= \frac{p}{192}(b_{out}^4 - b_{in}^4)cot^2\frac{\pi}{p}(1 + 3cot^2\frac{\pi}{p}). \tag{2.96}$$

Since we have $f(l_0) = \frac{\pi^2 E_b}{l_0^2}I$, one can get:

$$(\frac{b_{out}}{b_{in}})^2 = \sqrt{\frac{192f(l_0)l_0^2}{\pi^2 pE_b cot^2\frac{\pi}{p}b_{in}^4(3cot\frac{\pi}{p} + tan\frac{\pi}{p})}} + 1. \tag{2.97}$$

Mass of a hollow bar with a polygon cross-section is given by:

$$m_{ppoly} = \frac{\rho_b l_0 p}{4}cot\frac{\pi}{p}b_{in}^2(\sqrt{\frac{192f(l_0)l_0^2}{\pi^2 pE_b cot^2\frac{\pi}{p}b_{in}^4(3cot\frac{\pi}{p} + tan\frac{\pi}{p})}} + 1 - 1). \tag{2.98}$$

The moment of inertia of a bar with a circular cross-section is:

$$I_{cir} = \frac{\pi(r_{out}^4 - r_{in}^4)}{4},\ A_{cir} = \pi(r_{out}^2 - r_{in}^2). \tag{2.99}$$

Euler buckling force for a hollow bar with a circular cross-section is:

$$f(l_0) = \frac{\pi^3 E_b}{4l_0^2}(r_{out}^4 - r_{in}^4) = \frac{\pi^3 E_b}{4l_0^2} r_{in}^4((\frac{r_{out}}{r_{in}})^4 - 1). \tag{2.100}$$

Then, we get:

$$(\frac{r_{out}}{r_{in}})^2 = \sqrt{1 + \frac{4fl_0^2}{\pi^3 E_b r_{in}^4}}. \tag{2.101}$$

Mass of a hollow bar with a circular cross-section is given by:

$$m_{cir} = \rho_b \pi l_0 r_{in}^2 (\sqrt{1 + \frac{4f(l_0)l_0^2}{\pi^3 E_b r_{in}^4}} - 1). \tag{2.102}$$

Then to take the same compressive load $f(l_0)$, we can compare the mass of a polygon and a circular cross section bar:

$$\begin{aligned}\frac{m_{ppoly}}{m_{cir}} =& \frac{pcot\frac{\pi}{p}}{4\pi}(\frac{b_{in}}{r_{in}})^2(\sqrt{\frac{192f(l_0)l_0^2}{\pi^2 pE_b cot^2\frac{\pi}{p} b_{in}^4(3cot\frac{\pi}{p} + tan\frac{\pi}{p})} + 1} \\ & - 1)/(\sqrt{1 + \frac{4f(l_0)l_0^2}{\pi^3 E_b r_{in}^4}} - 1),\ p = 3, 4, 5, \cdots .\end{aligned} \tag{2.103}$$

In order to make a fair comparison of polygon cross-sections, we assume the inner cross section area of the polygon and circular hollow bar are the same, which satisfies $\pi r_{in}^2 = \frac{pb_{in}^2}{4} cot\frac{\pi}{p}$. The physical meaning is that the polygon and circular hollow bars have the same space to fit in the strings, instruments, electronics etc. Substitute $b_{in}^2 = \frac{4\pi}{pcot\frac{\pi}{p}} r_{in}^2$ into Eq. (2.103):

$$\zeta_{hp} = \frac{m_{ppoly}}{m_{cir}} = (\sqrt{\frac{12f(l_0)l_0^2 p}{\pi^4 E_b r_{in}^4(3cot\frac{\pi}{p} + tan\frac{\pi}{p})} + 1} - 1)/(\sqrt{1 + \frac{4f(l_0)l_0^2}{\pi^3 E_b r_{in}^4}} - 1),\ p = 3, 4, 5, \cdots . \tag{2.104}$$

Let us take a close look at this equation by an example, for a steel pipe, $E_b = 200$ GPa, $r_{in} = 0.01$ m, $l_0 = 1$ m, and $f(l_0)$ = 1, 10, 100, 1000 N, Figure 2.8 gives the results. The results show that

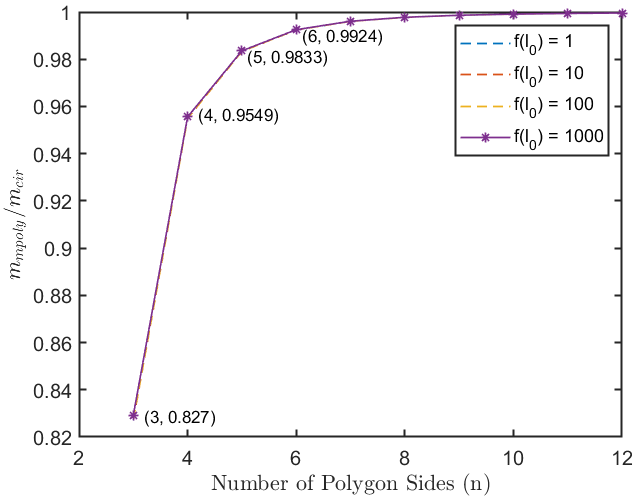

Figure 2.8: Mass ratio of a hollow bar with polygon and circular cross-section v.s. polygon sides (p). Reprinted with permission from [5].

to take the same compressive load, the mass of a polygon cross-section bar is smaller than a circular one. As the polygon sides increase, the bar mass increases, a triangle cross-section gives the minimal mass, which is 82.7% of a circular one. In other words, a triangular cross-section bar can save 17.3% mass compared to a circular one. And the compressive load $f(l_0)$ has little influence on the mass reduction ratio as long as the buckling is the mode of failure of the bar. Similarly, we use the same mass reduction coefficient ζ_{hp}, which satisfies $m_{ppoly} = \zeta_{hp} m_{cir},\ (p = 3,\ 4,\ 5, \cdots)$. For different cross section shape, for example, triangle $\zeta_3 = 0.8270$, square $\zeta_4 = 0.9549$, pentagon $\zeta_5 = 0.9833$, hexagon $\zeta_6 = 0.9924$.

Eq. (2.29) are for circular hollow bars. When buckling is the mode of failure of one bar, one can replace the bar with a regular hollow polygon bar to save mass. Then, Eq. (2.29) can be written as:

$$
\begin{aligned}
M =& \frac{\rho_s}{\sigma_s}(vec(\lfloor S^T S \rfloor))^T \gamma + \frac{\rho_b}{\sigma_b}(vec(\lfloor B^T B \rfloor (I - Q)))^T \lambda \\
&+ \zeta_{hp} \frac{\rho_b (vec(\lfloor B^T B \rfloor^{\frac{1}{2}} Q))^T}{\sqrt{\pi E_b}} (\sqrt{\pi^3 E_b r_{in}^4 + 4(\lfloor B^T B \rfloor^{\frac{3}{2}} Q)\lambda} - \pi r_{in}^2 \sqrt{\pi E_b}).
\end{aligned}
$$

□

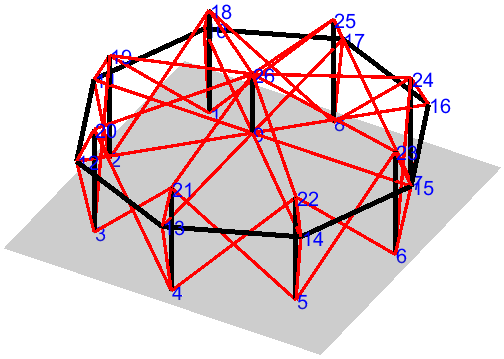

Figure 2.9: Tensegrity Shelter, structure complexity is 8 (gives an octagon in the middle), bars are in black and strings are in red. Reprinted with permission from [5].

2.10 Bar Joint Mass Penalty

It is also important to know the joint information of a tensegrity structure. Because as structure complexity increases, the numbers of nodes also increase. In a practical problem, the joint mass will also take a bigger portion of the total structure mass. Here, the joint mass penalty is assigned to the total structure mass according to the class number of each node (number of bars touching each other). Joint information vector J_{info} can be obtained from the absolute values of bar connectivity matrix $|C_b|$:

$$J_{info}^T = \mathbf{1}^{1\times\beta}|C_b|. \tag{2.105}$$

Each column of J_{info}^T gives the class number of each node. For example, a tensegrity shelter is shown in Figure 2.9. We can obtain J_{info}^T =[1, 1, 1, 1, 1, 1, 1, 1, 1, 2, 2, 2, 2, 2, 2, 2, 2, 1, 1, 1, 1, 1, 1, 1, 1, 1]. It is also easily accessible by programming to abstract the information of all classes of the structure as well as a class of each joint below. This is a Class 2 structure. Class 1 joints are 1, 2, 3, 4, 5, 6, 7, 8, 9, 18, 19, 20, 21, 22, 23, 24, 25, 26. Class 2 joints are 10, 11, 12, 13, 14, 15, 16, 17.

The penalty mass for joints can be usually treated as a small ratio of a bar mass [39]. For example, if a bar mass is 1 kg, one can assign Class 1 joint mass is 0.01 kg, Class 2 joint mass is 0.02 kg, and Class K joint mass is $0.01 \times K$ kg as a linear fashion.

2.11 Example: Deployable Tensegrity Lunar Tower

The great heroic success of the Apollo program has triggered a strong will, passion, and enthusiasm of the public. Till now, humans have developed various heavy rockets, put rovers on other planets, sent people to ISS (International Space Station), and launched probes to the Sun. The interest is now returning to the moon to utilize its resources. Various Lunar exploration missions have provided us with information about its abundant useful resources. For example, the entire lunar surface is covered with an unconsolidated layer of regolith [52], which can be used as a very efficient material for building a space habitat shield [53]. The moon is especially rich in Ca, Al, Si, O, Mg, Fe, and Ti [54]. A recent study also shows that a large amount of ice has a permanent presence in the shadowed lunar polar craters [55]. The goal of this section is to study a feasible design of a lightweight tower to support moon mining operations.

Scientists have been exploring the idea of mining the moon for some time. Mining ice on the moon can be achieved by using solar energy to heat the ice and store it as water [56]. Rock breakage by microwave techniques, mineral processing, and materials manufacturing for ISRU has also been discussed [57]. Tunnel Boring Machines could offer another safe and efficient approach for mining on the moon [58]. Sanders presented NASA's lunar ISRU strategy, which includes plans for regolith, polar water/volatile mining, commercial opportunities, rovers, and mission schedules [59]. The mining design of these works mainly focuses on rovers, operations, and extracting minerals. Some of the important issues are left unsolved for mining in the permanent shaded polar craters at the high latitude of the moon: 1) a structure to help collect and distribute solar energy efficiently (mirrors and solar panels to light up the operation area, store energy, and generate heat) and 2) supporting communication equipment. All these problems lead to the requirement of a lunar tower.

This section explores a tensegrity tower to facilitate the application of mining on the moon. In fact, a few studies have been made on tensegrity tower designs. For example, Sultan and Skelton demonstrated a deployment strategy for tensegrity structures by a multi-stage three-strut Snelson-type tensegrity tower [60]. Klimke and Soeren presented a construction process of a tensegrity tower [61]. Yildiz and Lesieutre studied the approach to obtain effective continuum beam stiffness properties of tensegrity towers with n struts [62]. However, none of these towers modeled gravity in the design process and viewed mass design and local & global stability as an integrated design process. In order to achieve a small amount of valuable supporting resources/mass in space as possible, this section presents the design and analysis of a minimal mass tensegrity lunar tower.

2.11.1 Tower Topology Design

Skelton and de Oliveira have proved that T-Bar and D-Bar systems require less mass than a continuum bar in taking the same compression load $f(l_0)$. A three-dimensional T-Bar unit is shown in Figure 2.10a [63]. Each longitudinal bar in the T-bar structure can be replaced with another T-bar tensegrity unit while preserving the total length of the structure. Repeating this self-similar process q times is defined as the complexity of the structure. Figure 2.11a shows a T-Bar structure of complexity $q = 3$.

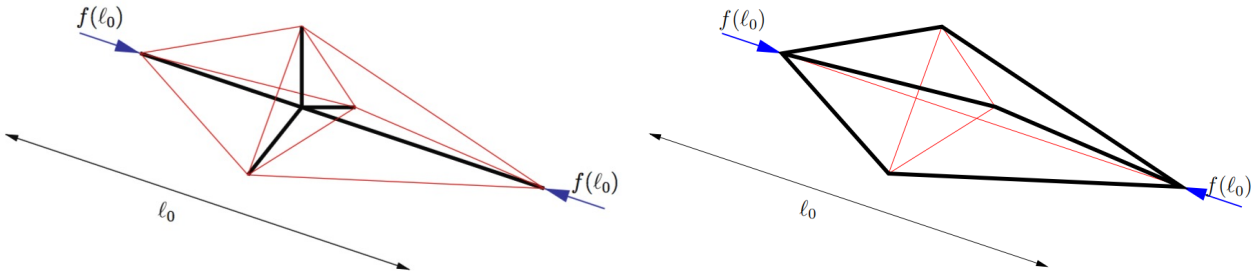

(a) 3D T-Bar unit.

(b) 3D D-Bar unit.

Figure 2.10: Three-dimensional tensegrity T-Bar and D-Bar unit, black lines are bars and red lines are strings.

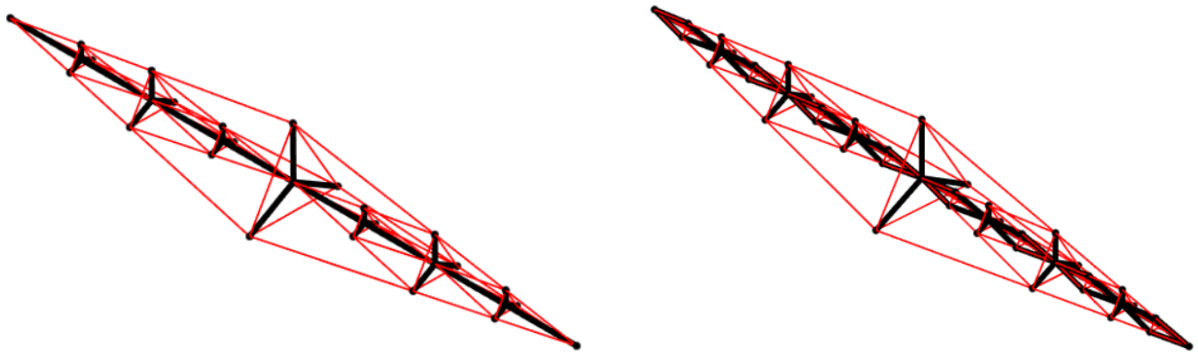

(a) Three-dimensional T_3 structure.

(b) Three-dimensional T_3D_1 structure.

Figure 2.11: Three-dimensional tensegrity T-Bar and T_nD_1-Bar structure.

The dual of the T-Bar unit is called a D-Bar structure, which is shown in Figure 2.10b. The D-bar is also shown to be a more efficient structure in taking a compressive load than a continuum bar [63]. Another advantage of the D-bar structure is its deployability. The length of the structure can be changed by controlling the length of the individual strings. We combine the two structures such that it is both deployable and mass efficient in taking compression. Let us start with a T-Bar structure with complexity $q = n$ and replace its longitudinal middle bars with 2^n D-Bar units to obtain a T_nD_1 structure. A 3-dimensional T_3D_1 is shown in Figure 2.11b. The same T_nD_1 structure is used to design towers as the payload on top of the tower will exert a compressive load on two ends of the structure. The simulation and experimental model is shown in Figure 2.12a. A deployable experimental model, shown in Figure 2.12b.

2.11.2 Tower Deployment Discussion

To construct the tower model, the metal materials for bars are available on the moon [64], the strings (for example, UHMWPE, Ultra High Molecular Weight Polyethylene) can be shipped from the earth. There are mainly two ways to deploy tensegrity structures: 1. Altering string rest-lengths, which are usually realized by a motor-pulley-cable system [65, 66]. 2. Using shape memory alloy (SMA) tendon wires, which are usually achieved by SMA and DC current supply devices [67, 68]. The first method has these properties: wider control bandwidth, less cost, more

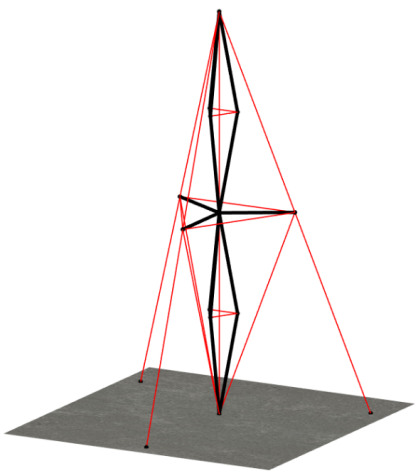

(a) Mathematical tower model.

(b) Experimental tower model.

Figure 2.12: Three-dimensional T_2D_1 tensegrity tower models.

environmentally robust, but mechanically more complicated than the second one. For this tower design, deployability can be achieved by shorting the middle string length of the D-Bar. A shape control algorithm for class-k tensegrity [7] can be applied to get the deploy sequence, shown in Figure 2.13.

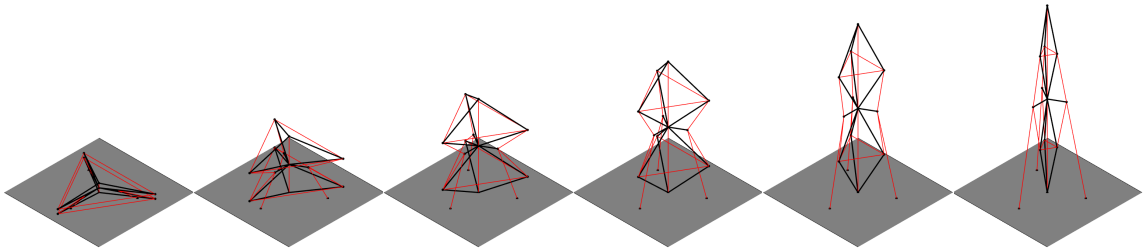

Figure 2.13: T_2D_1 Tower deployment from a stowed configuration to a fully deployable one by shrinking the strings in the D-Bar units.

2.11.3 A Family of Lunar Towers

The tensegrity tower provides a set of non-dimensional figures of merit, i.e., payload fraction, prestress, minimal mass complexity. A family of towers is shown in Figure 2.14. Thus, one has

the option to tune the structure topology based on the requirements of different applications. For a given tower height and payload, Skelton and de Oliveira showed that there exists an optimal structure complexity for a given compressive load. However, one must also take the construction feasibility into consideration since the bars can be yield nanoscales, and joint mass can be a big portion of total mass [63].

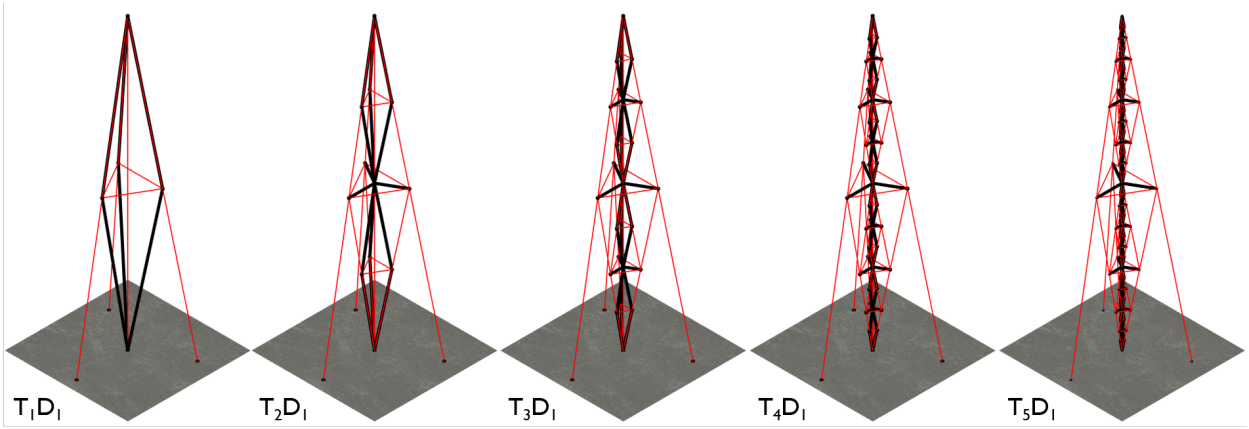

Figure 2.14: Deployable towers of varying complexity, the T-Bar and D-Bar angles (the angle between the sides of the two units and vertical line) are $\alpha_T = \alpha_D = \frac{\pi}{18}$.

2.11.4 Design Parameters Study of the Tower

The lunar craters vary in size from a few meters to 400 km, the depth of the craters are from less than 1 meter to 8 km, and a large portion of these craters is around 10 km in diameter and 1 km deep [69]. Here, we present a series of T_5D_1 tower designs in the presence of lunar gravity for various requirements. The payloads on the top of the tower include solar panels, communication devices, and mirrors with an estimated load of m_p = 250 kg. Therefore, the compressive force at the top of the tower is $F = m_p g_{moon} = 250 \times 1.62$ N = 405 N.

We are also interested to see how the structure mass varies with different structure materials. The three combinations are studied: Carbon bars and UHMWPE strings (C-UHMWPE), Carbon bars and Aluminum strings (C-Al), Aluminum bars and Aluminum strings (Al-Al). The material

properties are given in Table 2.5. The tower height varies from 50 m to 1.2 km, and the prestress ϵ_0 as a percentage of the payload force is from 10% to 30%. The the payload fraction (payload mass/structure mass $\times$ 100%) of the towers are shown in in Figure 2.15.

To illustrate the surface plot, let us take a look at the 850 m tall tower, the prestress v.s. payload fraction is shown in Figure 2.16. The results show that as prestress increases, the payload fraction decreases. For a fixed prestress value, i.e., 20% prestress, the tower height v.s. payload fraction is shown in Figure 2.17. The results show that as tower height increases, the payload fraction decreases exponentially for the T_5D_1 towers. That is, the tower height is a more sensitive parameter than prestress to the tower mass. From the material study, we know the structure mass ranking is: C-UHMWPE $\leq$ C-Al < Al-Al.

Table 2.5: Material property for bars and strings, source: http://www.matweb.com/.

Properties	Carbon	UHMWPE	Aluminum	Units
Yield Stress	1.72×10^9	2.70×10^9	1.10×10^8	Pa
Young's Modulus	1.38×10^{11}	1.20×10^{11}	6.00×10^{10}	Pa
Density	$1,500$	970	2,700	kg/m^3

2.11.5 Wind Disturbance Study

One of the most popular functions interpolating wind speed vertical distribution is [70]:

$$U = U_\infty(\frac{h}{h_0})^\alpha, \tag{2.106}$$

where U is the wind velocity at a different height, U_∞ is the standard measured wind velocity, h is the height, h_0 is the U_∞ at the reference height, α is the terrain roughness coefficient, for a general case α = 2. Wind speed is normally measured at a standard height of 10 m above open flat ground

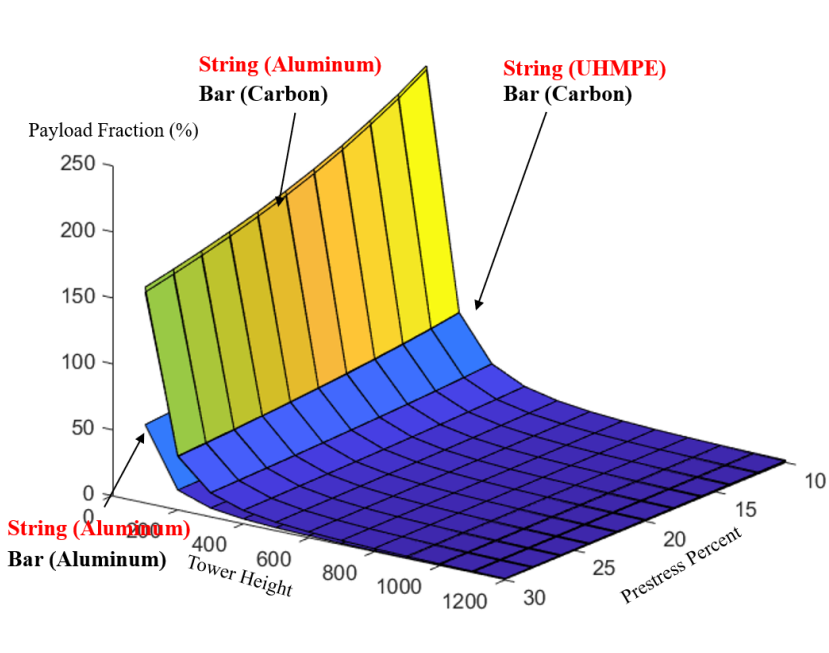

Figure 2.15: Payload Fraction, Tower Height, and Prestress Percent study of the deployable tensegrity tower.

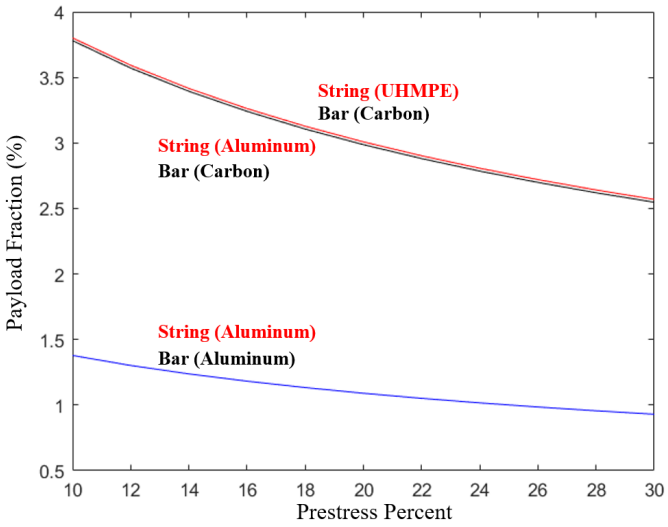

Figure 2.16: Prestress Percent v.s Payload Fraction of the deployable tower (tower height 850 m).

[71]. The drag force provided by the wind can be calculated as:

$$D = \frac{1}{2} C_d \rho S U^2, \tag{2.107}$$

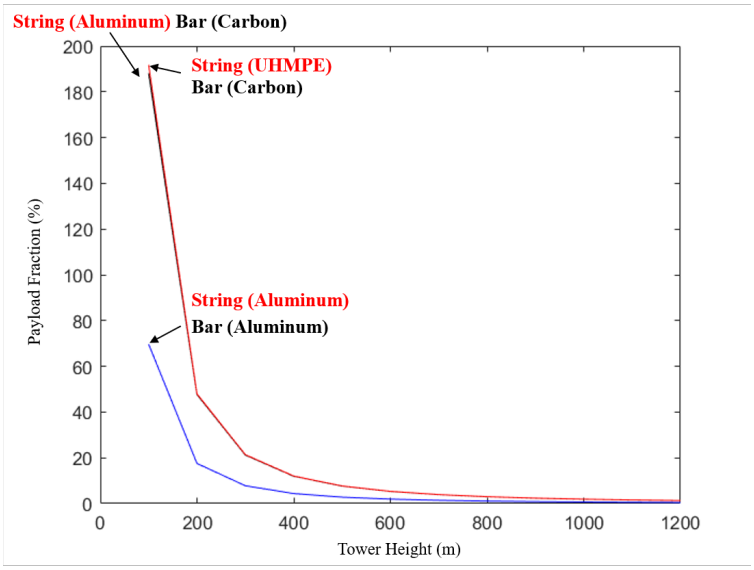

Figure 2.17: Tower Height v.s Payload Fraction of the deployable tower with a 20% prestress.

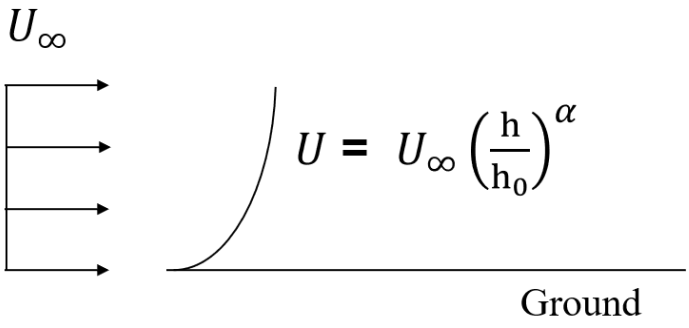

Figure 2.18: A typical wind velocity distribution profile.

where ρ is the air density (at 293K and 101.325 kPa, dry air has a density of 1.2041 kg/m^3) and C_d is the drag coefficient, here we use 1.0 for the bars. Results show that for a 100 m tall tower with 20% prestress to support 60 kg in earth gravity, and the structure mass is 156.46 kg with a safety factor of 1.2. The tower can sustain a wind speed of 9 m/s with a 1.2 structure safety factor without breaking any of the structural members while supporting itself.

2.11.6 Packaging Plan

The New Glenn rocket configuration is given in Table 2.6. Space for the payload: 7m in diameter, 20 m in height, and 769 m^3 loading volume. For an 800 m lunar tower supporting 250 kg load with 20% prestress, the tower mass is 8,311 kg. The details are given in Table 2.7, which fits comfortably in New Glen.

Table 2.6: New Glenn loading configuration, source: https://www.blueorigin.com/new-glenn/.

Items	Size
Height	2-stage 82 m (270 ft)
Diameter	7 m (23 ft)
Payload to LEO	45,000 kg (99,000 lb)
Payload to GTO	13,000 kg (29,000 lb)

Table 2.7: Bar mass information of the 800 m tall tower.

Bar Length	Number of Bars	Mass Fraction
8.82 m	24	1.15%
17.63 m	12	2.31%
25.38 m	96	73.48%
35.27 m	6	4.75%
70.53 m	3	9.27%
122.16 m	3	9.22%

2.12 Conclusion

This chapter presents a general framework of the minimal mass design for any solid or hollow bar tensegrity structures with and without gravity. The methodology yields several nonlinear programming problems. The choice of the cross-section of bars is discussed. Results show that for a solid and hollow bar (with the same inner cross-section area) if yielding is the mode of failure, one cannot save mass. If buckling is the mode of failure, one can use a solid or hollow triangular cross-section shape to save 9.06% or 17.3% mass compared with a circular one. We also parameterized the class number of a joint versus joints mass. Structure mass is slightly larger when considering gravity than one without gravity. For the deployable lunar tower example, a family of lunar towers and deployment methods are presented. The study of the T_5D_1 tower shows that to take a 250 kg payload and sustains the weight of the structure itself, prestress or tower height increases, structure mass increases. The structure mass is more sensitive to tower height than prestress in the strings. The string material change has little influence on the total structure mass. The material change of bars is critical to the total structure mass. A simplified wind model is studied for a 100 m tower to take a 60 kg payload with a 1.2 safety factor, and the tower can sustain a wind speed of 9 m/s. The packaging plan shows that the New Glenn rocket is able to fit the material for the 800 m lunar. This minimal mass design framework can be used for the static design of any truss or tensegrity structures. The principles developed in this chapter facilitate the understanding of both materials and structures.

3. INTEGRATING STRUCTURE DYNAMICS AND FLUIDS: TENSEGRITY SYSTEM DYNAMICS IN FLUIDS

This chapter presents the study of tensegrity system dynamics in fluids. It contains two parts: 1). tensegrity structures interface fluid directly, as shown in Figure 3.1. 2). tensegrity structures interface fluid by a skin (membrane) on the tensegrity structure, as shown in Figure 3.2. For the first part, this chapter provides compact vector and matrix forms of the nonlinear dynamics of class-1 and class-k tensegrity systems with fluid forces incorporated. Firstly, the equation of motion (both translation and rotation) of a single rod is modeled. Then, the fluid forces by fluid particles interacting with the rod are modeled and added to the derived dynamic equations of the rod. Then, by stacking all the governing equations of motion for each rod, compact vector and matrix forms of class-1 and class-k tensegrity dynamics are formulated. Three examples based on a three-dimensional prism model with and without considering fluid forces, with and without fluid inlet velocity, and landing to the ground with and without fluid influence are simulated and compared. Results show that the simulations match well with physics. The fluid provides significant damping to the dynamics of the structure. For the second part, this chapter studies tensegrity airfoil/hydrofoil interfaces fluid by the skin on the structure. The fluid forces on the foil surface are obtained by the panel method. Then, we develop a method for discretizing continuous airfoil curves based on shape accuracy. This method is compared with conventional methods (i.e. evenly spacing and cosine spacing methods). A tensegrity topology for shape controllable airfoil is proposed. The surface fluid forces are integrated into the surface supporting nodes of the structure, which can be used as the external force to simulate the tensegrity system dynamics. Finally, the foil examples are studied and compared to demonstrate the approach. This work enables the ability to do fluid-structure interaction studies of any tensegrity structures. The principles developed here can also be used for analyzing various kinds of tensegrity structures operating in the air or underwater.

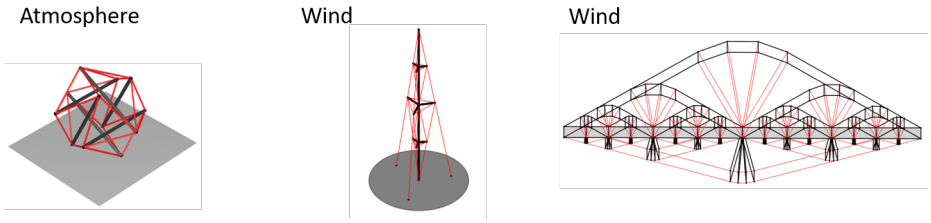

Figure 3.1: Structure interfaces fluid directly. From left to right: tensegrity lander, tensegrity T_2-Tower, and tensegrity bridge.

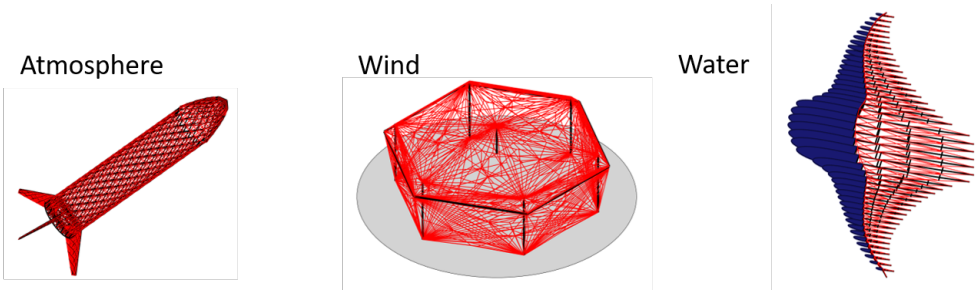

Figure 3.2: Structure interfaces fluid by a skin. From left to right: tensegrity rocket, tensegrity shelter, and tensegrity manta ray.

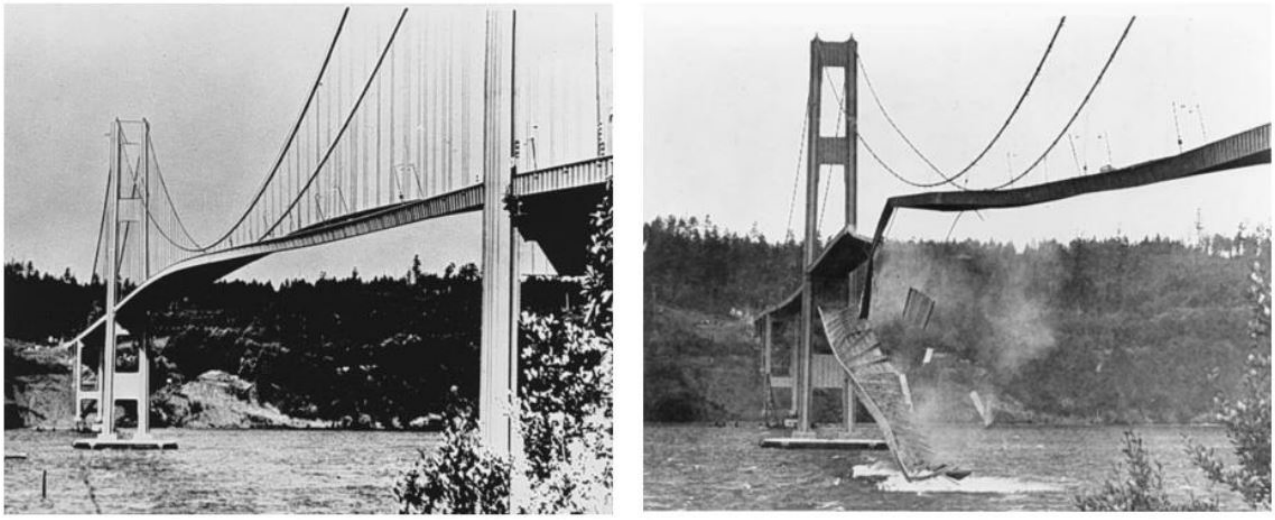

Figure 3.3: Left: High speed winds stimulate the vibration of the Tacoma Narrows Bridge, one can observe one of the oscillation modes of the bridge structure. Right: The resonance condition led to the crumble of the bridge on Nov. 7, 1940. Reprinted from UPI/Bettmann Newsphotos.

3.1 Introduction

Fluid-structure interaction (FSI) is an interdisciplinary study of how fluids and structures interact. The fluid pressure load may be large enough to cause the structure deformation, and in the meantime, the structure deformation can be significant enough to change the fluid flow itself as well. Failing to consider the FSI problems of some of the structures may leave out fundamental issues in modeling and lead to serious problems. For example, the Tacoma Narrows Bridge collapsed only four months later due to aeroelastic flutter [72, 73], shown in Figure 3.3. The blades of the airplanes and turbines can break due to FSI oscillations [74, 75]. The hemodynamical flow of blood in the heart is not a fixed geometry; the forces on the vessel walls can widen and stretch the tissue that changes the overall shape [76]. Thus, the coupling of the two subjects can provide us a deeper understanding of the psychics and guide our design and analysis structures. Currently, the research on FSI is still ongoing, and the problem, in general, is often too complex to solve analytically, and they are normally studied by experiments and numerical simulation [77]. This chapter develops an approach to simulate the tensegrity dynamics incorporated with fluid forces.

There are a few studies have been conducted on tensegrity dynamics. For example, Sulton et al. derived linearized equations of motion for tensegrity models around arbitrary equilibrium configurations [78]. In 2005, Skelton presented one of the simplest dynamics forms for class-1 structure by using non-minimal coordinates and assumed the compressive elements to have no inertia about the longitudinal axis [79]. Later, Wroldsen added wave forces to the dynamics of class-1 tensegrity structures [80]. Nagase et al. wrote the equations of motion in vector form for any class-k tensegrity system dynamics [81]. Cheong et al. extended the non-minimal dynamics to class-k tensegrity systems in a second-order matrix form [82]. Goyal et al. presented a compact matrix form of tensegrity dynamics by including massive strings, an analytical solution of Lagrange multipliers for class-k tensegrity structures, and bar length correction algorithms [83], a corresponding general software for modeling of any tensegrity structures can be found in [47]. Recently, Goyal et al. extended the model of the nonlinear dynamics to modulate the torque produced by the network of spatially distributed gyroscopes [84]. However, in all these

dynamics models, none of them considered fluid forces for class-k tensegrity systems, which limited our ability in analyzing fluid-based tensegrity structures, applications include aquaculture, robotic fish, airplanes, etc. Fluid-structure interaction (FSI) simulation by numerical computational fluid dynamics (CFD) software is an option to do the analysis, but this approach requires skillful modeling experience in fluid dynamics and a lot of computational resources. This study contains two contributions: Structure interfaces the fluid directly or via the membrane on the structure. For the first one, this study implements a simplified analytical fluid force model, which has been successfully applied and validated in the studies of aquatic animal swimming [85, 86, 87]. Then, we integrate the fluid model with the tensegrity network and provide a dynamics model to investigate the behaviors of tensegrity structure in the presence of fluid. For the second one, we study the fluid forces on an airfoil and hydrofoil based on the panel method. Then, the fluid forces are integrated into the structure nodes by force and moment equilibrium equations. The obtained fluid force is external forces that will be applied to the tensegrity dynamics. The approaches to these two cases can be used for analyzing tensegrity structures w/o skin that is operating in the fluids.

This chapter is structured as follows: Section 3.2 derives the translation and rotation equation of motion of one single rod. Section 3.3 models the fluid particles interacting with the rod and the corresponding fluid force expressions on the rod. Section 3.4 stacks all the equation of motion for each rod to form the tensegrity network and develops a compact vector form of class-1 and class-k structures. Section 3.5 presents a compact matrix form of class-1 and class-k structures. Section 3.6 discusses and compares the results of the dynamics by a 3D prism example by these cases: a free oscillation in the fluid w/o an inlet velocity, and landing w/o fluid. Section 3.7 described how we get the fluid forces on the skin of the structure. Section 3.8 discusses the error bound method for continuous airfoil shape discretization and the design of tensegrity airfoils. Section 3.9 presents how the fluid forces on the skin of the airfoil are transferred to the tensegrity structure. Section 3.10 gives the conclusions.

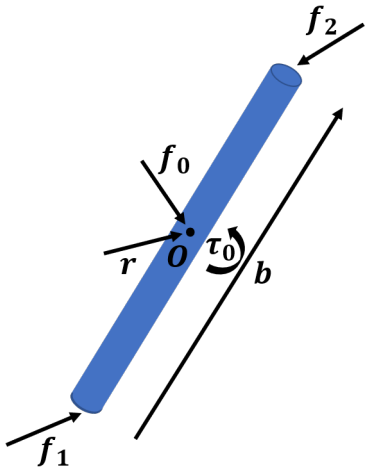

Figure 3.4: Tensegrity bar member vector with fluid force nomenclature.

3.2 Dynamics of A Single Rod

3.2.1 Rotational Dynamics

Let us consider a single rod immersed in an infinite volume of fluid field. The length of the rod is $||\boldsymbol{b}|| = l$, where $\boldsymbol{b}$ is a vector along the rod, shown in Figure 3.4. Vector $\boldsymbol{r}$ gives the position of the rod center of mass O. We separate the forces on the rod into two parts: fluid force ($\boldsymbol{f_0}$ and $\boldsymbol{\tau_0}$) and other external forces ($\boldsymbol{f_1}$ and $\boldsymbol{f_2}$ applied at the two nodes of the rod).

To describe the position of a rigid body, vectors are usually coordinatized in two different reference frames: inertia frame and body frame. Let the vectrices $\mathcal{E} = \begin{bmatrix} \boldsymbol{e}_1 & \boldsymbol{e}_2 & \boldsymbol{e}_3 \end{bmatrix}$ and $\mathcal{B} = \begin{bmatrix} \boldsymbol{b}_1 & \boldsymbol{b}_2 & \boldsymbol{b}_3 \end{bmatrix}$ denote the dextral set of unit vectors $\boldsymbol{e}_i$ which are inertially fixed and the body-fixed dextral set of $\boldsymbol{b}_i$ fixed in the coordinates of the rigid body [83]. The angular velocities of frame $\mathcal{B}$ relative to frame $\mathcal{E}$ is $\boldsymbol{\omega} = \mathcal{E}\omega^{\mathcal{E}} = \mathcal{B}\omega^{\mathcal{B}}$, where $\omega^{\mathcal{B}} = \begin{bmatrix} \omega_1^{\mathcal{B}} & \omega_2^{\mathcal{B}} & \omega_3^{\mathcal{B}} \end{bmatrix}^{\mathsf{T}}$. Coordinate transformation by a unitary direction cosine matrix Θ satisfies:

$$\mathcal{B} = \mathcal{E}\Theta, \ \Theta^{\mathsf{T}}\Theta = I. \tag{3.1}$$

Take the first time derivative of $\Theta^{\mathsf{T}}\Theta = I$, one can get:

$$\Theta^{\mathsf{T}}\dot{\Theta} = \tilde{\omega}^{\mathcal{B}} = \begin{bmatrix} 0 & -\omega_3^{\mathcal{B}} & \omega_2^{\mathcal{B}} \\ \omega_3^{\mathcal{B}} & 0 & -\omega_1^{\mathcal{B}} \\ -\omega_2^{\mathcal{B}} & \omega_1^{\mathcal{B}} & 0 \end{bmatrix}, \tag{3.2}$$

which is skew-symmetric matrix. Then, the time derivative of $\mathcal{B}$ can be obtained,

$$\dot{\mathcal{B}} = \mathcal{E}\dot{\Theta} = \mathcal{B}\Theta^{\mathsf{T}}\dot{\Theta} = \mathcal{B}\tilde{\omega}^{\mathcal{B}}. \tag{3.3}$$

Since the bar vector $\boldsymbol{b}$ described in body frame $\mathcal{B}$ is $\boldsymbol{b} = \mathcal{B}b^{\mathcal{B}}$, where $b^{\mathcal{B}}$ represents the components of the vector $\boldsymbol{b}$ as viewed in coordinate frame $\mathcal{B}$. With $\boldsymbol{b_3}$ along the rod, we have $b^{\mathcal{B}} = \begin{bmatrix} 0 & 0 & l \end{bmatrix}^{\mathsf{T}}$ and $\dot{b}^{\mathcal{B}} = 0$. The time derivative of vector $\boldsymbol{b}$ is:

$$\dot{\boldsymbol{b}} = \dot{\mathcal{B}}b^{\mathcal{B}} + \mathcal{B}\dot{b}^{\mathcal{B}} = \dot{\mathcal{B}}b^{\mathcal{B}} = \mathcal{B}\tilde{\omega}^{\mathcal{B}}b^{\mathcal{B}}. \tag{3.4}$$

Then, since we have $\tilde{\omega}\boldsymbol{b} = -\tilde{b}\boldsymbol{\omega}$ and $\tilde{\boldsymbol{b}}\tilde{\boldsymbol{b}} = -l^2 I + \boldsymbol{b}\boldsymbol{b}^{\mathsf{T}}$, one can obtain:

$$\boldsymbol{b} \times \dot{\boldsymbol{b}} = (\mathcal{B}b^{\mathcal{B}}) \times (\mathcal{B}\tilde{\omega}^{\mathcal{B}}b^{\mathcal{B}}) = \mathcal{B}\tilde{b}^{\mathcal{B}}\tilde{\omega}^{\mathcal{B}}b^{\mathcal{B}} \tag{3.5}$$

$$= -\mathcal{B}\tilde{b}^{\mathcal{B}}\tilde{b}^{\mathcal{B}}\omega^{\mathcal{B}} = -\mathcal{B}(\tilde{b}^{\mathcal{B}})^2\omega^{\mathcal{B}} \tag{3.6}$$

$$= \mathcal{B}(b^{\mathcal{B}^{\mathsf{T}}}b^{\mathcal{B}}I - b^{\mathcal{B}}b^{\mathcal{B}^{\mathsf{T}}})\omega^{\mathcal{B}} \tag{3.7}$$

$$= \mathcal{B}(\|b^{\mathcal{B}}\|^2 I - b^{\mathcal{B}}b^{\mathcal{B}^{\mathsf{T}}})\omega^{\mathcal{B}} \tag{3.8}$$

$$= \mathcal{B}\left(l^2 I - \begin{bmatrix} 0 & 0 & 0 \\ 0 & 0 & 0 \\ 0 & 0 & l^2 \end{bmatrix}\right)\omega^{\mathcal{B}} \tag{3.9}$$

$$= \mathcal{B}\begin{bmatrix} I_2 & 0 \\ 0 & 0 \end{bmatrix} l^2\omega^{\mathcal{B}} = \mathcal{B}l^2\begin{bmatrix} \omega_1^{\mathcal{B}} \\ \omega_2^{\mathcal{B}} \\ 0 \end{bmatrix} = l^2\boldsymbol{\omega}_b. \tag{3.10}$$

The angular momentum of bar $\boldsymbol{b}$ about its mass center O is:

$$\boldsymbol{h} = J\boldsymbol{b} \times \dot{\boldsymbol{b}} = \frac{m_b}{12}\boldsymbol{b} \times \dot{\boldsymbol{b}}, \tag{3.11}$$

where J is moment of inertia of the rod $J = \frac{1}{12}m_b l^2$, m_b is bar mass. Take the first time derivative of Eq. (3.11), we obtain:

$$\dot{\boldsymbol{h}} = J\dot{\boldsymbol{b}} \times \dot{\boldsymbol{b}} + J\boldsymbol{b} \times \ddot{\boldsymbol{b}} = J\boldsymbol{b} \times \ddot{\boldsymbol{b}}. \tag{3.12}$$

The time derivative of the angular momentum vector $\boldsymbol{h}$ equals to the sum of torques $\boldsymbol{\tau} = \boldsymbol{\tau_e} + \boldsymbol{\tau_0}$ acting on the bar member about its center of mass, where $\boldsymbol{\tau_0}$ is the torque generated by the fluid force, $\boldsymbol{\tau_e} = \frac{1}{2}\boldsymbol{b} \times (\boldsymbol{f}_2 - \boldsymbol{f}_1)$ is torque given by the force at the two nodes of the bar. Then we have the following:

$$\dot{\boldsymbol{h}} = J\boldsymbol{b} \times \ddot{\boldsymbol{b}} = \boldsymbol{\tau}, \tag{3.13}$$

$$\boldsymbol{\tau} = \boldsymbol{\tau_e} + \boldsymbol{\tau_0} = \frac{1}{2}\boldsymbol{b} \times (\boldsymbol{f}_2 - \boldsymbol{f}_1) + \boldsymbol{\tau_0}. \tag{3.14}$$

Eq. (3.13) can be written in any coordinates, but we choose inertial coordinates for simpler forms of final equations. To simplify notation hereafter, we define $b = b^{\mathcal{E}}$ where $\boldsymbol{b} = \mathcal{B}b^{\mathcal{B}} = \mathcal{E}b^{\mathcal{E}}$ [83]. Using inertial coordinates, Eq. (3.13) can be written as:

$$J\tilde{b}\ddot{b} = \frac{1}{2}\tilde{b}(f_2 - f_1) + \tau_0. \tag{3.15}$$

Since bar length is a constant, we have $||b|| = l$ or $b^\intercal b = l^2$. Take the first and second derivative of the bar length constraint, we get:

$$\dot{b}^\intercal b + b^\intercal \dot{b} = 2b^\intercal \dot{b} = 0, \tag{3.16}$$

$$\dot{b}^\intercal \dot{b} + b^\intercal \ddot{b} = 0,\ b^\intercal \ddot{b} = -\dot{b}^\intercal \dot{b} = -||\dot{b}||^2. \tag{3.17}$$

Write Eq. (3.15) and Eq. (3.17) together in matrix form as:

$$\begin{bmatrix} \tilde{b} \\ b^{\intercal} \end{bmatrix} \ddot{b} = \begin{bmatrix} \frac{1}{2J}\tilde{b}(f_2 - f_1) \\ -\dot{b}^{\intercal}\dot{b} \end{bmatrix} + \begin{bmatrix} \frac{\tau_0}{J} \\ 0 \end{bmatrix}. \tag{3.18}$$

One can solve this linear algebra problem for $\ddot{b}$. Notice that $\begin{bmatrix} \tilde{b} \\ b^{\intercal} \end{bmatrix}$ has full column rank, the unique solution for $\ddot{b}$ is:

$$\ddot{b} = \begin{bmatrix} \tilde{b} \\ b^{\intercal} \end{bmatrix}^{\dagger} \begin{bmatrix} \frac{1}{2J}\tilde{b}(f_2 - f_1) \\ -\dot{b}^{\intercal}\dot{b} \end{bmatrix} + \begin{bmatrix} \tilde{b} \\ b^{\intercal} \end{bmatrix}^{\dagger} \begin{bmatrix} \frac{\tau_0}{J} \\ 0 \end{bmatrix} \tag{3.19}$$

$$= \frac{1}{l^2}\begin{bmatrix} -\tilde{b} & b \end{bmatrix} \begin{bmatrix} \frac{1}{2J}\tilde{b}(f_2 - f_1) \\ -\dot{b}^{\intercal}\dot{b} \end{bmatrix} + \frac{1}{l^2}\begin{bmatrix} -\tilde{b} & b \end{bmatrix} \begin{bmatrix} \frac{\tau_0}{J} \\ 0 \end{bmatrix} \tag{3.20}$$

$$= \frac{1}{l^2}(-\frac{1}{2J}\tilde{b}\tilde{b}(f_2 - f_1) - b\dot{b}^{\intercal}\dot{b}) - \frac{1}{l^2}\tilde{b}\frac{\tau_0}{J} \tag{3.21}$$

$$= -\frac{1}{2Jl^2}(-l^2 I + bb^{\intercal})(f_2 - f_1) - \frac{1}{l^2}b\dot{b}^{\intercal}\dot{b} - \frac{1}{Jl^2}\tilde{b}\tau_0, \tag{3.22}$$

where superscript "†"denotes a matrix pseudo inverse. Rearranging equations gives the final vector form of the single rod rotational dynamics:

$$J\ddot{b} = \frac{1}{2}(f_2 - f_1) - \frac{1}{2l^2}bb^{\intercal}(f_2 - f_1) - \frac{J}{l^2}b\dot{b}^{\intercal}\dot{b} - \frac{1}{l^2}\tilde{b}\tau_0 \tag{3.23}$$

$$= \frac{1}{2}(I - \frac{bb^{\intercal}}{||b||^2})(f_2 - f_1) - \frac{J}{l^2}b\dot{b}^{\intercal}\dot{b} - \frac{1}{l^2}\tilde{b}\tau_0. \tag{3.24}$$

3.2.2 Translational Dynamics

The position of center of mass of the bar is given by vector $\boldsymbol{r}$. The fluid force working at the center of mass of the bar is $\boldsymbol{f_0}$ and the sum of the internal forces from the strings and the external forces, acting on the two ends of the bar, is described by $\boldsymbol{f_1}$ and $\boldsymbol{f_2}$, where $\boldsymbol{r} = \mathcal{E}r^{\mathcal{E}}$, $\boldsymbol{f}_i = \mathcal{E}f_i^{\mathcal{E}}$. From Newton's second law, we have $r = r^{\mathcal{E}}$ and $f_i = f_i^{\mathcal{E}}$. $m_b\ddot{\boldsymbol{r}} = \boldsymbol{f}_1 + \boldsymbol{f}_2 + \boldsymbol{f_0}$, which can be

written in the inertial coordinates as:

$$m_b \ddot{r} = f_0 + f_1 + f_2. \tag{3.25}$$

3.3 Modeling of Fluid Forces on the Rod

The fluid force contributions are only considered on bar members due to their relatively bigger diameter than the strings [80]. The continuously distributed fluid forces along the bar can be represented by a single force f_0 at the geometrical center O and torque τ_0, which are functions of velocities and angular velocities of the bar. Both vicious and fluid inertia forces are considered. The fluid force on the geometrical center of the bar f_0 (a sum of tangent force f_t and normal force f_n) and torque (τ_0) are given by [88]:

$$f_0 = f_t + f_n, \tag{3.26}$$

$$-f_t = 2.7 c_t l \sqrt{\rho \mu d ||v_n||} v_t, \tag{3.27}$$

$$-f_n = \mathrm{sgn}(v_n) c_p (\rho v_n^2/2) l d + c_a \rho \pi (d/2)^2 l (a_n - 2 v_t \dot{\theta}), \tag{3.28}$$

$$-\tau_0 = \frac{1}{12} \mathrm{sgn}(v_n) c_p \rho d l^3 v_n \dot{\theta} + \frac{1}{12} c_a \rho \pi (d/2)^2 l^3 \ddot{\theta}, \tag{3.29}$$

where

$$\dot{\theta} = \frac{\tilde{b}\dot{b}}{||b||^2}, \ddot{\theta} = \frac{\tilde{b}\ddot{b}}{||b||^2}, \tag{3.30}$$

$$v_t = \frac{bb^\intercal}{||b||^2}\dot{r}, v_n = (I - \frac{bb^\intercal}{||b||^2})\dot{r}, \tag{3.31}$$

$$a_t = \frac{bb^\intercal}{||b||^2}\ddot{r}, a_n = (I - \frac{bb^\intercal}{||b||^2})\ddot{r}, \tag{3.32}$$

where ρ and μ are the fluid density and viscosity, d is the diameter of the rod, $c_t = 1$ and $c_p = 0.9 \sim 1.1$ are the drag coefficients on a smooth circular cylinder in the range of Reynolds number $20 < R_e < 10^5$ from experiments [87], c_a is the dimensionless coefficient to account for different object shape (for cylinder, $c_a = 1$). v_t, v_n are velocities and a_t, a_n are accelerations of the center of

mass of the bar in tangential and normal direction, $\dot{\theta}$ and $\ddot{\theta}$ are the angular velocity and acceleration of the rod about $\boldsymbol{e}_3$ axis (the axis along the bar direction), sgn($\bullet$) takes the sign of the variable in the parentheses.

In order to write the dynamic equations in a standard second order form, we separate fluid force and torque into two parts, acceleration dependent one (with subscript A) and the rest (with subscript R), and move the acceleration dependent parts to the left hand side of Eq. (3.24). Let us first define:

$$f_0 = f_R + f_A, \tau_0 = \tau_R + \tau_A, \tag{3.33}$$

$$\begin{aligned} -f_R &:= \mathrm{sgn}(v_n) c_p (\rho v_n^2/2) l d - 2 m_A v_t \dot{\theta} \\ &+ 2.7 c_t l \sqrt{\rho \mu d ||v_n||} v_t, \end{aligned} \tag{3.34}$$

$$-f_A := m_A a_n, \tag{3.35}$$

$$-\tau_R := \mathrm{sgn}(v_n) \frac{1}{12} c_p \rho d l^3 v_n \dot{\theta}, -\tau_A := \frac{1}{12} m_A l^2 \ddot{\theta}, \tag{3.36}$$

where $m_A = c_a \rho \pi (d/2)^2 l$ is the mass of fluid being accelerated by the bar, usually called the added mass of fluid. The moment of inertia of a rod is $J = \frac{1}{12} m_b ||b||^2$, replace τ_0 in Eq. (3.24) by Eq. (3.33), we have:

$$\left[\frac{m_b}{12} + \frac{m_A}{12} \left(I - \frac{bb^\intercal}{||b||^2} \right) \right] \ddot{b} + \frac{m_b}{12} \frac{||\dot{b}||^2}{||b||^2} b = \frac{1}{2} \left(I - \frac{bb^\intercal}{||b||^2} \right) (f_2 - f_1) - \frac{\tilde{b}}{||b||^2} \tau_R, \tag{3.37}$$

$$\left[m_b + m_A \left(I - \frac{bb^\intercal}{||b||^2} \right) \right] \ddot{r} = f_2 + f_1 + f_R. \tag{3.38}$$

3.4 Vector Form of Tensegrity System Dynamics with Fluid Forces Incorporated

3.4.1 Class-1 Tensegrity with Fluid Incorporated

Let the connectivity matrices of class-1 structure be $C_b = \begin{bmatrix} -I_\beta & I_\beta \end{bmatrix}$ for bars, where β is the number of bars in the system, and C_s for strings, and $C_r = \frac{1}{2}\begin{bmatrix} I_\beta & I_\beta \end{bmatrix}$ [39]. Let us define:

$$H_i := I_3 - \frac{b_i b_i^\intercal}{||b_i||^2},\ m_i := m_{bi} I_3 + m_{A_i} H_i, \tag{3.39}$$

$$g_i := \frac{m_{bi}}{12}\frac{||\dot{b}_i||^2}{||b_i||^2},\ \kappa_i := -\frac{\tilde{b}_i}{||b_i||^2}. \tag{3.40}$$

Then, Eq. (3.37) and Eq. (3.38) can be written into a compact form:

$$\begin{bmatrix} \hat{m} & \\ & \frac{1}{12}\hat{m} \end{bmatrix}\begin{bmatrix} \ddot{r} \\ \ddot{b} \end{bmatrix} + \begin{bmatrix} 0 & 0 \\ 0 & \hat{g}\otimes I_3 \end{bmatrix}\begin{bmatrix} r \\ b \end{bmatrix} = \begin{bmatrix} 2C_r \otimes I_3 \\ \frac{1}{2}\hat{H}(C_b \otimes I_3) \end{bmatrix} f + \begin{bmatrix} f_R \\ \hat{\kappa}\tau_R \end{bmatrix}, \tag{3.41}$$

where $\hat{\bullet}$ is a diagonal operator that converts a vector into a diagonal matrix, $f = \begin{bmatrix} f_1^\intercal & f_2^\intercal & \cdots & f_{2\beta}^\intercal \end{bmatrix}^\intercal$ is the vector of nodal forces, $n = \begin{bmatrix} n_1^\intercal & n_2^\intercal & \cdots & n_{2\beta}^\intercal \end{bmatrix}^\intercal$ is the vector of node coordinates.

The nodal force f is then given by:

$$f = w + f_s + f_d + (P_c^\intercal \otimes I_3)t_c, \tag{3.42}$$

where w is the external forces applied at each node, f_s is the string forces, f_d is the string damping force, t_c is the internal force between joints.

If the tensegrity system is subject to m constraints, we have:

$$(P_c \otimes I_3)n = d_c, \tag{3.43}$$

where $P_c \in \mathbb{R}^{m\times 2\beta}$ is the constraint matrix, and $d_c \in \mathbb{R}^{3m}$ is a constant vector. Eq. (3.43) describes two types of constraint: $P_{c_{ij}} = 1$, $P_{c_{ik}} = -1$ and $d_{c_i} = 0$ when nodes j and k are connected by a

universal joint, where the subscript i is the i^{th} constraint, and j, k are the nodes index; $P_{c_{i,j}} = 1$ and $d_{c_i} \in \mathbb{R}^3$ when the j^{th} node is fixed to the ground.

The forces in the strings f_s can be written as:

$$f_s = -(C_s^\intercal \hat{\gamma} C_s \otimes I_3)n, \tag{3.44}$$

$$\gamma_i := \begin{cases} k_i(1 - l_{0_i}/l_i), & l_i > l_{0_i} \\ 0, & \text{else} \end{cases}, \tag{3.45}$$

where k_i, l_i and l_{0_i} are the string stiffness, length and rest length. Since we have $l_i^2 = s_i^\intercal s_i \Rightarrow \dot{l}_i = s_i^\intercal \dot{s}_i / l_i$ for each string, the damping force in each string is calculated by:

$$f_{d_i} := -\mu_i \dot{l}_i \frac{s_i}{l_i} = -\mu_i \frac{s_i^\intercal \dot{s}_i}{l_i^2} s_i, \tag{3.46}$$

written in a vector form, we have:

$$f_d = -(C_s^\intercal \hat{\zeta} C_s \otimes I_3)n, \tag{3.47}$$

$$\zeta_i := \begin{cases} \mu_i \dfrac{s_i^\intercal \dot{s}_i}{l_i^2}, & l_i > l_{0_i} \\ 0, & \text{else} \end{cases}, \tag{3.48}$$

where μ_i (N·s/m) is the damping coefficient.

The angular displacement between the contact surface, as described by the constraint Eq. (3.43), introduces resistive torques to bars. The resistive torque on bar i by bar k due to angular velocities ω_i and ω_k is given by:

$$\tau_{d_{ik}} = -\eta_{ik}(\omega_i - \omega_k), \ \omega_i = \frac{\tilde{b}_i \dot{b}_i}{||b_i||^2}, \tag{3.49}$$

where η_{ik} (N·m·s) is the damping coefficient between bar i and bar k. The vector form of resistive

torque is given by:

$$\tau_d = -2C_r P_c^{\mathsf{T}} \hat{\eta} P_c 2C_r^{\mathsf{T}} \omega = 4C_r P_c^{\mathsf{T}} \hat{\eta} P_c C_r^{\mathsf{T}} \hat{\kappa} \dot{b}. \tag{3.50}$$

τ_d is added to Eq. (3.41) by replacing τ_R by $\tau_R + \tau_d$.

Replace r, b, f and τ_R in Eq. (3.41) by $r = (C_r \otimes I_3)n$, $b = (C_b \otimes I_3)n$, Eq. (3.42) and $\tau_R + \tau_d$, where τ_d is given by Eq. (3.50), and also left multiply $\begin{bmatrix} C_r^{\mathsf{T}} & C_b^{\mathsf{T}} \end{bmatrix} \otimes I_3$ to Eq. (3.41) to make the mass matrix symmetric, we have:

$$M\ddot{n} + C\dot{n} + Kn = D(w + P^{\mathsf{T}} t_c) + z, \tag{3.51}$$

where:

$$M := (C_r^{\mathsf{T}} \otimes I_3)\hat{m}(C_r \otimes I_3) + \frac{1}{12}(C_b^{\mathsf{T}} \otimes I_3)\hat{m}(C_b \otimes I_3), \tag{3.52}$$

$$C := 4(C_b^{\mathsf{T}} \otimes I_3)\hat{\kappa}^{\mathsf{T}}(C_r P_c^{\mathsf{T}} \hat{\eta} P_c C_r^{\mathsf{T}} \otimes I_3)\hat{\kappa}(C_b \otimes I_3), \tag{3.53}$$

$$D := I - \frac{1}{2}(C_b^{\mathsf{T}} \otimes I_3)\Delta(C_b \otimes I_3), \tag{3.54}$$

$$\Delta := \text{block diagonal}\left(\frac{b_i b_i^{\mathsf{T}}}{||b_i||^2}\right), \tag{3.55}$$

$$K := D(C_s^{\mathsf{T}}(\hat{\gamma} + \hat{\zeta})C_s \otimes I_3) + (C_b^{\mathsf{T}} \otimes I_3)\hat{g}(C_b \otimes I_3), \tag{3.56}$$

$$z := (C_r^{\mathsf{T}} \otimes I_3)f_R + (C_b^{\mathsf{T}} \otimes I_3)\hat{\kappa}\tau_R, \tag{3.57}$$

$$P := P_c \otimes I_3. \tag{3.58}$$

The vector z is how we add the fluid force, which is composed of a force vector f_R at location r and a torque τ_R both of which are acceleration independent, and m_i is how we add the added mass effect of fluid (the fluid being accelerated by the bar) into the equation of motion. Note that Eq. (3.52) is the equation of motion for class-1 tensegrity with $P = \mathbf{0}$.

Suppose the constraints are linearly independent, we can write:

$$(P_c \otimes I_3)n = d_c \Rightarrow n = P^{\dagger} d_c + P^{\perp} n_c, \tag{3.59}$$

$$P^{\dagger} = P_c^{\dagger} \otimes I_3,\ P^{\perp} = P_c^{\perp} \otimes I_3, \tag{3.60}$$

where † means moore-penrose inverse, $P^{\perp}$ is the right null space of P. Replace n in Eq. (3.51) by above expression, we get:

$$\begin{bmatrix} MP^{\perp} & -DP^{\intercal} \end{bmatrix} \begin{bmatrix} \ddot{n}_c \\ t_c \end{bmatrix} = -CP^{\perp}\dot{n}_c - K(P^{\dagger} d_c + P^{\perp} n_c) + Dw + z. \tag{3.61}$$

Rewrite the above equation in a compact form, we have the equation of motion for class-k tensegrity:

$$\begin{bmatrix} \ddot{n}_c \\ t_c \end{bmatrix} = \begin{bmatrix} \left(MP^{\perp}\right)^{\intercal} \\ -\left(DP^{\intercal}\right)^{\intercal} \end{bmatrix} \Pi^{-1} \varphi, \tag{3.62}$$

where:

$$\Pi := MP^{\perp}(MP^{\perp})^{\intercal} + DP^{\intercal}\left(DP^{\intercal}\right)^{\intercal}, \tag{3.63}$$

$$\varphi := -CP^{\perp}\dot{n}_c - K(P^{\dagger} d_c + P^{\perp} n_c) + Dw + z. \tag{3.64}$$

3.4.2 Normalization on $P^{\perp}$ to Reduce Numerical Error

The condition number of Π is in order of 10^6 when the unit mass is in order of 10^{-1} [88]. If 99% of unit mass is on bar 1, the condition number of Π will be in order of 10^{10}. Note that the term $DP^{\intercal}$ in Π has entries close to 1 when entries of P is so (the case of nodal constraint). To reduce

numerical error, $P^{\perp}$ term in Π can be normalized as below:

$$\begin{bmatrix} M(P^{\perp}/\delta) & -DP^{\intercal} \end{bmatrix} \begin{bmatrix} \ddot{\bar{n}}_c \\ t_c \end{bmatrix} = -C(P^{\perp}/\delta)\dot{\bar{n}}_c - K(P^{\dagger}d_c + (P^{\perp}/\delta)\bar{n}_c) + Dw + z,\ \bar{n}_c := n_c\delta, \tag{3.65}$$

where δ is a scalar such that the entries of M/δ is close to 1. After such normalization, the condition number of Π can be reduced from 10^{10} to 10^{8}.

3.4.3 Computational Effort and Numerical Error Reduction

From the structure of the matrices, we know that there are many repeated block entries in Eq. (3.62) resulted from the structure of $C_r := \frac{1}{2}\begin{bmatrix} I & I \end{bmatrix}$ and $C_b := \begin{bmatrix} -I & I \end{bmatrix}$. We expand Eq. (3.62) to identify those repeated blocks to allow the computer to compute them only once. This also reduces the order of matrices by half in arithmetic operations. Furthermore, most matrices in Eq. (3.62) are block diagonal, and the matrices P, $P^{\dagger}$, and $P^{\perp}$ are sparse, the functions for sparse matrix in *matlab* help to reduce the computation effort and possible numerical errors. For example, the command *sparse* creates a sparse matrix by saving only the nonzero entries and their indices, and the arithmetic operators operate, for example, when we multiply two matrices, only on nonzero entries, which avoid unnecessary computation and numerical error from those zero entries.

By expanding, matrices in Eq. (3.62) can be rewritten as:

$$M = \begin{bmatrix} \frac{1}{3}\hat{m} & \frac{1}{6}\hat{m} \\ \frac{1}{6}\hat{m} & \frac{1}{3}\hat{m} \end{bmatrix},\ C = \begin{bmatrix} C_{11} & -C_{11} \\ -C_{11} & C_{11} \end{bmatrix}, \tag{3.66}$$

$$C_{11} := \hat{\kappa}^{\mathsf{T}} \left((P_1^{\mathsf{T}} + P_2^{\mathsf{T}}) \hat{\eta} (P_1 + P_2) \otimes I_3 \right) \hat{\kappa}, \tag{3.67}$$

$$P =: \begin{bmatrix} P_1 & P_2 \end{bmatrix},\ D = I - \frac{1}{2} \begin{bmatrix} \Delta & -\Delta \\ -\Delta & \Delta \end{bmatrix}, \tag{3.68}$$

$$K = \begin{bmatrix} K_{11} & K_{12} \\ K_{12}^{\mathsf{T}} & K_{22} \end{bmatrix} \otimes I_3 + \begin{bmatrix} \hat{g} & -\hat{g} \\ -\hat{g} & \hat{g} \end{bmatrix} \otimes I_3 - \frac{1}{2} \begin{bmatrix} \Delta \left((K_{11} - K_{12}^{\mathsf{T}}) \otimes I_3 \right) & \Delta \left((K_{12} - K_{22}^{\mathsf{T}}) \otimes I_3 \right) \\ \ominus & \ominus \end{bmatrix}, \tag{3.69}$$

$$K_{11} := C_{s_1}^{\mathsf{T}} (\hat{\gamma} + \hat{\zeta}) C_{s_1},\ K_{12} := C_{s_1}^{\mathsf{T}} (\hat{\gamma} + \hat{\zeta}) C_{s_2}, \tag{3.70}$$

$$K_{22} := C_{s_2}^{\mathsf{T}} (\hat{\gamma} + \hat{\zeta}) C_{s_2},\ C_s =: \begin{bmatrix} C_{s_1} & C_{s_2} \end{bmatrix}, \tag{3.71}$$

where $\ominus$ means the negative of the first row of the 2 by 1 block matrix. With above definition, the terms in φ in Eq. (3.62) were written as:

$$CP^{\perp}\dot{n}_c = \begin{bmatrix} C_{11}(P_{\perp_1} - P_{\perp_2})\dot{n}_c \\ \ominus \end{bmatrix},\ P^{\perp} =: \begin{bmatrix} P_{\perp_1} \\ P_{\perp_2} \end{bmatrix}, \tag{3.72}$$

$$P^{\dagger} d_c + P^{\perp} n_c = \begin{bmatrix} p_{c_1} + P_{\perp_1} n_c \\ p_{c_2} + P_{\perp_2} n_c \end{bmatrix},\ P^{\dagger} d_c =: \begin{bmatrix} p_{c_1} \\ p_{c_2} \end{bmatrix}, \tag{3.73}$$

$$Dw = \begin{bmatrix} w_1 \\ w_2 \end{bmatrix} - \frac{1}{2} \begin{bmatrix} \Delta(w_1 - w_2) \\ \ominus \end{bmatrix},\ w =: \begin{bmatrix} w_1 \\ w_2 \end{bmatrix}, \tag{3.74}$$

The terms in Π matrix in Eq. (3.62) are written as:

$$MP^{\perp} = \begin{bmatrix} \hat{m}(\frac{1}{3}P_{\perp_1} + \frac{1}{6}P_{\perp_2}) \\ \hat{m}(\frac{1}{6}P_{\perp_1} + \frac{1}{3}P_{\perp_2}) \end{bmatrix}, \tag{3.75}$$

$$DP^{\intercal} = \begin{bmatrix} P_1^{\intercal} \\ P_2^{\intercal} \end{bmatrix} - \frac{1}{2} \begin{bmatrix} \Delta(P_1^{\intercal} - P_2^{\intercal}) \\ \ominus \end{bmatrix}, \tag{3.76}$$

$$\Pi := MP^{\perp}(P^{\perp})^{\intercal}M + DP^{\intercal}PD =: \begin{bmatrix} \Pi_{11} & \Pi_{12} \\ \Pi_{12}^{\intercal} & \Pi_{22} \end{bmatrix}. \tag{3.77}$$

Using block matrix inverse formula:

$$\begin{bmatrix} A & B \\ C & D \end{bmatrix}^{-1} = \begin{bmatrix} \Theta_{11} & \Theta_{12} \\ \Theta_{21} & \Theta_{22} \end{bmatrix}, \tag{3.78}$$

where:

$$\Theta_{11} = (A - BD^{-1}C)^{-1}, \tag{3.79}$$

$$\Theta_{12} = -A^{-1}B(D - CA^{-1}B)^{-1}, \tag{3.80}$$

$$\Theta_{21} = -D^{-1}C(A - BD^{-1}C)^{-1}, \tag{3.81}$$

$$\Theta_{22} = (D - CA^{-1}B)^{-1}. \tag{3.82}$$

The inverse of Π is then given by:

$$\Pi^{-1} = \begin{bmatrix} \Lambda_{11} & \Lambda_{12} \\ \Lambda_{21} & \Lambda_{22} \end{bmatrix}, \tag{3.83}$$

where:

$$\Lambda_{11} = (\Pi_{11} - \Pi_{12}\Pi_{22}^{-1}\Pi_{12}^{\intercal})^{-1}, \tag{3.84}$$

$$\Lambda_{12} = -\Pi_{11}^{-1}\Pi_{12}(\Pi_{22} - \Pi_{12}^{\intercal}\Pi_{11}^{-1}\Pi_{12})^{-1}, \tag{3.85}$$

$$\Lambda_{21} = -\Pi_{22}^{-1}\Pi_{12}^{\intercal}(\Pi_{11} - \Pi_{12}\Pi_{22}^{-1}\Pi_{12}^{\intercal})^{-1}, \tag{3.86}$$

$$\Lambda_{22} = (\Pi_{22} - \Pi_{12}^{\intercal}\Pi_{11}^{-1}\Pi_{12})^{-1}. \tag{3.87}$$

For class-1 tensegrity, we still need to inverse M directly, which is given by:

$$M^{-1} = \begin{bmatrix} 4\hat{m}^{-1} & -2\hat{m}^{-1} \\ -2\hat{m}^{-1} & 4\hat{m}^{-1} \end{bmatrix}. \tag{3.88}$$

3.4.4 Calculate Initial Values of n_c from n

In simulation, we set the initial conditions of the structure, and then check the time response. n is chosen to satisfy the constraints, the initial values of n_c for *ode* solvers (*ode45* is usually used) can be calculated from:

$$P^{\perp}n_c = (n - P^{\dagger}d_c), \tag{3.89}$$

we have:

$$n_c = (P^{\perp})^{\dagger}(n - P^{\dagger}d_c). \tag{3.90}$$

3.5 Matrix Formulation of Tensegrity Dynamics with Fluid Force Incorporated

The dynamics of any given rod member in a tensegrity structure in the presence of fluid force are given by Eq. (3.37) and Eq. (3.38). To describe a full tensegrity structure, it basically stacks 2β vector equations for a system containing β rod members. In order to simplify the equation structure, one can assemble them in a matrix form.

We name nodes at the base of bar vectors as $N := \begin{bmatrix} n_1 & \cdots & n_{2\beta} \end{bmatrix}$, for a network of β bars, define the $3 \times \beta$ matrix $B := \begin{bmatrix} b_1 & \cdots & b_\beta \end{bmatrix}$. The mass centers of the bars is defined as $R := \begin{bmatrix} r_1 & \cdots & r_\beta \end{bmatrix}$, where r_i is the ith column of matrix R. The internal forces acting on nodes caused by string tensions is $NC_s^\intercal \gamma C_s$, the full force matrix expression can then be written as $F := W - NC_s^\intercal \hat{\gamma} C_s$. Fluid forces can be assembled as $F_R := \begin{bmatrix} f_{n_{11}} + f_{t_1} & \cdots & f_{n_{1\beta}} + f_{t_\beta} \end{bmatrix}$, $\Delta_R := \begin{bmatrix} \tau_{R_1} & \cdots & \tau_{R_\beta} \end{bmatrix}$. Let us also define $\tilde{B} := \begin{bmatrix} \tilde{b}_1 & \cdots & \tilde{b}_\beta \end{bmatrix}$ and $\boldsymbol{e} := \begin{bmatrix} 1 & \cdots & 1 \end{bmatrix}^\intercal$, we have the following expression:

$$\begin{aligned} &\ddot{B}\hat{m}\frac{1}{12} + B\left(\left\lfloor \dot{B}^\intercal \dot{B} \right\rfloor \hat{m}\hat{l}^{-2}\frac{1}{12} + \lfloor B^\intercal F C_b^\intercal \rfloor \hat{l}^{-2}\frac{1}{2}\right) \\ &= FC_b^\intercal \frac{1}{2} + e^\intercal \otimes I_3 \left\lfloor \tilde{B}^\intercal \Delta_R \right\rfloor \hat{l}^{-2}, \end{aligned} \tag{3.91}$$

$$\ddot{R}\hat{m} = 2FC_r^\intercal + F_R, \tag{3.92}$$

where F_R, $\hat{\tau}_R$ and m are how we add the acceleration-independent and dependent fluid forces and torques into the equation, and $l_i := ||b_i||$. Define [83]:

$$-\hat{\lambda} := \left\lfloor \dot{B}^\intercal \dot{B} \right\rfloor \hat{m}\hat{l}^{-2}\frac{1}{12} + \lfloor B^\intercal F C_b^\intercal \rfloor \hat{l}^{-2}\frac{1}{2}, \tag{3.93}$$

$$M := \frac{1}{12} C_b^\intercal \hat{m} C_b + C_r^\intercal \hat{m} C_r, \tag{3.94}$$

$$K := C_s^\intercal \hat{\gamma} C_s - C_b^\intercal \hat{\lambda} C_b, \tag{3.95}$$

with the following formula:

$$\frac{1}{2}C_b^\intercal C_b + 2C_r^\intercal C_r = I, \ \begin{bmatrix} C_b \\ C_r \end{bmatrix} = \begin{bmatrix} \frac{1}{2}C_b^\intercal & 2C_r^\intercal \end{bmatrix}^{-1}, \tag{3.96}$$

Eq. (3.91) and Eq. (3.92) can be written into:

$$\ddot{N}M + NK = W + e^\intercal \otimes I_3 \left\lfloor \tilde{B}^\intercal \Delta_R \right\rfloor \hat{l}^{-2} C_b + F_R C_r. \tag{3.97}$$

When the system is subject to constraint of form [83]:

$$NP = D,\ P \in \mathbb{R}^{\beta \times m}. \tag{3.98}$$

The constraint force T is given by:

$$T = \Omega P^{\mathsf{T}}, \tag{3.99}$$

and W in Eq. (3.97) is replaced by $W + \Omega P^{\mathsf{T}}$. A analytical solution for Ω can be found in [83].

We can also add an additional constraint that the $\boldsymbol{e}_2$ coordinate of n_1 remains constant d_y, i.e.:

$$\boldsymbol{e}_2^{\mathsf{T}} N \boldsymbol{e}_1 = d_y, \boldsymbol{e}_2 = \begin{bmatrix} 0 & 1 & 0 \end{bmatrix}^{\mathsf{T}} \in \mathbb{R}^3, \tag{3.100}$$

$$\boldsymbol{e}_1 = \begin{bmatrix} 1 & \mathbf{0} \end{bmatrix}^{\mathsf{T}} \in \mathbb{R}^{3\beta}. \tag{3.101}$$

The total constraint is $\begin{bmatrix} NP & \boldsymbol{e}_2^{\mathsf{T}} N \boldsymbol{e}_1 \end{bmatrix} = \begin{bmatrix} D & d_y \end{bmatrix}$ which can not be written in the form of Eq. (3.98). So Eq. (3.98) is only applicable to constraints on vectors n_i, $i = 1, \cdots, 2\beta$, but not on individual entries n_{i_x}, n_{i_y}, n_{i_z}. The vector form equation of motion in section 3.4 is more suitable for compact expression:

$$\boldsymbol{e}_2^{\mathsf{T}} (\boldsymbol{e}_1^{\mathsf{T}} \otimes I_3) n = d_y,\ \mathsf{P} n = \mathsf{d}, \tag{3.102}$$

where:

$$\mathsf{P} := \begin{bmatrix} P \\ ((e_1 \otimes I_3) e_2)^{\mathsf{T}} \end{bmatrix},\ \mathsf{d} := \begin{bmatrix} d \\ d_y \end{bmatrix}. \tag{3.103}$$

3.6 Numerical Study of the Tensegrity Interfaces the Fluid Directly

It has been observed that DNA has a similar structure as tensegrity prism, where rigid bundles of DNA double helices resist compressive forces exerted by segments of singles tranded DNA

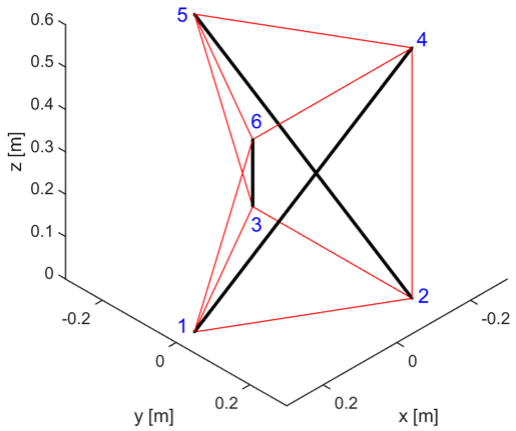

Figure 3.5: A 3D three-bar prism, thick black lines are bars and thin red lines are strings, prism height is 0.5 m, and bar length is 0.6952 m.

that acts as tension-bearing cables [2]. Many research on tensegrity prism has been conducted to study its properties in lightweight [39], configuration method for connecting [89], deployability by stimulus-responsive polymers [90], stiffness of the prism towers [62], etc.

Thus, 3D three-bar prism example, shown in Figure 3.5, is chosen to verify the derived tensegrity dynamics. In the absence of external forces, the prism unit structure has a known equilibrium solution, if the top and bottom string members have force density value $\gamma_{top} = \gamma_{btm}$, the vertical string members must have force density value $\gamma_{vtc} = \sqrt{3}\gamma_{top} = \sqrt{3}\gamma_{btm}$ [39].

For convenience in subsequent comparison, the radii for all the bars are set to be 0.02 m, radius of the top and bottom triangle circumscribed circles are r_{top} = 0.25 m and r_{btm} = 0.25 m, and prism height is h = 0.5 m. To demonstrate the dynamic response of the tensegrity structure, bar masses are specified as 0.5 kg. Initial force density values are specified as $\lambda = 15$ N/m, $\gamma_{top} = \gamma_{btm} = \gamma_{vtc} = 5\sqrt{3}$ N/m to induce motion. Bar lengths, based on specified initial node positions, are 0.6952 m long and all string members are given stiffness values of k_s = 2,000 N/m, string damping coefficient μ_i = 0.1 N·s/m, friction coefficient between joints, bar i and bar k, η_{ik} = 0 N·m·s. We choose the added mass coefficient c_a = 1, friction coefficient c_t = 1, pressure coefficient c_p = 1. We point out here that to achieve accurate results, these coefficients should be obtained by physical experiments. Fluid density ρ = 1,000 kg/m^3, fluid viscosity $\mu = 1.0 \times 10^{-3}$

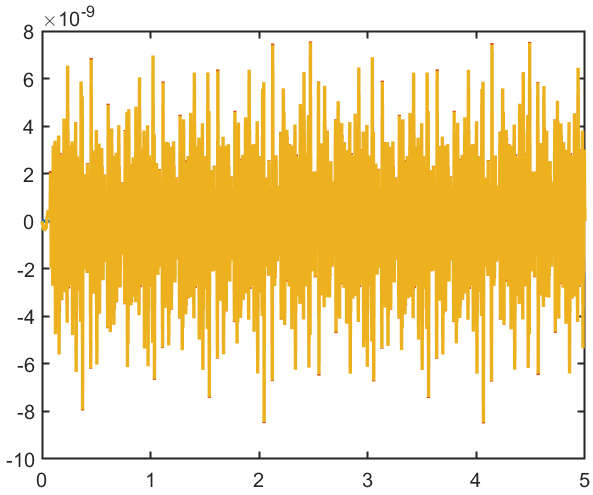

Figure 3.6: Bar length errors of the prism.

Pa·s, and simulation time t_f = 5 s. The x, y, and z coordinates of nodes 1, 2, and 3 are fixed to the ground.

3.6.1 Example 1: Free Oscillation in the Static Fluid

For this case, we compare the motion of the flexible structure dynamic simulation with and without fluid. The three-figure time-lapse plots are given in Figures 3.8 and 3.9. The coordinate and velocity time history of nodes 4, 5, and 6 of the prism unit without fluid are given in Figures 3.10 and 3.11. From these two figures, we can see that the prism is experiencing a free periodical oscillation. The coordinate and velocity time history of nodes 4, 5, and 6 of the prism unit in the presence of fluid are given in Figures 3.12 and 3.13. It is shown that the structure quickly damped to its equilibrium. Comparing the results with no fluid results, we can see that the water provides large damping to the dynamics response of the structure, which agrees with the physics. The bar length and fixed node errors of the prism is shown in Figures 3.6 and 3.7.

3.6.2 Example 2: Free Oscillation in the Fluid with an Inlet Velocity

For this case, we compare the motion of the flexible structure dynamic with a fluid inlet velocity of 0 m/s and 3 m/s in the x-direction. The three-figure time-lapse plots are given in Figures 3.9 and

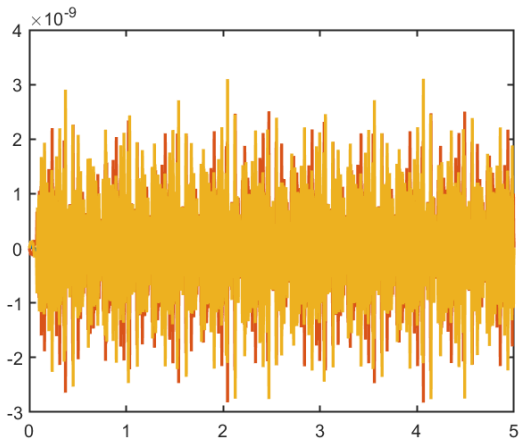

Figure 3.7: X-, Y-, and Z-coordinate errors of the fixed nodes of the prism.

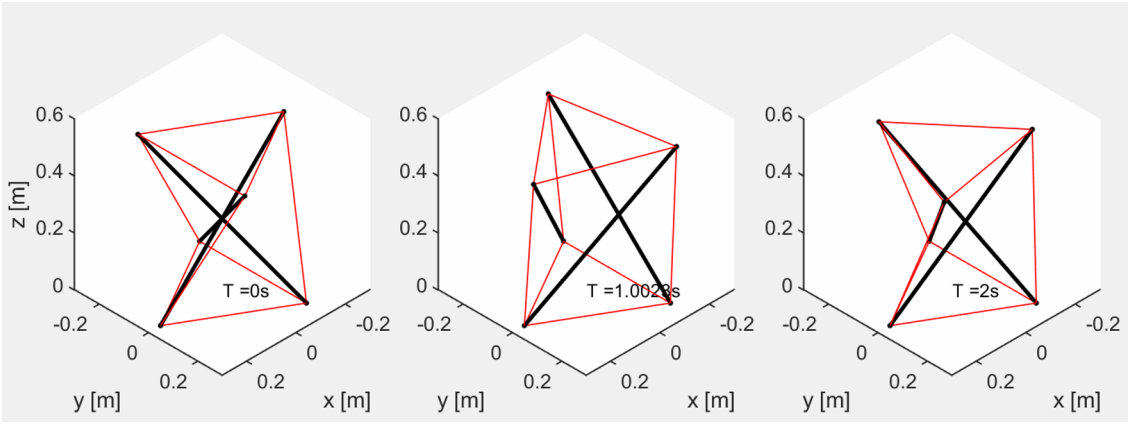

Figure 3.8: Free oscillation of the prism (no fluid) at T = 0s, 1s, and 2s.

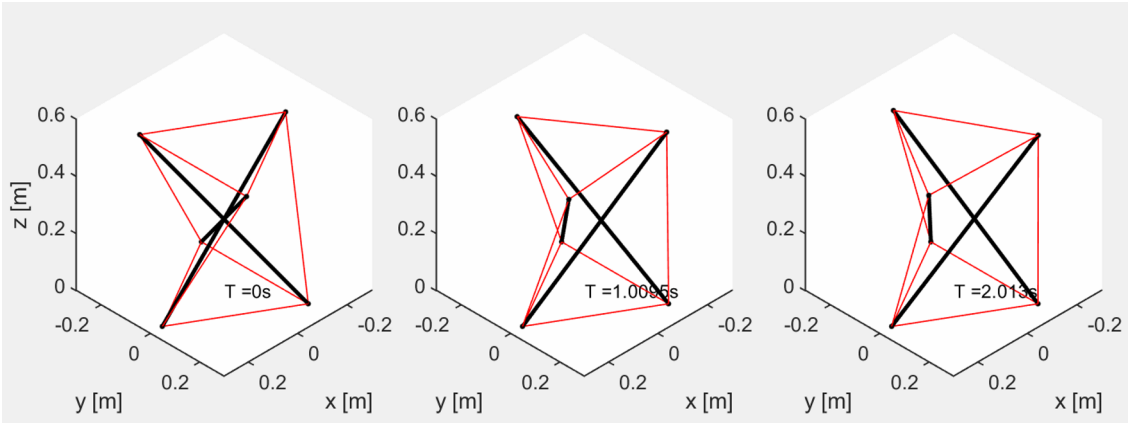

Figure 3.9: Free oscillation of the prism (immersed in the fluid) at T = 0s, 1s, and 2s.

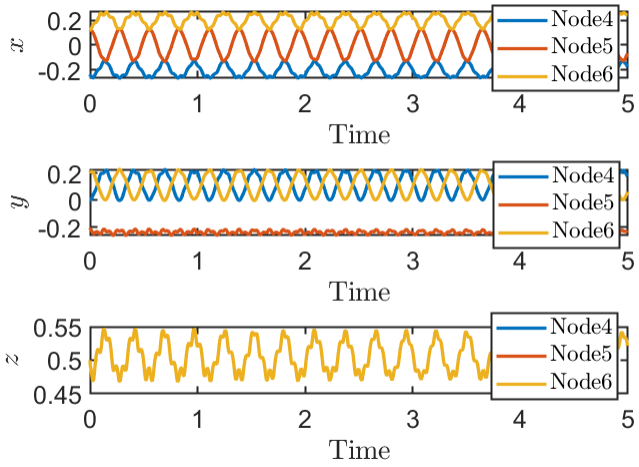

Figure 3.10: Coordinate time history of node 4, 5 and 6 from the free oscillation of the prism (no fluid).

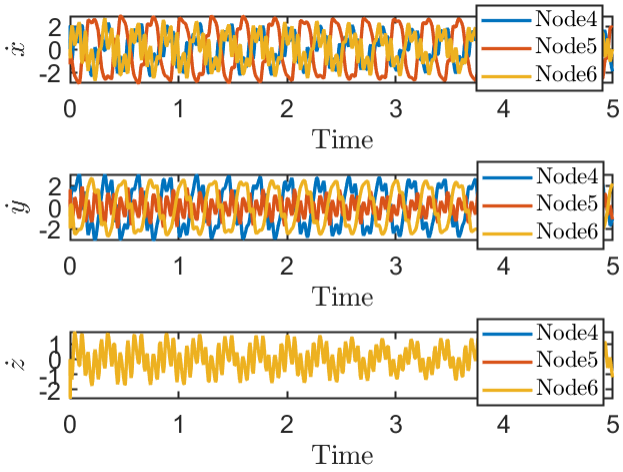

Figure 3.11: Velocity time history of node 4, 5 and 6 from the free oscillation of the prism (no fluid).

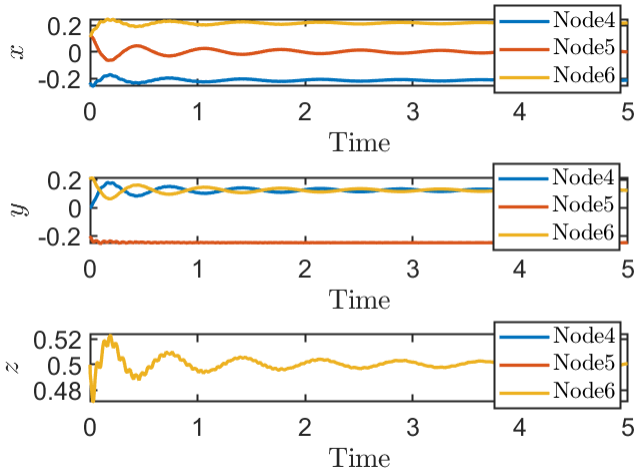

Figure 3.12: Coordinate time history of node 4, 5 and 6 from the free oscillation of the prism (immersed in the fluid).

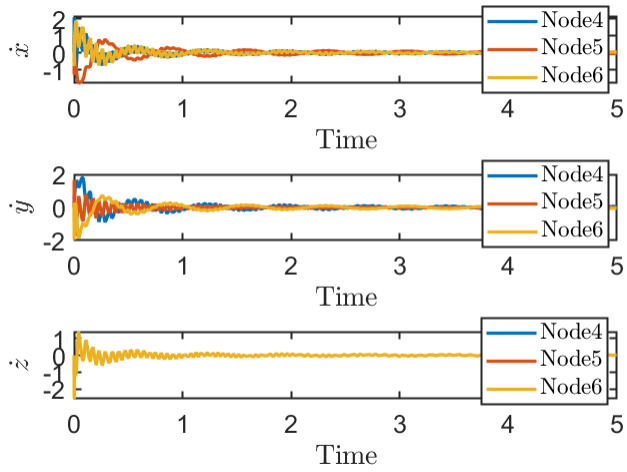

Figure 3.13: Velocity time history of node 4, 5 and 6 from the free oscillation of the prism unit (immersed in the fluid).

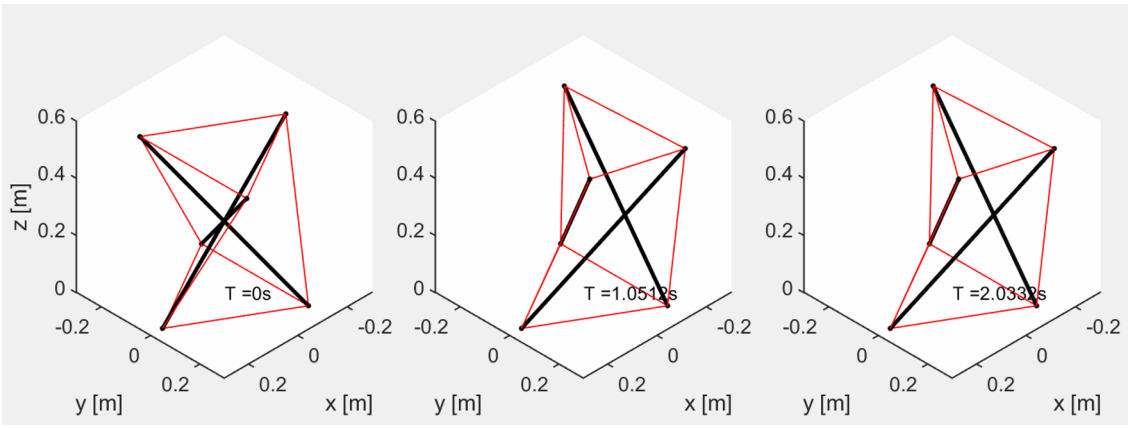

Figure 3.14: Dynamics simulation of the prism (fluid inlet velocity 3 m/s in x-direction) at T = 0s, 1s, and 2s.

3.14. The coordinate and velocity time history of nodes 4, 5, and 6 of the prism unit in the presence of static fluid are given in Figures 3.12 and 3.13. It is shown that the structure quickly damped to its equilibrium. The coordinate and velocity time history of nodes 4, 5, and 6 of the prism unit in the presence of fluid with 3 m/s velocity in the x-direction are given in Figures 3.15 and 3.16. The result shows that the structure quickly damped to its equilibrium and the whole structure moves towards the x-direction, shown in Figure 3.14. Comparing the results for fluid with and without velocity, we can conclude that the fluid provides large damping to the dynamics response of the structure and a pushing force to the whole structure in the fluid velocity direction, which matches well with the physics.

3.6.3 Example 3: Landing in the Presence of Fluid

Landing problem has attracted a lot attentions from various researchers [91, 92, 93]. All these simulations are assuming a non-fluid environment. This is true for lunar or asteroid landing, but for other scenarios, the influence of fluid should be considered. For example, landing on the ocean floor, Earth, Mars, and Titan would require the consideration of fluid. The example is to demonstrate the capability of the formulation to perform the dynamic simulation with inputs from the external environment (gravity and fluid). A dynamic simulation result was shown when the prism lander was dropped from a height of 1 m (distance between the bottom nodes of the prism

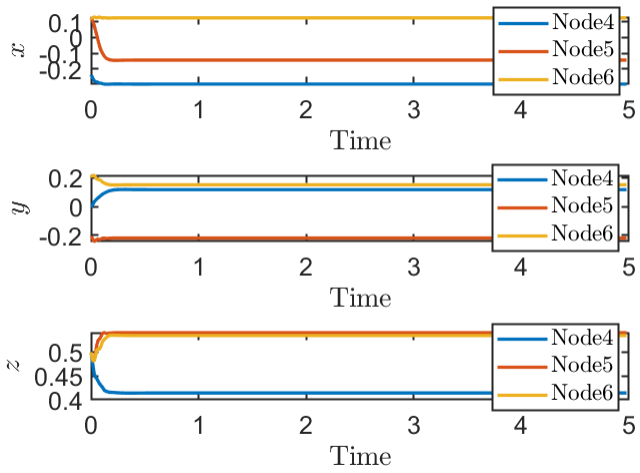

Figure 3.15: Coordinate time history of node 4, 5 and 6 from the dynamics simulation of the prism unit (fluid inlet velocity 3 m/s in x-direction).

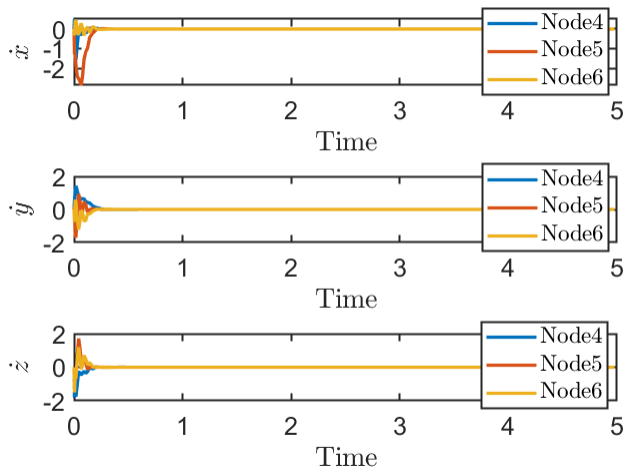

Figure 3.16: Velocity time history of node 4, 5 and 6 from the dynamics simulation of the prism unit (fluid inlet velocity 3 m/s in x-direction).

and the ground). For this simulation, the frictionless ground was modeled as a spring-damper system of stiffness k_g = 3,000 N/m and damping c_g = 3 N·s/m. An initial prestress value of all the bars and vertical strings $\lambda = \lambda_v$ = 15 N/m, force densities in the top and bottom strings are $\gamma_t = \gamma_b = \lambda/\sqrt{3} = 5\sqrt{3}$ N/m, which result in self-equilibrium for the structure without gravity force [39]. We should point out that adding gravity in landing to the structure will slightly change the equilibrium configuration, and one can observe this phenomenon before the structure hitting the ground, shown in the x and y coordinates and velocities at 0 s $\sim$ 0.52 s in Figure 3.19 and 0 s $\sim$ 0.84 s in Figure 3.21.

For this case, we compare the motion of the flexible structure landing simulation with and without fluid. The three-figure time-lapse plots are given in Figures 3.17 and 3.18. The coordinate and velocity time history of nodes 4, 5, and 6 of the prism unit without fluid are given in Figures 3.19 and 3.20. From these two figures, we can see that it takes about 0.52 s for the prism to hit the ground. After hitting the ground, the prism is experiencing a big bouncing up and down with small damping from the ground. The coordinate and velocity time history of nodes 4, 5, and 6 of the prism unit in the presence of fluid are given in Figures 3.21 and 3.22. It is shown that it takes a little longer, 0.84 s, for the prism to hit the ground because of the fluid damping influence. After hitting the ground, the structure quickly damped to its equilibrium. Comparing the results with no fluid results, we can see that the water provides large damping to the landing process, which takes a longer time to land on the floor but damped quicker to its equilibrium.

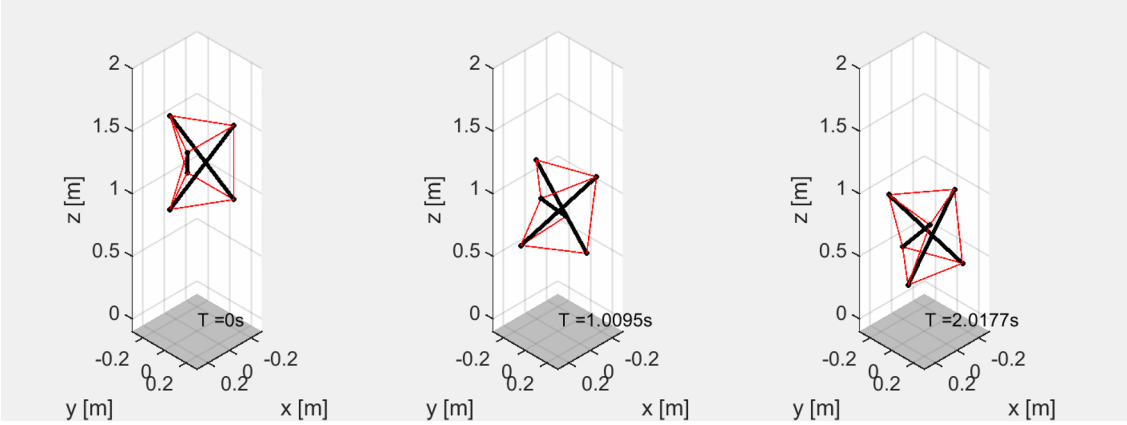

Figure 3.17: Landing simulation of the prism (no fluid) at T = 0s, 1s, and 2s.

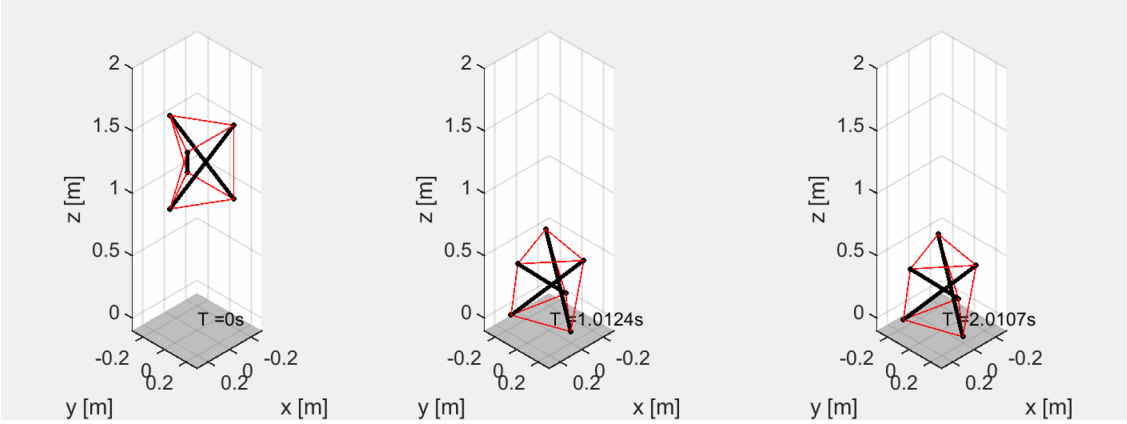

Figure 3.18: Landing simulation of the prism unit (immersed in the fluid) at T = 0s, 1s, and 2s.

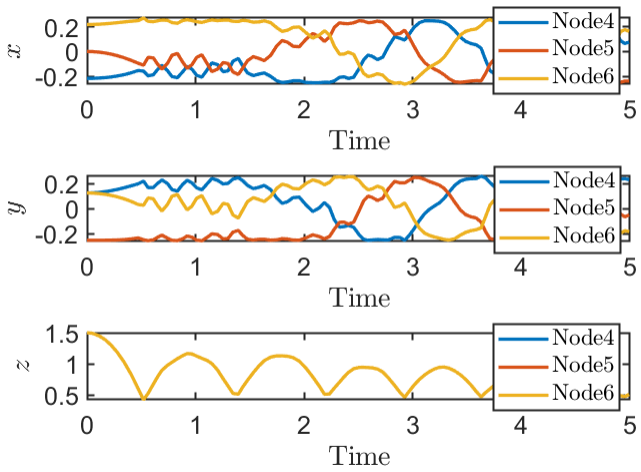

Figure 3.19: Coordinate time history of node 4, 5 and 6 from the landing simulation of the prism unit (no fluid).

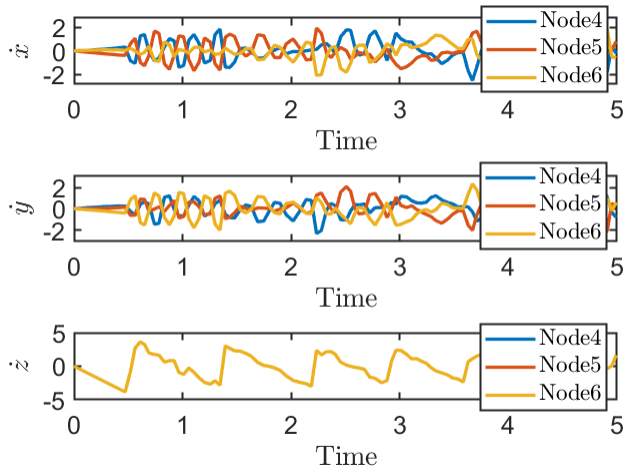

Figure 3.20: Velocity time history of node 4, 5 and 6 from the landing simulation of the prism unit (no fluid).

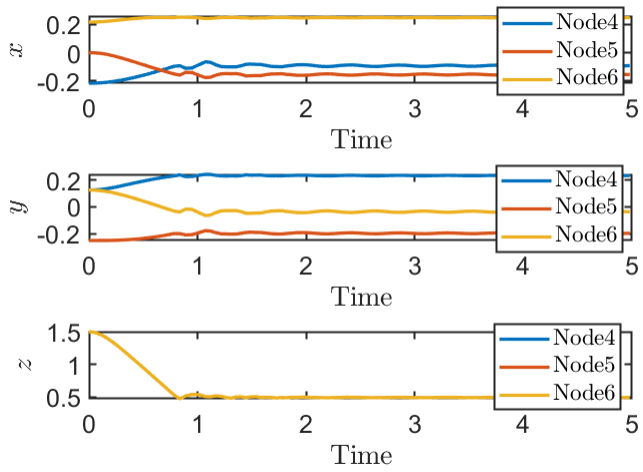

Figure 3.21: Coordinate time history of node 4, 5 and 6 from the landing simulation of the prism unit (with fluid).

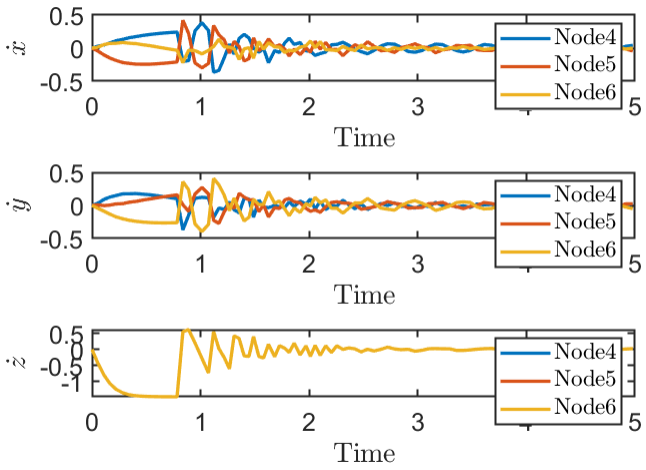

Figure 3.22: Velocity time history of node 4, 5 and 6 from the landing simulation of the prism unit (with fluid).

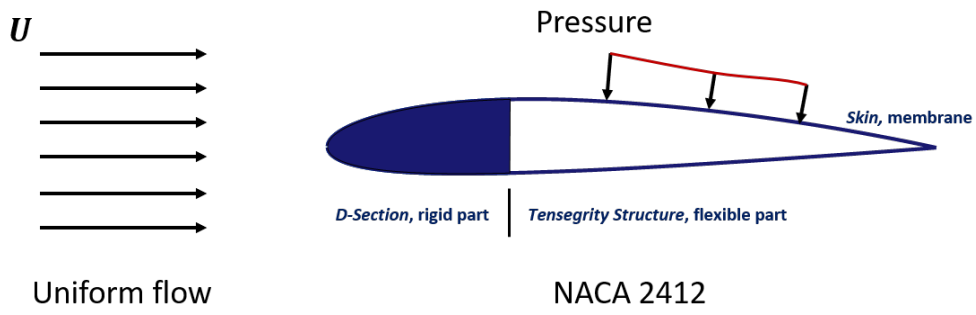

Figure 3.23: Schematic diagram of a uniform fluid with velocity U flows over an airfoil.

3.7 Fluid Forces on the Skin of the Structure

For many fluid-based structure applications, the overall structure is covered with skin to achieve desired aerodynamics/hydrodynamics performances. The skin works as an interface, can transfer the forces between the fluid and inner supporting structure. As we know, fluid forces can be very complicated when dealing with turbulence, supersonic flows, and complex geometric models. And there are still many opening research problems in these topics. To simplify the problem, in this section, we implemented the most common structure in aerospace/ocean engineering, airfoil, to demonstrate 1). obtain fluid forces on the skin of the structure by the panel method, 2). integrate the continuously distributed fluid forces on the skin to the forces on the structure nodes with force and moment equilibrium satisfied. For the first problem, we adopted the panel method to obtain the fluid forces. The Panel method, specially designed for analysis of foil structures, is an approach developed by a group led by Hess and Smith at Douglas Aircraft in the late 1950s and early 1960s [94], and was adopted to solve lifting flows at Boeing by Rubbert [95]. This method is widely adopted by researchers due to its accuracy and time-saving in computations [96, 97]. Under the following assumptions, the fluid forces on the foils are obtained by the panel method.

Assumption 3.7.1. *The fluid is assumed to be:*

1. Ideal fluids: incompressible, irrotational, steady, and in-viscid.

2. The overall structure is immersed in an infinite volume of fluid field.

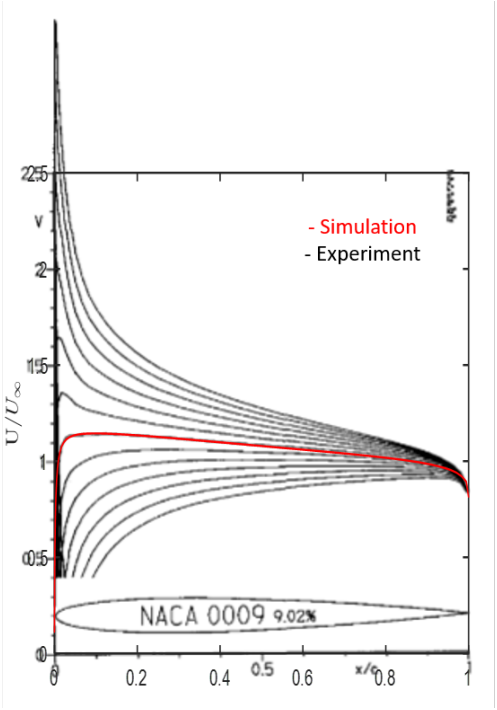

Figure 3.24: In-viscid velocity distribution along the foil chord, the comparison between simulation and experiment data of NACA 0009 at 0° attack of angle. The experimental data (Reprinted from [6].) is in black and simulation result is in red.

3. The flow has a uniform velocity at the inlet.

Let an airfoil immersed in a large enough volume of fluid. The uniform flow has a velocity of U. By implementing the panel method described in [98], we first verify the accuracy of the method by comparing the simulation and experimental data of a NACA 0009. The experimental data is in-viscid velocity distribution obtained from [6]. The comparison is shown in Figure 3.24, and the result shows that the experimental and simulation plots match well.

We choose Reynolds number Re = 10^6, the pressure distribution and pressure coefficient of NACA 0012 and NACA 2412 at different attack angles (0° and 8°) can be obtained, as shown in Figures 3.25 - 3.28. The airfoil is in green, high pressure (pressure arrow is pointing to the surface of the foil) in red and low pressure (pressure arrow is away from the surface of the foil) in blue.

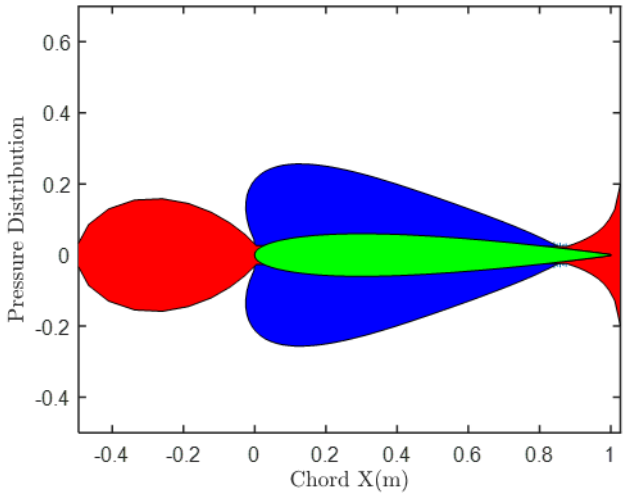

Figure 3.25: The pressure distribution NACA 0012, AOA 0°.

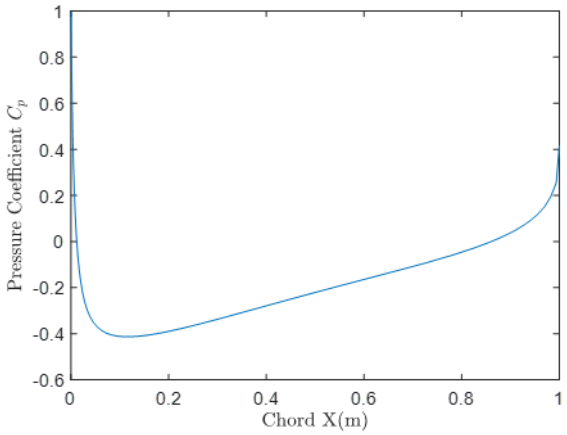

Figure 3.26: The pressure coefficients of NACA 0012, AOA 0°. Since the foil is symmetric, the pressure coefficient curves of the upper and lower surfaces are coincide with one another.

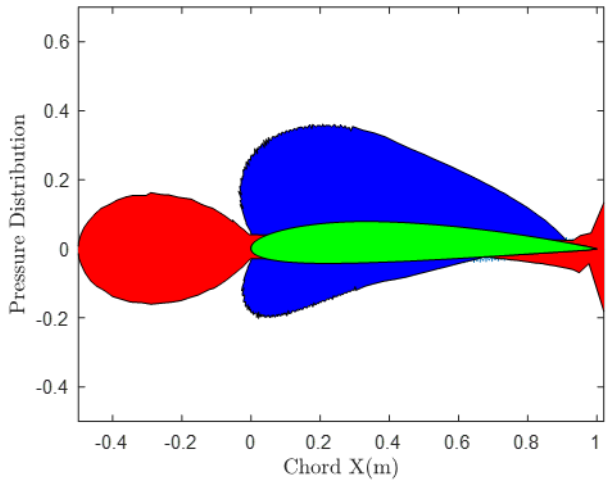

Figure 3.27: The pressure distribution of NACA 2412, AOA 0°. The red, blue, and green area are high pressure, low pressure, and the foil shape, respectively.

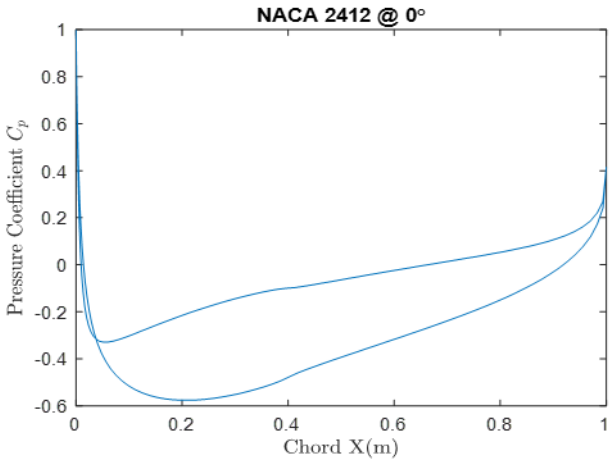

Figure 3.28: The pressure coefficients of NACA 0012, AOA 0°. The upper and bottom curves are for the lower and upper surfaces, respectively.

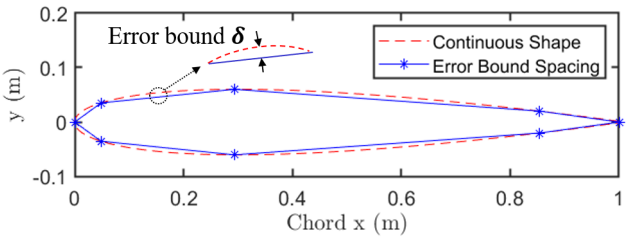

Figure 3.29: Illustration of error bound spacing method by NACA0012 with error bound $\delta = 0.008$ m. The red dotted curve and the blue solid line are the continuous and discrete airfoil shape. Error bound δ is the maximum distance between the continuous shape and discrete line segment in the discrete section. Reprinted with permission from [7].

3.8 Tensegrity Airfoil Design

This section focuses on an error bound method for the discretization of continuous airfoils and a representation of the tensegrity airfoil topology based on matrix notations.

3.8.1 Error Bound Method

Let us assume the chord length of an airfoil is 1, the number of discrete points is p. There are two widely used spacing methods (evenly and cosine spacing) for discretizing an airfoil in the computational fluid dynamics (CFD) field [99, 100]. The definition of evenly and cosine spacing is the x-coordinates of the discrete points on the airfoil satisfy a linear function $x_i = \frac{i}{p}$, $(i = 1, 2, 3, \ldots, p)$ or a cosine function $x_i = 0.5[1 - cos(\frac{\pi}{p}i)], (i = 1, 2, 3, \ldots, p)$. However, these two methods could not quantify the shape accuracy of the discretized shape compared to a continuous shape. In other words, one cannot specify how big the shape error is merely by the control points one uses. It might not bother much when one is allowed to have a sufficient number of discrete points, but when it comes to describing an airfoil with limited points, it reveals the importance to obtain a better discrete shape. In consequence, this chapter proposes an error bound spacing method, see Figure 3.29, which discretizes an airfoil and provides a quantitative representation of airfoil shape accuracy. This may improve the performance prediction of airfoil designs.

Error Bound Method: *Given the exact airfoil shape, approximate the shape with straight-line segments. Choose the location of the nodes of the straight-line segments such that the maximum*

error between the defined shape and each straight-line segment is less than a specified value δ.

Algorithm 4: Error Bound Spacing Algorithm

1) Let $y = f(x),\ x \in [0, 1]$ be the function of a continuous airfoil shape, an error bound value be δ.
2) Let $x_0 \in x$ be the start point of discretization, then $x \in [0, x_0]$ is the continuous part (called the "D-Section") and $x \in [x_0, 1]$ is the discrete part.
3) Let (x_2, y_2) be the next discrete point, the line function of segment (x_0, y_0) and (x_2, y_2) is:

$$Ax + By + C = 0, \tag{3.104}$$

where $A = (y_2 - y_0)/(x_2 - x_0),\ B = -1,$ and $C = y_0 - Ax_0$.
4)The point $(x_1, y_1), x_1 \in (x_0, x_2)$ has the largest distance with the line segment:

$$d = \frac{|Ax_1 + By_1 + C|}{\sqrt{A^2 + B^2}}. \tag{3.105}$$

5) Obtain all the discrete points:
while $x \leq 1$ **do**

$$\begin{cases} f'(x)|_{x=x_1} = \frac{y_2 - y_0}{x_2 - x_0} \\ \frac{||Ax_1 + By_1 + C||}{\sqrt{A^2 + B^2}} = \delta \end{cases}, \text{ solve for } x_2$$

Store (x_2, y_2) and update $x_0 \leftarrow x_2$.

end while

Following the definition, an algorithm can be formulated to obtain the coordinates of the discrete points, shown in Algorithm 4. Let an example to illustrate the advantage of the error bound method comparing with evenly and cosine spacing ones, shown in Figure 3.30. It is clear that the error bound method has better accuracy for the same number of discrete points, and the error bound δ also provides a quantitative sense of the accuracy of the discrete airfoil.

3.8.2 Topology of Tensegrity Airfoil

Having located the nodes of the straight-line approximation of the desired shape, we now must show the interior tensegrity structure of the airfoil. Inspired by the structure of vertebra, we connect the discrete points in a similar pattern, as shown in Figure 3.31. The blue area in Figure 3.31 is the

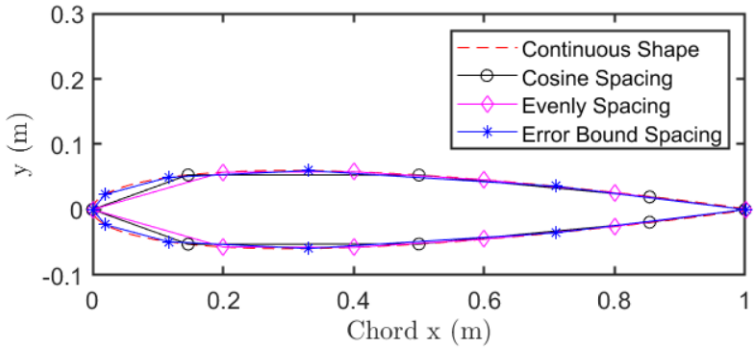

Figure 3.30: Comparison of cosine spacing, evenly spacing, and error bound spacing methods by NACA 0012 with same amount of discrete points. Reprinted with permission from [7].

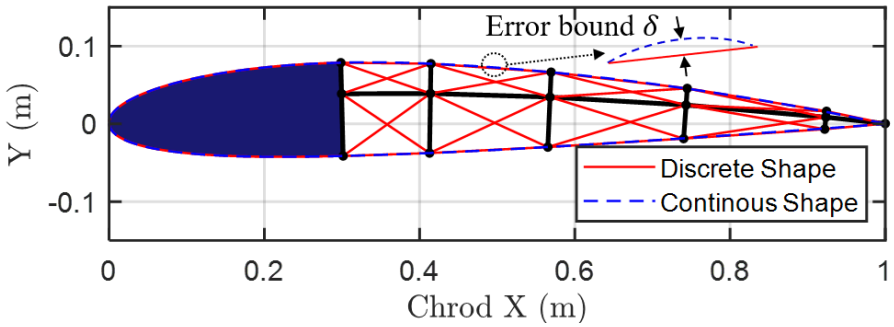

Figure 3.31: Tensegrity airfoil configuration, blue shaded area is the rigid body (normally called the D-Section), black and red lines are bars and strings.

D-section, also called D-box, is a structure in a letter D form in the front of the airfoil widely used in wing structure construction.

The notation of nodes, bars, and strings of a tensegrity airfoil with any complexity q is given in Fig. 3.32, where q is the number of horizontal bars in the tensegrity structure. The discrete points on the surface of the airfoil (nodes $\boldsymbol{n}_{q+1}, \boldsymbol{n}_{q+2}, \cdots, \boldsymbol{n}_{3q+1}$) are determined by error bound spacing method developed in [7], which is defined as the maximum error between the continuous surface shape and each straight-line segment is less than a specified value δ. The coordinate of node $\boldsymbol{n}_i$ ($i = 1, 2, \cdots, q$) is determined by the nodes above and below this point with a same ratio $\mu \in (0, 1)$, which satisfies $\boldsymbol{n}_i = \mu \boldsymbol{n}_{q+1+i} + (1-\mu)\boldsymbol{n}_{2q+1+i}$.

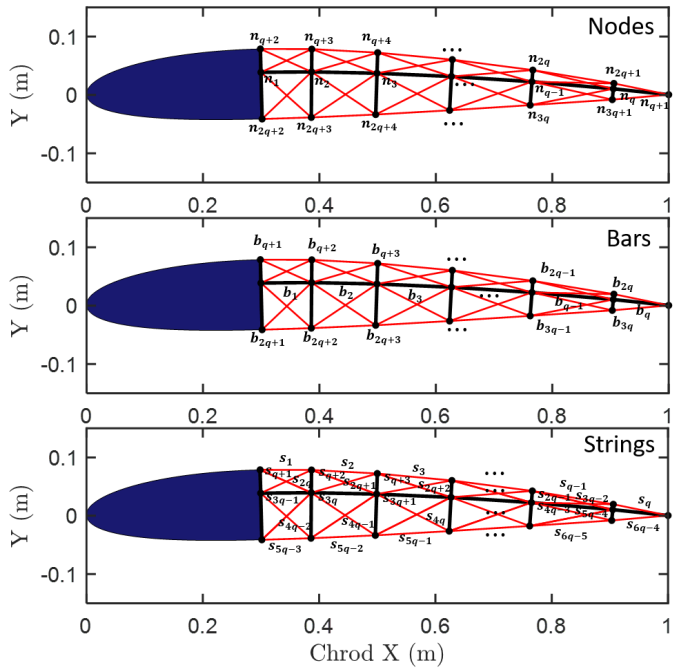

Figure 3.32: Node, bar, and string notations of a tensegrity airfoil with complexity q.

3.8.3 General Modeling of Tensegrity Airfoil

We define nodal, bar, string, bar connectivity, and string connectivity matrices: N, B, S, C_b, and C_s to describe a tensegrity airfoil with any complexity q. The nodal matrix $N = [\boldsymbol{n}_1, \boldsymbol{n}_2, \cdots, \boldsymbol{n}_{3q+1}]$, its each column represents the x-, y-, and z-coordinate of each node ($\boldsymbol{n}_i = \begin{bmatrix} x_i & y_i & z_i \end{bmatrix}^T$). C_S and C_B are connectivity matrices (with 0, -1, and 1 contained in each column) of strings and bars. The bar and string matrices $B = [\boldsymbol{b}_1, \boldsymbol{b}_2, \cdots, \boldsymbol{b}_{3q}] = NC_b^T$, $S = [\boldsymbol{s}_1, \boldsymbol{s}_2, \cdots, \boldsymbol{s}_{6q-4}] = NC_s^T$, where $\boldsymbol{b}_j$ ($j = 1, 2, \cdots, 3q$) and $\boldsymbol{s}_k$ ($k = 1, 2, \cdots, 6q-4$) are the jth bar and kth string. $C_{b_{in}}$ and $C_{s_{in}}$

whose two elements in each row denotes the start and end node of one bar or string:

$$C_{b_{in}} = \begin{cases} [i, i+1],\ 1 \le i \le q \\ [i-q, i+1],\ q+1 \le i \le 2q \\ [i-2q, i+1],\ 2q+1 \le i \le 3q \end{cases}, \tag{3.106}$$

$$C_{s_{in}} = \begin{cases} [i+1+q, i+2+q],\ 1 \le i \le q-1 \\ [q+i, i],\ 2 \le i \le q \\ [i, q+2+i],\ 1 \le i \le q-1 \\ [i, 2q+2+i],\ 1 \le i \le q-1 \\ [2q+i, i],\ 2 \le i \le q \\ [i+1+2q, i+2+2q],\ 1 \le i \le q-1 \\ [2q+1, q+1],\ [3q+1, q+1] \end{cases}. \tag{3.107}$$

Then, a function can be written to convert $C_{b_{in}}$ and $C_{s_{in}}$ to C_b and C_s [47]. A set of tensegrity airfoils with different structure complexities are shown in Figure 3.33.

3.9 Transfer the Skin Forces to the Tensegrity Airfoil

The airfoil is normally separated into two parts: 1). D-section, the front head of the foil, usually called D-section; 2). The rest part, where we put tensegrity structure and a membrane skin on it, as shown in Figure 3.23. From Figures 3.25 and 3.27 we know, the fluid has a non-uniform, continuous fluid pressure on the foils. The tensegrity structure is discrete on the skin. We are interested in the forces on the structure nodes which is transferred by the membrane skin. Since the membrane can not take bending, so it can not tolerate any moment. That is, the discrete nodes

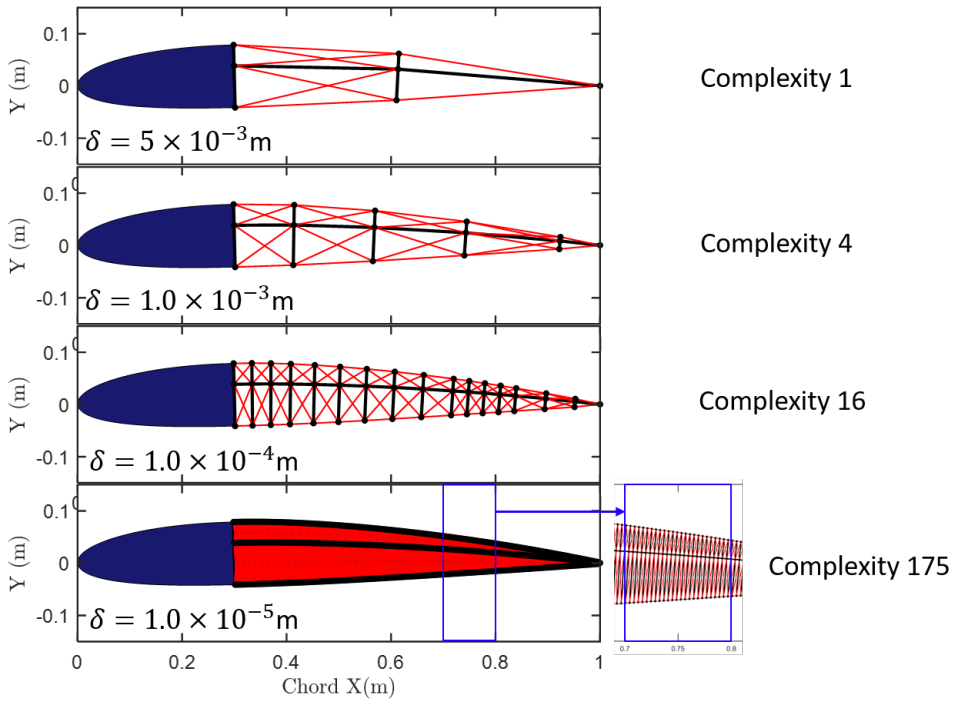

Figure 3.33: Discretize the airfoil by error bound method. The structure complexity is the number of T-Bars in the tail structure.

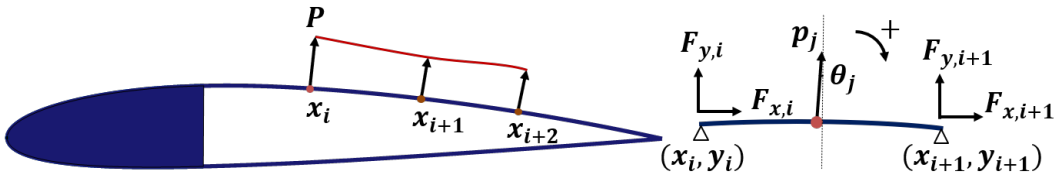

Figure 3.34: The continuous pressure distribution on the airfoil, which can be transferred to the supporting nodes of the structure.

of the structure must balance the forces and moments:

$$\boldsymbol{F} = \int \boldsymbol{P} dx, \tag{3.108}$$

$$\boldsymbol{M} = \int \boldsymbol{r} \times \boldsymbol{F} dx, \tag{3.109}$$

where $\boldsymbol{F}$ and $\boldsymbol{P}$ are denoted in the FBD (free body diagram), as shown in Figure 3.34. We also define $\delta y = y_i - y_{i+1}$, $\delta x = x_{i+1} - x_i$, and discrete pressure p_j on the foil (Δx is the gradient of the discrete pressure distribution of the foil in the x-direction), we have:

$$\begin{bmatrix} 1 & 1 & 0 & 0 \\ 0 & 0 & 1 & 1 \\ \delta y & 0 & \delta x & 0 \\ 0 & -\delta y & 0 & -\delta x \end{bmatrix} \begin{bmatrix} F_{x,i} \\ F_{x,i+1} \\ F_{y,i} \\ F_{y,i+1} \end{bmatrix} = \begin{bmatrix} -\sum p_j \sin\theta_j \Delta x \\ -\sum p_j \cos\theta_j \Delta x \\ -\sum p_j \sin\theta_j \Delta x (y_i - y_j) + \sum p_j \cos\theta_j \Delta x (x_j - x_i) \\ -\sum p_j \sin\theta_j \Delta x (y_j - y_{i+1}) + \sum p_j \cos\theta_j \Delta x (x_{i+1} - x_j) \end{bmatrix}. \tag{3.110}$$

Now, let us illustrate the algorithm by two tensegrity based on NACA 0012 and NACA 2412 foils ($\delta = 0.001$). The fluid forces of the tensegrity foils in Figures 3.35 and 3.36 on the discrete nodes are given in Tables 3.1 and 3.2. As we can see, since the NACA 0012 is symmetric, the forces in the X-direction at the upper surface and the lower surface are the same, the forces in the X-direction at the upper surface and the lower surface are of the same value but in the opposite direction, which agrees with the physics. Similarly, NACA 2412 is an asymmetric airfoil. The unevenly distributed fluid forces are given in Table 3.2. Then, the dynamics of the tensegrity can be modeled by adding these fluid forces into the external force matrix W of the tensegrity dynamics equation in Eq. (3.97).

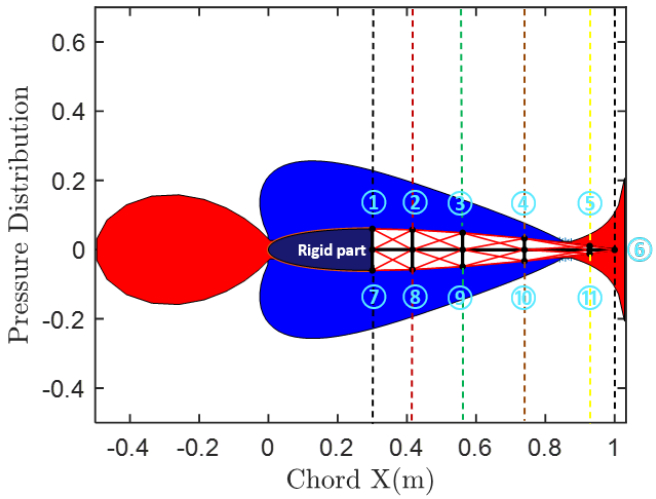

Figure 3.35: The continuous pressure distribution on a tensegrity NACA 0012 airfoil, which can be transferred to the supporting nodes (① - ⑪) of the structure. Black lines and red lines in the foil structure are bars and strings.

Table 3.1: Fluid force at the discrete points of the tensegrity NACA 0012 @ 0° AOA. The first value in the parentheses

	Upper Surface	Lower Surface
Rigid Head	(0.0092,-0.1242)	(0.0092, 0.1242)
② ⑧	(-0.0011, -0.0342)	(-0.0011, 0.0342)
③ ⑨	(-0.0021, -0.0356)	(-0.0021, 0.0356)
④ ⑩	(-0.0016, -0.0204)	(-0.0016, 0.0204)
⑤ ⑪	(0.0005, 0.0053)	(0.0005, -0.0053)
⑥	(0.0012,0.0000)	

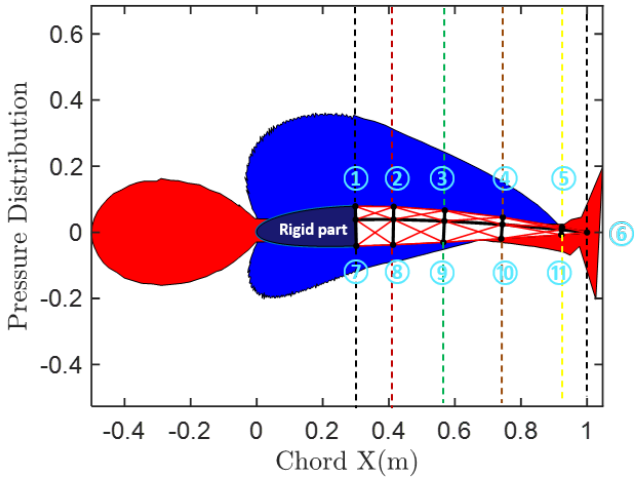

Figure 3.36: The continuous pressure distribution on a tensegrity NACA 2412 airfoil, which can be transferred to the D-section and supporting nodes (① - ⑪) of the structure.

Table 3.2: Fluid Force at the discrete points of the tensegrity NACA 2412 @ 0° AOA.

	Upper Surface	Lower Surface
Rigid Head	(0.0191,-0.1766)	(0.0035, 0.0770)
② ⑧	(-0.0024, -0.0700)	(-0.0005, 0.0139)
③ ⑨	(-0.0052, -0.0604)	(-0.0002, 0.0064)
④ ⑩	(-0.0044, -0.0383)	(0.0005, -0.0060)
⑤ ⑪	(0.0010, -0.0042)	(0.0010,-0.0015)
⑥	(0.0009,-0.0026)	

3.10 Conclusion

This chapter contains two parts. For the first part, we formulated the dynamics of tensegrity structures that interface the fluid directly. Firstly, we derived the dynamics of one single rod. The continuously distributed fluid forces along the bar are represented by a single force at the geometrical center and a torque. Then, the fluid forces are added to the derived dynamics of

equations. By stacking all the equations of motion for each rod, compact vector and matrix forms of class-1 and class-k tensegrity dynamics are formulated. Finally, based on a three-dimensional prism model, we simulate and compared results without considering fluid forces, fluid velocity, and gravity forces. Results show that fluid forces and velocity can give the structure damping and pushing force to the dynamics response of the structure, which agrees with the physics. This study gives an analytical dynamics formulation of fluid-structure interaction of any class-1 and class-k tensegrity structures. For the second part, we presented structures interfaces fluid by a skin(membrane) on the tensegrity structure by two tensegrity foils. The approach is achieved by using the panel method to compute the fluid pressure on the foil, integrating the fluid forces on the structure nodes with force and moment equilibrium satisfied. Results show that the fluid model is accurate for foil analysis compared with experimental data of NACA 0009. An airfoil discretization method to bound the local error of each node is introduced and combined with the design of tensegrity airfoils. Finally, we showed the normalized fluid forces transferred to tensegrity airfoils NACA 0012 and NACA 2412. The principles developed in this chapter enable our ability to study various kinds of fluid-based tensegrity structures.

4. INTEGRATING STRUCTURE DYNAMICS AND MATERIALS: TENSEGRITY SYSTEM DYNAMICS BASED ON FINITE ELEMENT METHOD

This chapter presents a finite element analysis approach to nonlinear and linearized tensegrity dynamics based on the Lagrangian method with nodal coordinate vectors as the generalized coordinates. In this chapter, nonlinear tensegrity dynamics with and without constraints are first derived. The equilibrium equations in three standard forms (in terms of nodal coordinate, force density, and force vectors) and the compatibility equation are also given. Then, we present the linearized dynamics and modal analysis equations with and without constraints. The developed approach is capable of conducting the following comprehensive dynamics studies for any tensegrity structures accurately: 1. Performing rigid body dynamics with acceptable errors, which is achieved by setting relatively high stiffness for bars in the simulation. 2. Simulating FEM dynamics accurately, where bars and strings can have elastic or plastic deformations. 3. Dealing with various kinds of boundary conditions, for example, fixing or applying static/dynamic loads at any nodes in any direction (i.e., gravitational force, some specified forces, or arbitrary seismic vibrations). 4. Conducting accurate modal analysis, including natural frequency and corresponding modes. Three examples, a double pendulum, a cantilever truss with external force, and a T_2D_1 tensegrity tower, are carefully selected and studied. The results are compared with rigid body dynamics and FEM software ANSYS. This study provides a deep insight into structures, materials, performances, as well as an interface towards integrating control theories.

4.1 Introduction

Tensegrity has shown its great attraction to both artists and engineers, a few research on tensegrity dynamics has been conducted. The existing tensegrity dynamics can be classified into two categories based on the assumptions of whether the bars are rigid or not [101]. The first category belongs to rigid body dynamics derived by Newton-Euler's principle or analytical dynamics with assumptions that bars are rigid and strings are linear elastic. For example, Sultan *et al.* derived

linearized equations of motion for tensegrity models around arbitrary equilibrium configurations [78]. Skelton presented one of the simplest dynamics forms for class-1 structure by using non-minimal coordinates and assuming the compressive elements to have no inertia about the longitudinal axis [79]. Kan *et al.* presented a sliding cable element for multibody dynamics with an application to the deployment of clustered tensegrity [102]. Cefalo and Mirats-Tur proposed a dynamic model based on the Lagrangian method for class-1 tensegrity systems with quaternions as the variables [103]. Goyal *et al.* presented a compact matrix form of tensegrity dynamics by including massive strings [83], a corresponding general software for modeling of any tensegrity structures can be found in [47]. Recently, Goyal *et al.* extended the model of the nonlinear dynamics to modulate the torque produced by the network of spatially distributed gyroscopes [84]. The second one is non-rigid body dynamics formulated by the FEM by assuming that all structure members are elastic/plastic. For example, Murakami studied the static and dynamic equations of tensegrity with large deformation in Eulerian and Lagrangian formulations [104]. Faroughi *et al.* presented a nonlinear dynamic analysis of space truss structures based on the dynamics of 3D co-rotational (CR) rods [105]. Rimoli developed a physics-based reduced-order model to capture the buckling and post-buckling behavior of bars [106]. Kan *et al.* derived the dynamic analysis of clustered tensegrity structures via the framework of the positional formulation FEM [101]. However, most of these dynamics equations are achieved by deriving the dynamics of one element and stacking all the structural elements into an assembled matrix or vector form. For the insight knowledge of the nonlinear tensegrity dynamics and future convenience for the field of structural control, a closed-form of dynamics derived from a system-level is needed, which is presented in this chapter.

This chapter is organized as follows: Section 4.2 describes bar and string assumptions, nodal coordinates and connectivity matrices notations, and geometric and physical properties of the tensegrity system in compact vector forms. Section 4.3 formulates the shape function of an element, kinetic energy, strain, and gravitational potential energy of the whole structure. Then, tensegrity dynamics with and without boundary constraints are derived by the Lagrangian method. By neglecting the time derivative terms in the dynamics equation, we also give the equilibrium

equations in three standard equivalent forms (in terms of nodal vector, force density, and force vector). Section 4.4 derives the linearized tensegrity dynamics and modal analysis equations with and without boundary constraints. Section 4.5 demonstrates three examples (dynamic response of a double pendulum, dynamics response and modal analysis of a cantilever truss with an external force, and seismic analysis of a tensegrity tower) and compares results with rigid body dynamics and FEM software ANSYS. Section 4.6 summarises the conclusions.

4.2 Assumptions and Notations of the Tensegrity System

4.2.1 Assumptions of Structural Members

Under the following assumptions of structural members (bars and strings), the mathematical formulation of any tensegrity systems is established.

Assumption 4.2.1. *The structural members (bars and strings) in the tensegrity system have these properties:*

1). The structural members are axially loaded, all structural members are connected by frictionless pin-joints.

2). The structural members are not rigid, and they are allowed to have elastic or plastic deformation.

3). The structural members have negligible inertia about their longitudinal axes.

4). Each structural member is homogeneous along its length and of an equal cross-section. Thus, the mass of each structural member is distributed uniformly along its length.

5). If $||\boldsymbol{s}_{i0}|| > ||\boldsymbol{s}_i||$, where the rest length and actual length of the ith string are denoted by $||\boldsymbol{s}_{i0}||$ and $||\boldsymbol{s}_i||$, and $\|\boldsymbol{v}\|$ is the Euclidean norm of vector $\boldsymbol{v}$, since a string can never push along its length, tension in the string should be substituted to zero.

4.2.2 Geometric Properties of Structural Elements

The position of each node in the structure can be expressed in any frame, we choose to label them with Cartesian coordinates in an inertially fixed frame. Assume the tensegrity structure has n_n number of nodes, the X-, Y-, and Z-coordinates of the *i*th node $\boldsymbol{n}_i$ ($i = 1, 2, \cdots, n_n$) can be

labeled as x_i, y_i, and z_i. One can also write $\boldsymbol{n}_i \in \mathbb{R}^3$ in a vector form:

$$\boldsymbol{n}_i = \begin{bmatrix} x_i & y_i & z_i \end{bmatrix}^T . \tag{4.1}$$

By stacking $\boldsymbol{n}_i$ for $i = 1, 2, \cdots, n_n$ together, we can obtain the nodal coordinate vector $\boldsymbol{n} \in \mathbb{R}^{3n_n}$ for the whole structure:

$$\boldsymbol{n} = \begin{bmatrix} \boldsymbol{n}_1^T & \boldsymbol{n}_2^T & \cdots & \boldsymbol{n}_{n_n}^T \end{bmatrix}^T , \tag{4.2}$$

or in a matrix form, which is called nodal coordinate matrix $\boldsymbol{N} \in \mathbb{R}^{3\times n_n}$:

$$\boldsymbol{N} = \begin{bmatrix} \boldsymbol{n}_1 & \boldsymbol{n}_2 & \cdots & \boldsymbol{n}_{n_n} \end{bmatrix} . \tag{4.3}$$

Connectivity matrices denote the topology of the structure or, in other words, how the structural members (bars and strings) are connected at each node. Conventionally, the connectivity matrices contain two types: string connectivity and bar connectivity, labeled as $\boldsymbol{C}_s \in \mathbb{R}^{\alpha\times n_n}$ and $\boldsymbol{C}_b \in \mathbb{R}^{\beta\times n_n}$, where α and β are the number of strings and bars in the structure [47].

Since both bars and strings are allowed to have elastic or plastic deformation, we do not need to distinguish the connectivity by the types of structural members in this FEM formulation. Thus, we use a matrix $\boldsymbol{C} \in \mathbb{R}^{n_e\times n_n}$ to represent the topology of the whole structure, where n_e is the number of all the structural elements, which satisfies $n_e = \alpha + \beta$. The *i*th row of $\boldsymbol{C}$, denoted as $\boldsymbol{C}_i = [\boldsymbol{C}]_{(i,:)} \in \mathbb{R}^{1\times n_n}$, represents the *i*th structural element, starting form node *j* ($j = 1, 2, \cdots, n_n$) to node *k* ($k = 1, 2, \cdots, n_n$), shown in Figure 4.1. The *m*th ($m = 1, 2, \cdots, n_n$) entry of $\boldsymbol{C}_i$ satisfies:

$$[\boldsymbol{C}]_{im} = \begin{cases} -1, \ m = j \\ \ \ 1, \ m = k \\ \ \ 0, \ m = else \end{cases} . \tag{4.4}$$

For n_e number of structural elements, the overall structure connectivity matrix $\boldsymbol{C} \in \mathbb{R}^{n_e\times n_n}$ can be

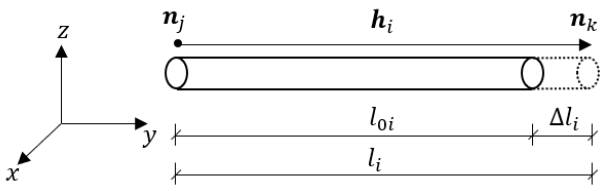

Figure 4.1: Structure member vector $\boldsymbol{h}_i$, determined by node $\boldsymbol{n}_j$ and node $\boldsymbol{n}_k$ in the Cartesian coordinates, has a length of $l_i = ||\boldsymbol{h}_i|| = l_{0i} + \Delta l_i$, where l_{0i} is the rest length and Δl_i is the displacement.

written as:

$$\boldsymbol{C} = \begin{bmatrix} \boldsymbol{C}_1^T & \boldsymbol{C}_2^T & \cdots & \boldsymbol{C}_{n_e}^T \end{bmatrix}^T. \tag{4.5}$$

Define the nodal coordinate vector of the *i*th element $\boldsymbol{n}_i^e \in \mathbb{R}^6$ as:

$$\boldsymbol{n}_i^e = \begin{bmatrix} \boldsymbol{n}_j \\ \boldsymbol{n}_k \end{bmatrix} = \begin{bmatrix} x_j & y_j & z_j & x_k & y_k & z_k \end{bmatrix}^T. \tag{4.6}$$

One can also abstract $\boldsymbol{n}_i^e$ from the structure nodal coordinate vector $\boldsymbol{n}$:

$$\boldsymbol{n}_i^e = \bar{\boldsymbol{C}}_i \otimes \mathbf{I}_3 \boldsymbol{n}, \tag{4.7}$$

where $\mathbf{I}_3 \in \mathbb{R}^{3\times3}$ is a identity matrix, $\bar{\boldsymbol{C}}_i$ is a self-defined transformation matrix, whose *p*th column satisfies:

$$[\bar{C}_i]_{(:,p)} = \begin{cases} \begin{bmatrix} 1 & 0 \end{bmatrix}^T, & p = j \\ \begin{bmatrix} 0 & 1 \end{bmatrix}^T, & p = k \\ \begin{bmatrix} 0 & 0 \end{bmatrix}^T, & p = else \end{cases}. \tag{4.8}$$

Let us look at the ith structure element $\boldsymbol{h}_i$, its geometry properties is shown in Figure 4.1, the

element vector is given by:

$$\boldsymbol{h}_i = \boldsymbol{n}_k - \boldsymbol{n}_j = \boldsymbol{C}_i \otimes \mathbf{I}_3 \boldsymbol{n}. \tag{4.9}$$

Stack all the structure elements in a matrix form, one can obtain:

$$\boldsymbol{H} = \begin{bmatrix} \boldsymbol{h}_1 & \boldsymbol{h}_2 & \cdots & \boldsymbol{h}_{n_e} \end{bmatrix} = \boldsymbol{N}\boldsymbol{C}^T. \tag{4.10}$$

The length of the *i*th structure element l_i satisfies:

$$l_i = \|\boldsymbol{h}_i\| = (\boldsymbol{n}^T(\boldsymbol{C}_i^T\boldsymbol{C}_i) \otimes \mathbf{I}_3\boldsymbol{n})^{\frac{1}{2}}. \tag{4.11}$$

Then, the overall structure element length vector $\boldsymbol{l} \in \mathbb{R}^{n_e}$ is:

$$\boldsymbol{l} = \begin{bmatrix} l_1 & l_2 & \cdots & l_{n_e} \end{bmatrix}^T. \tag{4.12}$$

The rest length vector $\boldsymbol{l}_0 \in \mathbb{R}^{n_e}$ of the whole structure is:

$$\boldsymbol{l}_0 = \begin{bmatrix} l_{01} & l_{02} & \cdots & l_{0n_e} \end{bmatrix}^T, \tag{4.13}$$

where rest length is defined as the length of an structure element with no tension or compression.

4.2.3 Physical Properties of Structural Elements

A typical stress-strain curve of an element is given in Figure 4.2. The stress in the element satisfies:

$$\sigma = E\epsilon, \tag{4.14}$$

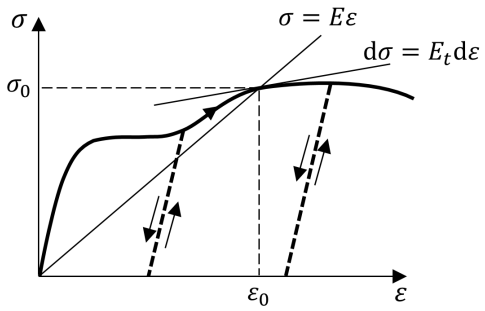

Figure 4.2: A typical stress-strain curve of structure elements, where E and E_t are called secant modulus and tangent modulus of the material. The curve includes elastic or plastic deformation phases. The dotted lines indicate stress-strain levels for unloading cases at certain points of the stress-strain curve.

where E is the secant modulus and ϵ is the strain, and this equation can represent the stress of any material including linear elastic, multi-linear elastic, plastic, etc. The derivative of Eq. (4.14) is:

$$\mathrm{d}\sigma = E_t \mathrm{d}\epsilon, \tag{4.15}$$

where E_t is tangent modulus. For elastic material, the secant modulus is identical to its tangent modulus. We discuss the elastic and plastic properties of materials here because later we will show that the developed dynamics are capable of doing analysis of both kinds of materials.

Suppose material density is ρ, the cross section area, secant modulus, tangent modulus of the ith element are respectively A_i, E_i E_{ti}, the element mass m_i satisfies $m_i = \rho A_i l_{0i}$. Denote the cross section area vector, mass vector, secant modulus and tangent modulus vector of the structure as $\boldsymbol{A}$, $\boldsymbol{m}$, $\boldsymbol{E}$ and $\boldsymbol{E}_t \in \mathbb{R}^{n_e}$, one can write:

$$\boldsymbol{A} = \begin{bmatrix} A_1 & A_2 & \cdots & A_{n_e} \end{bmatrix}^T, \tag{4.16}$$

$$\boldsymbol{m} = \begin{bmatrix} m_1 & m_2 & \cdots & m_{n_e} \end{bmatrix}^T = \rho \hat{\boldsymbol{A}} \boldsymbol{l}_0, \tag{4.17}$$

$$\boldsymbol{E} = \begin{bmatrix} E_1 & E_2 & \cdots & E_{n_e} \end{bmatrix}^T, \tag{4.18}$$

$$\boldsymbol{E}_t = \begin{bmatrix} E_{t1} & E_{t2} & \cdots & E_{tn_e} \end{bmatrix}^T, \tag{4.19}$$

where $\hat{\boldsymbol{v}}$ transforms vector $\boldsymbol{v}$ into a diagonal matrix, whose diagonal entries are the elements of vector $\boldsymbol{v}$ and elsewhere are zeros.

The internal force of the *i*th element is $t_i = A_i\sigma_i = E_iA_i(l_i - l_{0i})/l_{0i}$, the internal force vector of the structure $\boldsymbol{t} \in \mathbb{R}^{n_e}$ can be written as:

$$\boldsymbol{t} = \begin{bmatrix} t_1 & t_2 & \cdots & t_{n_e} \end{bmatrix}^T = \hat{\boldsymbol{E}}\hat{\boldsymbol{A}}\hat{\boldsymbol{l}}_0^{-1}(\boldsymbol{l} - \boldsymbol{l}_0). \tag{4.20}$$

Force density of the *i*th element is given by $x_i = t_i/l_i$, the force density vector of all the structure elements is:

$$\boldsymbol{x} = \hat{\boldsymbol{l}}^{-1}\boldsymbol{t} = \hat{\boldsymbol{E}}\hat{\boldsymbol{A}}(\boldsymbol{l}_0^{-1} - \boldsymbol{l}^{-1}), \tag{4.21}$$

where $\boldsymbol{v}^{-1}$ represents a vector whose entry is the reciprocal of its corresponding entry in $\boldsymbol{v}$. The force density vector $\boldsymbol{x}$ is normally defined in the from of $\boldsymbol{x} = \begin{bmatrix} \boldsymbol{\lambda}^T & \boldsymbol{\gamma}^T \end{bmatrix}^T$ with the information of $\boldsymbol{\lambda}$ and $\boldsymbol{\gamma}$ are force density vectors of bars and strings [5]. We should point out that Eqs. (4.20) and (4.21) can be used to compute force vector and force density vector for either elastic or plastic materials by using different secant modulus **E** of the materials.

4.3 Nonlinear Tensegrity Dynamics Formulation

4.3.1 Energy Equation Formulation

4.3.1.1 Shape Function of the Structure Element

Since the structure member is axially loaded, the displacement of the material particles are along the bar/string vectors. We assume the displacements of material particles on the structure member are in a uniform manner [107]. Here, we introduce a scalar μ to help expressing the coordinates of point $\boldsymbol{p}_i$ on the ith member between node $\boldsymbol{n}_j$ and node $\boldsymbol{n}_k$ in the *i*th structure element, shown in Figure 4.3. Thus, the location of a point $\boldsymbol{p}_i$ on the structure member can be

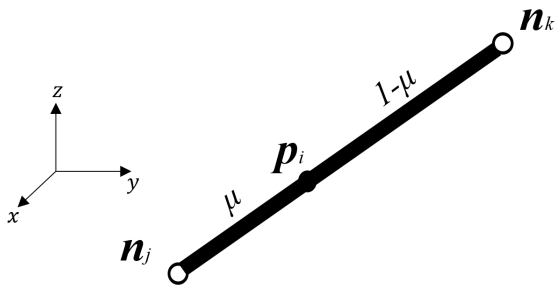

Figure 4.3: Shape function of an element, scalar μ helps to locate the position of point $\boldsymbol{p}_i$ on the ith structure element in between node $\boldsymbol{n}_j$ and node $\boldsymbol{n}_k$ in the Cartesian coordinates.

computed as a linear function in terms of μ:

$$\boldsymbol{p_i} = \begin{bmatrix} 1 & \mu \end{bmatrix} \otimes \mathbf{I}_3 \begin{bmatrix} \boldsymbol{a}_0 \\ \boldsymbol{a}_1 \end{bmatrix}, \tag{4.22}$$

where $\boldsymbol{a}_0$ and $\boldsymbol{a}_1 \in \mathbb{R}^3$ are unknowns. Substitute the nodal coordinate of $\boldsymbol{n}_j$, $\boldsymbol{n}_k$ with μ = 0 and 1 into Eq. (4.22), we have:

$$\begin{bmatrix} 1 & 0 \\ 1 & 1 \end{bmatrix} \otimes \mathbf{I}_3 \begin{bmatrix} \boldsymbol{a}_0 \\ \boldsymbol{a}_1 \end{bmatrix} = \begin{bmatrix} \boldsymbol{n}_j \\ \boldsymbol{n}_k \end{bmatrix}. \tag{4.23}$$

Then, the solution of Eq. (4.23) is:

$$\begin{bmatrix} \boldsymbol{a}_0 \\ \boldsymbol{a}_1 \end{bmatrix} = \begin{bmatrix} 1 & 0 \\ -1 & 1 \end{bmatrix} \otimes \mathbf{I}_3 \begin{bmatrix} \boldsymbol{n}_j \\ \boldsymbol{n}_k \end{bmatrix}. \tag{4.24}$$

Substitute Eq. (4.24) into Eq. (4.22), we have:

$$\boldsymbol{p}_i = \begin{bmatrix} 1-\mu & \mu \end{bmatrix} \otimes \mathbf{I}_3 \begin{bmatrix} \boldsymbol{n}_j \\ \boldsymbol{n}_k \end{bmatrix} = \boldsymbol{N}^e \boldsymbol{n}_i^e, \tag{4.25}$$

$$\boldsymbol{N}^e = \begin{bmatrix} 1-\mu & \mu \end{bmatrix} \otimes \mathbf{I}_3, \tag{4.26}$$

where $\boldsymbol{N}^e \in \mathbb{R}^{3\times 6}$ is usually called the shape function of a structure element.

4.3.1.2 Kinetic Energy

The kinetic energy T for the whole structure equals the sum of kinetic energy of material particles in all the structure elements, which can be written as a function of particle velocity $\dot{\boldsymbol{p}}_i$:

$$T = \sum_{i=1}^{n_e} \frac{1}{2} \int_0^1 m_i \|\dot{\boldsymbol{p}}_i\|^2 d\mu. \tag{4.27}$$

Substitute Eq. (4.7) and Eq. (4.25) into Eq. (4.27), we have:

$$T = \sum_{i=1}^{n_e} \frac{1}{2} \int_0^1 m_i (\boldsymbol{N}^e \bar{\boldsymbol{C}}_i \otimes \mathbf{I}_3 \dot{\boldsymbol{n}})^2 d\mu \tag{4.28}$$

$$= \sum_{i=1}^{n_e} \frac{m_i}{12} \dot{\boldsymbol{n}}^T (\bar{\boldsymbol{C}}_i^T \begin{bmatrix} 2 & 1 \\ 1 & 2 \end{bmatrix} \bar{\boldsymbol{C}}_i) \otimes \mathbf{I}_3 \dot{\boldsymbol{n}} \tag{4.29}$$

$$= \sum_{i=1}^{n_e} \frac{m_i}{12} \dot{\boldsymbol{n}}^T (\bar{\boldsymbol{C}}_i^T (\begin{bmatrix} 1 \\ 1 \end{bmatrix} [1\ 1] + \lfloor \begin{bmatrix} 1 \\ 1 \end{bmatrix} [1\ 1] \rfloor) \bar{\boldsymbol{C}}_i) \otimes \mathbf{I}_3 \dot{\boldsymbol{n}} \tag{4.30}$$

$$= \sum_{i=1}^{n_e} \frac{1}{12} \dot{\boldsymbol{n}}^T (|\boldsymbol{C}|_i^T m_i |\boldsymbol{C}|_i + \lfloor |\boldsymbol{C}|_i^T m_i |\boldsymbol{C}|_i \rfloor) \otimes \mathbf{I}_3 \dot{\boldsymbol{n}} \tag{4.31}$$

$$= \frac{1}{12} \dot{\boldsymbol{n}}^T (|\boldsymbol{C}|^T \hat{m} |\boldsymbol{C}| + \lfloor |\boldsymbol{C}|^T \hat{m} |\boldsymbol{C}| \rfloor) \otimes \mathbf{I}_3 \dot{\boldsymbol{n}} \tag{4.32}$$

$$= \frac{1}{2} \dot{\boldsymbol{n}}^T \boldsymbol{M} \dot{\boldsymbol{n}}, \tag{4.33}$$

where $|\boldsymbol{V}|$ is an operator getting the absolute value of each element for a given matrix, and the operator $\lfloor \boldsymbol{V} \rfloor$ sets every off-diagonal element of the square matrix to zero. $\boldsymbol{M} \in \mathbb{R}^{3n_n \times 3n_n}$ is called the mass matrix of the structure:

$$\boldsymbol{M} = \frac{1}{6} (|\boldsymbol{C}|^T \hat{\boldsymbol{m}} |\boldsymbol{C}| + \lfloor |\boldsymbol{C}|^T \hat{\boldsymbol{m}} |\boldsymbol{C}| \rfloor) \otimes \mathbf{I}_3. \tag{4.34}$$

Since the matrix $\boldsymbol{M}$ is symmetric, we can have the following equation:

$$\frac{\mathrm{d}}{\mathrm{d}t}\frac{\partial T}{\partial \dot{\boldsymbol{n}}} = \boldsymbol{M}\ddot{\boldsymbol{n}}. \tag{4.35}$$

Note that we use denominator layout notation in matrix calculus, which means the derivative of a scalar by a column vector is still a column vector.

4.3.1.3 Strain Potential Energy for Elastic/Plastic Deformation

We consider elastic and plastic deformation of structure members. To unify the two cases, the strain potential energy V_e of the whole structure caused by elements' internal force can be written into an integral form:

$$V_e = \sum_i^{n_e} V_{ei} \tag{4.36}$$

$$= \sum_i^{n_e} \int_{l_{0i}}^{l_i} t_i \mathrm{d}u \tag{4.37}$$

$$= \sum_i^{n_e} \int_{l_{0i}}^{l_i} \frac{E_i A_i (u - l_{0i})}{l_{0i}} \mathrm{d}u, \tag{4.38}$$

where $\mathrm{d}u$ is the differential of the structure member length. The derivative of strain potential energy V_e with respect to nodal coordinate vector $\boldsymbol{n}$ is:

$$\frac{\partial V_e}{\partial \boldsymbol{n}} = \sum_i^{n_e} \frac{\partial V_{ei}}{\partial l_i}\frac{\partial l_i}{\partial \boldsymbol{n}} \tag{4.39}$$

$$= \sum_i^{n_e} \frac{E_i A_i (l_i - l_{0i})}{l_{0i}}\frac{\partial l_i}{\partial \boldsymbol{n}} \tag{4.40}$$

$$= \sum_i^{n_e} t_i \frac{\partial l_i}{\partial \boldsymbol{n}}. \tag{4.41}$$

The derivative of element's length l_i with respect to nodal coordinate vector $\boldsymbol{n}$ can be obtained from Eq. (4.11):

$$\frac{\partial l_i}{\partial \boldsymbol{n}} = \frac{(\boldsymbol{C}_i^T \boldsymbol{C}_i) \otimes \mathbf{I}_3 \boldsymbol{n}}{l_i}. \tag{4.42}$$

Substitute Eq. (4.42) into Eq. (4.41), and use the definition of force density $x_i = f_i/l_i$ in the *i*th structure element, we have:

$$\frac{\partial V_e}{\partial \boldsymbol{n}} = \sum_i^{n_e} x_i (\boldsymbol{C}_i^T \boldsymbol{C}_i) \otimes \mathbf{I}_3 \boldsymbol{n} \tag{4.43}$$

$$= (\boldsymbol{C}^T \hat{\boldsymbol{x}} \boldsymbol{C}) \otimes \mathbf{I}_3 \boldsymbol{n} \tag{4.44}$$

$$= \boldsymbol{K} \boldsymbol{n}, \tag{4.45}$$

where $\boldsymbol{K} \in \mathbb{R}^{3n_n \times 3n_n}$ is the stiffness matrix of the tensegrity structure:

$$\boldsymbol{K} = (\boldsymbol{C}^T \hat{\boldsymbol{x}} \boldsymbol{C}) \otimes \mathbf{I}_3. \tag{4.46}$$

4.3.1.4 Gravitational Potential Energy

In many cases that the tensegrity structures are in the presence of a gravity field. Suppose the gravity force is exerted towards the negative direction of the Z-axis, the acceleration of gravity is g, for example, on earth $g = 9.8m/s^2$. The gravitational potential energy V_g can be written as:

$$V_g = \sum_i^{n_e} \frac{m_i g}{2} (z_j^i + z_k^i) \tag{4.47}$$

$$= \sum_i^{n_e} \frac{m_i g}{2} |\boldsymbol{C}_i| \otimes \begin{bmatrix} 0 & 0 & 1 \end{bmatrix} \boldsymbol{n} \tag{4.48}$$

$$= \frac{g}{2} \boldsymbol{m}^T |\boldsymbol{C}| \otimes \begin{bmatrix} 0 & 0 & 1 \end{bmatrix} \boldsymbol{n}, \tag{4.49}$$

where z_j^i and z_k^i are Z-coordinates of node $\boldsymbol{n}_j$ and node $\boldsymbol{n}_k$ of the *i*th structure element. $(z_j^i + z_k^i)/2$ is the Z-coordinate of mass center of the *i*th element. Then, the partial derivative of V_g with respect

to $\boldsymbol{n}$ is:

$$\frac{\partial V_g}{\partial \boldsymbol{n}} = \frac{g}{2}(|\boldsymbol{C}|^T \boldsymbol{m}) \otimes \begin{bmatrix} 0 & 0 & 1 \end{bmatrix}^T = \boldsymbol{g}, \tag{4.50}$$

where $\boldsymbol{g} \in \mathbb{R}^{3n_n}$ is the gravitational force vector in all nodes. For structure analysis without gravity, one can just set $\boldsymbol{g} = \boldsymbol{0}$.

4.3.2 Tensegrity Dynamics Based on the Lagrangian Method

For general cases, the position, velocity, or acceleration of some nodes in the structure are usually fixed or given. Adding these constraints to the dynamics will restrict the motion in certain dimensions. Thus the dynamics can be reduced into a smaller space. Thus, to compute the reduced-order dynamics, free nodes and fix nodes must be separated.

Let us define vector $\boldsymbol{a} = \begin{bmatrix} a_1 & a_2 & \cdots & a_{n_a} \end{bmatrix}^T \in \mathbb{R}^{n_a}$ and vector $\boldsymbol{b} = \begin{bmatrix} b_1 & b_2 & \cdots & b_{n_b} \end{bmatrix}^T \in \mathbb{R}^{n_b}$, in which the element values of $\boldsymbol{a}$ and $\boldsymbol{b}$ are the indices of free and constrained entries in the nodal coordinate vector $\mathbf{n}$. n_a and n_b is the number of free and constrained nodal coordinates, and they satisfy $n_a + n_b = 3n_n$. We use $\boldsymbol{n}_a$ and $\boldsymbol{n}_b$ to represent the free and constrained nodal coordinate vector. $\boldsymbol{E}_a \in \mathbb{R}^{3n_n \times n_a}$ and $\boldsymbol{E}_b \in \mathbb{R}^{3n_n \times n_b}$ are the matrix to abstract $\boldsymbol{n}_a$ and $\boldsymbol{n}_b$ from $\boldsymbol{n}$:

$$\boldsymbol{E}_a(:, i) = \mathbf{I}_{3n}(:, a_i), \ \boldsymbol{E}_b(:, i) = \mathbf{I}_{3n}(:, b_i). \tag{4.51}$$

The relation between $\boldsymbol{n}_a$, $\boldsymbol{n}_b$, and $\boldsymbol{n}$ is:

$$\boldsymbol{n}_a = \boldsymbol{E}_a^T \boldsymbol{n}, \ \boldsymbol{n}_b = \boldsymbol{E}_b^T \boldsymbol{n}. \tag{4.52}$$

Note that $\begin{bmatrix} \boldsymbol{E}_a & \boldsymbol{E}_b \end{bmatrix}$ is an orthonormal matrix, so given $\boldsymbol{n}_a$ and $\boldsymbol{n}_b$, the nodal coordinate vector $\boldsymbol{n}$

can be obtained by:

$$\boldsymbol{n} = \begin{bmatrix} \boldsymbol{E}_a^T \\ \boldsymbol{E}_b^T \end{bmatrix}^{-1} \begin{bmatrix} \boldsymbol{n}_a \\ \boldsymbol{n}_b \end{bmatrix} = \begin{bmatrix} \boldsymbol{E}_a & \boldsymbol{E}_b \end{bmatrix} \begin{bmatrix} \boldsymbol{n}_a \\ \boldsymbol{n}_b \end{bmatrix}. \tag{4.53}$$

The nonlinear tensegrity dynamics in the presence of constraints and gravity is given and proved by the Lagrangian Method as follows:

Theorem 4.3.1. *The finite element formulation for nonlinear tensegrity dynamics in the presence of constraints and gravity is given by the two equivalent forms in terms of entire coordinate vector* $\boldsymbol{n}$ *and free node vector* $\boldsymbol{n}_a$*:*

$$\boldsymbol{E}_a^T(\boldsymbol{M}\ddot{\boldsymbol{n}} + \boldsymbol{D}\dot{\boldsymbol{n}} + \boldsymbol{K}\boldsymbol{n}) = \boldsymbol{E}_a^T\left(\boldsymbol{f}_{ex} - \boldsymbol{g}\right), \tag{4.54}$$

$$\boldsymbol{M}_{aa}\ddot{\boldsymbol{n}}_a + \boldsymbol{D}_{aa}\dot{\boldsymbol{n}}_a + \boldsymbol{K}_{aa}\boldsymbol{n}_a = \boldsymbol{E}_a^T\boldsymbol{f}_{ex} - \boldsymbol{M}_{ab}\ddot{\boldsymbol{n}}_b - \boldsymbol{D}_{ab}\dot{\boldsymbol{n}}_b - \boldsymbol{K}_{ab}\boldsymbol{n}_b - \boldsymbol{E}_a^T\boldsymbol{g}, \tag{4.55}$$

where $\boldsymbol{M}_{aa}$ *and* $\boldsymbol{M}_{ab}$ *are mass matrices.* $\boldsymbol{D}_{aa}$ *and* $\boldsymbol{D}_{ab}$ *are damping matrices.* $\boldsymbol{K}_{aa}$ *and* $\boldsymbol{K}_{ab}$ *are stiffness matrices.* $\boldsymbol{f}_{ex}$ *is external forces on the structure nodes, and* $\boldsymbol{g}$ *is gravity vector, which satisfy:*

$$\boldsymbol{M}_{aa} = \boldsymbol{E}_a^T\boldsymbol{M}\boldsymbol{E}_a,\ \boldsymbol{M}_{ab} = \boldsymbol{E}_a^T\boldsymbol{M}\boldsymbol{E}_b, \tag{4.56}$$

$$\boldsymbol{D}_{aa} = \boldsymbol{E}_a^T\boldsymbol{D}\boldsymbol{E}_a,\ \boldsymbol{D}_{ab} = \boldsymbol{E}_a^T\boldsymbol{D}\boldsymbol{E}_b, \tag{4.57}$$

$$\boldsymbol{K}_{aa} = \boldsymbol{E}_a^T\boldsymbol{K}\boldsymbol{E}_a,\ \boldsymbol{K}_{ab} = \boldsymbol{E}_a^T\boldsymbol{K}\boldsymbol{E}_b, \tag{4.58}$$

and $\boldsymbol{M}$*,* $\boldsymbol{D}$*,* $\boldsymbol{K}$*, and* $\boldsymbol{g}$ *are given in Eqs. (4.34), (4.62), (4.46), and (4.50).*

Proof. If the tensegrity structure has boundary constraints, the degree of freedom reduces to n_a, thus the free nodal coordinate vector $\boldsymbol{n}_a$ is the generalized coordinate. Then, the Lagrange's

equation is:

$$\frac{\mathrm{d}}{\mathrm{dt}}\left(\frac{\partial L}{\partial \dot{\boldsymbol{n}}_a}\right) - \frac{\partial L}{\partial \boldsymbol{n}_a} = \boldsymbol{f}_{npa}, \tag{4.59}$$

where $L = T - V$ is the Lagrangian function, and T and V are the kinetic energy and potential energy of the system, $\boldsymbol{f}_{npa}$ is the non-potential force exerted on free nodal coordinate, and its relation with $\boldsymbol{f}_{np}$ is:

$$\boldsymbol{f}_{npa} = \boldsymbol{E}_a^T \boldsymbol{f}_{np}, \tag{4.60}$$

where $\boldsymbol{f}_{np}$ is the non-potential force vector on the nodes of the tensegrity structures in our derivation.

The non-potential force $\boldsymbol{f}_{np}$ is the sum of damping force $\boldsymbol{f}_d$ and external force $\boldsymbol{f}_{ex}$:

$$\boldsymbol{f}_{np} = \boldsymbol{f}_d + \boldsymbol{f}_{ex}. \tag{4.61}$$

The damping force is assumed to be linear in terms of $\dot{n}$ as:

$$\boldsymbol{f}_d = -\boldsymbol{D}\dot{\boldsymbol{n}}, \tag{4.62}$$

where $\boldsymbol{D} \in \mathbb{R}^{3n_n \times 3n_n}$ is the damping matrix of the structure.

The potential energy of the whole structure is the sum of strain energy V_e and gravitational potential energy V_g:

$$V = V_e + V_g. \tag{4.63}$$

Then, the Lagrangian's function can be written as:

$$L = T - (V_e + V_g). \tag{4.64}$$

The left hand side of Eq. (4.59) is:

$$\frac{\mathrm{d}}{\mathrm{dt}}\left(\frac{\partial L}{\partial \dot{\boldsymbol{n}}_a}\right)-\frac{\partial L}{\partial \boldsymbol{n}_a}=\frac{\partial \boldsymbol{n}}{\partial \boldsymbol{n}_a}\left[\frac{\mathrm{d}}{\mathrm{dt}}\left(\frac{\partial L}{\partial \dot{\boldsymbol{n}}}\right)-\frac{\partial L}{\partial \boldsymbol{n}}\right] \tag{4.65}$$

$$=\boldsymbol{E}_a^T\left[\frac{\mathrm{d}}{\mathrm{dt}}\left(\frac{\partial L}{\partial \dot{\boldsymbol{n}}}\right)-\frac{\partial L}{\partial \boldsymbol{n}}\right]. \tag{4.66}$$

Substitute Eqs. (4.60), (4.66) into Eq. (4.59), we have the dynamics of tensegrity for the free nodal coordinates:

$$\boldsymbol{E}_a^T(\boldsymbol{M}\ddot{\boldsymbol{n}}+\boldsymbol{D}\dot{\boldsymbol{n}}+\boldsymbol{K}\boldsymbol{n})=\boldsymbol{E}_a^T\left(\boldsymbol{f}_{ex}-\boldsymbol{g}\right). \tag{4.67}$$

From the above equation, we can see that the dynamic equation Eq. (4.67) with constraints is just the $\boldsymbol{a}$ rows of Eq. (4.71). Substitute Eq. (4.53) into Eq. (4.67) and arrange terms related to $\boldsymbol{n}_a$ in left side, we obtain Eq. (4.55). We can also have the following form in term of $\ddot{\boldsymbol{n}}_a$ for programming convenience:

$$\ddot{\boldsymbol{n}}_a=\boldsymbol{M}_{aa}^{-1}\boldsymbol{E}_a^T\left(\boldsymbol{f}_{ex}-\boldsymbol{g}-\boldsymbol{M}\boldsymbol{E}_b\ddot{\boldsymbol{n}}_b-\boldsymbol{D}\dot{\boldsymbol{n}}-\boldsymbol{K}\boldsymbol{n}\right). \tag{4.68}$$

For dynamics without constraints, all the structure nodes are free nodes. We have $n_a = n_n$, $\boldsymbol{E}_a \in \mathbb{R}^{3n_n \times n_a} = \mathbf{I}_{3n_n}$, and Eqs. (4.67) and (4.68) reduce into:

$$\boldsymbol{M}\ddot{\boldsymbol{n}}+\boldsymbol{D}\dot{\boldsymbol{n}}+\boldsymbol{K}\boldsymbol{n}=\boldsymbol{f}_{np}-\boldsymbol{g}, \tag{4.69}$$

$$\ddot{\boldsymbol{n}}=\boldsymbol{M}^{-1}\left(\boldsymbol{f}_{ex}-\boldsymbol{g}-\boldsymbol{D}\dot{\boldsymbol{n}}-\boldsymbol{K}\boldsymbol{n}\right). \tag{4.70}$$

□

Thus, with Eq. (4.69) and Theorem 4.3.1, we have the following theorem for nonlinear tensegrity dynamics without constraints:

Theorem 4.3.2. *The finite element formulation for nonlinear tensegrity dynamics in the presence*

of gravity is given by:

$$\boldsymbol{M}\ddot{\boldsymbol{n}} + \boldsymbol{D}\dot{\boldsymbol{n}} + \boldsymbol{K}\boldsymbol{n} = \boldsymbol{f}_{ex} - \boldsymbol{g}, \tag{4.71}$$

where $\boldsymbol{M}$, $\boldsymbol{D}$, and $\boldsymbol{K}$ are mass, damping, and stiffness matrices given in Eqs. (4.34), (4.62), and (4.46), f_{ex} is external forces on the structure nodes, and $\boldsymbol{g}$ is gravity vector show in Eq. (4.50).

Since we have derived the dynamics, we want to discuss a little bit more about statics, which can be easily obtained by substitute acceleration and velocity terms to zero ($\ddot{\boldsymbol{n}} = \dot{\boldsymbol{n}} = 0$). Here, we give the equilibrium equation in three standard forms in terms of nodal vector, force density vector, and force vector as the following theorem.

Theorem 4.3.3. *The three following tensegrity static equilibrium equations are equivalent:*

1). Tensegrity statics in terms of nodal coordinate vector $\boldsymbol{n}$:

$$\boldsymbol{E}_a^T\boldsymbol{K}\boldsymbol{n} = \boldsymbol{E}_a^T(\boldsymbol{f}_{ex} - \boldsymbol{g}),\ \boldsymbol{K} = (\boldsymbol{C}^T\hat{\boldsymbol{x}}\boldsymbol{C}) \otimes \boldsymbol{I}_3. \tag{4.72}$$

2). Tensegrity statics in terms of force density vector $\boldsymbol{x}$:

$$\boldsymbol{E}_a^T\boldsymbol{A}_1\boldsymbol{x} = \boldsymbol{E}_a^T(\boldsymbol{f}_{ex} - \boldsymbol{g}),\ \boldsymbol{A}_1 = \left(\boldsymbol{C}^T \otimes \boldsymbol{I}_3\right)\boldsymbol{b.d.}(\boldsymbol{H}). \tag{4.73}$$

3). Tensegrity statics in terms of force vector $\boldsymbol{t}$:

$$\boldsymbol{E}_a^T\boldsymbol{A}_2\boldsymbol{t} = \boldsymbol{E}_a^T(\boldsymbol{f}_{ex} - \boldsymbol{g}),\ \boldsymbol{A}_2 = \left(\boldsymbol{C}^T \otimes \boldsymbol{I}_3\right)\boldsymbol{b.d.}(\boldsymbol{H})\hat{\boldsymbol{l}}^{-1}. \tag{4.74}$$

Proof. Let the acceleration part $\ddot{\boldsymbol{n}}$ and velocity part $\dot{\boldsymbol{n}}$ in Eq. (4.67) be zeros, the dynamics equation will be reduced into a static equilibrium equation in terms of nodal coordinate vector $\boldsymbol{n}$:

$$\boldsymbol{E}_a^T\boldsymbol{K}\boldsymbol{n} = \boldsymbol{E}_a^T(\boldsymbol{f}_{ex} - \boldsymbol{g}). \tag{4.75}$$

This proofs the first statement of Theorem 4.3.3.

Since $\boldsymbol{K}$, given in Eq. (4.46), is a function of $\boldsymbol{n}$, the product $\boldsymbol{K}\boldsymbol{n}$ is nonlinear in $\boldsymbol{n}$. Eq. (4.75)

is a nonlinear equilibrium equation. However, the term $\boldsymbol{Kn}$ can be also written linearly in terms of force density vector $\boldsymbol{x}$:

$$\boldsymbol{Kn} = \left(\boldsymbol{C}^T \otimes \mathbf{I}_3\right)\left(\widehat{\boldsymbol{x}} \otimes \mathbf{I}_3\right)\left(\boldsymbol{C} \otimes \mathbf{I}_3\right)\boldsymbol{n} \tag{4.76}$$

$$= \left(\boldsymbol{C}^T \otimes \mathbf{I}_3\right)\overbrace{\left(\mathbf{I}_{n_e} \otimes \mathbf{I}_{3,1}\boldsymbol{x}\right)}\left(\boldsymbol{C} \otimes \mathbf{I}_3\right)\boldsymbol{n} \tag{4.77}$$

$$= \left(\boldsymbol{C}^T \otimes \mathbf{I}_3\right)\overbrace{\left(\left(\boldsymbol{C} \otimes \mathbf{I}_3\right)\boldsymbol{n}\right)\mathbf{I}_{n_e} \otimes \mathbf{I}_{3,1}}\boldsymbol{x} \tag{4.78}$$

$$= \left(\boldsymbol{C}^T \otimes \mathbf{I}_3\right)\boldsymbol{b.d.}(\boldsymbol{H})\boldsymbol{x}. \tag{4.79}$$

Substitute Eq. (4.79) into Eq. (4.75), we have a linear form of equilibrium equation:

$$\boldsymbol{E}_a^T\boldsymbol{A}_1\boldsymbol{x} = \boldsymbol{E}_a^T(\boldsymbol{f}_{ex} - \boldsymbol{g}), \tag{4.80}$$

where $\boldsymbol{A}_1 \in \mathbb{R}^{3n_n \times n_e}$ is the equilibrium matrix with force density $\boldsymbol{x}$ as variable:

$$\boldsymbol{A}_1 = \left(\boldsymbol{C}^T \otimes \mathbf{I}_3\right)\boldsymbol{b.d.}(\boldsymbol{H}), \tag{4.81}$$

where $\boldsymbol{b.d.}(V)$ is the block diagonal matrix of V. This proofs the first and second statements of Theorem 4.3.3 are equivalent.

The equilibrium equation can also be written linearly in terms of force vector $\boldsymbol{t}$ by substitute Eq. (4.21) into Eq. (4.80):

$$\boldsymbol{E}_a^T\boldsymbol{A}_2\boldsymbol{t} = \boldsymbol{E}_a^T(\boldsymbol{f}_{ex} - \boldsymbol{g}), \tag{4.82}$$

where $\boldsymbol{A}_2 \in \mathbb{R}^{3n_n \times n_e}$ is the equilibrium matrix with force vector $\boldsymbol{t}$ as variable:

$$\boldsymbol{A}_2 = \boldsymbol{A}_1 \hat{\boldsymbol{l}}^{-1} = \left(\boldsymbol{C}^T \otimes \mathbf{I}_3\right) \boldsymbol{b.d.}(\boldsymbol{H}) \hat{\boldsymbol{l}}^{-1}. \tag{4.83}$$

This proves the second and third statements of Theorem 4.3.3 are equivalent. □

Similarly, for statics without constraints, we have $n_a = n_n$, $\boldsymbol{E}_a \in \mathbb{R}^{3n_n \times n_a} = \mathbf{I}_{3n_n}$, and Eqs. (4.75), (4.80), and (4.82) reduce into:

$$\boldsymbol{K}\boldsymbol{n} = \boldsymbol{f}_{ex} - \boldsymbol{g},\ \boldsymbol{A}_1\boldsymbol{x} = \boldsymbol{f}_{ex} - \boldsymbol{g},\ \boldsymbol{A}_2\boldsymbol{t} = \boldsymbol{f}_{ex} - \boldsymbol{g}. \tag{4.84}$$

4.4 Linearized Tensegrity Dynamics and Modal Analysis

4.4.1 Linearized Tensegrity Dynamics

Theorem 4.4.1. *The finite element linearized tensegrity dynamics with constraints has the following two equivalent analytical forms:*

$$\boldsymbol{E}_a^T(\boldsymbol{M}\mathrm{d}\ddot{\boldsymbol{n}} + \boldsymbol{D}\mathrm{d}\dot{\boldsymbol{n}} + \boldsymbol{K}_T\mathrm{d}\boldsymbol{n}) = \boldsymbol{E}_a^T\mathrm{d}\boldsymbol{f}_{ex}, \tag{4.85}$$

$$\boldsymbol{M}_{aa}\mathrm{d}\ddot{\boldsymbol{n}}_a + \boldsymbol{D}_{aa}\mathrm{d}\dot{\boldsymbol{n}}_a + \boldsymbol{K}_{Taa}\mathrm{d}\boldsymbol{n}_a = \boldsymbol{E}_a^T\mathrm{d}\boldsymbol{f}_{ex} - \boldsymbol{M}_{ab}\mathrm{d}\ddot{\boldsymbol{n}}_b - \boldsymbol{D}_{ab}\mathrm{d}\dot{\boldsymbol{n}}_b - \boldsymbol{K}_{Tab}\mathrm{d}\boldsymbol{n}_b, \tag{4.86}$$

where the tangent stiffness matrix $\boldsymbol{K}_{T_{aa}}$,$\boldsymbol{K}_{T_{ab}}$ is:

$$\boldsymbol{K}_{Taa} = \boldsymbol{E}_a^T\boldsymbol{K}_T\boldsymbol{E}_a,\ \boldsymbol{K}_{Tab} = \boldsymbol{E}_a^T\boldsymbol{K}_T\boldsymbol{E}_b, \tag{4.87}$$

$$\boldsymbol{K}_T = \left(\boldsymbol{C}^T\widehat{\boldsymbol{x}}\boldsymbol{C}\right) \otimes \boldsymbol{I}_3 + \boldsymbol{A}_1\widehat{\boldsymbol{E}_t}\widehat{\boldsymbol{A}}\hat{\boldsymbol{l}}^{-3}\boldsymbol{A}_1^T, \tag{4.88}$$

$\boldsymbol{M}_{aa}$, $\boldsymbol{M}_{ab}$, $\boldsymbol{D}_{aa}$, $\boldsymbol{D}_{ab}$ are given in Eqs. (4.56) - (4.58).

Proof. Since the stiffness matrix $\boldsymbol{K}$ is a function of nodal coordinate vector $\boldsymbol{n}$, the dynamics Eq. (4.71) is nonlinear. The mass matrix $\boldsymbol{M}$ and damping matrix $\boldsymbol{D}$ are constant. To linearize the dynamic equation considering constraints, we can take the total derivative of Eq. (4.67) and keep

the linear terms:

$$\boldsymbol{E}_a^T(\boldsymbol{M}\mathrm{d}\ddot{\boldsymbol{n}} + \boldsymbol{D}\mathrm{d}\dot{\boldsymbol{n}} + \boldsymbol{K}_T\mathrm{d}\boldsymbol{n}) = \boldsymbol{E}_a^T\mathrm{d}\boldsymbol{f}_{ex}. \tag{4.89}$$

The tangent stiffness matrix $\boldsymbol{K}_T$ can be calculated as:

$$\boldsymbol{K}_T = \left[\frac{\partial(\boldsymbol{K}\boldsymbol{n})}{\partial \boldsymbol{n}}\right]^T = \boldsymbol{K} + \left[\frac{\partial \boldsymbol{x}}{\partial \boldsymbol{n}}\frac{\partial(\boldsymbol{K}\boldsymbol{n})}{\partial \boldsymbol{x}}\right]^T. \tag{4.90}$$

The partial derivative of force density vector $\boldsymbol{x}$ to nodal coordinate vector $\boldsymbol{n}$ can be obtained from Eq. (4.21):

$$\frac{\partial \boldsymbol{x}}{\partial \boldsymbol{n}} = \frac{\partial\left[\widehat{\boldsymbol{E}_t}\widehat{\boldsymbol{A}}\left(\boldsymbol{l}_0^{-1} - \boldsymbol{l}^{-1}\right)\right]}{\partial \boldsymbol{n}} \tag{4.91}$$

$$= \frac{\partial \boldsymbol{l}}{\partial \boldsymbol{n}}\frac{\partial\left(-\boldsymbol{l}^{-1}\right)}{\partial \boldsymbol{l}}\widehat{\boldsymbol{A}}\widehat{\boldsymbol{E}_t} \tag{4.92}$$

$$= \boldsymbol{B}_l^T\hat{\boldsymbol{l}}^{-2}\widehat{\boldsymbol{A}}\widehat{\boldsymbol{E}_t} \tag{4.93}$$

$$= \boldsymbol{A}_1\hat{\boldsymbol{l}}^{-3}\widehat{\boldsymbol{A}}\widehat{\boldsymbol{E}_t}. \tag{4.94}$$

The derivative of $\boldsymbol{K}\boldsymbol{n}$ with respect to force density $\boldsymbol{x}$ is derived from Eq. (4.81), then we have:

$$\frac{\partial(\boldsymbol{K}\boldsymbol{n})}{\partial \boldsymbol{x}} = \frac{\partial\left(\boldsymbol{A}_1\boldsymbol{x}\right)}{\partial \boldsymbol{x}} = \boldsymbol{A}_1^T. \tag{4.95}$$

Substitute Eqs. (4.94) and (4.95) into Eq. (4.90), one can obtain the tangent stiffness matrix $\boldsymbol{K}_T$:

$$\boldsymbol{K}_T = \left(\boldsymbol{C}^T\widehat{\boldsymbol{x}}\boldsymbol{C}\right)\otimes\mathbf{I}_3 + \boldsymbol{A}_1\widehat{\boldsymbol{E}_t}\widehat{\boldsymbol{A}}\hat{\boldsymbol{l}}^{-3}\boldsymbol{A}_1^T. \tag{4.96}$$

The first part of Eq. (4.96) is usually called the geometry stiffness matrix $\boldsymbol{K}_G = \left(\boldsymbol{C}^T\widehat{\boldsymbol{x}}\boldsymbol{C}\right)\otimes\mathbf{I}_3$, which is determined by structure topology and force density. The second part is called the material stiffness $\boldsymbol{K}_E = \boldsymbol{A}_1\widehat{\boldsymbol{E}_t}\widehat{\boldsymbol{A}}\hat{\boldsymbol{l}}^{-3}\boldsymbol{A}_1^T$, which is governed by structure configuration and elements' axial stiffness.

Substitute Eq.(4.53) into Eq. (4.89), we have:

$$\boldsymbol{M}_{aa}\mathrm{d}\ddot{\boldsymbol{n}}_a + \boldsymbol{D}_{aa}\mathrm{d}\dot{\boldsymbol{n}}_a + \boldsymbol{K}_{Taa}\mathrm{d}\boldsymbol{n}_a = \boldsymbol{E}_a^T\mathrm{d}\boldsymbol{f}_{ex} - \boldsymbol{M}_{ab}\mathrm{d}\ddot{\boldsymbol{n}}_b - \boldsymbol{D}_{ab}\mathrm{d}\dot{\boldsymbol{n}}_b - \boldsymbol{K}_{Tab}\mathrm{d}\boldsymbol{n}_b, \tag{4.97}$$

in which $\boldsymbol{K}_{Taa}$ and $\boldsymbol{K}_{Tab}$ are given by:

$$\boldsymbol{K}_{Taa} = \boldsymbol{E}_a^T\boldsymbol{K}_T\boldsymbol{E}_a,\ \boldsymbol{K}_{Tab} = \boldsymbol{E}_a^T\boldsymbol{K}_T\boldsymbol{E}_b. \tag{4.98}$$

□

The linearized dynamics equation can also be written into a standard state space form:

$$\begin{aligned}\frac{\mathrm{d}}{\mathrm{d}t}\begin{bmatrix}\mathrm{d}\boldsymbol{n}_a\\ \mathrm{d}\dot{\boldsymbol{n}}_a\end{bmatrix} &= \begin{bmatrix}\mathbf{0} & \mathbf{I}\\ -\boldsymbol{M}_{aa}^{-1}K_{Taa} & -\boldsymbol{M}_{aa}^{-1}\boldsymbol{D}_{aa}\end{bmatrix}\begin{bmatrix}\mathrm{d}\boldsymbol{n}_a\\ \mathrm{d}\dot{\boldsymbol{n}}_a\end{bmatrix}\\ &+ \begin{bmatrix}\mathbf{0}\\ \boldsymbol{E}_a^T\mathrm{d}\boldsymbol{f}_{ex} - \boldsymbol{M}_{ab}\mathrm{d}\ddot{\boldsymbol{n}}_b - \boldsymbol{D}_{ab}\mathrm{d}\dot{\boldsymbol{n}}_b - \boldsymbol{K}_{Tab}\mathrm{d}\boldsymbol{n}_b\end{bmatrix},\end{aligned} \tag{4.99}$$

as an interface to integrate structure and control designs.

For dynamics without constraints, all the structure nodes are free nodes. We have $n_a = n_n$, $\boldsymbol{E}_a \in \mathbb{R}^{3n_n\times n_a} = \mathbf{I}_{3n_n}$, and Theorem 4.4.1 can be written as the following statement.

Theorem 4.4.2. *The finite element linearized tensegrity dynamics with no constraints has the following analytical form:*

$$\boldsymbol{M}\mathrm{d}\ddot{\boldsymbol{n}} + \boldsymbol{D}\mathrm{d}\dot{\boldsymbol{n}} + \boldsymbol{K}_T\mathrm{d}\boldsymbol{n} = \mathrm{d}\boldsymbol{f}_{ex}, \tag{4.100}$$

where the tangent stiffness matrix $\boldsymbol{K}_T$ satisfies:

$$\boldsymbol{K}_T = \left(\boldsymbol{C}^T\widehat{\boldsymbol{x}}\boldsymbol{C}\right)\otimes\boldsymbol{I}_3 + \boldsymbol{A}_1\widehat{\boldsymbol{E}_t}\widehat{\boldsymbol{A}}\hat{\boldsymbol{l}}^{-3}\boldsymbol{A}_1^T, \tag{4.101}$$

and $\boldsymbol{M}$ is given in Eq. (4.34), D is damping matrix, and f_{ex} is external forces on the structure

nodes.

Similarly, one can write the linearized dynamics equation with constraints into a state space form:

$$\frac{\mathrm{d}}{\mathrm{d}t}\begin{bmatrix}\mathrm{d}\boldsymbol{n}\\ \mathrm{d}\dot{\boldsymbol{n}}\end{bmatrix}=\begin{bmatrix}\mathbf{0} & \mathbf{I}\\ -\boldsymbol{M}^{-1}\boldsymbol{K}_T & -\boldsymbol{M}^{-1}\boldsymbol{D}\end{bmatrix}\begin{bmatrix}\mathrm{d}\boldsymbol{n}\\ \mathrm{d}\dot{\boldsymbol{n}}\end{bmatrix}+\begin{bmatrix}\mathbf{0}\\ \mathrm{d}\boldsymbol{f}_{ex}\end{bmatrix}, \tag{4.102}$$

which can be used to integrate structure and control designs.

4.4.2 Modal Analysis of Linearized Model

By setting damping matrix $\boldsymbol{D}=\mathbf{0}$ and external force $\boldsymbol{f}_{ex}=\mathbf{0}$ in Eq. (4.100), the free vibration response can be obtained from Eq. (4.97) by neglecting damping and external force:

$$\boldsymbol{M}_{aa}\mathrm{d}\ddot{\boldsymbol{n}}_a+\boldsymbol{K}_{Taa}\mathrm{d}\boldsymbol{n}_a=\mathbf{0}. \tag{4.103}$$

The solution to the homogeneous Eq. (4.103) have the following form:

$$\mathrm{d}\boldsymbol{n}=\boldsymbol{\varphi}\sin(\omega t-\theta), \tag{4.104}$$

which represents a periodic response with a typical frequency ω. Substitute Eq. (4.104) into Eq. (4.107), we have:

$$\left(\boldsymbol{K}_{Taa}-\omega^2\boldsymbol{M}_{aa}\right)\boldsymbol{\varphi}\sin(\omega t-\theta)=\mathbf{0}, \tag{4.105}$$

and since $\sin(\omega t-\theta)\neq 0$ for most times, we have:

$$\boldsymbol{K}_{Taa}\boldsymbol{\varphi}=\omega^2\boldsymbol{M}_{aa}\boldsymbol{\varphi}, \tag{4.106}$$

which is a standard eigenvalue problem. The ω is known as the natural frequency of the system and $\boldsymbol{\varphi}$ is the corresponding mode.

For dynamics without constraints, all the structure nodes are free nodes. We have $n_a = n_n$, $\boldsymbol{E}_a \in \mathbb{R}^{3n_n \times n_a} = \mathbf{I}_{3n_n}$. Eqs. (4.103) and (4.106) reduces into:

$$\boldsymbol{M}\mathrm{d}\ddot{\boldsymbol{n}} + \boldsymbol{K}_T\mathrm{d}\boldsymbol{n} = \mathbf{0},\ \boldsymbol{K}_T\boldsymbol{\varphi} = \omega^2\boldsymbol{M}\boldsymbol{\varphi}. \tag{4.107}$$

4.5 Numerical Examples

We believe a general dynamics should be capable of conducting these kinds of studies for any tensegrity structures: 1. Rigid body dynamics with acceptable errors (by setting relatively high stiffness for bars in the FEM simulation). 2. Finite element method (FEM) dynamics that allow bars and strings to have elastic or plastic deformations. 3. The dynamics should allow various kinds of boundary conditions, for example, nodes are fixed or in the presence of static or dynamic external forces (i.e., gravitational force, some specified forces, or arbitrary seismic vibrations, etc.). 4. Accurate modal analysis, including natural frequency and corresponding modes.

Thus, three dynamic examples (a double pendulum, a cantilever truss with external force, and seismic analysis of a tensegrity tower) are carefully selected and studied to verify the proposed nonlinear tensegrity FEM dynamics (we call it TsgFEM). The obtained results are compared with other dynamics simulation methods, including analytical results and commercial FEM software ANSYS.

4.5.1 Example 1: Dynamics of A Double Pendulum

Let the mass of the two bars in the double pendulum be $m_1 = m_2 = m$ with a length of $l_1 = l_2 = l$, from geometric properties shown in Figure 4.4, one can write,

$$\mathrm{x}_1 = \frac{l}{2}\sin\theta_1,\ y_1 = -\frac{l}{2}\cos\theta_1, \tag{4.108}$$

$$x_2 = l(\sin\theta_1 + \frac{1}{2}\sin\theta_2), \tag{4.109}$$

$$y_2 = -l(\cos\theta_1 + \frac{1}{2}\cos\theta_2). \tag{4.110}$$

Define $\mathrm{L} = \mathrm{T} - \mathrm{V}$, where T and V are kinetic energy and potential energy of the system, then:

$$\mathrm{L} = \frac{m}{2}\left(\dot{x}_1^2 + \dot{y}_1^2 + \dot{x}_2^2 + \dot{y}_2^2\right) + \frac{1}{2}I\left(\dot{\theta}_1^2 + \dot{\theta}_2^2\right) - mg\left(y_1 + y_2\right), \tag{4.111}$$

where $I = \frac{1}{12}ml^2$ is moment of inertia about the center of mass of the bar. Using Lagrangian method, and $m = 1$ kg and $l = 1$ m, we get:

$$8\ddot{\theta}_1 + 3\ddot{\theta}_2\cos\left(\theta_1 - \theta_2\right) + 3\dot{\theta}_2^2\sin\left(\theta_1 - \theta_2\right) + 9\frac{g}{l}\sin\left(\theta_1\right) = 0, \tag{4.112}$$

$$2\ddot{\theta}_2 + 3\ddot{\theta}_1\cos\left(\theta_1 - \theta_2\right) - 3\dot{\theta}_1^2\sin\left(\theta_1 - \theta_2\right) + 3\frac{g}{l}\sin\left(\theta_2\right) = 0. \tag{4.113}$$

This example is chosen to check if the structure behaves close to rigid body dynamics with an acceptable error if we use high stiffness materials for bars. The time history of nodal positions will be compared with analytical results from rigid body dynamics. The initial configuration of a double pendulum is shown in Figure 4.4, and node 1 is fixed to the wall. The two bars have same length $l = 1$ m, same mass $m = 1$ kg, and same hanging angle $\theta_1 = \theta_2 = 45^\circ$. The cross-sectional area and Young's modulus are $A = 10^{-4}$ m^2 and $E = 2.06 \times 10^{11}$ Pa, respectively. In the analysis of the dynamics, the time step and total simulation time are chosen to be $\Delta t = 5 \times 10^{-5}$ s and $t = 5$ s. There is no damping, and only gravitational force is considered as the external force.

Figure 4.5 shows the time history of nodal position by TsgFEM. Figure 4.6 gives the error of the nodal position between TsgFEM and the analytical solution obtained from rigid body dynamics. Figure 4.7 is the error of bar length between TsgFEM and rigid body dynamics. From these figures, we can see that the error of bar length ($10^{-7} \sim 10^{-6}$ m) and error of nodal coordinates ($10^{-5} \sim 10^{-4}$ m) are relatively small and oscillate periodically with high frequency. This is reasonable because the strain is allowed in TsgFEM, and the high-frequency oscillation is caused by the high axial stiffness of the bar. The TsgFEM can capture the periodic elongation of bars if the time step is properly chosen. In signal processing of Nyquist rate, the sampling frequency should be at least two times of signal frequency, and normally engineers use 5 ~ 10 times, we choose a time step of $\Delta t = \mathrm{T}_{min}/8 = \pi/4\omega_{max}$, where T_{min} is the shortest period corresponding to the

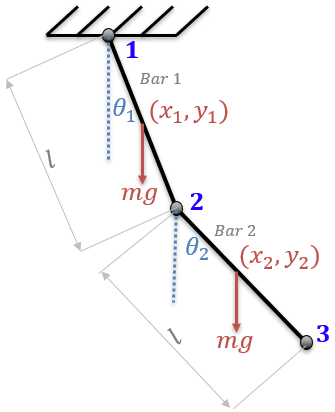

Figure 4.4: Schematic diagram of a double pendulum in the presence of gravity. The two bars have same mass and length.

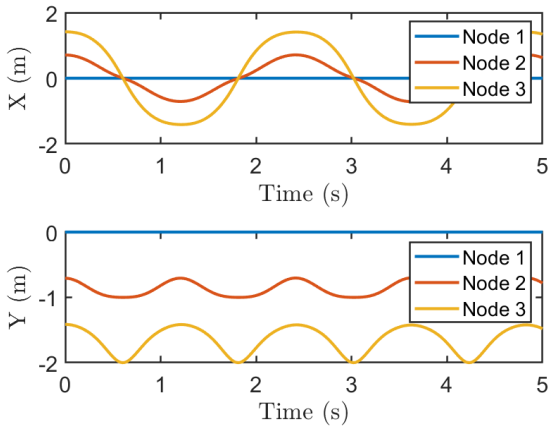

Figure 4.5: X- and Y-coordinate time histories of node 1, 2, and 3 of the double pendulum.

highest natural frequency calculated by Eq. (4.106) to capture the highest vibration mode of the bar as well as guarantee the convergence in solving the dynamics equation.

4.5.2 Example 2: Cantilever Truss in External Force

This example is selected to verify the proposed dynamics method is capable of doing modal analysis as well as conducting time history analysis of structures with linear-elastic, multilinear elastic, and plastic materials. The natural frequency, mode shapes, and time history information of the structure obtained by TsgFEM will be compared with commercial FEM software ANSYS.

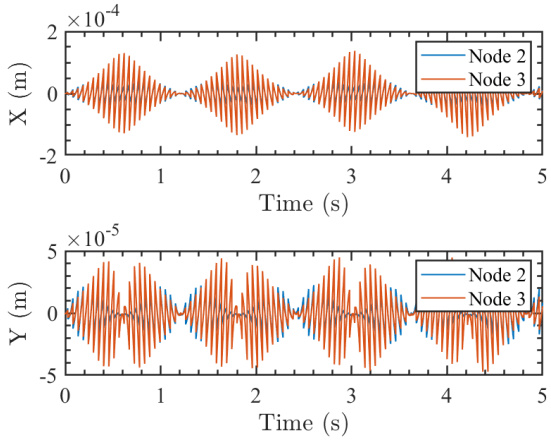

Figure 4.6: X- and Y-coordinate error time histories of node 2 and 3 between the TsgFEM dynamics and rigid body dynamics .

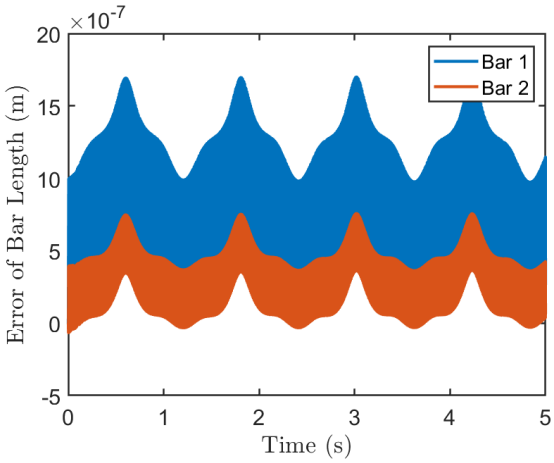

Figure 4.7: Bar length errors of the two bars in the double pendulum by TsgFEM simulation.

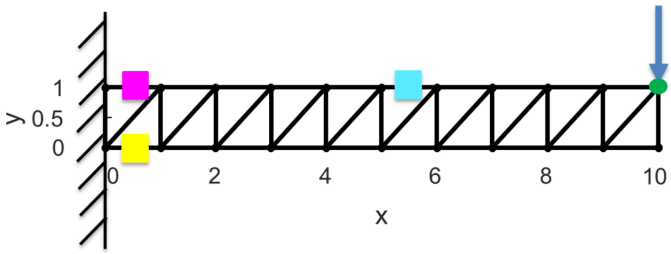

Figure 4.8: Configuration of a planer truss in the presence of a step load P with the left two nodes fixed to a wall in the given direction. The aspect ratio (length over width) of the truss is 10:1. We examine the strain-stress time histories of the purple, yellow, and blue elements marked by square blocks as well the Y-coordinate time history of the green dot.

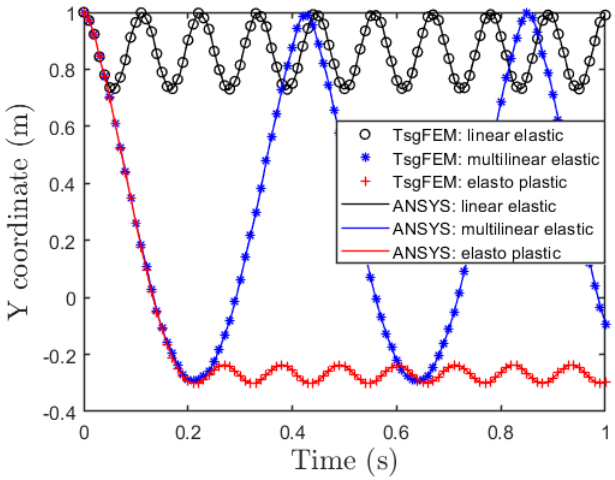

Figure 4.9: The Y-coordinate time history of the green dot in Figure 4.8 by using three kinds of materials: linear elastic, multilinear elastic, and elasto plastic. And a comparison of nodal coordinate time histories between TsgFEM and ANSYS.

Figure 4.8 shows a 10 m $\times$ 1 m planer truss. The left two nodes at the wall are fixed. A step load $P = 1 \times 10^5$ N in the downward direction of the Y-axis is exerted on the green dot at time $t = 0$ s. Cross-section area of each element is A = 0.0025 m^2. Young's modulus of linear elastic material is $E = 2.0604 \times 10^{11}$ Pa. The multilinear elastic material is defined by two points (1.456×10^{-6}, 300 MPa), (2.333×10^{-6}, 435 MPa) in the piece-wise stress-strain curve. The elastoplastic material uses a bi-linear kinematic hardening plasticity model, in which Young's modulus is $E = 2.0604 \times 10^{11}$ Pa, the yield stress is 300 MPa, and the tangent modulus in plastic is $E_t = 6.1799 \times 10^9$ Pa. Damping and gravitational force is not considered in this example. Time step is $\Delta t = 10^{-4}$ s, and total analysis time is $t = 1$ s.

The dynamic response of the Y-coordinate of the green node for different materials and comparison with ANSYS in Figure 4.8 are compared and given in Figure 4.9. In ANSYS, the transient analysis is used with a consistent mass matrix. The average errors of y-coordinate of node H between TsgFeM and ANSYS with linear elastic, multilinear elastic, and elastoplastic material are 0.09%, 0.53%, and 0.06%, respectively. For the three kinds of materials, the stress-strain of the purple, yellow,and blue blocks and corresponding structure deformation in Figure 4.8 at at t = 0.5 s and t

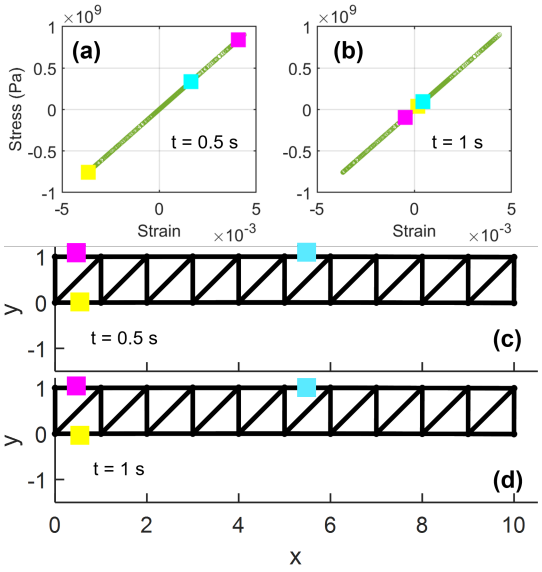

Figure 4.10: For linear elastic material of structure members, (a) and (b) are stress-strain of the purple, yellow, and blue blocks at t = 0.5 s and t = 1 s. (c) and (d) are corresponding structure deformation at t = 0.5 s and t = 1 s.

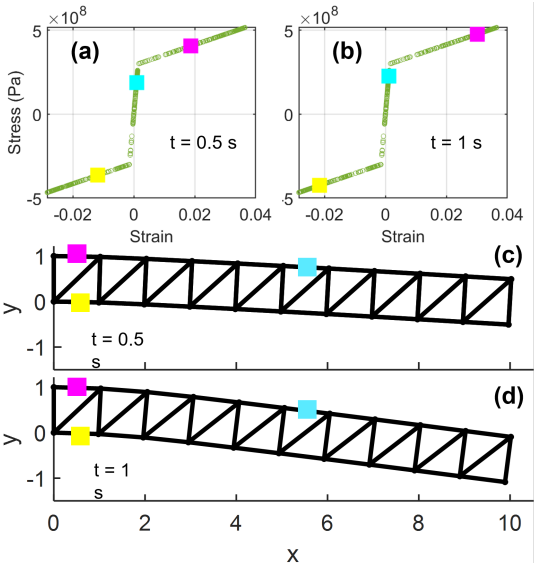

Figure 4.11: For multilinear elastic material of structure members, (a) and (b) are stress-strain of the purple, yellow, and blue blocks at t = 0.5 s and t = 1 s. (c) and (d) are corresponding structure deformation at t = 0.5 s and t = 1 s.

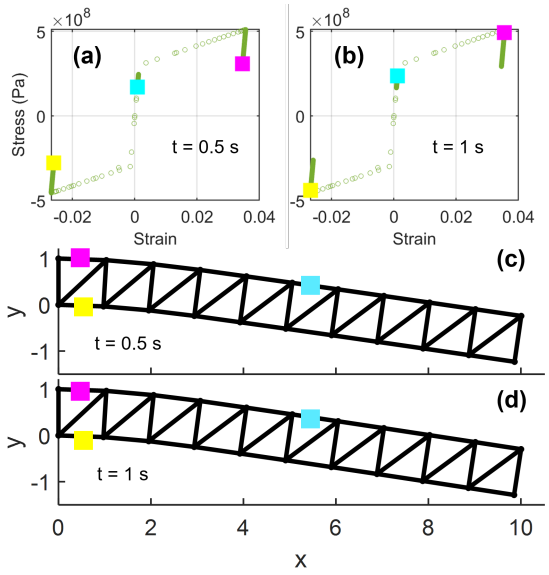

Figure 4.12: For plastic material of structure members, (a) and (b) are stress-strain of the purple, yellow, and blue blocks at t = 0.5 s and t = 1 s. (c) and (d) are corresponding structure deformation at t = 0.5 s and t = 1 s.

= 1 s are given in Figures 4.10-4.12.

The natural frequency and first four modes of the cantilever truss calculated by TsgFEM are compared with ANSYS, as shown in Figures 4.13-4.15. The comparative error of frequency by the two methods is 3.6640×10^{-13}.

4.5.3 Example 3: Seismic Simulation of a Tensegrity Tower

A T_2D_1 tensegrity tower is picked as an example to verify the proposed dynamics approach has the ability to do modal analysis and seismic simulation of tensegrity structures with pinned node constraints. The tensegrity tower is 10 m high, and the angles of the T-Bar and D-Bar units are $\alpha_T = \alpha_D = \frac{\pi}{18}$. The payload on top node of the tower is 60 kg, we use aluminum bars (OD 4"or 101.6 mm, wall thickness 0.035"or 0.889 mm) and UHMWPE strings (OD 4 mm) to build the structure, as shown in Figure 4.16. The Young's modulus, density, and yield strength of the aluminum bars and UHMWPE strings are 60 Gpa, 2,700 kg/m^3, 78 Mpa, and 120 Gpa, 970 kg/m^3, 2.7 Gpa, respectively. Figure 4.17 shows the first four mode shapes of the tensegrity tower obtained by TsgFEM. Figure 4.18 gives all the natural frequencies of the tower. Since the bottom five nodes

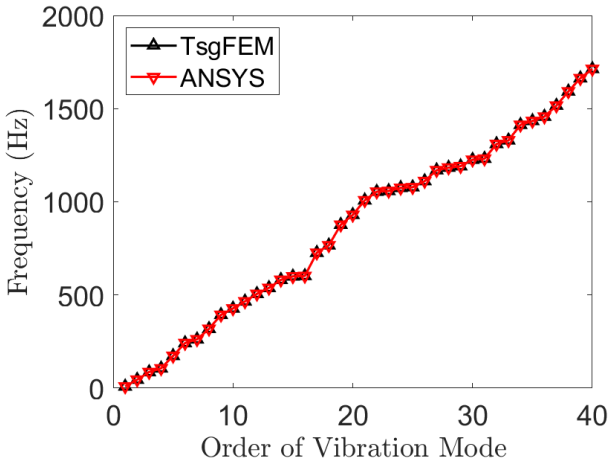

Figure 4.13: Natural frequencies of the planer truss with respect to the order of vibration mode by TsgFEM and ANSYS. Since the left two nodes of the planar truss is fixed, there are 20 free nodes (40 DOF) in the structure. The number of order of vibration modes is 40.

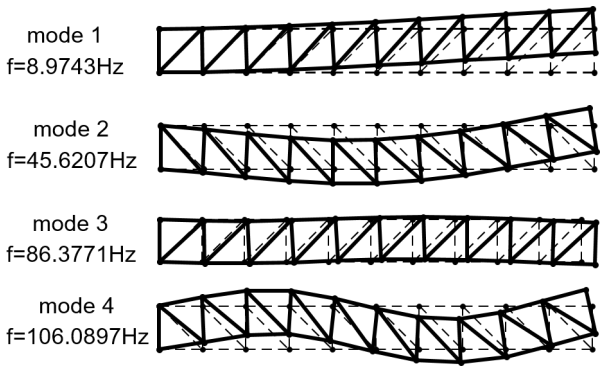

Figure 4.14: The first four mode shapes of the truss obtained by TsgFEM. The solid line sub-figures from top to bottom are: mode 1, f = 8.9734 Hz; mode 2, f = 45.6159 Hz; mode 3, f = 86.3678 Hz; and mode 4, f = 106.0784 Hz. The dotted lines under the solid lines are shapes of the original truss structure.

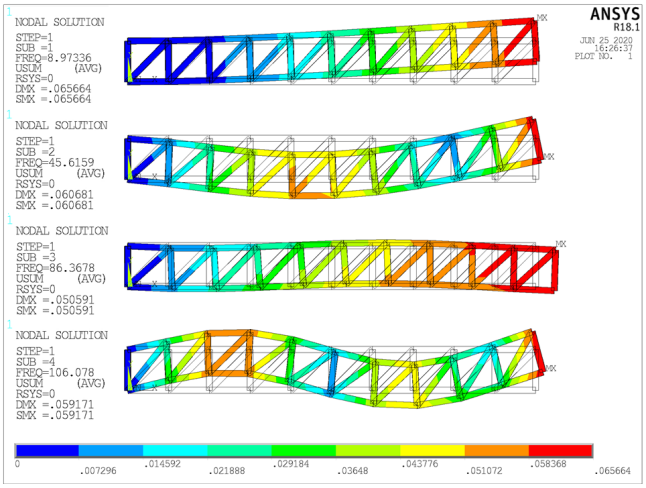

Figure 4.15: The first four mode shapes of the truss obtained by ANSYS. The colorful sub-figures from left to right are: mode 1, f = 8.9734 Hz; mode 2, f = 45.6159 Hz; mode 3, f = 86.3678 Hz; and mode 4, f = 106.0784 Hz. The light grey lines attached with each colorful mode shapes are the original truss structures. One can also see the natural frequencies obtained from ANSYS on the left side of this plot.

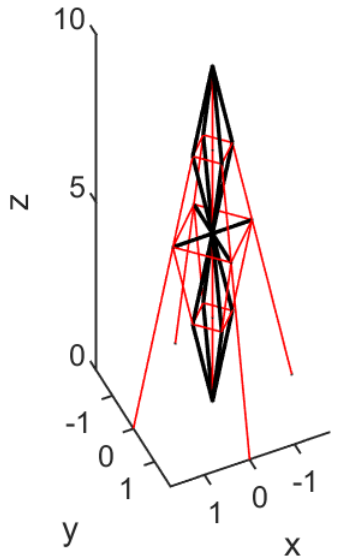

Figure 4.16: Configuration of the 10m tall 3D T_2D_1 tensegrity tower with four sides, the angles of the T-Bar and D-Bar units are $\alpha_T = \alpha_D = \frac{\pi}{18}$. Thus, the bottom base radius of the tower is $10 \times \tan(\frac{\pi}{18})$ = 1.7633 m.

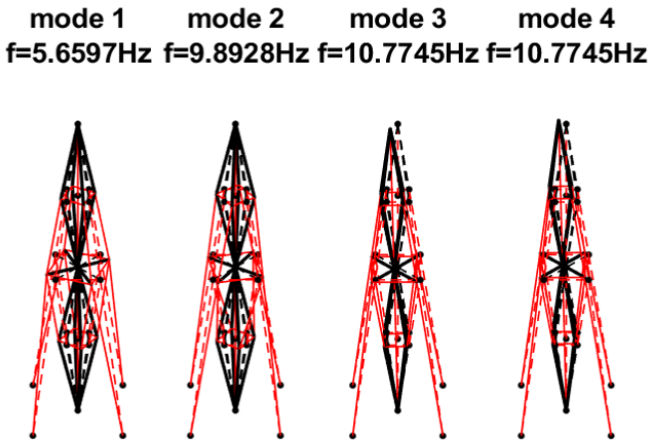

Figure 4.17: The first four mode shapes of the tensegrity tower obtained by TsgFEM. The solid line sub-figures from left to right are: mode 1, f = 5.6597 Hz; mode 2, f = 9.8929 Hz; mode 3, f = 10.7745 Hz; and mode 4, f = 10.7745 Hz. The dotted lines under the solid lines are shapes of the original tower structure.

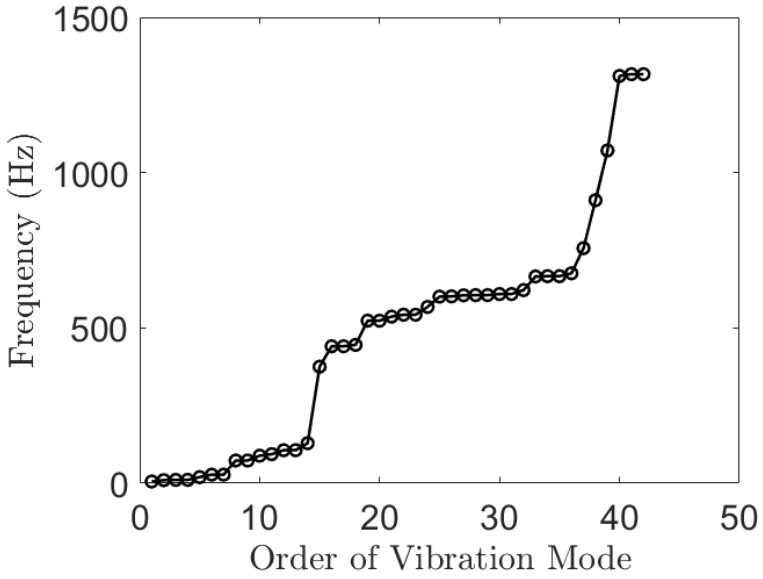

Figure 4.18: Natural frequencies of the tower with respect to the order of vibration mode by TsgFEM. Since the bottom five nodes of the tower is fixed, there are 14 free nodes (42 DOF) in the structure. The number of order of vibration modes is 42.

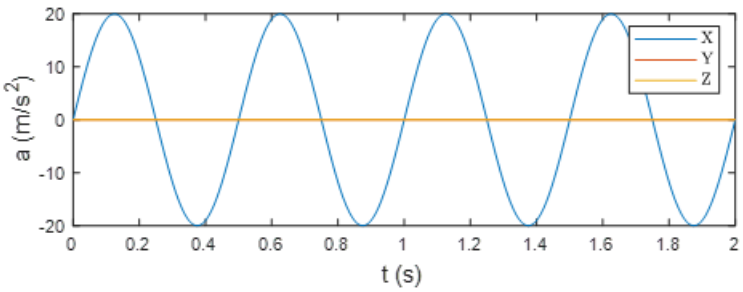

Figure 4.19: Earthquake signal which is the acceleration time history of the free nodes in X-direction, with an amplitude of 20 m/s^2 and 2 Hz frequency.

of the tower on the ground are fixed, there are 13 free nodes. Each free node has 3 DOF, the overall structure has 42 DOF.

To simulate the seismic dynamics, we give a sine wave acceleration signal in X-direction to all the 13 free nodes of the tower. $\ddot{x} = 20\sin(2\pi f_s t)$, where f_s is frequency of the seismic wave. To stabilize the tower, one also needs to prestress the strings to achieve certain stiffness of the tower. We assign the force densities in the bars and compute all the string force densities by the static equilibrium equation. Since the structure is axially symmetric, the force densities in the four bars at the same height (we call it a 4-bar group, in this tower, there are five 4-bar groups) should have the same force densities. That is, force densities in the five 4-bar groups from top to bottom are 4,900 N, 4,900 N, 490 N, 9,800 N, and 4,900 N. We simulate two cases to demonstrate the seismic analysis, f_s = 2 Hz and f_s = 10.7745 Hz, the seismic signals are shown in Figure 4.19 and Figure 4.20, the total simulation time is 2s, damping matrix D = 0, and the time step is 0.001s. The corresponding dynamic response of the top node is shown in Figure 4.21 and Figure 4.22. As we can see for f_s = 2 Hz, we can see the maximum vibration value of the top node in the X-direction is 7.5mm. However, for f_s = 10.7745 Hz, the vibration of the top node in x-direction begins to diverge (vibration of the top node goes up to 0.44 m in 2s). The physical meaning is that the seismic signal triggers the 3rd vibration mode of the tower since the frequency of the seismic signal and the 3rd mode frequency is the same.

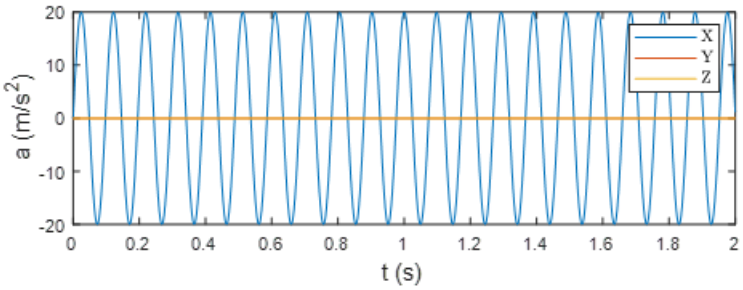

Figure 4.20: Earthquake signal which is the acceleration time history of the free nodes in X-direction, with an amplitude of 20 m/s^2 and 10.7745 Hz frequency.

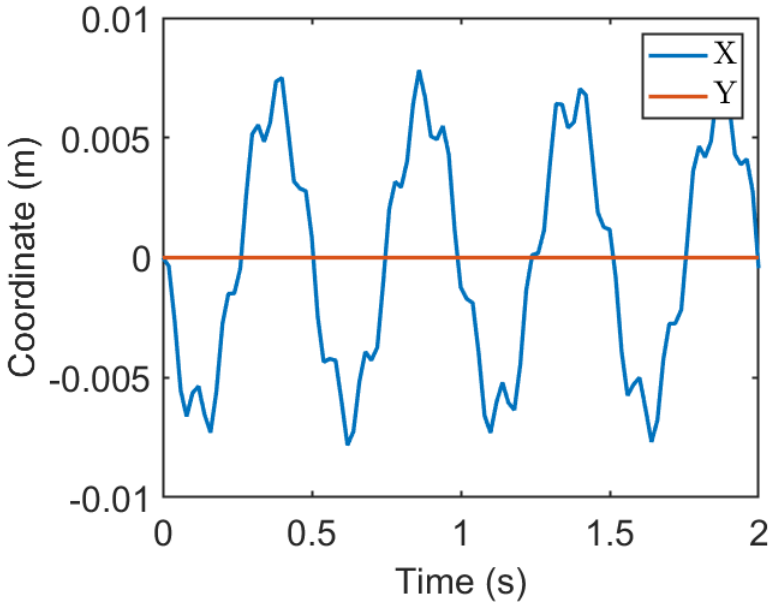

Figure 4.21: Time history of the top node of the tower in X- and Y-direction for the $f_s = 2$ Hz earthquake signal case.

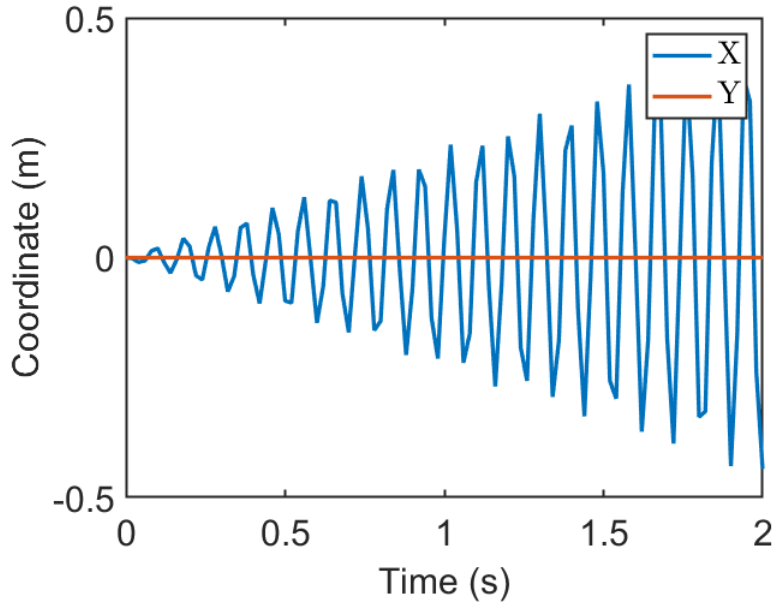

Figure 4.22: Time history of the top node of the tower in X- and Y-direction for the $f_s = 10.7745$ Hz earthquake signal case.

4.6 Conclusion

A finite element analysis approach to nonlinear tensegrity dynamics based on the Lagrangian method with a nodal coordinate vector as the variable is given in this chapter. This approach allows one to conduct comprehensive studies on any tensegrity systems with any node constraints and various load conditions (i.e., gravitational force, some specified forces, and arbitrary seismic vibrations). Results show that this method is very accurate compared with analytical solutions of rigid body dynamics and FEM software ANSYS. For example, in the double pendulum simulation, the bar length error is $10^{-7} \sim 10^{-6}$ m. In the truss example, comparative frequency errors are 3.6640×10^{-13}, the average comparative error of node coordinates in the linear elastic, multilinear elastic, and elastoplastic material simulation is 0.09%, 0.53%, and 0.06% compared with ANSYS. In the seismic simulation, for $f_s = 2$ Hz seismic signal in X-direction, the vibration of the top node of the 10 m high tensegrity T_2D_1 tower is 7.5 mm. However, for $f_s = 10.7745$ Hz seismic signal in X-direction, it triggers the 3$^{\text{rd}}$ vibration mode of the tower (vibration of the top node goes up to 0.44 m in 2s), which agrees well with physics. The accurate linearized model in the state space form

can be an interface to integrate other disciplines, such as control and signal processing. This study paves a way to perform accurate tensegrity simulations as well as comprehensive understandings of the performance of both structures and materials.

5. INTEGRATING STRUCTURE AND CONTROL DESIGN: THE SHAPE CONTROL OF TENSEGRITY STRUCTURES*

In this chapter, a general control approach for tensegrity structures is presented. The approach is demonstrated by the design and control of morphing airfoils. Firstly, based on reduced order Class-k tensegrity dynamics, a shape control law for tensegrity systems is derived. A morphing tensegrity airfoil example is given to demonstrate successful shape control. This work paves a road towards integrating structure and control design, the principles developed here can also be used for 3D morphing airfoil design and control of various kinds of tensegrity structures.

5.1 Introduction

The Wright Brothers made the first sustainable, controllable, powered, heavier than air manned flight in 1903. The fundamental breakthrough was their invention of a three-axis control method for improving fly control stability of the wing box structure by morphing the shape of the wing during flight [108].

Morphing airfoil is gaining significant attention by researchers with the thriving prosperity of the aerospace industry. Compared to a fixed-wing, a flexible profile is more adjustable to various flight conditions. The fundamental concept of achieving certain aerodynamic performance by means of changing the shape of a wing motivates us to solve the following problems: find an efficient airfoil structure and control laws to adjust various flight regimes. The existing morphing technologies (wing slats, flaps, spoiler, aileron, winglet, and trims) can achieve some desired performance. And many researchers have pointed out the challenges of this area. Sofla [109], Lachenal [110], Kuribayashi [111], and Liu [90] summarized shape morphing status and challenges, mainly focusing on the direction of shape memory alloys (SMA), piezoelectric actuators (PZT), shape memory polymers (SMP), and stimulus-responsive polymers (SRP). Valasek [112], Barbarino

*Part of this chapter is reprinted with permission from "Design and control of tensegrity morphing airfoils" by Muhao Chen, Jiacheng Liu, and Robert E. Skelton, 2020. Mechanics Research Communications, Volume 103, 103480, Copyright [2020] by Elsevier Ltd.

[113], and Reich [114] addressed important issues on morphing aircraft, bio-inspiration, smart structures, power requirements and smart actuators. Santer showed load-path-based topology optimization for adaptive wing structures [115, 116]. However, few of them start with a system point of view to solve the structure and control problem in an integrative manner. This study presents our system which integrates structure and control designs using a novel tensegrity morphing airfoil.

The conceptual design and physical model of the tensegrity wing are presented in the book Tensegrity System by Skelton and Mauricio 2009, which was a DARPA sponsored *smart structures* research program. The design in their book is a light weight fixed wing, composed of 2D airfoil solid pieces connected with tensegrity T-Bar topology [39]. Henrickson et al. [117] presents a 2D cross-bar topology airfoil (a class-1 tensegrity structure) design and demonstrate the morphing ability. These design shows the tensegrity system brings more functionalities to wing design such as minimum mass, deployability, and shape control. In a similar way to a bird's wing, the strings in the tensegrity wing are functioning as muscles to warp the whole wing to achieve various aerodynamic performance requirements. Some researchers have discussed their ideas in morphing wing design, for example, Moored studies the deflection [118] and shape optimization [119] of the wing in span-wise direction by tensegrity beams and plates, Jones shows his idea in fuzzy control strategy for morphing [120]. James presented a control theory to formulate computationally feasible procedures for aerodynamic design [121]. However, we argue that control design after wing design destroys the flying efficiency that is so carefully treated in the structure design in the first place [39]. Instead of using control systems to push the structure away from its equilibrium, we propose to simply modify the equilibrium of tensegrity structures to achieve the new desired shape with little control effort. As feedback, less control power also exerts less stress on structural components to accomplish the same objectives. Thus, the best performance cannot be achieved by separating structure and control designs. This chapter starts from airfoil shape discretization methods, presents a practical airfoil topology design, and a nonlinear control law for any Class-k structures.

This chapter is structured as follows: Section 5.2 introduces tensegrity principles, nonlinear Class-k dynamics, reduced-order form, and nonlinear shape control laws. Section 5.3 gives a case study and results of an tensegrity airfoil. Section 5.4 presents the conclusions.

5.2 Tensegrity Dynamics and Control

5.2.1 Class-k Tensegrity Dynamics

The accurate quantitative knowledge of structural behavior should be given in a simple, compact form. Tensegrity dynamics were first analytically studied by Motro, Najari, and Jouanna in 1987 [122], since then many kinds of research followed. Skelton et al. (2001) introduced a non-minimal coordinates method without using the conventional angular velocities for rigid bodies [123] simplified the math a lot. Recent work by Goyal et al. give a complete description of tensegrity dynamics by including string mass, class-k bar-length correction, and analytic solutions of Lagrange multiplier Ω [83]:

$$\ddot{N}M_s + NK_s = W + \Omega P^T, \tag{5.1}$$

$$M_s = \begin{bmatrix} C_{nb}^T(C_b^T \hat{J} C_b + C_r^T \hat{m}_b C_r) & C_{ns}^T \hat{m}_s \end{bmatrix}, \tag{5.2}$$

$$K_s = \begin{bmatrix} C_s^T \hat{\gamma} C_{sb} - C_{nb}^T C_b^T \hat{\lambda} C_b & C_s^T \hat{\gamma} C_{ss} \end{bmatrix}, \tag{5.3}$$

where $\hat{\lambda}$ is:

$$\begin{aligned} \hat{\lambda} = &- \hat{J}\hat{l}^{-2}\lfloor \dot{B}^T \dot{B} \rfloor - \frac{1}{2}\hat{l}^{-2}\lfloor B^T(W + \Omega P^T \\ &- S\hat{\gamma}C_s)C_{nb}^T C_b^T \rfloor, \end{aligned} \tag{5.4}$$

and the operator $\lfloor \bullet \rfloor$ sets every off-diagonal element of the square matrix operand to zero, $N \in R^{3\times n}$ (n is the total number of nodes) is the nodal matrix with each column denotes x, y, and z coordinates of each node, $M_s \in R^{n\times n}$ is mass matrix of all the bars and strings, $K_s \in R^{n\times n}$ is the stiffness matrix, $W \in R^{3\times n}$ contains the external force at each node, $\Omega \in R^{3\times c}$ (c is number

of constraints $NP = D$), the Lagrange multipliers required to maintain these constraints can be thought of as contact forces at the Class-k nodes [82]. Ω is the matrix of Lagrange multipliers associated with the constraint $NP = D$, $P \in R^{c\times n}$ is the constraint matrix, denoting which nodes are the Class-k nodes and which nodes are grounded. $B = \begin{bmatrix} \boldsymbol{b}_1 & \boldsymbol{b}_2 & \cdots & \boldsymbol{b}_\beta \end{bmatrix} \in R^{3\times\beta}$ and $S = \begin{bmatrix} \boldsymbol{s}_1 & \boldsymbol{s}_2 & \cdots & \boldsymbol{s}_\alpha \end{bmatrix} \in R^{3\times\sigma}$ ($\boldsymbol{b}_i$ and $\boldsymbol{s}_i$ are bar and string vectors, β and σ represent the number of bars and number of string) are bar and string matrices whose columns are bar or string vectors, C_b and C_s are the connectivity matrix of bars and strings (consists of a "-1" at the i^{th} column, a "$+1$" at the j^{th} column, and zeros elsewhere to define a structure member connecting from $\boldsymbol{n}_i$ to $\boldsymbol{n}_j$.), they satisfy $B = NC_b^T$ and $S = NC_s^T$. The nodes have two types: bar nodes $N_b \in R^{3\times 2\beta}$, which are the endpoints of bars, and string nodes $N_s \in R^{3\times\sigma}$, which are the locations of string-to-string connections that have a point mass associated with them, $N = \begin{bmatrix} N_b & N_s \end{bmatrix}$. Then, the bar and string nodes can be extracted from the node matrix N with the definition of two connectivity matrices, C_{nb} and C_{ns}. C_s is divided into two parts: the first, C_{sb}, describing bar-to-string joints and the second, C_{ss}, describing string-to-string joints. $\hat{\bullet}$ is an operator that converts a vector into a diagonal matrix. $\hat{m}_b$, $\hat{m}_s$, $\hat{\gamma}$, $\hat{\lambda}$ are bar mass, string mass, string force density, and bar force density matrices respectively. $\hat{J}$ is the bar moment of inertia matrix, which satisfies $J_i = \frac{m_{bi}}{12} + \frac{m_{bi}r_{bi}^2}{4l_i^2}$, and r_{bi} and l_i are the radius and length of the i^{th} bar.

Adding the linear constraints to the dynamics will restrict the motion in certain dimensions. We separate the moving and stationary nodes by performing a Singular Value Decomposition of the matrix P to eliminate unnecessary computations of stationary nodes, the order of dynamics equation can be reduced into [83]:

$$\ddot{\eta}_2 M_2 + \eta_2 K_2 = \widetilde{W}, \tag{5.5}$$

where $\eta = [\eta_1 \quad \eta_2] \triangleq NU = [NU_1 \quad NU_2]$, $M_2 = U_2^T M_s U_2$, $K_2 = U_2^T K_s U_2, \widetilde{W} = WU_2 - \eta_1 U_1^T K_s U_2$, $\eta_1 = DV\Sigma_1^{-1}$, $NP = D$, $P = U\Sigma V^T = \begin{bmatrix} U_1 & U_2 \end{bmatrix} \begin{bmatrix} \Sigma_1 \\ 0 \end{bmatrix} V^T$.

5.2.2 Coordinate Transformation

5.2.2.1 X Matrix Definition

From the above, the reduced order dynamics can be written in a standard second order differential equation form. Let X matrix be the product of the η_2 and M_2 matrices. Since M_2 is the mass matrix for the tensegrity system and it is non-singular, an expression for η_2 in terms of X can then be written as:

$$X = \eta_2 M_2 \rightarrow \eta_2 = X M_2^{-1} \tag{5.6}$$

$$\dot{X} = \dot{\eta_2} M_2 \rightarrow \dot{\eta_2} = \dot{X} M_2^{-1} \tag{5.7}$$

$$\ddot{X} = \ddot{\eta_2} M_2 \rightarrow \ddot{\eta_2} = \ddot{X} M_2^{-1}. \tag{5.8}$$

5.2.2.2 Conversion of Matrix Dynamics

Substitute equations (5.6) - (5.8) into equation (5.1), one can get:

$$\ddot{X} + X M_2^{-1} K_2 = \widetilde{W}. \tag{5.9}$$

Take the i^{th} element of the first and second terms of the equation (5.4) and use the fact $\hat{\boldsymbol{x}}\boldsymbol{y} = \hat{\boldsymbol{y}}\boldsymbol{x}$, where $\boldsymbol{x}$ and $\boldsymbol{y}$ are vectors, equation (5.4) can be written as:

$$-\lambda_i = \frac{J_i ||\dot{\boldsymbol{b}}_i||^2}{l_i^2} + \frac{1}{2l_i^2} \boldsymbol{b}_i^T W C_{nb}^T C_b^T \boldsymbol{e}_i +$$

$$\frac{1}{2l_i^2} \boldsymbol{b}_i^T \Omega P^T C_{nb}^T C_b^T \boldsymbol{e}_i - \frac{1}{2l_i^2} \boldsymbol{b}_i^T \widehat{S C_s C_{nb}^T C_b^T \boldsymbol{e}_i \gamma}, \tag{5.10}$$

where $\boldsymbol{b_i}$ is the vector of each bar, $\boldsymbol{e}_i$ is a vector with 1 in the i^{th} elements and zeros else where.

Stack all the elements of vector λ we get:

$$-\lambda = \underbrace{\begin{bmatrix} \frac{J_1||\dot{\boldsymbol{b}}_1||^2}{l_1^2} + \frac{1}{2l_1^2}\boldsymbol{b}_1^T W C_{nb}^{\mathsf{T}} C_b^T \boldsymbol{e}_1 + \frac{1}{2l_1^2}\boldsymbol{b}_1^T \Omega P^{\mathsf{T}} C_{nb}^{\mathsf{T}} C_b^T \boldsymbol{e}_1 \\ \vdots \\ \frac{J_i||\dot{\boldsymbol{b}}_i||^2}{l_i^2} + \frac{1}{2l_i^2}\boldsymbol{b}_i^T W C_{nb}^{\mathsf{T}} C_b^T \boldsymbol{e}_i + \frac{1}{2l_i^2}\boldsymbol{b}_i^T \Omega P^{\mathsf{T}} C_{nb}^{\mathsf{T}} C_b^T \boldsymbol{e}_i \\ \vdots \\ \frac{J_\beta||\dot{\boldsymbol{b}}_\beta||^2}{l_\beta^2} + \frac{1}{2l_\beta^2}\boldsymbol{b}_\beta^T W C_{nb}^{\mathsf{T}} C_b^T \boldsymbol{e}_\beta + \frac{1}{2l_\beta^2}\boldsymbol{b}_\beta^T \Omega P^{\mathsf{T}} C_{nb}^{\mathsf{T}} C_b^T \boldsymbol{e}_\beta \end{bmatrix}}_{\tau}$$

$$- \underbrace{\begin{bmatrix} \overbrace{\quad\quad} \\ \frac{1}{2l_1^2}\boldsymbol{b}_1^T S C_s C_{nb}^{\mathsf{T}} C_b^T \boldsymbol{e}_1 \\ \vdots \\ \overbrace{\quad\quad} \\ \frac{1}{2l_i^2}\boldsymbol{b}_i^T S C_s C_{nb}^{\mathsf{T}} C_b^T \boldsymbol{e}_i \\ \vdots \\ \overbrace{\quad\quad} \\ \frac{1}{2l_\beta^2}\boldsymbol{b}_\beta^T S C_s C_{nb}^{\mathsf{T}} C_b^T \boldsymbol{e}_\beta \end{bmatrix}}_{\Lambda} \gamma. \tag{5.11}$$

We can express in a compact matrix form,

$$-\lambda = \Lambda\gamma + \tau. \tag{5.12}$$

5.2.3 Shape Control Law

5.2.3.1 Shape Objectives

L specifies the axes of interest for the system nodes, R denotes which of those system nodes are nodes of interest. By multiplying $Y_c = L\eta_2 R$, one can, therefore, extract the current values of the node coordinates of interest for the node configuration N:

$$Y_c = LNU_2R = L\eta_2 R = LXM_2^{-1}R. \tag{5.13}$$

$\bar{Y}$ is a matrix containing the desired values for the node coordinates of interest. The error matrix E between the current and desired node coordinates of interest can then be written:

$$E = Y_c - \bar{Y}. \tag{5.14}$$

5.2.3.2 Error Dynamics

To achieve the desired shape control, the error matrix E and its first and second-time derivatives should all go to zero. This goal is expressed as follows. Let Ψ and Φ be chosen matrices such that:

$$\ddot{E} + \Psi\dot{E} + \Phi E = 0 \tag{5.15}$$

is a stable equation about the value $E = 0$. Using equations (5.9), (5.13), and (5.14), the equation (5.15) becomes:

$$L(\widetilde{W} - XM_2^{-1}K_2)M_2^{-1}R + \Psi L\dot{X}M_2^{-1}R + \Phi LXM_2^{-1}R - \Phi\bar{Y} = 0. \tag{5.16}$$

This can be expanded and rearranged:

$$LXM_2^{-1}K_2M_2^{-1}R = L\widetilde{W}M_2^{-1}R + \Psi L\dot{X}M_2^{-1}R + \Phi LXM_2^{-1}R - \Phi\bar{Y} \tag{5.17}$$

Substitute $K_2 = U_2^T K_s U_2$ and K_s from equation (5.3) into the left hand side of this equation:

$$\begin{aligned} LXM_2^{-1}K_2M_2^{-1}R &= LXM_2^{-1}U_2^T K_s U_2 M_2^{-1}R \\ &= LXM_2^{-1}U_2^T \begin{bmatrix} C_s^{\mathsf{T}}\hat{\gamma}C_{sb} - C_{nb}^{\mathsf{T}}C_b^{\mathsf{T}}\hat{\lambda}C_b & C_s^{\mathsf{T}}\hat{\gamma}C_{ss} \end{bmatrix} U_2 M_2^{-1}R. \end{aligned} \tag{5.18}$$

Let us take a look at the mass matrix again,

$$M_2 = U_2^{\mathsf{T}} M_s U_2 \tag{5.19}$$

$$\begin{aligned} M_s &= \begin{bmatrix} C_{nb}^{\mathsf{T}}(C_b^{\mathsf{T}}\hat{J}C_b + C_r^{\mathsf{T}}\hat{m}_b C_r) & C_{ns}^{\mathsf{T}}\hat{m}_s \end{bmatrix} \\ &= \begin{bmatrix} C_b^T & C_r^T & 0 \\ 0 & 0 & I \end{bmatrix} \begin{bmatrix} \hat{J} & 0 & 0 \\ 0 & \hat{m}_b & 0 \\ 0 & 0 & \hat{m}_s \end{bmatrix} \begin{bmatrix} C_b & 0 \\ C_r & 0 \\ 0 & I \end{bmatrix} \end{aligned}$$

Using $\begin{bmatrix} \frac{1}{2}C_b^{\mathsf{T}} & 2C_r^{\mathsf{T}} \end{bmatrix}^{-1} = \begin{bmatrix} C_b^{\mathsf{T}} & C_r^{\mathsf{T}} \end{bmatrix}^{\mathsf{T}}$, it can also be shown that:

$$\begin{bmatrix} \frac{1}{2}C_b^{\mathsf{T}} & 2C_r^{\mathsf{T}} & 0 \\ 0 & 0 & I \end{bmatrix}^{-1} = \begin{bmatrix} C_b & 0 \\ C_r & 0 \\ 0 & I \end{bmatrix}. \tag{5.20}$$

Then, M_s^{-1} can be obtained,

$$
\begin{aligned}
M_s^{-1} &= \begin{bmatrix} \frac{1}{2}C_b^{\mathsf{T}} & 2C_r^{\mathsf{T}} & 0 \\ 0 & 0 & I \end{bmatrix} \begin{bmatrix} \hat{J} & 0 & 0 \\ 0 & \hat{m}_b & 0 \\ 0 & 0 & \hat{m}_s \end{bmatrix}^{-1} \begin{bmatrix} \frac{1}{2}C_b & 0 \\ 2C_r & 0 \\ 0 & I \end{bmatrix} \\
&= \begin{bmatrix} \frac{1}{2}C_b^{\mathsf{T}} & 2C_r^{\mathsf{T}} & 0 \\ 0 & 0 & I \end{bmatrix} \begin{bmatrix} \hat{J} & 0 & 0 \\ 0 & \hat{m}_b & 0 \\ 0 & 0 & \hat{m}_s \end{bmatrix}^{-1} \begin{bmatrix} \frac{1}{2}C_bC_{nb} \\ 2C_rC_{nb} \\ C_{ns} \end{bmatrix} \\
&= \begin{bmatrix} \frac{1}{4}C_b^{\mathsf{T}}\hat{J}^{-1}C_bC_{nb} + 4C_r^{\mathsf{T}}\hat{m}_b^{-1}C_rC_{nb} \\ \hat{m}_s^{-1}C_{ns} \end{bmatrix}. \qquad (5.21)
\end{aligned}
$$

Let $M_{s1} = \frac{1}{4}C_b^{\mathsf{T}}\hat{J}^{-1}C_bC_{nb} + 4C_r^{\mathsf{T}}\hat{m}_b^{-1}C_rC_{nb}$ and $M_{s2} = \hat{m}_s^{-1}C_{ns}$, M_s can be simply written as $M_s = \begin{bmatrix} M_{s1} \\ M_{s2} \end{bmatrix}$. Then, $M_2^{-1} = U_2^T \begin{bmatrix} M_{s1} \\ M_{s2} \end{bmatrix} U_2$.
Equation (5.18) can be written as:

$$
\begin{aligned}
LXM_2^{-1}K_2M_2^{-1}R = LXM_2^{-1}U_2^T(&C_s^{\mathsf{T}}\hat{\gamma}C_{sb}M_{s1} \\
&-C_{nb}^{\mathsf{T}}C_b^{\mathsf{T}}\hat{\lambda}C_bM_{s1} + C_s^{\mathsf{T}}\hat{\gamma}C_{ss}M_{s2})U_2R. \qquad (5.22)
\end{aligned}
$$

Take the i^{th} column on both sides,

$$
\begin{aligned}
LXM_2^{-1}K_2M_2^{-1}R\boldsymbol{e}_i = LXM_2^{-1}U_2^T(&C_s^{\mathsf{T}}\hat{\gamma}C_{sb}M_{s1}U_2R\boldsymbol{e}_i \\
&- C_{nb}^{\mathsf{T}}C_b^{\mathsf{T}}\hat{\lambda}C_bM_{s1}U_2R\boldsymbol{e}_i + C_s^{\mathsf{T}}\hat{\gamma}C_{ss}M_{s2}U_2R\boldsymbol{e}_i). \qquad (5.23)
\end{aligned}
$$

Using the fact $\hat{\boldsymbol{x}}\boldsymbol{y} = \hat{\boldsymbol{y}}\boldsymbol{x}$, we have:

$$LXM_2^{-1}K_2M_2^{-1}R\boldsymbol{e}_i = LXM_2^{-1}U_2^T(\widehat{C_s^T C_{sb} M_{s1} U_2 R\boldsymbol{e}_i \gamma}$$

$$+ \widehat{C_s^T C_{ss} M_{s2} U_2 R\boldsymbol{e}_i \gamma} - \widehat{C_{nb}^{\mathsf{T}} C_b^{\mathsf{T}} C_b M_{s1} U_2 R\boldsymbol{e}_i \lambda}). \tag{5.24}$$

Recalling that $-\lambda = \Lambda\gamma + \tau$,

$$LXM_2^{-1}K_2M_2^{-1}R\boldsymbol{e}_i = LXM_2^{-1}U_2^T[(\widehat{C_s^T C_{sb} M_{s1} U_2 R\boldsymbol{e}_i}$$

$$+ \widehat{C_s^T C_{ss} M_{s2} U_2 R\boldsymbol{e}_i} + \widehat{C_{nb}^{\mathsf{T}} C_b^{\mathsf{T}} C_b M_{s1} U_2 R\boldsymbol{e}_i \Lambda})\gamma$$

$$+ \widehat{C_{nb}^{\mathsf{T}} C_b^{\mathsf{T}} C_b M_{s1} U_2 R\boldsymbol{e}_i \tau}]. \tag{5.25}$$

5.2.3.3 Control Law

From equations (5.17) and (5.25), one can simplify this into a compact matrix form $\mu = \Gamma\gamma$ with definitions of μ_i and Γ_i, in which μ is the stack of each μ_i matrix and Γ is similarly a stack of

each Γ_i matrix:

$$\mu = \Gamma\gamma, \tag{5.26}$$

$$\mu_i = (L\widetilde{W}M_2^{-1}R + \Psi L\dot{X}M_2^{-1}R + \Phi LXM_2^{-1}R - \Phi\bar{Y})\boldsymbol{e}_i$$

$$- LXM_2^{-1}U_2^T\widehat{C_{nb}^{\mathsf{T}}C_b^{\mathsf{T}}C_bM_{s1}U_2R\boldsymbol{e}_i}\tau, \tag{5.27}$$

$$\Gamma_i = LXM_2^{-1}U_2^T(\widehat{C_s^TC_{sb}M_{s1}U_2R\boldsymbol{e}_i} + \widehat{C_s^TC_{ss}M_{s2}U_2R\boldsymbol{e}_i}$$

$$+ \widehat{C_{nb}^{\mathsf{T}}C_b^{\mathsf{T}}C_bM_{s1}U_2R\boldsymbol{e}_i}\Lambda). \tag{5.28}$$

Since control variable γ is composed of force densities of the strings, it also satisfies $\gamma \geq 0$ (strings are always in tension), the least square problem we choose to solve at each increment of real time Δt, is min $||\mu - \Gamma\gamma||^2,\ \gamma \geq 0$. Let the rest length of the i^{th} string be denoted by s_{i0}, extensional stiffness by k_i, damping constant by c_i, and string vector by $\boldsymbol{s}_i$. Assuming that strings follow Hooke's law and the viscous friction damping model, the tension in a string is:

$$\gamma_i = \frac{||\boldsymbol{t}_i||}{||\boldsymbol{s}_i||} = \begin{cases} k_i(1 - \dfrac{\boldsymbol{s}_{i0}}{||\boldsymbol{s}_i||}) + c_i\dfrac{\boldsymbol{s}_i^T\dot{\boldsymbol{s}}_i}{||\boldsymbol{s}_i||^2} & \text{if} \quad ||\boldsymbol{s}_i|| \geq \boldsymbol{s}_{i0} \\ 0 & \text{if} \quad ||\boldsymbol{s}_i|| < \boldsymbol{s}_{i0} \end{cases}. \tag{5.29}$$

Then, we have rest length $\boldsymbol{s}_{i0}$:

$$\boldsymbol{s}_{i0} = ||\boldsymbol{s}_i||[1 - \frac{1}{k_i}(\gamma_i - c_i\frac{\boldsymbol{s}_i^T\dot{\boldsymbol{s}}_i}{||\boldsymbol{s}_i||^2})]. \tag{5.30}$$

We can also write the string tension (a product of string length and string force density) in a matrix

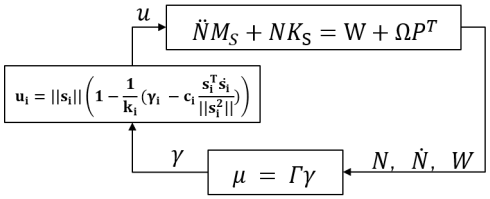

Figure 5.1: Close loop system, where u is control input and u_i is the rest length of the i^{th} string, given by equation (5.30). Reprinted with permission from [7].

form:

$$T = S\hat{\gamma} = (S - S_0)\hat{k} + S\lfloor S^T\dot{S}\rfloor\lfloor S^T S\rfloor^{-1}\hat{c}, \tag{5.31}$$

where $S_0 = S\lfloor S^T S\rfloor^{-\frac{1}{2}}\hat{\boldsymbol{s}}_0$ represents the matrix containing the rest length vectors. The overall control system is shown in Figure 5.1.

5.3 Control of Morphing Airfoils

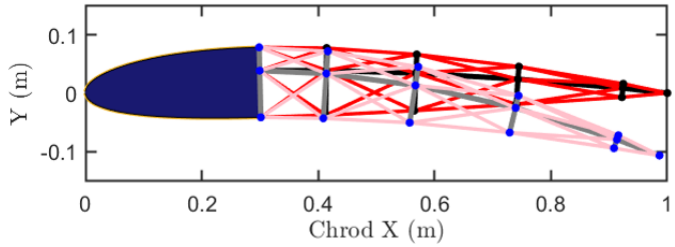

Figure 5.2: Initial and morphing configuration of the tensegrity NACA 2412 airfoil, top one (bars in black, strings in red, and nodes in black) is the initial state, and the bottom one (bars in grey, strings in pink, and nodes in blue) is the morphing target.

We choose NACA 2412 airfoil, with a chord length $c = 1$ m, $0 \sim 0.3$ m as the rigid part, vertical bar length ratio $\mu = 1/3$, and error bound $\delta = 0.001$ m to generate the initial configuration of the tensegrity foil by the error bound method described in Section 3.8. In this example, there are five horizontal bars ($q = 5$). The morphing targets are generated by the rotation of the horizontal bars

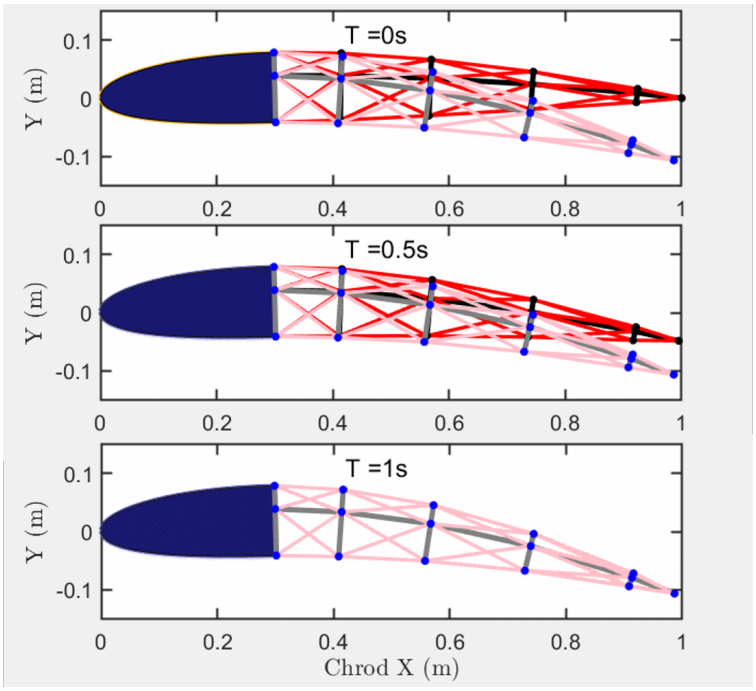

Figure 5.3: Time history of the tensegrity morphing airfoil at T = 0s, 0.5s, and 1s.

(bars $\boldsymbol{b}_1, \boldsymbol{b}_2, \cdots, \boldsymbol{b}_5$) in the tensegrity structure in a linear manner while keeping the length of every bar unchanged during deformation. That is, bar $\boldsymbol{b}_1$ rotates $\theta_1 = \frac{\pi}{72}$, bar $\boldsymbol{b}_2$ rotates $\theta_2 = \frac{\pi}{36}$, and up to bar $\boldsymbol{b}_5$ rotates $\theta_5 = \frac{5\pi}{72}$, the vertical bars remain the same angle with the horizontal bars as the initial configuration. The final morphing target is shown in Fig. 5.2. Then, based on the morphing target, coordinates of control targets $\bar{Y}$ can be calculated. In the control simulation, we choose time step $dt = 0.001s$, stability coefficients $\Psi = 2.5$ and $\Phi = 4$, mass of the longest bar and string are 1 kg and 0.01 kg, and the masses of the shorter bars and strings are scaled accordingly. Nodes n_1, n_{q+2}, and n_{2q+2} in Figure 3.32 are fixed with the D-Section, in our case structure complexity $q = 5$, $\boldsymbol{n}_1$, $\boldsymbol{n}_7$, and $\boldsymbol{n}_{12}$ are not controlled. Since we are controlling x and y coordinates, matrix $L = [1\ 0\ 0; 0\ 1\ 0; 0\ 0\ 0]$, matrix $R^{16\times13}$ (generated by $I^{16\times16}$ with columns 1, 7 and 12 being deleted). Fig. 5.3 shows a time history of airfoil configuration while tracking a trajectory at time T = 0s, 0.5s, and 1s which demonstrates the successful shape control at a final time. For the above simulation, Figure 5.4 is the length change of each string.

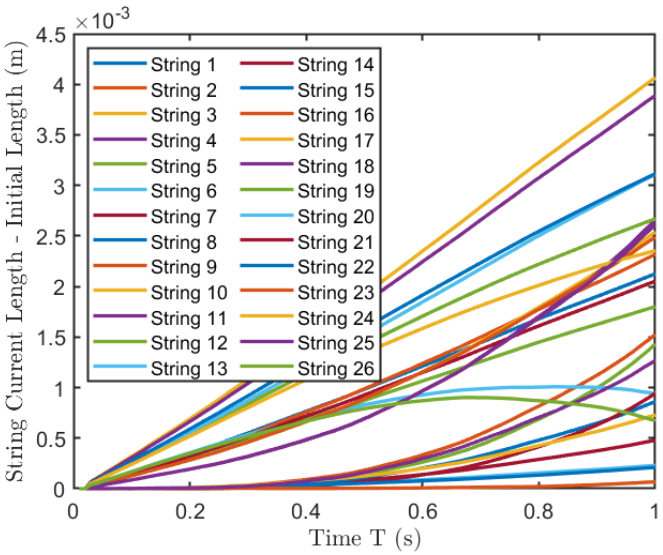

Figure 5.4: String length time history, string current length minus string initial length v.s. time.

5.4 Conclusion

This chapter offers an approach to integrate structure and control design. Based on the non-linear reduced-order class-k tensegrity dynamics, a non-linear control law is derived. The control variables (force densities in strings) appear linearly in the non-linear dynamics. A NACA 2412 airfoil with specified morphing targets is chosen to verify the developed design. The approach can also be used for design and shape control of other tensegrity structures.

6. INTEGRATING CONTROL AND SIGNAL PROCESSING: SENSOR/ACTUATOR SELECTION FOR TENSEGRITY ROBOTS

This chapter presents a systematic design approach to integrate the economic sensor/actuator selection and covariance control design for tensegrity robots. The objective is to minimize the output covariance of the tensegrity robots subject to the specified sensor/actuator budget and control covariance upper bounds by solving the precision of sensor/actuator and output feedback control law problems simultaneously. To achieve this goal, we first present the linearized tensegrity dynamics with any constraints in a standard state-space form. Followed by an uncertainty study of joints in the tensegrity structures with no control. Then, together with a linear dynamic output-feedback controller, we give the closed-loop system formulation. The economic sensor/actuator selection method and the feedback control law problem are converted into an equivalent convex problem, given by a set of LMIs (linear matrix inequalities). To verify the proposed algorithms, the error of the nonlinear and linearized dynamics are first compared and checked. A 2D tensegrity morphing airfoil is then implemented to examine the integrated algorithm. The principles developed in this chapter can be used to analyze the performance of various types of structures as well as an interface to integrate structure, control, and signal processing designs. These methods include but are not limited to tensegrity structures.

6.1 Introduction

Traditionally, structure design, sensor/actuator selection, and control algorithm are isolated disciplines. Each of these disciplines is quite sophisticated and mature. Structure engineers first design the structure, signal processing guys select the sensor/actuator and then control people write an algorithm to achieve the morphing objective. This is certainly not a good way to reduce the required control energy and instrument cost as well as guarantee the system performance [124]. The sensor/actuator should be selected based on the budget for the control. However, the control may be limited by the precision of some of the sensors and actuators. Then, the sensors and

actuators need to be reselected, and the control law has to be redesigned. Thus, the sensor/actuator selection and control problems are not independent [125, 126].

In fact, few attempts have been made to integrate sensor and actuator selection and control design. For example, Singh et al. demonstrated a combined H_∞ feedback control design for both LTI (linear time invariant) and LPV (linear parameter varying) systems and optimal sensors and actuator selection, and the problem yields to a mixed Boolean semi-definite programming optimization problem [127]. Argha et al. formulated and analyzed a framework for a multi-channel H_2 dynamic output feedback controller and also incorporated the penalizing the number of actuators and sensors [128]. Güney and Eskinat introduced a closed-loop optimal location selection method for actuators and sensors in flexible structures based on a H_∞ controller and a gradient-based unconstrained minimization approach [129]. Fahroo and Demetriou investigated the optimization of a quadratic performance criterion with respect to the location of the actuators and/or the sensors for active noise regulator and reference tracking control problems [130]. Westermayer et al. proposed an optimal placement approach that exploits the flexible structure and incorporates controllability and observability-based measures, as well as knowledge on actuator and sensor properties [131]. However, few of them start from a covariance point of view, integrate the structure dynamics, signal processing, and control design. This chapter determines the precision of sensor/actuator and output feedback control law simultaneously such that the output covariance of the system is minimized, subject to the specified sensor/actuator budget and control covariance upper bounds.

This chapter is organized as follows: Section 6.2 formulates the linearized tensegrity dynamics in a state-space form. Section 6.3 presents the joint uncertainty analysis of tensegrity structures. Section 6.4 derives the economic sensor/actuator selection methods and covariance control law, and the problem turns out to be a convex problem expressed by a set of LMIs. Section 6.5 first checks the accuracy of the linearized tensegrity dynamics and then verifies the developed algorithm by the two tensegrity robots, a 2D tensegrity morphing airfoil. Section 6.6 summarises the conclusions.

6.2 Linearized Tensegrity Dynamics

Then, one can write the linearized dynamics equation with constraints Eq. (4.99) into a compact state space form:

$$\underbrace{\frac{\mathrm{d}}{\mathrm{d}t}\begin{bmatrix}\mathrm{d}\boldsymbol{n}_a\\ \mathrm{d}\dot{\boldsymbol{n}}_a\end{bmatrix}}_{x_p\in\mathbb{R}^{2n_a}} = \underbrace{\begin{bmatrix}\mathbf{0} & \mathbf{I}\\ -\boldsymbol{M}_{aa}^{-1}K_{Taa} & -\boldsymbol{M}_{aa}^{-1}\boldsymbol{D}_{aa}\end{bmatrix}}_{\mathcal{A}_p\in\mathbb{R}^{2n_a\times 2n_a}}\underbrace{\begin{bmatrix}\mathrm{d}\boldsymbol{n}_a\\ \mathrm{d}\dot{\boldsymbol{n}}_a\end{bmatrix}}_{x_p\in\mathbb{R}^{2n_a}} + \underbrace{\begin{bmatrix}\mathbf{0}\\ \boldsymbol{M}_{aa}^{-1}-\boldsymbol{M}_{aa}^{-1}\boldsymbol{K}_{l_0a}\end{bmatrix}}_{\mathcal{B}_p\in\mathbb{R}^{2n_a\times(n_a+n_e)}}\underbrace{\begin{bmatrix}\mathrm{d}\boldsymbol{f}_{exa}\\ \mathrm{d}\boldsymbol{l}_0\end{bmatrix}}_{u\in\mathbb{R}^{(n_a+n_e)}}$$
$$+\underbrace{\begin{bmatrix}\mathbf{0}\\ \boldsymbol{M}_{aa}^{-1}(-\boldsymbol{M}_{ab}\mathrm{d}\ddot{\boldsymbol{n}}_b-\boldsymbol{D}_{ab}\mathrm{d}\dot{\boldsymbol{n}}_b-\boldsymbol{K}_{Tab}\mathrm{d}\boldsymbol{n}_b)\end{bmatrix}}_{\mathcal{G}\in\mathbb{R}^{2n_a}}, \tag{6.1}$$

for the fixed pinned nodes we have $\mathrm{d}\boldsymbol{n}_b = \mathrm{d}\dot{\boldsymbol{n}}_b = \mathrm{d}\ddot{\boldsymbol{n}}_b = 0$, which gives $\mathcal{G} = 0$, and the equation can be simply expressed as $\dot{x_p} = \mathcal{A}_p x_p + \mathcal{B}_p u$.

6.3 Uncertainty Analysis of Tensegrity Structures

6.3.1 Uncertainty Analysis

For a output feedback problem of a tensegrity structure at an equilibrium state with plant noise w_p, the linear system is given as the following:

$$\text{Plant: } \dot{x}_p = \mathcal{A}_p x_p + \mathcal{B}_p u + \mathcal{D}_p w_p, \tag{6.2}$$

$$\text{Output: } y = \mathcal{C}_p x_p, \tag{6.3}$$

where x_p, u, and y are state, control input, and output vectors of the plant. $\mathcal{C}_p$, $\mathcal{D}_p$ are matrices with proper dimensions. w_p is the plant noise vector, which is normally modeled as independent zero mean Gaussian white noises with covariances $\mathcal{W}_p$:

$$E_\infty(w_p) = 0,\ E_\infty(w_p w_p^T) = \mathcal{W}_p, \tag{6.4}$$

where $E_\infty(\bullet) = \lim_{t\to\infty} E(\bullet)$ is the asymptotic expected value of the certain variable. Since the noise sources w_s, x, u are mutually independent (uncorrelated), the following is true $E_\infty(w_p \cdot x^T) = 0$, $E_\infty(w_p \cdot u^T) = 0$, and $E_\infty(x \cdot u^T) = 0$. For a stable system we have $\dot{X} = 0$, and the state covariance matrix can be obtained by solving the following equation:

$$0 = \mathcal{A}_p X \mathcal{A}_p^T + \mathcal{B}_p U \mathcal{B}_p^T + \mathcal{D}_p \mathcal{W}_p \mathcal{D}_p^T, \tag{6.5}$$

where X, U are defined as $X = E_\infty(x_p x_p^T)$ and $U = E_\infty(uu^T)$. Then, solve Eq. (6.5) for X, we can compute the output covariance:

$$Y = \mathcal{C}_p X \mathcal{C}_p^T. \tag{6.6}$$

Then, for the given covariance of plant noise, we can compute the output covariance of the system to predict the performance of the designed tensegrity structure.

6.3.2 Numerical Examples

We are interested in knowing the value of position variance of one subset of nodes, given the fact that some other subsets of nodes are inaccurate with given variance. For this joint uncertainty problem, we choose a T_2D_1 tensegrity tower to demonstrate the algorithm, the model is shown in Figure 6.1, a same tower as described in Section 4.5.3.

The tower is 10 m high with a 60 kg payload on the top node. The bars are aluminum hollow pipe (OD 4"or 101.6 mm, wall thickness 0.035"or 0.889 mm), and strings are UHMWPE (OD 4 mm). The Young's modulus, density, and yield strength of the aluminum and UHMWPE are 60 Gpa, 2,700 kg/m^3, 78 Mpa, and 120 Gpa, 970 kg/m^3, 2.7 Gpa. To stabilize the tower, we choose damping to be d = 0.5, and the damping matrix D = $2d \max \sqrt{MEAl_0^{-1}}) I_{3\times n_n}$ is from the critical damping ratio formula. the force densities in the five 4-bar groups from top to bottom are designed to be 4,900 N, 4,900 N, 490 N, 9,800 N, and 4,900 N. By computing the equilibrium equation, and we can get force densities in all the strings. The bottom five nodes of the tower on the ground

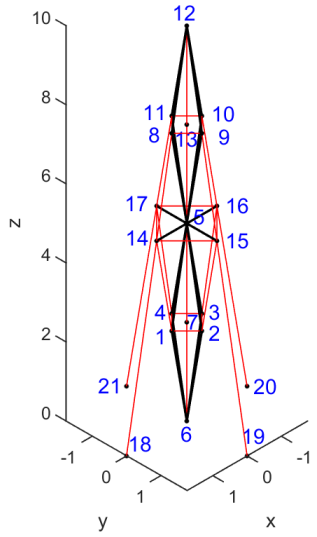

Figure 6.1: Node notation of the 10m tall 3D T_2D_1 tensegrity tower with four sides, the angles of the T-Bar and D-Bar units are $\alpha_T = \alpha_D = \frac{\pi}{18}$.

are fixed. Nodes 7 and 13 are plotted to show the middle plane of the D-Bar units, and they are not computed in the dynamics. Thus, there are 14 free nodes (nodes 1, 2, 3, 4, 5, 8, 9, 10, 11, 12, 14, 15, 16, 17), and each free node has 3 DOF, the overall structure has 42 DOF. That is, we have 84 states (positions and velocities) of the model. First, we check the eigenvalues of the linearized tensegrity tower model, as given in Table 6.1. As we can see, all the eigenvalues are negative, which means the initial tower structure is stable.

The inaccurate node positions can be modeled as plant noises, described by the state noise vector w_p. The relatively small uncertainties of nodes in states will be transferred to the dynamics of the system, which can be modeled by $\mathscr{D}_p = \mathscr{A}_p$. In this problem, we only care about the influence of node uncertainties, and the control input is set to be $u = 0$. Now, by giving some subset of inaccurate nodes with given variance $\mathscr{W}_p$, and if the structure is stable (by checking the stability of the structure), we can compute the value of position variance of nodes of interest. Let us consider the following cases.

Case 1: The uncertainty of node 15 is shown in Figure 6.2, which means the position of node

Table 6.1: Eigenvalues of linearized model of the tensegrity tower, values $\times 10^3$.

-4.1951 + 7.0895i	-0.7617 + 2.3536i	-1.5039 - 3.1354i	-1.7498 + 0.0000i
-4.1951 - 7.0895i	-0.7617 - 2.3536i	-1.3302 + 3.5365i	-1.7498 + 0.0000i
-3.9639 + 6.9113i	-3.3838 + 0.0000i	-1.3302 - 3.5365i	-2.6501 + 0.0000i
-3.9639 - 6.9113i	-3.3838 + 0.0000i	-1.3285 + 3.0920i	-2.6501 + 0.0000i
-4.1934 + 5.2617i	-1.5192 + 3.1388i	-1.3285 - 3.0920i	-1.2302 + 0.0000i
-4.1934 - 5.2617i	-1.5192 - 3.1388i	-1.3065 + 1.2999i	-0.1374 + 0.0000i
-8.3905 + 0.0000i	-1.3399 + 3.0939i	-1.3065 - 1.2999i	-0.1218 + 0.0000i
-6.7249 + 0.0000i	-1.3399 - 3.0939i	-1.3430 + 3.5796i	-2.6550 + 0.0000i
-7.0408 + 0.0000i	-1.2070 + 0.5237i	-1.3430 - 3.5796i	-2.6531 + 0.0000i
-6.0368 + 0.0000i	-1.2070 - 0.5237i	-1.3386 + 3.5790i	-0.0811 + 0.0000i
-3.9639 + 6.9113i	-2.4590 + 0.0000i	-1.3386 - 3.5790i	-0.0811 + 0.0000i
-3.9639 - 6.9113i	-2.5192 + 0.0000i	-1.3386 + 3.5790i	-1.2302 + 0.0000i
-1.6208 + 5.4008i	-0.8396 + 0.0000i	-1.3386 - 3.5790i	-0.0182 + 0.0000i
-1.6208 - 5.4008i	-1.7948 + 0.0000i	-1.3430 + 3.5796i	-0.0182 + 0.0000i
-7.0408 + 0.0000i	-1.3285 + 3.0920i	-1.3430 - 3.5796i	-0.1307 + 0.0000i
-6.2761 + 0.0000i	-1.3285 - 3.0920i	-1.3065 + 1.2999i	-0.1307 + 0.0000i
-6.2761 + 0.0000i	-1.3323 + 3.5921i	-1.3065 - 1.2999i	-0.0031 + 0.0000i
-1.1016 + 3.8929i	-1.3323 - 3.5921i	-1.3283 + 3.5389i	-0.0031 - 0.0000i
-1.1016 - 3.8929i	-1.5039 + 3.1354i	-1.3283 - 3.5389i	-0.0013 + 0.0000i
-4.1948 + 2.2322i	-1.5039 - 3.1354i	-1.3285 + 3.5367i	-0.0003 + 0.0000i
-4.1948 - 2.2322i	-1.5039 + 3.1354i	-1.3285 - 3.5367i	-0.0030 + 0.0000i

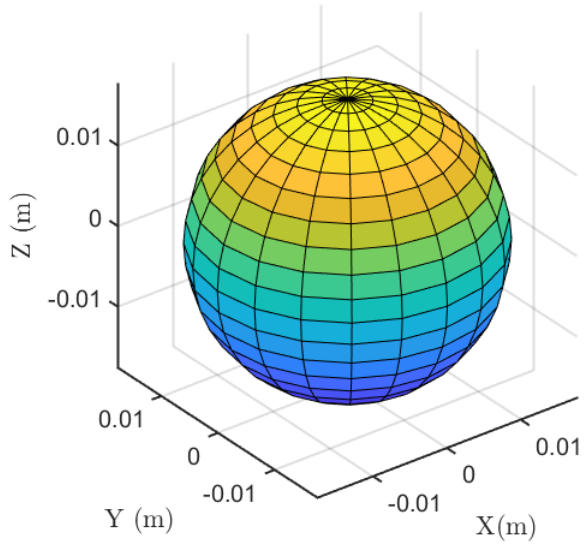

Figure 6.2: The position uncertainty of node 15, radius of the sphere is 0.0176 m, which is 2% of length of the bar starting from node 15 to node 5 (bar length is l = 0.8816 m).

15 is located in the sphere, and the center of the sphere is the ideal design. The radius of the sphere is 2% of length of the bar starting from node 15 to node 5 (bar length is l = 0.8816 m), $2\%l$ = 0.0176 m. The influence to node 12 by the uncertainty of node 15 is given in Figure 6.3. The radius of the ellipsoid is 0.0078 m, 0.0177 m, and 0.0338 m. As we can see, for the same uncertainty 0.0176 m of node 15 in X- and Y-direction. The influence on the uncertainty of node 12 in the Y-direction (0.0176 m) is larger than in the X-direction (0.0078 m). This agrees with physics because X-direction is along the bar vector (from node 5 to node 15), and Y-direction is perpendicular to the bar vector. The geometric uncertainty of node 15 in X-direction mainly influences the T-Bar unit (by node 5, 14, 15, 16, 17), but the uncertainty of node 15 in Y-direction will influence both the T-Bar unit and the axial symmetric property (about the node6 - node 12 axis). Similarly, the uncertainty in the Z-direction has the largest impact on node 12 than in the X- and Y-direction because it changes the T-bar unit, symmetric properties in the axial (about the node6 - node 12 axis), and bilateral (about the T-Bar unit plane) directions.

Case 2: Let the uncertainty sphere of node 2 or node 9 or node 15 varies from 0% to 3% (of

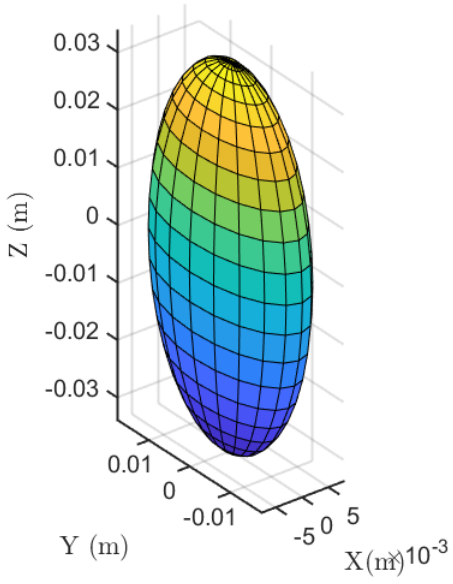

Figure 6.3: The position uncertainty of node 12, radius of the ellipsoid is 0.0078 m, 0.0177 m, and 0.0338 m.

length of the bar starting from node 15 to node 5, bar length is l = 0.8816 m). The L_2 norm of the node 12 is shown in Figure 6.4. Results show that as the uncertainty percentages increase, the L_2 norm of the uncertainty of node 12 increases. Node 9 in the upper D-Bar unit has a larger impact on node 12 than node 2 in the lower D-Bar unit. And node 15 in the T-Bar unit has the least influence on node 12. The results make sense because node 9 is closer to node 12, and D-Bar units are critical to the symmetric properties in the axial (about the node6 - node 12 axis) and bilateral (about the T-Bar unit plane) directions.

Case 3: We are also interested in the combinations of uncertainties of a set of nodes. Let us take the combination of uncertainty spheres of node 2, node 9, node 15 varies from 0% to 3% (of the length of the bar starting from node 15 to node 5, bar length is l = 0.8816 m) as an example. The L_2 norm of the node 12 is shown in Figure 6.5. Results show that as the uncertainty percentages increase, the L_2 norm of the uncertainty of node 12 increases. Comparing the results in Figure 6.4, the more nodes have uncertainties, the bigger the L_2 norm of the uncertainty of node 12 is. The lower node combinations (node 2 and node 15) have a lower impact on node 12 than the

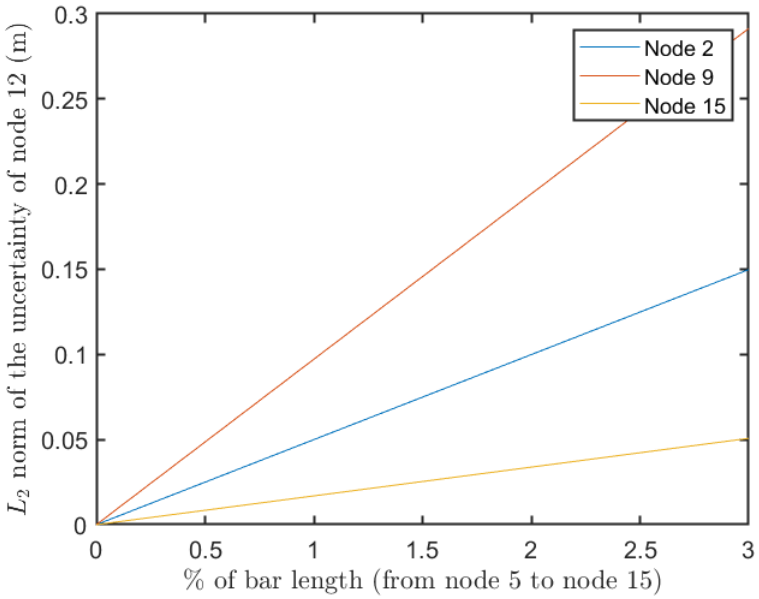

Figure 6.4: The position uncertainty of node 12 by the influence of node 2, node 9, and node 15 with a uncertainty of varies from 0-3% of the length of the bar (starting from node 15 to node 5, bar length is l = 0.8816 m).

upper combinations (node 9 and node 15). The L_2 norm of node 12 by the combination of node 2 and node 9 is greater than the combination of nodes 2&15 and nodes 9&15, which is saying the precision of D-Bar units is more important in this T_2D_1 structure.

6.4 Integrated sensor/actuator selection and covariance control design

To control a real plant, we usually deal with three noises: sensor noise, actuator noise and noise from the plant itself. A linear description of such as system is given as the following:

$$\text{Plant: } \dot{x}_p = \mathcal{A}_p x_p + \mathcal{B}_p u + \mathcal{D}_p w_p + \mathcal{D}_a w_a, \tag{6.7}$$

$$\text{Output: } y = \mathcal{C}_p x_p, \tag{6.8}$$

$$\text{Measurement: } z = \mathcal{M}_p x_p + \mathcal{E} w_s, \tag{6.9}$$

where x_p, u, y, and z are state, control input, output, and measurement vectors of the plant. $\mathcal{C}_p$, $\mathcal{D}_p$, $\mathcal{D}_a$, $\mathcal{M}_p$, and $\mathcal{E}$ are matrices with proper dimensions. w_p, w_a, and w_s are plant, actuator, and

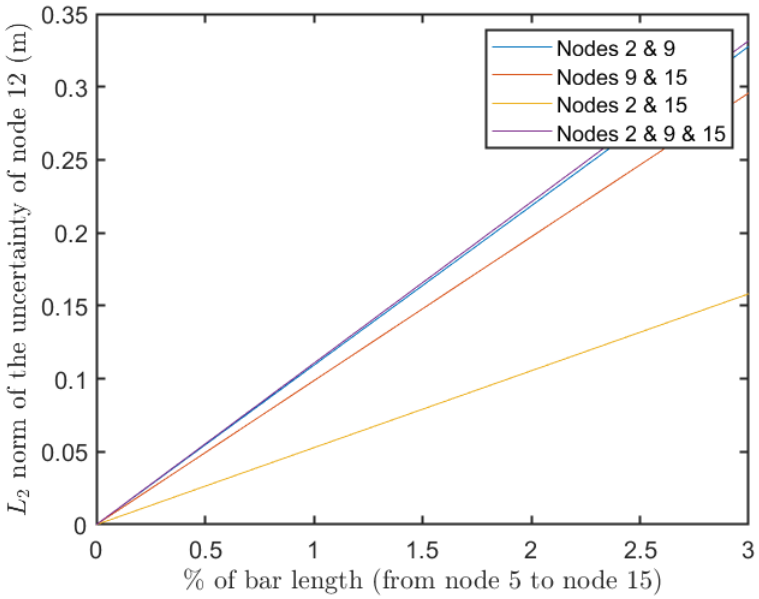

Figure 6.5: The position uncertainty of node 12 by the influence of node 2, node 9, and node 15 with a uncertainty of varies from 0-3% of the length of the bar (starting from node 15 to node 5, bar length is l = 0.8816 m).

sensor noise vectors, which are modeled as independent zero mean Gaussian white noises with covariances $\mathcal{W}_p$, $\mathcal{W}_a$, and $\mathcal{W}_s$:

$$E_\infty(w_p) = 0,\ E_\infty(w_p w_p^T) = \mathcal{W}_p \delta(t-\tau), \tag{6.10}$$

$$E_\infty(w_a) = 0,\ E_\infty(w_a w_a^T) = \mathcal{W}_a \delta(t-\tau), \tag{6.11}$$

$$E_\infty(w_s) = 0,\ E_\infty(w_s w_s^T) = \mathcal{W}_s \delta(t-\tau). \tag{6.12}$$

Since the noise sources w_s, w_p, w_a are mutually independent (uncorrelated), the following is true $E_\infty(w_s \cdot w_p^T) = 0$, $E_\infty(w_s \cdot w_a^T) = 0$, and $E_\infty(w_a \cdot w_p^T) = 0$.

For a given plant, the covariance matrix $\mathcal{W}_p$ is assumed to be known. Although sensors or actuators may produce noises at different levels, for given actuators and sensors, $\mathcal{W}_a$ and $\mathcal{W}_s$ are also known. A plant may have various sensors or actuators of different importance; some are more sensitive to noise that requires higher precisions, some don't. In this chapter, we propose

a SAS method that would guide us on selections of sensors and actuators while satisfying three pre-specified conditions: performance requirements ($\bar{Y}$), budget constraints ($\bar{\$}$), and control energy constraint ($\bar{U}$) [132]. Specifically, this method determines the importance of all sensors and actuators and allocates a given limited budget on them as precision accordingly. Hence, $\mathcal{W}_a$ and $\mathcal{W}_s$ associated with actuators and sensors are initially treated as unknown matrices, which will be computed by the SAS method. In addition, the SAS further produces a closed-loop controller that achieves such goals.

For the simplicity and practical considerations, we propose these notations and assumptions: 1). Noises from sensors and actuators entering the dynamical system are uncorrelated, so sensor and actuator covariance matrices W_a and W_s are diagonal. 2). Precisions of all the sensors and actuators are grouped into two vectors γ_s and γ_a. 3). The sensor/actuator noise is inversely proportional to the sensor/actuator precision, that is, $\mathcal{W}_a^{-1} = \text{diag}(\gamma_a)$ and $\mathcal{W}_s^{-1} = \text{diag}(\gamma_s)$, where diag($\bullet$) is an operator that converts a vector into a diagonal matrix. 4). The sensor/actuator price is proportional to its precision. The price vectors associated to sensors and actuators per unit precision are denoted as p_a and p_s. The total money spent on the sensors and actuators is denoted as: $\$ = p_s^T \gamma_s + p_a^T \gamma_a$.

Denote a linear dynamic output feedback controller of the following form:

$$\text{Controller dynamics: } \dot{x}_c = \mathcal{A}_c x_c + \mathcal{B}_c z, \tag{6.13}$$

$$\text{Control: } u = \mathcal{C}_c x_c + \mathcal{D}_c z, \tag{6.14}$$

where x_c is the controller state vector, $\mathcal{A}_c$, $\mathcal{B}_c$, $\mathcal{C}_c$, and $\mathcal{D}_c$ are matrices associated with the controller in proper dimensions.

We define the closed-loop state $\tilde{x}$ and the noise vector w as the following:

$$\tilde{x} := \begin{bmatrix} x_p^T & x_c^T \end{bmatrix}^T, \; w := \begin{bmatrix} w_p^T & w_a^T & w_s^T \end{bmatrix}^T. \tag{6.15}$$

From Eqs. (6.7) - (6.9) and (6.13) - (6.15), the closed-loop system can be written as:

$$\text{Closed-loop system: } \dot{\tilde{x}} = \mathcal{A}_{cl}\tilde{x} + \mathcal{B}_{cl}w, \tag{6.16}$$

$$\text{System Output: } y = \mathcal{C}_{cl}\tilde{x}, \tag{6.17}$$

$$\text{Control: } u = \mathcal{E}_{cl}\tilde{x} + \mathcal{F}_{cl}w, \tag{6.18}$$

where:

$$\mathcal{A}_{cl} = \mathcal{A} + \mathcal{B}\mathcal{G}\mathcal{M},\ \mathcal{B}_{cl} = \mathcal{D} + \mathcal{B}\mathcal{G}\mathcal{E},\ \mathcal{C}_{cl} = \mathcal{C}, \tag{6.19}$$

$$\mathcal{E}_{cl} = \mathcal{H}\mathcal{G}\mathcal{M},\ \mathcal{F}_{cl} = \mathcal{H}\mathcal{G}\mathcal{E}, \tag{6.20}$$

and

$$\mathcal{A} = \begin{bmatrix} \mathcal{A}_p & 0 \\ 0 & 0 \end{bmatrix},\ \mathcal{B} = \begin{bmatrix} \mathcal{B}_p & 0 \\ 0 & I \end{bmatrix},\ \mathcal{E} = \begin{bmatrix} 0 & 0 & \mathcal{E} \\ 0 & 0 & 0 \end{bmatrix},$$
$$\mathcal{M} = \begin{bmatrix} \mathcal{M}_p & 0 \\ 0 & I \end{bmatrix},\ \mathcal{G} = \begin{bmatrix} \mathcal{D}_c & \mathcal{C}_c \\ \mathcal{B}_c & \mathcal{A}_c \end{bmatrix},$$
$$\mathcal{D} = \begin{bmatrix} \mathcal{D}_p & \mathcal{D}_a & 0 \\ 0 & 0 & 0 \end{bmatrix},\ \mathcal{C} = \begin{bmatrix} \mathcal{C}_p & 0 \end{bmatrix},\ \mathcal{H} = \begin{bmatrix} I & 0 \end{bmatrix}.$$

For later convenience, we also define the covariances of closed-loop state, output, and control as: $\tilde{X} = E_\infty(\tilde{x}\tilde{x}^T)$, $Y = E_\infty(yy^T)$, and $U = E_\infty(uu^T)$. The objective of the SAS is to find how to allocate the money on the sensors and actuators under the constraints of control covariance bound $\bar{U}$, sensor and actuator budget bound $\bar{\$}$, measured output covariance bound $\bar{Y}$, and the limited precision of the sensors and actuators available in the market $\bar{\gamma}_s$ and $\bar{\gamma}_a$. The problem can be described concisely by the Theorem 6.4.1.

Theorem 6.4.1. *Let positive definite matrices $\bar{U}$, $\bar{Y}$, a positive scalar $\bar{\$}$ and positive vectors $\bar{\gamma}_s$, $\bar{\gamma}_a$ be given. Consider a plant (6.7) - (6.9), find a closed-loop controller (6.13) and precision*

allocation of sensors (γ_s) and actuators (γ_a) such that the closed-loop system (6.16) is asymptotically stable, its output covariance Y, input covariance U, money spent on sensors and actuators $\$$ are bounded above by $\bar{Y}$, $\bar{U}$, and $\bar{\$}$, while $\gamma_a < \bar{\gamma}_a$ and $\gamma_s < \bar{\gamma}_s$ are satisfied. The mathematical description is given as follows:

$$\begin{cases} \textit{Given:} & \bar{U},\ \bar{Y},\ \bar{\$},\ \bar{\gamma}_s,\ \bar{\gamma}_a, \\ \textit{Find:} & \gamma_s,\ \gamma_a,\ \{\mathcal{A}_c,\mathcal{B}_c,\mathcal{C}_c,\mathcal{D}_c\}, \\ \textit{s.t.} & Y < \bar{Y},\ U < \bar{U},\ \$ < \bar{\$}, \\ & \gamma_s < \bar{\gamma}_s,\ \gamma_a < \bar{\gamma}_a. \end{cases} \tag{6.21}$$

A solution exists if and only if there are vectors γ_s, γ_a and matrices X, $\mathcal{Y}$, $\mathcal{L}$, $\mathcal{F}$, and $\mathcal{Q}$ such that the following linear matrix inequalities are satisfied:

$$\begin{cases} \textit{Given:} & \bar{U},\ \bar{Y},\ \bar{\$},\ \bar{\gamma}_s,\ \bar{\gamma}_a, \\ \textit{Find:} & \gamma_s,\ \gamma_a,\ X,\ \mathcal{Y},\ \mathcal{L},\ \mathcal{F},\ Q, \\ \textit{s.t.} & p_s^T\gamma_s + p_a^T\gamma_a < \bar{\$},\ \gamma_s < \bar{\gamma}_s,\ \gamma_a < \bar{\gamma}_a, \\ & \begin{bmatrix} \bar{Y} & \mathcal{C}X & \mathcal{C} \\ (\bullet)^T & X & I \\ (\bullet)^T & (\bullet)^T & \mathcal{Y} \end{bmatrix} > 0, \\ & \begin{bmatrix} \bar{U} & \mathcal{L} & 0 \\ (\bullet)^T & X & I \\ (\bullet)^T & (\bullet)^T & \mathcal{Y} \end{bmatrix} > 0, \\ & \begin{bmatrix} \textit{Sym}(\Phi_{11}) & \Phi_{12} \\ (\bullet)^T & \Phi_{22} \end{bmatrix} < 0, \end{cases} \tag{6.22}$$

where:

$$\Phi_{11} = \begin{bmatrix} \mathcal{A}_p X + \mathcal{B}_p \mathcal{L} & \mathcal{A}_p \\ \mathcal{Q} & Y\mathcal{A}_p + \mathcal{F}\mathcal{M}_p \end{bmatrix}, \tag{6.23}$$

$$\Phi_{21} = \begin{bmatrix} \mathcal{D}_p & \mathcal{D}_a & 0 \\ \mathcal{Y}\mathcal{D}_a & \mathcal{Y}\mathcal{D}_a & \mathcal{F}\mathcal{E} \end{bmatrix}, \tag{6.24}$$

$$\Phi_{11} = \begin{bmatrix} -\mathcal{W}_p^{-1} & 0 & 0 \\ 0 & -\Gamma_a & 0 \\ 0 & 0 & -\Gamma_s \end{bmatrix}, \tag{6.25}$$

and Sym$(\bullet) = (\bullet) + (\bullet)^T$*. Under these conditions, all closed-loop controllers can be found as:*

$$\begin{bmatrix} \mathcal{A}_c & \mathcal{B}_c \\ \mathcal{C}_c & \mathcal{D}_c \end{bmatrix} = \begin{bmatrix} \mathcal{V}^{-1} & -\mathcal{V}^{-1}\mathcal{Y}\mathcal{B}_p \\ 0 & I \end{bmatrix} \begin{bmatrix} \mathcal{Q} - \mathcal{Y}\mathcal{A}_p X & \mathcal{F} \\ \mathcal{L} & 0 \end{bmatrix} \begin{bmatrix} \mathcal{U}^{-1} & 0 \\ -\mathcal{M}_p X \mathcal{U}^{-1} & I \end{bmatrix}, \tag{6.26}$$

where $\mathcal{V}$ *and* $\mathcal{U}$ *are nonsingular square matrices satisfying* $\mathcal{Y}X + \mathcal{V}\mathcal{U} = I$*.*

Proof. To reach the conditions in Eq. (6.21), the following inequalities shall be satisfied.

1). Total money spent on sensors and actuators should be limited by the budget constraint:

$$p_a^T \gamma_a + p_s^T \gamma_s < \bar{\$}, \tag{6.27}$$

$$\gamma_a < \bar{\gamma}_a, \tag{6.28}$$

$$\gamma_s < \bar{\gamma}_s, \tag{6.29}$$

2). Take the covariance of Eq. (6.16), the asymptotically stable system should satisfy:

$$\begin{bmatrix} \boldsymbol{\mathcal{A}}_{cl}\tilde{X} + \tilde{X}\boldsymbol{\mathcal{A}}_{cl}^{T} & \boldsymbol{B}_{cl} \\ \boldsymbol{B}_{cl}^{T} & -W^{-1} \end{bmatrix} < 0. \tag{6.30}$$

3). Take the covariance of Eqs. (6.17) and (6.18) and using Schur's complement:

$$\begin{bmatrix} \bar{Y} & \boldsymbol{C}_{cl}\tilde{X} \\ \tilde{X}\boldsymbol{C}_{cl}^{T} & \tilde{X} \end{bmatrix} > 0, \tag{6.31}$$

$$\begin{bmatrix} \bar{U} & \boldsymbol{\mathcal{E}}_{cl}\tilde{X} \\ \tilde{X}\boldsymbol{\mathcal{E}}_{cl}^{T} & \tilde{X} \end{bmatrix} > 0. \tag{6.32}$$

Since $\boldsymbol{\mathcal{A}}_{cl}\tilde{X}$ and $\boldsymbol{\mathcal{E}}_{cl}\tilde{X}$ are the product of unknown variables $\mathcal{G}$, $\boldsymbol{\mathcal{A}}_{cl}$ and $\boldsymbol{\mathcal{E}}_{cl}$, Eqs. (6.30) and (6.32) are non-convex matrices. Due to the many nice properties of LMI, such as get a global optimization solution and fast in computation, we would like to convert Eqs. (6.30) and (6.32) into LMIs.

Denote the state covariance matrix $\tilde{X}$ from Eq. (6.15) and its inverse as the following:

$$\tilde{X} = \begin{bmatrix} X & \mathcal{U}^{T} \\ \mathcal{U} & X_c \end{bmatrix}, \; \tilde{X}^{-1} = \begin{bmatrix} \mathcal{Y} & \mathcal{V} \\ \mathcal{V}^{T} & \mathcal{Y}_c \end{bmatrix}. \tag{6.33}$$

Define the following transformation [133]:

$$T = \begin{bmatrix} I & \mathcal{Y} \\ 0 & \mathcal{V}^{T} \end{bmatrix}. \tag{6.34}$$

Eqs. (6.30), (6.31), and (6.32) are equivalent to the following inequalities by a congruence transformation:

$$\begin{bmatrix} T^T & 0 \\ 0 & I \end{bmatrix} \begin{bmatrix} \boldsymbol{\mathcal{A}}_{cl}\tilde{X} + \tilde{X}\boldsymbol{\mathcal{A}}_{cl}^T & \boldsymbol{B}_{cl} \\ \boldsymbol{B}_{cl}^T & -W^{-1} \end{bmatrix} \begin{bmatrix} T & 0 \\ 0 & I \end{bmatrix} < 0, \tag{6.35}$$

$$\begin{bmatrix} I & 0 \\ 0 & T^T \end{bmatrix} \begin{bmatrix} \bar{Y} & \boldsymbol{\mathcal{C}}_{cl}\tilde{X} \\ \tilde{X}\boldsymbol{\mathcal{C}}_{cl}^T & \tilde{X} \end{bmatrix} \begin{bmatrix} I & 0 \\ 0 & T \end{bmatrix} > 0, \tag{6.36}$$

$$\begin{bmatrix} I & 0 \\ 0 & T^T \end{bmatrix} \begin{bmatrix} \bar{U} & \boldsymbol{\mathcal{E}}_{cl}\tilde{X} \\ \tilde{X}\boldsymbol{\mathcal{E}}_{cl}^T & \tilde{X} \end{bmatrix} \begin{bmatrix} I & 0 \\ 0 & T \end{bmatrix} > 0, \tag{6.37}$$

we get:

$$\begin{bmatrix} T^T(\boldsymbol{\mathcal{A}}_{cl}\tilde{X} + \tilde{X}\boldsymbol{\mathcal{A}}_{cl}^T)T & T^T\boldsymbol{\mathcal{B}}_{cl} \\ \boldsymbol{\mathcal{B}}_{cl}^T T & -W^{-1} \end{bmatrix} < 0, \tag{6.38}$$

$$\begin{bmatrix} \bar{Y} & \boldsymbol{\mathcal{C}}_{cl}\tilde{X}T \\ T^T\tilde{X}\boldsymbol{\mathcal{C}}_{cl}^T & T^T\tilde{X}T \end{bmatrix} > 0, \tag{6.39}$$

$$\begin{bmatrix} \bar{U} & \boldsymbol{\mathcal{E}}_{cl}\tilde{X}T \\ T^T\tilde{X}\boldsymbol{\mathcal{E}}_{cl}^T & T^T\tilde{X}T \end{bmatrix} > 0. \tag{6.40}$$

Eqs. (6.38), (6.39), (6.40) and become LMIs if the following matrices are affine for some transformation T:

$$T^T\boldsymbol{\mathcal{A}}_{cl}\tilde{X}T, T^T\boldsymbol{\mathcal{B}}_{cl}, \boldsymbol{\mathcal{C}}_{cl}\tilde{X}T, T^T\tilde{X}T, \boldsymbol{\mathcal{E}}_{cl}\tilde{X}T. \tag{6.41}$$

Substitute the transformation matrix T defined in Eq. (6.34), these matrices are found as:

$$T^T \boldsymbol{\mathcal{A}}_{cl} \tilde{X} T = \begin{bmatrix} \Theta_{11} & \mathcal{A}_p \\ \Theta_{21} & \Theta_{22} \end{bmatrix}, \tag{6.42}$$

$$T^T \boldsymbol{\mathcal{B}}_{cl} = \begin{bmatrix} \mathcal{D}_p & \mathcal{D}_a & 0 \\ \mathcal{Y}\mathcal{D}_p & \mathcal{Y}\mathcal{D}_a & \mathcal{V}B_c\mathcal{E} \end{bmatrix}, \tag{6.43}$$

$$\boldsymbol{\mathcal{C}}_{cl} \tilde{X} T = \begin{bmatrix} \mathcal{C}_p X & \mathcal{C}_p \end{bmatrix}, \tag{6.44}$$

$$T^T \tilde{X} T = \begin{bmatrix} X & I \\ I & \mathcal{Y} \end{bmatrix}, \tag{6.45}$$

$$\boldsymbol{\mathcal{E}}_{cl} \tilde{X} T = \begin{bmatrix} D_c \mathcal{M}_p X & 0 \end{bmatrix}, \tag{6.46}$$

where $\Theta_{11} = \mathcal{A}_p X + \mathcal{B}_p \mathcal{D}_c \mathcal{M}_p X + \mathcal{B}_p \mathcal{C}_c \mathcal{U}$, $\Theta_{21} = \mathcal{V}\mathcal{A}_c\mathcal{U} + \mathcal{Y}\mathcal{A}_p X + \mathcal{V}\mathcal{B}_c\mathcal{M}_p X$, $\Theta_{22} = \mathcal{Y}\mathcal{A}_p + \mathcal{V}\mathcal{B}_c\mathcal{M}_p$.

Denote the change of variables as the following:

$$\mathcal{L} = D_c \mathcal{M}_p X, \tag{6.47}$$

$$\mathcal{F} = \mathcal{V} B_c, \tag{6.48}$$

$$\mathcal{Q} = \mathcal{V} A_c \mathcal{U} + \mathcal{Y}\mathcal{A}_p X + \mathcal{V} B_c \mathcal{M}_p X. \tag{6.49}$$

Matrices (6.46) - (6.42) now can be written as:

$$E_{cl} \tilde{X} T = \begin{bmatrix} \mathcal{L} & 0 \end{bmatrix}, \tag{6.50}$$

$$T^T \boldsymbol{\mathcal{A}}_{cl} \tilde{X} T = \begin{bmatrix} \mathcal{A}_p X + \mathcal{B}_p \mathcal{L} & \mathcal{A}_p \\ \mathcal{Q} & \mathcal{Y}\mathcal{A}_p + \mathcal{F}\mathcal{M}_p \end{bmatrix}, \tag{6.51}$$

$$T^T B_{cl} = \begin{bmatrix} \mathcal{D}_p & \mathcal{D}_a & 0 \\ \mathcal{Y}\mathcal{D}_p & \mathcal{Y}\mathcal{D}_a & \mathcal{F}\mathcal{E} \end{bmatrix}. \tag{6.52}$$

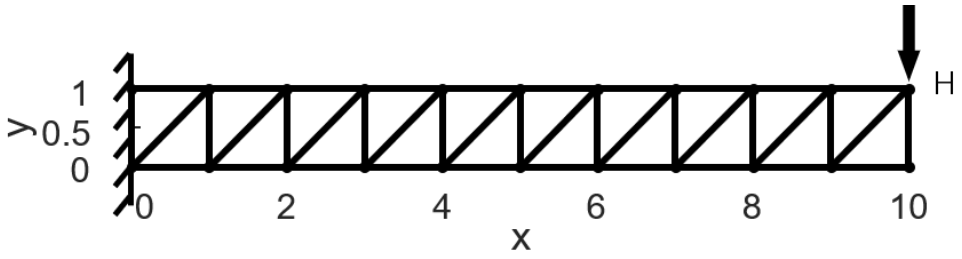

Figure 6.6: Configuration of a planer truss in the presence of a step load at the node H with the left two nodes fixed to a wall in the given direction. The aspect ratio (length over width) of the truss is 10:1.

Eqs. (6.31) - (6.30) are now transformed into the LMIs in (6.22), whcih can be solved by *MATLAB* CVX toolbox.

□

6.5 Numerical examples

6.5.1 Comparison between nonlinear and linearized models

Before using the linearized tensegrity dynamics, we have to verify the linearized dynamics Eq. (6.1) is accurate enough compared with nonlinear dynamics Eq. (4.67) for analysis. Here, we take a planer cantilever truss (22 nodes, including the two fixed ones to the vertical wall) with a vertical force at the end node for the nonlinear and linearized models to see the coordinate errors, as shown in Fig. 6.6. The cantilever truss is 10 m long and 1 m wide. The black lines are steel bars. The radius, density, and Young's modulus of the bars are 0.0282 m, 7,870 kg/m^3, 206.04 GPa, respectively. We choose time step 1.0×10^{-4} s and vertical force F = -1.0×10^6 N to perform the simulation.

The error time history of the X- and Y-coordinates of all the nodes between the nonlinear and linearized dynamics are shown in Figs. 6.8 and 6.9. The configuration of the two models at t = 0.5 s, 1 s, and 5 s are shown in Fig. 6.7. It is clear that as the deformation increase, the non-linearity becomes larger, which brings more errors between the linear and nonlinear models. For relative large deformations, i.e., t = 5 s, the coordinate of the node at the bottom right obtained by the

nonlinear model is (9.805,-1.351) and by the linear model is (9.913,-1.37). The maximum error in X-direction and Y-direction is 0.108 m and 0.019 m, which is 1.08% and 1.9% with respect to the horizontal length 10 m and vertical length 1 m of the truss. For small deformations, i.e., t = 0.5 s, the coordinate of the node at the bottom right obtained by the nonlinear model is (9.93,-0.6323) and by the linear model is (9.955,-0.6326). The maximum error in X-direction and Y-direction is 0.025 m and 0.0003 m, which is 0.25% and 0.03% with respect to the horizontal and vertical length of the truss. That is, the linearized dynamics model is accurate.

6.5.2 Case 1: Economic sensor/actuator selection for tensegrity airfoils

The sensor/actuator selection algorithm is applied to the tensegrity airfoil structure presented in section 6.2. A complexity of $q = 5$ has been chosen to demonstrate the algorithm, as shown in Figure 6.10. For this example, sensors are selected to measure the positions in $X-$ and $Y-$ directions of the 13 nodes, while actuators are selected to control the 26 strings. Other parameters are chosen as: sensor/actuator budget $\bar{\$}$ = 50, actuator precision limit $\bar{\gamma}_a = 16$, sensor precision limit $\bar{\gamma}_s = 16$, actuator precision unit price p_a = 1, sensor precision unit price p_s = 1, control upper bound $\bar{U} = 0.1I$, plant noise $W_p = 0.01I$. The specific distribution of how precision is allocated on each actuator and sensor under the limit of the budget is listed in Tables 6.2 and 6.3. It can be seen that among the 26 actuators, the indices of the top eight actuators are 14, 5, 10, 15, 11, 16, 1, and 6, which are mainly concentrated close to the trailing edge sections of the tensegrity airfoil. While, among the 26 sensors, the indices of the top eight sensors are 10, 26, 24, 22, 4, 14, 6, 16 are mainly locates below the middle horizontal bar of the tensegrity airfoil. The results agree with intuitive is that: 1). The trailing edge of the foil is more flexible, which requires more sensors close to the end of the tail. 2). The strings below the middle horizontal bars have bigger lever arms than the upper side, which makes the structure bend downward more easily. In other words, the lower side strings are more efficient in control, which are suitable to be selected as actuators. The list of allocations of precision can also help guide the selection of actuators and sensors.

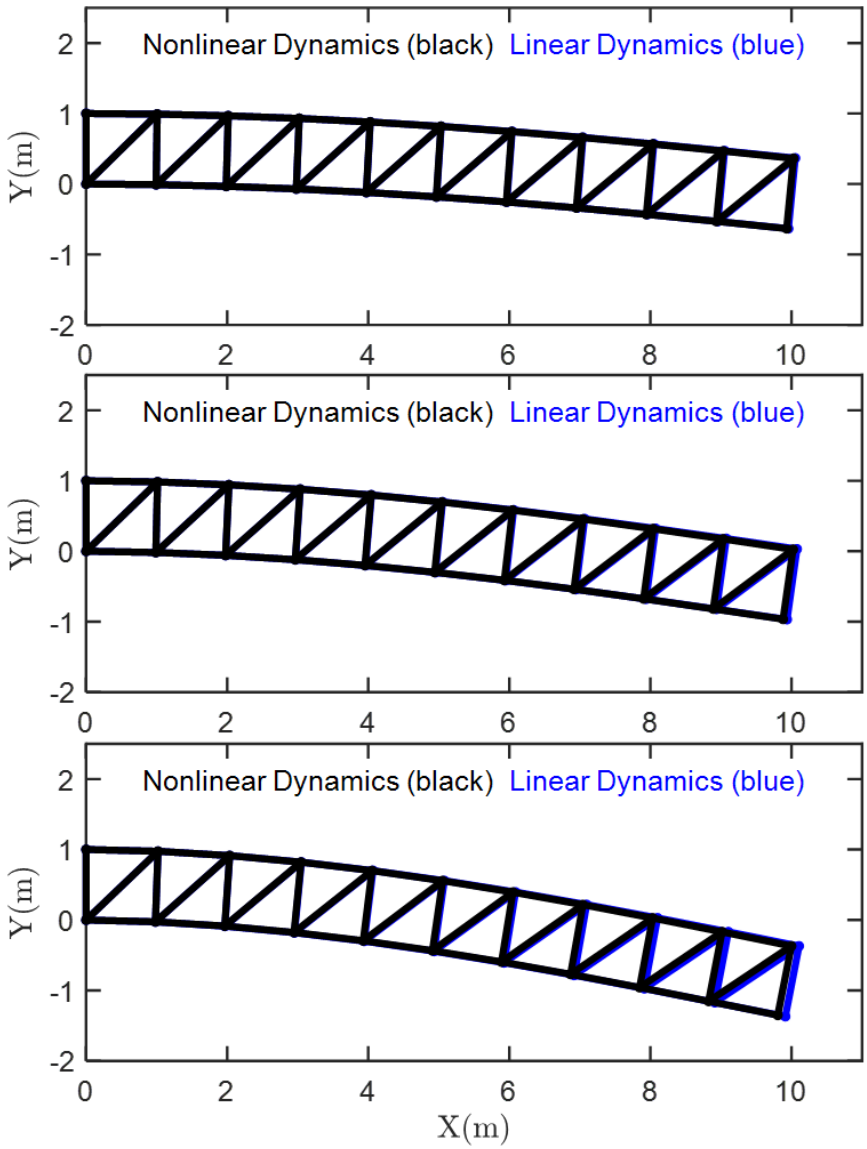

Figure 6.7: Comparison between the nonlinear and linear dynamics models. Sub-figures from top to bottom are dynamics response of the two models at t = 0.5 s, t = 1 s, and t = 5s.

Table 6.2: Precision allocation results for actuators.

Precision Rank	Precision Allocation	Actuator Index
1	3.3270	14
2	3.0800	5
3	2.2628	10
4	2.0854	15
5	2.0018	11
6	1.9177	16
7	1.9134	1
8	1.9013	6
9	1.8601	12
10	1.8269	2
11	1.8133	17
12	1.7854	20
13	1.7829	13
14	1.7440	22
15	1.7362	24
16	1.7189	3
17	1.7169	26
18	1.7109	18
19	1.6657	7
20	1.6582	4
21	1.5349	8
22	1.5132	21
23	1.4898	23
24	1.4760	25
25	1.4139	9
26	1.2124	19

Table 6.3: Precision allocation results for sensors.

Precision Rank	Precision Allocation	Sensor Index
1	0.5833	10
2	0.3477	26
3	0.2942	24
4	0.1301	22
5	0.1158	4
6	0.1093	14
7	0.1030	6
8	0.0778	16
9	0.0413	8
10	0.0273	18
11	0.0033	2
12	0.0033	12
13	0.0032	20
14	0.0012	11
15	0.0012	19
16	0.0012	17
17	0.0012	13
18	0.0012	21
19	0.0012	15
20	0.0011	23
21	0.0011	25
22	0.0010	9
23	0.0010	7
24	0.0010	5
25	0.0009	3
26	0.0009	1

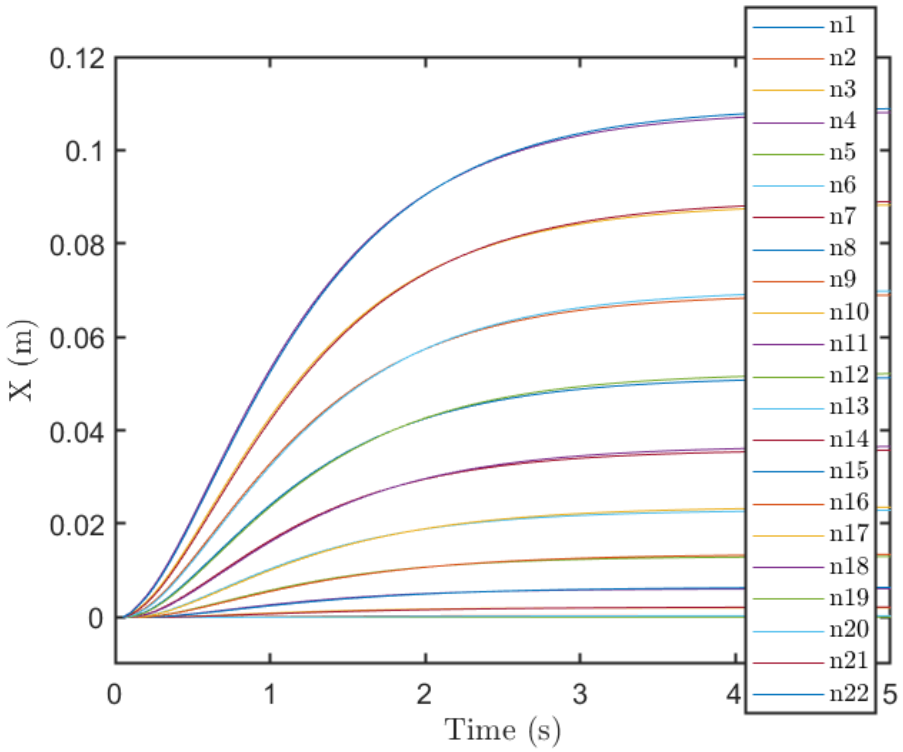

Figure 6.8: The coordinate error between the nonlinear and linear dynamics model of all the nodes in X-direction.

6.5.3 Case 2: Sensitive study of the budget, control, and performance

In this section we conduct different cases of control energy $\bar{U}$ and budget constraints $\bar{\$}$, and solve the problem given by Eq. (6.22) while optimizing a scalar of $tr(\bar{Y})$. The tensegrity morphing airfoil example in section 6.5.2 has been employed, while $\bar{U}$ = [1.0×10^{-6}, 1.0×10^{-5}, 1.0×10^{-4}, 1.0×10^{-3}, 1.0×10^{-2}, 1.0×10^{-1}, 1.0] and $\bar{\$}$ = [10, 20, 40, 80, 160, 320, 640, 1,280] are investigated. The result is shown in in Figure 6.11.

Let us have a close look at the surface plot and analyze the plot in two aspects. 1). The influence of Sensor/Actuator Cost. For Control Energy vector $\bar{U}_1 = 1.0 \times 10^{-6}$ and all the Sensor/Actuator Cost $\bar{\$}$, the output covariance is $\bar{Y}_{\bar{U}_1,\bar{\$}}$ = [14.41, 7.246, 3.648, 1.852, 0.9587, 0.512, 0.4206, 0.4205]. For Control Energy vector $\bar{U}_7 = 1.0$ and all the Sensor/Actuator Cost $\bar{\$}$, the output covariance is $\bar{Y}_{\bar{U}_7,\bar{\$}}$ = [13.54, 6.798, 3.42, 1.735, 0.8915, 0.4747, 0.3227, 0.3102]. One may notice that the enhancement of performance due to budget increase is huge at the beginning but would diminish

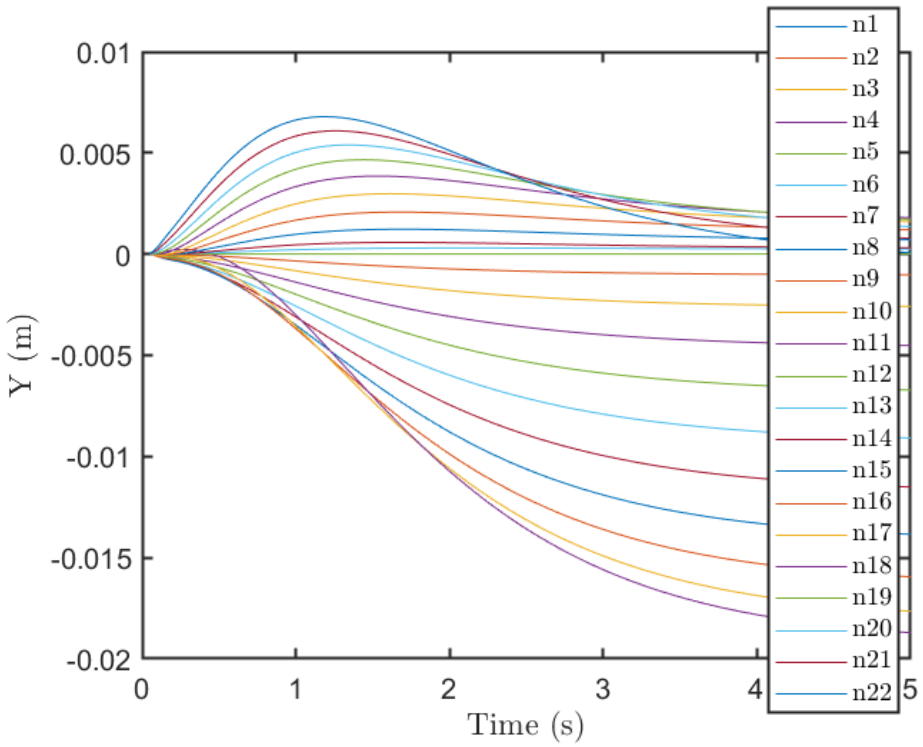

Figure 6.9: The coordinate error between the nonlinear and linear dynamics model of all the nodes in Y-direction.

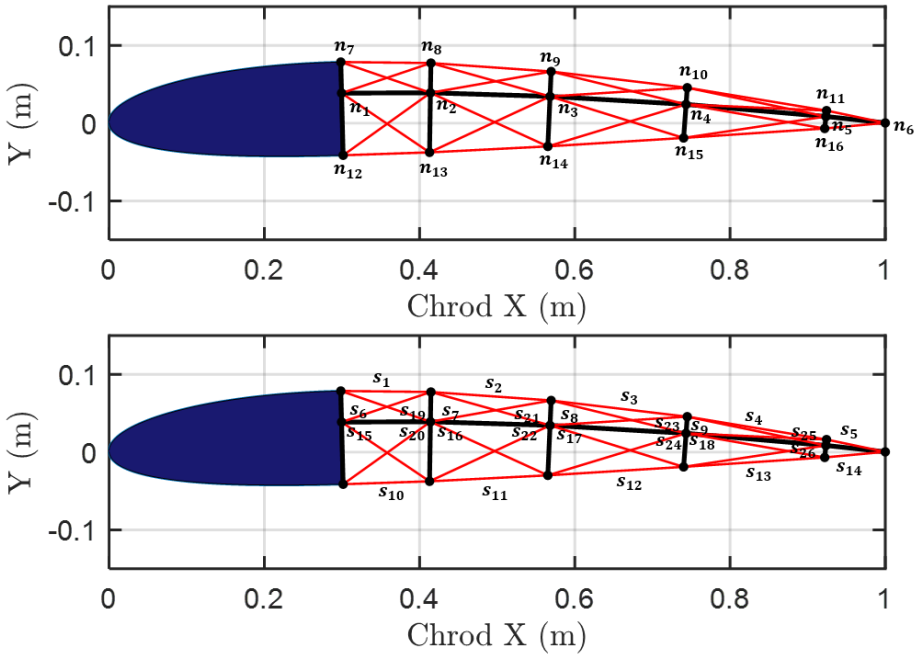

Figure 6.10: Node and string notations of the tensegrity NACA 2412 airfoil.

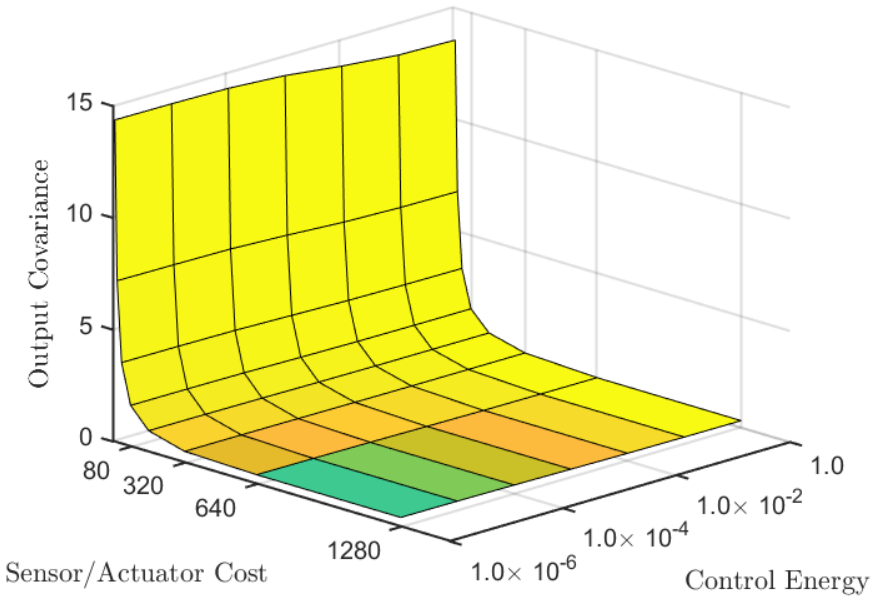

Figure 6.11: Sensitive Study of the control energy, sensor/actuator cost, and output covariance. The x-axis is the sensor/actuator cost $\bar{\$}$ = [10, 20, 40, 80, 160, 320, 640, 1,280]. The y-axis is the control energy $\bar{U}$ = [1.0×10^{-6}, 1.0×10^{-5}, 1.0×10^{-4}, 1.0×10^{-3}, 1.0×10^{-2}, 1.0×10^{-1}, 1.0].

as more funds are added. When budget is insufficient, adding funds would allow more precision allocation on sensitive actuators and sensors that would impact performance more than others. With more funds available, eventually, there will be no more improvement when all sensors and actuators are saturated with the highest possible precision in the market. 2.) The influence of Control Energy. For Sensor/Actuator Cost $\bar{\$}_1 = 10$ and Control Energy vector $\bar{U}$, the output covariance is $\bar{Y}_{\bar{U},\bar{\$}_1}$ = [14.41, 14.39, 14.34, 14.17, 13.85, 13.61, 13.54]. For Sensor/Actuator Cost $\bar{\$}_8 = 1,280$ and Control Energy vector $\bar{U}$, the output covariance is $\bar{Y}_{\bar{U},\bar{\$}_8}$ = [0.4205, 0.4114, 0.3908, 0.3632, 0.3305, 0.3269, 0.3102]. It can be observed that as control energy increases, the output covariance decreases, which means the system performance is becoming better. But the slope is relatively small. Comparing the Sensor/Actuator Cost and Control Energy influence, we can see that cost is a more important parameter than control energy. That is to say, when the cost is bounded, one can increase the system performance, but not as obvious as increasing the budget. This result will be instructive for early-stage structure and control system design.

6.6 Conclusion

This chapter presents a method for integrating the economic sensor/actuator selection and covariance control design for tensegrity robots. We first derived the linearized tensegrity dynamics and formulated it as a standard state-space form. The accuracy of the linear model is tested by a truss example subject to a downward vertical force at the end to simulate its bending. The node coordinate errors by the nonlinear and linear tensegrity model are compared. Results show that as the deformation of the truss increase, the node coordinate errors becomes bigger. For a relatively large deformation, the maximum error between the nonlinear and linear model in x- and y-direction are 1.08% and 1.9%. Then, using the linear dynamic model, we first studied the uncertainty of joints by a T_2D_1 tower example. Results show that as the uncertainty increases in one node or a combination of several nodes, the impact on the top node of the tower increases. The L_2 norm of the top node is more influenced by the uncertainty of the D-bar units in the T_2D_1 tower than the T-Bar unit. Then, we give the algorithm for minimizing the output covariance of the tensegrity robots subject to the specified sensor/actuator budget and control covariance upper bounds by solving the precision of the sensor/actuator. The problem is converted into an equivalent convex problem, given by LMIs. The approach is demonstrated by a 2D tensegrity morphing airfoil. Results show that sensors (obtain node positions) at the trailing edge and the actuators (change the string length) at the bottom of the structure are more important. In the sensitive study, results show that sensor/actuator budgets are critical than control energy to promote the output performance. The approaches developed in this chapter paves the way to the economic sensor/actuator selection for integrating structure and control designs.

7. CONCLUSIONS

Universities have compartmentalized science into small packages for easy management. But as students learn the individual component technologies, they are required to integrate these disciplines in ways that they had no theory for in their education. So, the traditional approach to design systems is making a structure first, then performing material studies and fluid analysis, and then adding control. Of course, this is not the best way to do the system design, i.e., one can make a structure very hard to control. Indeed, engineering has left us with many components technologies without rules how we could component together to make systems. And the purpose of this research is to show how we can integrate structure, materials, fluids, and control designs. Due to the many benefits of tensegrity structures, the tensegrity paradigm is chosen to demonstrate the fundamental integration ideas. The major conclusions of this work are as follows.

A general framework of the minimal mass design for any solid or hollow bar tensegrity structures with and without gravity is derived. Results show that if yielding is the mode of failure for a solid and hollow bar (with the same inner cross-section area), one cannot save mass. If buckling is the mode of failure, one can use a solid or hollow triangular cross-section shape to save 9.06% or 17.3% mass compared with a circular one. A family of deployable lunar towers and deployment methods are presented and studied, including mass, tower height, prestress, payload, disturbances, and packaging plan. This minimal mass design framework can be used for the static design of any truss or tensegrity structures.

The dynamics of class-1 and class-k structures with fluid forces incorporated are formulated. Results show that fluid forces and velocity can give the structure damping and pushing force to the dynamics response of the structure. Then, we also presented structures interfaces fluid by a skin (membrane) on the tensegrity structure. We also present an approach to airfoil discretization and tensegrity airfoil design. The fluid forces are obtained by the panel method and then integrated into the structure nodes with force and moment equilibrium satisfied. The developed principles enable our ability to study various kinds of fluid-based tensegrity structures.

A finite element analysis approach to nonlinear tensegrity dynamics based on the Lagrangian method with a nodal coordinate vector as the variable is derived. This approach allows comprehensive studies on any tensegrity systems accurately: 1. Performing rigid body dynamics with acceptable errors is achieved by setting relatively high stiffness for bars in the simulation. 2. Simulating FEM dynamics accurately, where bars and strings can have elastic or plastic deformations. 3. Dealing with various kinds of boundary conditions, for example, fixing or applying static/dynamic loads at any nodes in any direction (i.e., gravity, specified forces, or arbitrary vibrations). 4. Conducting accurate modal analysis, including natural frequency and corresponding modes. The method is compared with analytical solutions of rigid body dynamics and FEM software ANSYS. This study provides a very accurate tensegrity dynamics simulation method. The results allow one to have a more comprehensive understanding of the performance of both structures and materials.

Based on the class-k tensegrity dynamics, a nonlinear shape control law for tensegrity structures is derived. The control variables, force densities in strings, turn out to be linearly in the nonlinear control law. The shape control law demonstrated the successful control of the morphing airfoils. The approach can also be used to design tensegrity wings and shape control of other general tensegrity structures.

A method for integrating the economic sensor/actuator selection and covariance control design for tensegrity robots is given. A linearized tensegrity dynamics model is formulated, and the accuracy is tested. Using the linearized tensegrity dynamic model, we present the algorithm for minimizing the output covariance of the tensegrity robots subject to the specified sensor/actuator budget and control covariance upper bounds by solving the precision of the sensor/actuator. The problem is converted into several LMIs. The approach is demonstrated by a 2D tensegrity morphing airfoil. The approach allows one to select sensors and actuators with certain performance, control energy, and budget limitations satisfied.

The contribution of the system design approaches would allow us to have a better understating of physics, more efficient use of materials, more cost-effective design, less control energy, and better performance of engineering systems.

REFERENCES

[1] D. E. Ingber, N. Wang, and D. Stamenović, "Tensegrity, cellular biophysics, and the mechanics of living systems," Reports on Progress in Physics, vol. 77, no. 4, p. 046603, 2014.

[2] T. Liedl, B. Högberg, J. Tytell, D. E. Ingber, and W. M. Shih, "Self-assembly of three-dimensional prestressed tensegrity structures from dna," Nature nanotechnology, vol. 5, no. 7, pp. 520–524, 2010.

[3] M. Kjær, "Role of extracellular matrix in adaptation of tendon and skeletal muscle to mechanical loading," Physiological reviews, vol. 84, no. 2, pp. 649–698, 2004.

[4] G. Scarr, "A consideration of the elbow as a tensegrity structure," International Journal of Osteopathic Medicine, vol. 15, no. 2, pp. 53–65, 2012.

[5] M. Chen and R. E. Skelton, "A general approach to minimal mass tensegrity," Composite Structures, p. 112454, 2020.

[6] M. S. Selig, Summary of low speed airfoil data. SOARTECH publications, 1995.

[7] M. Chen, J. Liu, and R. E. Skelton, "Design and control of tensegrity morphing airfoils," Mechanics Research Communications, vol. 103, p. 103480, 2020.

[8] T. Bliss, T. Iwasaki, and H. Bart-Smith, "Central pattern generator control of a tensegrity swimmer," IEEE/ASME Transactions on Mechatronics, vol. 18, no. 2, pp. 586–597, 2012.

[9] A. P. Sabelhaus, H. Zhao, E. L. Zhu, A. K. Agogino, and A. M. Agogino, "Model-predictive control with inverse statics optimization for tensegrity spine robots," IEEE Transactions on Control Systems Technology, 2020.

[10] A. H. Simmons, C. A. Michal, and L. W. Jelinski, "Molecular orientation and two-component nature of the crystalline fraction of spider dragline silk," Science, vol. 271, no. 5245, pp. 84–87, 1996.

[11] R. B. Fuller, Synergetics: explorations in the geometry of thinking. Estate of R. Buckminster Fuller, 1982.

[12] H. Lalvani, "Origins of tensegrity: views of emmerich, fuller and snelson," International Journal of Space Structures, vol. 11, no. 1-2, pp. 27–27, 1996.

[13] S. Ma, M. Chen, and R. E. Skelton, "Design of a new tensegrity cantilever structure," Composite Structures, p. 112188, 2020.

[14] K. Koohestani, "On the analytical form-finding of tensegrities," Composite Structures, vol. 166, pp. 114–119, 2017.

[15] X.-F. Yuan, S. Ma, and S.-H. Jiang, "Form-finding of tensegrity structures based on the levenberg–marquardt method," Computers & Structures, vol. 192, pp. 171–180, 2017.

[16] J. Y. Zhang and M. Ohsaki, "Adaptive force density method for form-finding problem of tensegrity structures," International Journal of Solids & Structures, vol. 43, no. 18-19, pp. 5658–5673, 2006.

[17] S. Lee and J. Lee, "A novel method for topology design of tensegrity structures," Composite Structures, vol. 152, pp. 11–19, 2016.

[18] S. Ma, X.-F. Yuan, and S.-D. Xie, "A new genetic algorithm-based topology optimization method of tensegrity tori," KSCE Journal of Civil Engineering, vol. 23, no. 5, pp. 2136–2147, 2019.

[19] X. Xu, Y. Wang, and Y. Luo, "An improved multi-objective topology optimization approach for tensegrity structures," Advances in Structural Engineering, vol. 21, no. 1, pp. 59–70, 2018.

[20] G. Carpentieri, F. Fabbrocino, M. De Piano, V. Berardi, L. Feo, and F. Fraternali, "Minimal mass design of strengthening techniques for planar and curved masonry structures," in 7th European Congress on Computational Methods in Applied Sciences and Engineering,(ECCOMAS 2016), Chania, Crete, Greece, 2016.

[21] A. Fraddosio, G. Pavone, and M. D. Piccioni, "Minimal mass and self-stress analysis for innovative v-expander tensegrity cells," Composite Structures, vol. 209, pp. 754–774, 2019.

[22] M. Chen, R. Goyal, M. Majji, and R. E. Skelton, "Deployable tensegrity lunar tower," arXiv preprint arXiv:2009.12958, 2020.

[23] M. Chen, R. Goyal, M. Majji, and R. E. Skelton, "Design and analysis of a growable artificial gravity space habitat," Aerospace Science and Technology, vol. 106, p. 106147, 2020.

[24] K. Nagase and R. Skelton, "Double-helix tensegrity structures," Aiaa Journal, vol. 53, no. 4, pp. 847–862, 2015.

[25] G. Carpentieri, R. E. Skelton, and F. Fraternali, "Minimum mass and optimal complexity of planar tensegrity bridges," International Journal of Space Structures, vol. 30, no. 3-4, pp. 221–243, 2015.

[26] A. Fraddosio, S. Marzano, G. Pavone, and M. D. Piccioni, "Morphology and self-stress design of v-expander tensegrity cells," Composites Part B: Engineering, vol. 115, pp. 102–116, 2017.

[27] S. D. Guest, "The stiffness of tensegrity structures," IMA Journal of Applied Mathematics, vol. 76, no. 1, pp. 57–66, 2011.

[28] K. Liu, T. Zegard, P. P. Pratapa, and G. H. Paulino, "Unraveling tensegrity tessellations for metamaterials with tunable stiffness and bandgaps," Journal of the Mechanics and Physics of Solids, vol. 131, pp. 147–166, 2019.

[29] L.-Y. Zhang, S.-X. Li, S.-X. Zhu, B.-Y. Zhang, and G.-K. Xu, "Automatically assembled large-scale tensegrities by truncated regular polyhedral and prismatic elementary cells," Composite Structures, vol. 184, pp. 30–40, 2018.

[30] A. Amendola, G. Carpentieri, M. De Oliveira, R. Skelton, and F. Fraternali, "Experimental investigation of the softening–stiffening response of tensegrity prisms under compressive loading," Composite Structures, vol. 117, pp. 234–243, 2014.

[31] F. Fraternali, G. Carpentieri, and A. Amendola, "On the mechanical modeling of the extreme softening/stiffening response of axially loaded tensegrity prisms," Journal of the Mechanics and Physics of Solids, vol. 74, pp. 136–157, 2015.

[32] C. Sultan, Modeling, design, and control of tensegrity structures with applications. 1999.

[33] Y. Ma, Q. Zhang, Y. Dobah, F. Scarpa, F. Fraternali, R. E. Skelton, D. Zhang, and J. Hong,

"Meta-tensegrity: Design of a tensegrity prism with metal rubber," Composite Structures, vol. 206, pp. 644–657, 2018.

[34] K. Pajunen, P. Johanns, R. K. Pal, J. J. Rimoli, and C. Daraio, "Design and impact response of 3d-printable tensegrity-inspired structures," Materials & Design, vol. 182, p. 107966, 2019.

[35] Q. Zhang, D. Zhang, Y. Dobah, F. Scarpa, F. Fraternali, and R. E. Skelton, "Tensegrity cell mechanical metamaterial with metal rubber," Applied Physics Letters, vol. 113, no. 3, p. 031906, 2018.

[36] L. Zhao and E. A. P. Hernandez, "Theoretical study of tensegrity systems with tunable energy dissipation," Extreme Mechanics Letters, vol. 32, p. 100567, 2019.

[37] A. P. Sabelhaus, J. Bruce, K. Caluwaerts, P. Manovi, R. F. Firoozi, S. Dobi, A. M. Agogino, and V. SunSpiral, "System design and locomotion of superball, an untethered tensegrity robot," in 2015 IEEE international conference on robotics and automation (ICRA), pp. 2867–2873, IEEE, 2015.

[38] Z. Wang, K. Li, Q. He, and S. Cai, "A light-powered ultralight tensegrity robot with high deformability and load capacity," Advanced Materials, vol. 31, no. 7, p. 1806849, 2019.

[39] R. E. Skelton and M. C. De Oliveira, Tensegrity systems, vol. 1. Springer, 2009.

[40] R. E. Skelton and K. Nagase, "Tensile tensegrity structures," International Journal of Space Structures, vol. 27, no. 2-3, pp. 131–137, 2012.

[41] A. Tibert and S. Pellegrino, "Review of form-finding methods for tensegrity structures," International Journal of Space Structures, vol. 18, no. 4, pp. 209–223, 2003.

[42] M. Masic, R. E. Skelton, and P. E. Gill, "Algebraic tensegrity form-finding," International Journal of Solids and Structures, vol. 42, no. 16-17, pp. 4833–4858, 2005.

[43] L.-Y. Zhang, Y. Li, Y.-P. Cao, and X.-Q. Feng, "Stiffness matrix based form-finding method of tensegrity structures," Engineering structures, vol. 58, pp. 36–48, 2014.

[44] K. Nagase and R. Skelton, "Minimal mass tensegrity structures," Journal of The International Association for Shell and Spatial Structures, vol. 55, no. 1, pp. 37–48, 2014.

[45] G. Carpentieri, M. Modano, F. Fabbrocino, L. Feo, and F. Fraternali, "On the minimal mass reinforcement of masonry structures with arbitrary shapes," Meccanica, vol. 52, no. 7, pp. 1561–1576, 2017.

[46] F. Fraternali, G. Carpentieri, M. Modano, F. Fabbrocino, and R. Skelton, "A tensegrity approach to the optimal reinforcement of masonry domes and vaults through fiber-reinforced composite materials," Composite Structures, vol. 134, pp. 247–254, 2015.

[47] R. Goyal, M. Chen, M. Majji, and R. E. Skelton, "Motes: Modeling of tensegrity structures," Journal of Open Source Software, vol. 4, no. 42, p. 1613, 2019.

[48] R. E. Skelton, T. Iwasaki, and D. E. Grigoriadis, A unified algebraic approach to control design. CRC Press, 1997.

[49] U. Boz, R. Goyal, and R. E. Skelton, "Actuators and sensors based on tensegrity d-bar structures," Frontiers in Astronomy and Space Sciences, vol. 5, p. 41, 2018.

[50] R. Goyal, E. A. Peraza Hernandez, and R. E. Skelton, "Analytical study of tensegrity lattices for mass-efficient mechanical energy absorption," International Journal of Space Structures, vol. 34, no. 1-2, pp. 3–21, 2019.

[51] J. M. Gere and B. J. Goodno, "Mechanics of materials eight edition," 2009.

[52] G. H. Heiken, D. T. Vaniman, and B. M. French, "Lunar sourcebook-a user's guide to the moon," Research supported by NASA,. Cambridge, England, Cambridge University Press, 1991, 753 p. No individual items are abstracted in this volume., 1991.

[53] M. Chen, Y. Shen, R. Goyal, M. Majji, and R. E. Skelton, "Energy analysis of growth adaptable artificial gravity space habitat," in 2018 AIAA SPACE and Astronautics Forum and Exposition, p. 5109, 2018.

[54] I. A. Crawford, "Lunar resources: A review," Progress in Physical Geography, vol. 39, no. 2, pp. 137–167, 2015.

[55] P. Spudis, D. Bussey, S. Baloga, J. Cahill, L. Glaze, G. Patterson, R. Raney, T. Thompson, B. Thomson, and E. Ustinov, "Evidence for water ice on the moon: Results for anomalous polar craters from the lro mini-rf imaging radar," Journal of Geophysical Research: Planets,

vol. 118, no. 10, pp. 2016–2029, 2013.

[56] M. Duke, R. Gustafson, and E. Rice, "Mining of lunar polar ice," in 36th AIAA Aerospace Sciences Meeting and Exhibit, p. 1069, 1998.

[57] P. Tukkaraja, W. Cross, S. S. Ajitha, and B. Jasthi, "Lunar mining and processing for in situ resource utilization," in Earth and Space 2018: Engineering for Extreme Environments, pp. 401–413, American Society of Civil Engineers Reston, VA, 2018.

[58] J. Rostami, C. Dreyer, and B. Blair, "Lunar tunnel boring machines," in Earth and Space 2018: Engineering for Extreme Environments, pp. 240–252, American Society of Civil Engineers Reston, VA, 2018.

[59] G. Sanders, "Nasa Lunar ISRU Strategy," 2019.

[60] C. Sultan and R. Skelton, "Deployment of tensegrity structures," International Journal of Solids and Structures, vol. 40, no. 18, pp. 4637–4657, 2003.

[61] H. Klimke and S. Stephan, "The making of a tensegrity tower," in IASS 2004 Symposium, International Association for Shell and Spatial Structures, 2004.

[62] K. Yildiz and G. A. Lesieutre, "Effective beam stiffness properties of n-strut cylindrical tensegrity towers," AIAA Journal, vol. 57, no. 5, pp. 2185–2194, 2019.

[63] R. E. Skelton and M. C. de Oliveira, Tensegrity Systems. Springer US, 2009.

[64] D. Schrunk, B. Sharpe, B. L. Cooper, and M. Thangavelu, The moon: Resources, future development and settlement. Springer Science & Business Media, 2007.

[65] M. E. Abdallah, R. Platt, B. Hargrave, and F. Permenter, "Position control of tendon-driven fingers with position controlled actuators," in 2012 IEEE International Conference on Robotics and Automation, pp. 2859–2864, IEEE, 2012.

[66] C. Sultan, "Tensegrity deployment using infinitesimal mechanisms," International Journal of Solids and Structures, vol. 51, no. 21-22, pp. 3653–3668, 2014.

[67] V. Bundhoo, E. Haslam, B. Birch, and E. J. Park, "A shape memory alloy-based tendon-driven actuation system for biomimetic artificial fingers, part i: design and evaluation," Robotica, vol. 27, no. 1, pp. 131–146, 2009.

[68] H.-I. Kim, M.-W. Han, S.-H. Song, and S.-H. Ahn, "Soft morphing hand driven by sma tendon wire," Composites Part B: Engineering, vol. 105, pp. 138–148, 2016.

[69] R. J. Pike, "Depth/diameter relations of fresh lunar craters: Revision from spacecraft data," Geophysical Research Letters, vol. 1, no. 7, pp. 291–294, 1974.

[70] A. Molina-García, A. Fernández-Guillamón, E. Gómez-Lázaro, A. Honrubia-Escribano, and M. C. Bueso, "Vertical wind profile characterization and identification of patterns based on a shape clustering algorithm," IEEE Access, vol. 7, pp. 30890–30904, 2019.

[71] M. Jarraud, "Guide to meteorological instruments and methods of observation (wmo-no. 8)," World Meteorological Organisation: Geneva, Switzerland, vol. 29, 2008.

[72] G. Arioli and F. Gazzola, "A new mathematical explanation of what triggered the catastrophic torsional mode of the tacoma narrows bridge," Applied Mathematical Modelling, vol. 39, no. 2, pp. 901–912, 2015.

[73] A. Larsen, "Aerodynamics of the tacoma narrows bridge-60 years later," Structural Engineering International, vol. 10, no. 4, pp. 243–248, 2000.

[74] A. Korobenko, J. Yan, S. Gohari, S. Sarkar, and Y. Bazilevs, "Fsi simulation of two back-to-back wind turbines in atmospheric boundary layer flow," Computers & Fluids, vol. 158, pp. 167–175, 2017.

[75] T. Nakata and H. Liu, "A fluid–structure interaction model of insect flight with flexible wings," Journal of Computational Physics, vol. 231, no. 4, pp. 1822–1847, 2012.

[76] T. Richter, Fluid-structure interactions: models, analysis and finite elements, vol. 118. Springer, 2017.

[77] G. Hou, J. Wang, and A. Layton, "Numerical methods for fluid-structure interaction—a review," Communications in Computational Physics, vol. 12, no. 2, pp. 337–377, 2012.

[78] C. Sultan, M. Corless, and R. E. Skelton, "Linear dynamics of tensegrity structures," Engineering Structures, vol. 24, no. 6, pp. 671–685, 2002.

[79] R. Skelton, "Dynamics and control of tensegrity systems," in IUTAM symposium on vibration control of nonlinear mechanisms and structures, pp. 309–318, Springer, 2005.

[80] A. S. Wroldsen, V. Johansen, R. E. Skelton, and A. J. Sørensen, "Hydrodynamic loading of tensegrity structures," in Proceedings of SPIE, the International Society for Optical Engineering, pp. 61660C–1, Society of Photo-Optical Instrumentation Engineers, 2006.

[81] K. Nagase and R. Skelton, "Network and vector forms of tensegrity system dynamics," Mechanics Research Communications, vol. 59, pp. 14–25, 2014.

[82] J. Cheong and R. E. Skelton, "Nonminimal dynamics of general class k tensegrity systems," International Journal of Structural Stability and Dynamics, vol. 15, no. 02, p. 1450042, 2015.

[83] R. Goyal and R. E. Skelton, "Tensegrity system dynamics with rigid bars and massive strings," Multibody System Dynamics, vol. 46, no. 3, pp. 203–228, 2019.

[84] R. Goyal, M. Chen, M. Majji, and R. E. Skelton, "Gyroscopic tensegrity robots," IEEE Robotics and Automation Letters, vol. 5, no. 2, pp. 1239–1246, 2020.

[85] T. Iwasaki, J. Chen, and W. O. Friesen, "Biological clockwork underlying adaptive rhythmic movements," PNAS, vol. 111, no. 3, pp. 978–983, 2014.

[86] J. Chen, W. O. Friesen, and T. Iwasaki, "Mechanisms underlying rhythmic locomotion: Body-fluid interaction in undulatory swimming," J. Exp. Biol., vol. 214, pp. 561–574, 2011.

[87] G. I. Taylor, "Analysis of the swimming of long and narrow animals," Proceedings of the Royal Society of London. Series A. Mathematical and Physical Sciences, vol. 214, no. 1117, pp. 158–183, 1952.

[88] J. Chen, Mechanisms underlying undulatory swimming: From neuromuscular activation to body-fluid interactions. University of Virginia, 2011.

[89] H. Liu, J. Geng, and A. Luo, "Tensegrity configuration method for connecting tensegrity units along their axes," Composite Structures, vol. 162, pp. 341–350, 2017.

[90] K. Liu, J. Wu, G. H. Paulino, and H. J. Qi, "Programmable deployment of tensegrity structures by stimulus-responsive polymers," Scientific reports, vol. 7, no. 1, p. 3511, 2017.

[91] K. Kim, A. K. Agogino, and A. M. Agogino, "Rolling locomotion of cable-driven soft spherical tensegrity robots," Soft robotics, 2020.

[92] A. Luo and H. Liu, "Analysis for feasibility of the method for bars driving the ball tensegrity robot," Journal of Mechanisms and Robotics, vol. 9, no. 5, 2017.

[93] J. J. Rimoli, "On the impact tolerance of tensegrity-based planetary landers," in 57th AIAA/ASCE/AHS/ASC Structures, Structural Dynamics, and Materials Conference, p. 1511, 2016.

[94] J. L. Hess and A. O. Smith, "Calculation of potential flow about arbitrary bodies," Progress in Aerospace Sciences, vol. 8, pp. 1–138, 1967.

[95] P. E. Rubbert, "Theoretical characteristics of arbitrary wings by a non-planar vortex lattice method," Rept. D6-9244, 1964.

[96] L. L. Erickson, Panel methods: An introduction, vol. 2995. National Aeronautics and Space Administration, Office of Management . . . , 1990.

[97] J. L. Hess, "Panel methods in computational fluid dynamics," Annual Review of Fluid Mechanics, vol. 22, no. 1, pp. 255–274, 1990.

[98] M. Drela, "Xfoil: An analysis and design system for low reynolds number airfoils," in Low Reynolds number aerodynamics, pp. 1–12, Springer, 1989.

[99] C. L. Ladson, C. W. Brooks Jr, A. S. Hill, and D. W. Sproles, "Computer program to obtain ordinates for naca airfoils," 1996.

[100] L. Leifsson and S. Koziel, "Aerodynamic shape optimization by variable-fidelity computational fluid dynamics models: A review of recent progress," Journal of Computational Science, vol. 10, pp. 45–54, 2015.

[101] Z. Kan, H. Peng, B. Chen, and W. Zhong, "Nonlinear dynamic and deployment analysis of clustered tensegrity structures using a positional formulation fem," Composite Structures, vol. 187, pp. 241–258, 2018.

[102] Z. Kan, H. Peng, B. Chen, and W. Zhong, "A sliding cable element of multibody dynamics with application to nonlinear dynamic deployment analysis of clustered tensegrity," International Journal of Solids & Structures, p. S0020768317304730, 2017.

[103] M. Cefalo and J. M. Mirats-Tur, "A comprehensive dynamic model for class-1 tensegrity

systems based on quaternions," International journal of solids and structures, vol. 48, no. 5, pp. 785–802, 2011.

[104] H. Murakami, "Static and dynamic analyses of tensegrity structures. part ii. quasi-static analysis," International Journal of Solids and Structures, vol. 38, no. 20, pp. 3615–3629, 2001.

[105] S. Faroughi, H. H. Khodaparast, and M. I. Friswell, "Non-linear dynamic analysis of tensegrity structures using a co-rotational method," International Journal of Non-Linear Mechanics, vol. 69, pp. 55–65, 2015.

[106] J. J. Rimoli, "A reduced-order model for the dynamic and post-buckling behavior of tensegrity structures," Mechanics of Materials, vol. 116, pp. 146–157, 2018.

[107] K.-J. Bathe, "Finite element method," Wiley encyclopedia of computer science and engineering, pp. 1–12, 2007.

[108] G. Padfield and B. Lawrence, "The birth of flight control: An engineering analysis of the Wright brothers' 1902 glider," The Aeronautical Journal, vol. 107, no. 1078, pp. 697–718, 2003.

[109] A. Sofla, S. Meguid, K. Tan, and W. Yeo, "Shape morphing of aircraft wing: Status and challenges," Materials & Design, vol. 31, no. 3, pp. 1284–1292, 2010.

[110] X. Lachenal, S. Daynes, and P. M. Weaver, "Review of morphing concepts and materials for wind turbine blade applications," Wind energy, vol. 16, no. 2, pp. 283–307, 2013.

[111] K. Kuribayashi, K. Tsuchiya, Z. You, D. Tomus, M. Umemoto, T. Ito, and M. Sasaki, "Self-deployable origami stent grafts as a biomedical application of ni-rich tini shape memory alloy foil," Materials Science and Engineering: A, vol. 419, no. 1-2, pp. 131–137, 2006.

[112] J. Valasek, Morphing aerospace vehicles and structures, vol. 57. John Wiley & Sons, 2012.

[113] S. Barbarino, O. Bilgen, R. M. Ajaj, M. I. Friswell, and D. J. Inman, "A review of morphing aircraft," Journal of intelligent material systems and structures, vol. 22, no. 9, pp. 823–877, 2011.

[114] G. Reich and B. Sanders, "Introduction to morphing aircraft research," Journal of aircraft, vol. 44, no. 4, pp. 1059–1059, 2007.

[115] M. Santer and S. Pellegrino, "Topology optimization of adaptive compliant aircraft wing leading edge," in 48th AIAA/ASME/ASCE/AHS/ASC Structures, Structural Dynamics, and Materials Conference, p. 1714, 2007.

[116] M. Santer and S. Pellegrino, "Topological optimization of compliant adaptive wing structure," AIAA journal, vol. 47, no. 3, pp. 523–534, 2009.

[117] J. V. Henrickson, R. E. Skelton, and J. Valasek, "Shape control of tensegrity airfoils," in AIAA Guidance, Navigation, and Control Conference, p. 1864, 2016.

[118] K. W. Moored and H. Bart-Smith, "The analysis of tensegrity structures for the design of a morphing wing," Journal of Applied Mechanics, vol. 74, no. 4, pp. 668–676, 2007.

[119] K. W. Moored, S. A. Taylor, T. K. Bliss, and H. Bart-Smith, "Optimization of a tensegrity wing for biomimetic applications," in Decision and Control, 2006 45th IEEE Conference on, pp. 2288–2293, IEEE, 2006.

[120] M. Jones and K. Cohen, "Fuzzy control of a tensegrity based morphing uav wing," in Infotech@ Aerospace 2011, p. 1561, 2011.

[121] A. Jameson, "Aerodynamic design via control theory," Journal of scientific computing, vol. 3, no. 3, pp. 233–260, 1988.

[122] R. Motro, S. Najari, and P. Jouanna, "Static and dynamic analysis of tensegrity systems," in Shell and Spatial Structures: Computational Aspects, pp. 270–279, Springer, 1987.

[123] R. E. Skelton, J. P. Pinaud, and D. L. Mingori, "Dynamics of the shell class of tensegrity structures," Journal of the Franklin Institute, vol. 338, no. 2-3, pp. 255–320, 2001.

[124] R. Goyal and R. E. Skelton, "Joint optimization of plant, controller, and sensor/actuator design," in 2019 American Control Conference (ACC), pp. 1507–1512, IEEE, 2019.

[125] F. Li and R. E. Skelton, "Sensor/actuator selection for tensegrity structures," in Proceedings of the 45th IEEE Conference on Decision and Control, pp. 2332–2337, IEEE, 2006.

[126] M. Van De Wal and B. De Jager, "A review of methods for input/output selection,"

Automatica, vol. 37, no. 4, pp. 487–510, 2001.

[127] T. Singh, M. De Mauri, W. Decré, J. Swevers, and G. Pipeleers, "Feedback control of linear systems with optimal sensor and actuator selection," Journal of Vibration and Control, p. 1077546320939836, 2020.

[128] A. Argha, S. W. Su, A. Savkin, and B. Celler, "A framework for optimal actuator/sensor selection in a control system," International Journal of Control, vol. 92, no. 2, pp. 242–260, 2019.

[129] M. Güney and E. Eşkinat, "Optimal actuator and sensor placement in flexible structures using closed-loop criteria," Journal of Sound and Vibration, vol. 312, no. 1-2, pp. 210–233, 2008.

[130] F. Fahroo and M. A. Demetriou, "Optimal actuator/sensor location for active noise regulator and tracking control problems," Journal of Computational and Applied Mathematics, vol. 114, no. 1, pp. 137–158, 2000.

[131] C. Westermayer, A. Schirrer, M. Hemedi, and M. Kozek, "An advanced criterion for optimal actuator and sensor placement on complex flexible structures," IFAC Proceedings Volumes, vol. 42, no. 2, pp. 114–119, 2009.

[132] F. Li, M. C. de Oliveira, and R. E. Skelton, "Integrating information architecture and control or estimation design," SICE Journal of Control, Measurement, and System Integration, vol. 1, no. 2, pp. 120–128, 2008.

[133] F. Li, Economic resource allocation in system simulation and control design. PhD thesis, UC San Diego, 2006.